Complex Materials via Colloidal Crystallization

Dissertation
zur Erlangung des Grades
"Doktor der Naturwissenschaften"
im Promotionsfach Chemie

am Fachbereich Chemie, Pharmazie und Geowissenschaften
der Johannes Gutenberg-Universität in Mainz

vorgelegt von

Markus Retsch

geboren in Augsburg

Mainz, 2009

Die vorliegende Arbeit wurde in der Zeit von Oktober 2006 bis März 2009 in der Materialforschungsgruppe am Max-Planck-Institut für Polymerforschung angefertigt.

Dekan:

1. Berichterstatter:

2. Berichterstatter:

Übrige Mitglieder der Prüfungskommission:

Tag der mündlichen Prüfung: 04. Mai 2009

Wenn nicht geschehen wird,
was wir wollen,
so wird geschehen,
was besser ist.

Martin Luther

Table of Content

Abbreviations

2D	two-dimensional
3D	three-dimensional
AA	acrylic acid
ABA.2HCl	2,2′-Azobis(2-methylpropionamidine) dihydrochloride
AFM	atomic force microscopy
AllylMA	allyl methacrylate
BG	Bragg gap
BLS	Brillouin light scattering
BZ	Brillouin zone
CC	colloidal crystal
CVD	chemical vapor deposition
DIC	differential interference contrast
DSDP	dry, sparsely distributed particles
EDX	energy dispersive x-ray spectroscopy
fcc	face-centered cubic
HG	hybridization gap
IOIO	inverse opal in inverse opal
KOH	potassium hydroxide
KPS	potassium persulfate
LSPR	local surface plasmon resonance
MABP	4-Metharyloyloxybenzophenon
METAC	[2-(Methacryloyloxy)ethyl]trimethylammonium chloride
MMA	methyl methacrylate
MQ	milliQ water
NaPSS	sodium 4-vinylbenzenesulfonic acid
nBA	n-butyl acrylate
NR_4^+	N-trimethoxysilylpropyl-N,N,N-trimethylammonium chloride
NSL	nanosphere lithography
OM	optical microscopy
PDI	polydispersity index
PMMA	polymethylmethacrylate
PS	polystyrene
PS-COOH	PS latex with COOH surface groups
PS-SO_3H	PS latex with sulfonate surface groups
PS-SO_4H	PS latex with sulfate surface groups
RH	relative humidity
RIE	reactive ion etching
RMS	root means square
RT	room temperature
SAM	self-assembled monolayer
sccm	standard cubic centimeters per minute
SDS	sodium dodecylsulfate
SEM	scanning electron microscopy
TEOS	tetraethyl orthosilicate
Tg	glass transition temperature
VLD	vertical lifting deposition

Summary

The work presented in this thesis deals with complex materials, which were obtained by self-assembly of monodisperse colloidal particles, also called colloidal crystallization.
Two main fields of interest were investigated, the first dealing with the fabrication of colloidal monolayers and nanostructures, which derive there from. The second turned the focus on the phononic properties of colloidal particles, crystals, and glasses.
For the fabrication of colloidal monolayers a method is introduced, which is based on the sparse distribution of dry colloidal particles on a parent substrate. In the ensuing floating step the colloidal monolayer assembles readily at the three-phase-contact line, giving a 2D hexagonally ordered film under the right conditions. The unique feature of this fabrication process is an anisotropic shrinkage, which occurs alongside with the floating step. This phenomenon is exploited for the tailored structuring of colloidal monolayers, leading to designed hetero-monolayers by inkjet printing. Furthermore, the mechanical stability of the floating monolayers allows the deposition on hydrophobic substrates, which enables the fabrication of ultraflat, nanostructured surfaces. Densely packed arrays of crescent shaped nanoparticles have also been synthesized. It is possible to stack those arrays in a 3D manner allowing to mutually orientate the individual layers.
In a step towards 3D mesoporous materials a methodology to synthesize hierarchically structured inverse opals is introduced. The deposition of colloidal particles in the free voids of a host inverse opal allows for the fabrication of composite inverse opals on two length scales.
The phononic properties of colloidal crystals and films are characterized by Brillouin light scattering (BLS). At first the resonant modes of colloidal particles consisting of polystyrene, a copolymer of methylmethacrylate and butylacrylate, and of a silica core-PMMA shell topography are investigated, giving insight into their individual mechanical properties. The infiltration of colloidal films with an index matching liquid allows measuring the phonon dispersion relation. This leads to the assignment of band gaps to the material under investigation. Here, two band gaps could be found, one originating from the fcc order in the colloidal crystal (Bragg gap), the other stemming from the vibrational eigenmodes of the colloidal particles (hybridization gap).

1. General Introduction

Miniaturization has been gaining an increasing interest throughout the last two decades, leading to the field of nano-technology. Reducing the size of an object down to the nanometer range has several consequences on the fabrication strategies and on the physical properties of the resulting material. On the one hand classic assembly strategies by placing objects individually to their desired spots cease working, on the other hand the properties of the material is increasingly governed by its interface.

Two distinct approaches can be distinguished for the synthesis of nanostructured materials, these being a top-down or bottom-up approach. In the first case a bulk material is shaped to its desired size by removal of excessive material. Methods to achieve this are lithographic (electron-beam, 2-photon polymerization, UV) or etching (plasma, wet chemical) techniques. On the contrary, the bottom-up approach starts from single molecules, which are arranged into larger and larger structures to finally result in the desired material. Peculiar interaction forces are exploited to properly assemble the building blocks. Examples are hydrogen bonding in DNA, phase separation in block copolymer films, electrostatic interaction in layer-by-layer polyelectrolyte stacks, or capillary forces on colloidal particles.

Colloidal particles are generally objects of any shape with a size in the range from 1 nm to 1 µm.[1] They represent important components in current technologies such as foods, inks, paints, coatings, or cosmetics. Figure 1.1 shows a partial list of colloidal systems and their size range.

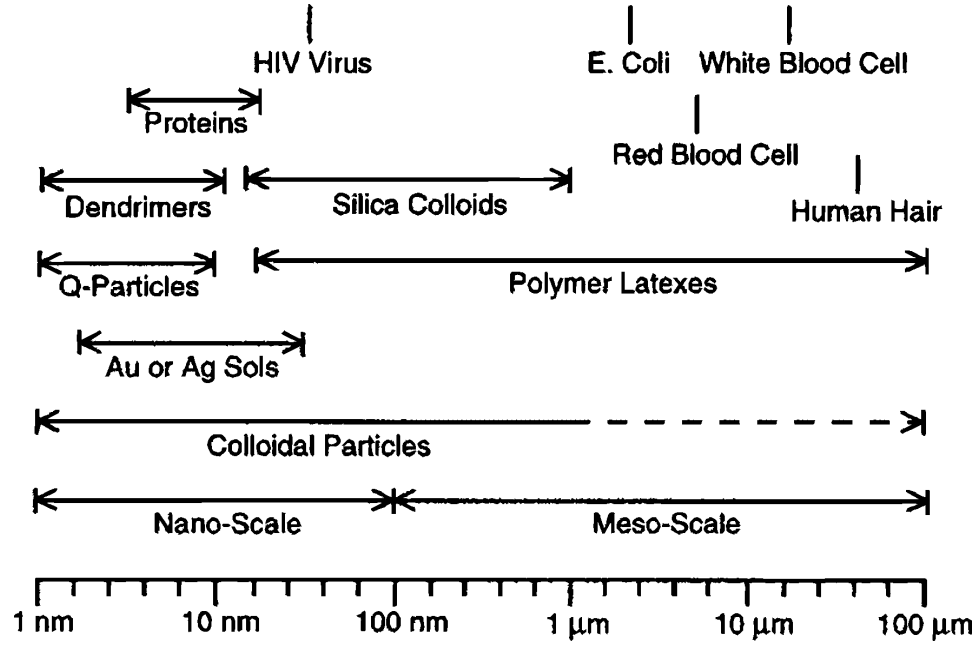

Figure 1.1. *A list of some representative colloidal systems, together with their typical size ranges. In this chart, the upper limit of the critical dimension for colloids has been extended from 1 µm to 100 µm.*[2]

Special attention has been paid to the fabrication of spherical colloidal particles, due to their relative ease of synthesis compared to non-spherical particles. One mainly distinguishes between inorganic (such as silica) and organic (such as polystyrene) particles.

1.1. Nanoparticle Synthesis

Colloidal polymer particles, consisting of polystyrene (PS), polymethyl methacrylate (PMMA), or others, are mainly synthesized by emulsion polymerization[3] or a variation of this, such as micro-,[4, 5] miniemulsion,[6, 7] emulsifier-free,[8-10] or dispersion polymerization.[11] These systems have been well investigated and only a brief summary will be given here.[12-14]

The polymerization in a micelle in an aqueous environment ensures an efficient heat transport and keeps the viscosity of the system low at all stages. Emulsion polymerization is therefore widely used in industry. The classic emulsion polymerization consists of monomer, surfactant, initiator, and water and yields uniformly size dispersed particles. The heterogeneity of such a system at an early stage is schematically depicted in Figure 1.2.

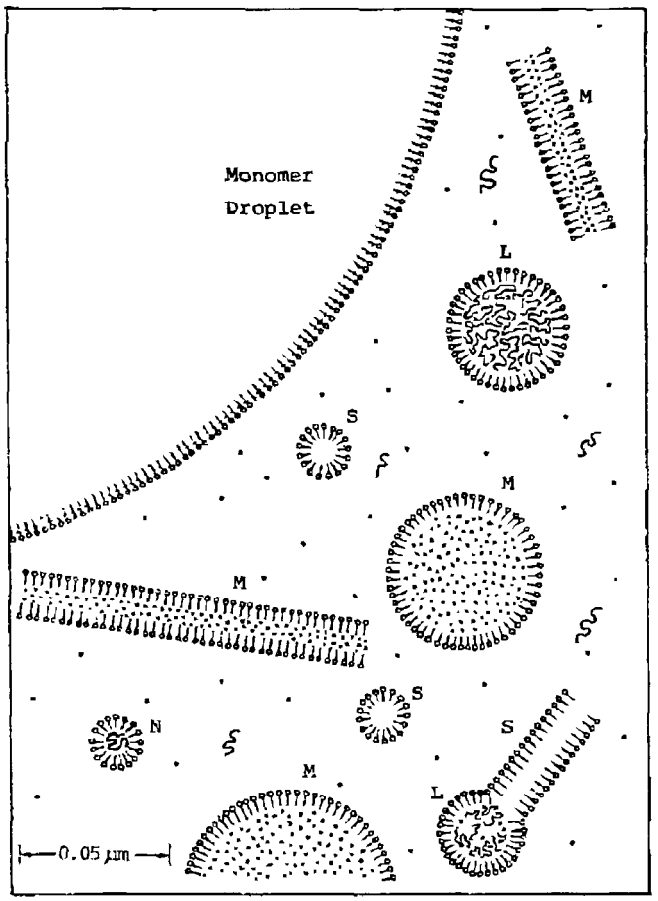

Figure 1.2. *Scheme of an emulsion polymerization at an early stage. A variety of species as indicated in the legend are present.*[13, 15]

Initiation starts in the aqueous phase by reaction of the water-soluble initiator with the water-insoluble monomer (the solubility product of the monomer in water is very small). Nucleation of particles can occur in three ways:

- micellar nucleation: a free radical in the aqueous phase enters a monomer swollen micelle (M).
- droplet nucleation: a free radical in the aqueous phase enters a monomer droplet.
- homogenous nucleation: a growing oligoradical in the aqueous phase exceeds its solubility and precipitates. Several precipitated oligoradicals aggregate until stable micelles are formed.

Normally the number of nucleated particles exceeds the number of monomer droplets by orders of magnitude. Therefore, after the nucleation stage the polymerization continues exclusively in the micelles by monomer diffusion from the monomer droplet reservoirs to the nuclei until the entire amount of monomer is consumed. The monomer conversion of emulsion polymerizations is typically > 90 %. A quantitative description of particle formation and growth in emulsion polymerization was established by Smith and Ewart.[16]

Some differences among the various emulsion polymerization techniques need to be pointed out. Introduction of functional moieties such as dyes or (magnetic) nanoparticles is not compatible with emulsion polymerization due to the nucleation step in the beginning and the growth by diffusion of the monomer from the droplets to the micelles. Besides an uneven distribution of functional groups in the beginning of the polymerization, no further functionalities can be incorporated into the particles, as these molecules or particles can not be transported through the aqueous phase to the centre of reaction. Therefore, micro- or miniemulsion needs to be employed. Both systems already start with the entire monomer being distributed in the micelles; no monomer droplets are present anymore. Polymerization takes place in the preformed nano-reactors, which contain the desired functionalities. The major difference between micro- and miniemulsion polymerization are the sizes of the final particles ranging from 50 – 500 nm (miniemulsion) and 10 – 100 nm (microemulsion). Furthermore, miniemulsions require a high shear force (provided by sonication) to break down the monomer droplets and co-surfactants to decrease Ostwald ripening, whereas microemulsions are thermodynamically stable.

However, even though these systems show uniform size distributions they mostly do not match the requirements for the fabrication of colloidal crystals, which need polydispersities < 5 %. This is due to the gradual initiation of monomer swollen micelles and a

size distribution of the initial nanoreactors. Emulsifier-free emulsion polymerization circumvents this problem. Due to the absence of surfactants only homogenous nucleation occurs at early stages. If this initiation stage is fast, a set of homogenous nuclei is formed, which successively grow to the same size until the monomer is completely consumed. Particles ranging from 100 nm to 1 μm can be obtained.[17] Again functional groups such as dyes can not be loaded into the particles by this routine. (Experimental details on emulsifier-free emulsion polymerization are given in chapter 3).

In order to obtain functionalized and monodisperse particles at the same time a seeded growth is used in most cases. In a first reaction small seed particles containing the desired functionality are formed by micro- or miniemulsion. In a second step these particles are used as seed and further growing renders them monodisperse due to the Laplace pressure.

Inorganic particles are mainly synthesized by precipitation or sol gel reactions.[18] In most cases they involve a nucleation and growth step, similar to emulsion polymerizations. These two stages need to be strictly separated in order to obtain monodisperse samples.[2, 19] In particular silica nanoparticles have been investigated in detail after Stöber introduced a simple method to synthesize them monodispersely.[20] Uniform spheres from 50 nm to 2 μm can be obtained. The final particle size depends on many parameters, which need to be carefully adjusted. These parameters are precursor-, ammonia-, and water concentration, as well as the reaction temperature.[21, 22] Only recently a phase-transfer method was developed by Hartlen *et al.*,[23] which allows the synthesis of monodisperse silica particles as small as 15 nm. Quite commonly seeded growth techniques are employed for the fabrication of monodisperse silica particles. This can be done in a step by step manner as proposed by Bogush *et al.*,[24] or in a continuous fashion as outlined by Giesche.[25] Silica particles can be labelled with dyes[26] and their surface functionality can be tuned over a wide range by silanization.[27]

The synthesis of core-shell particles gives rise to even more complex particles with a large spectrum of properties.[27-31]

1.2. Colloidal Crystal and Inverse Opal Fabrication

As outlined above conventional pick and drop methods to assemble materials in the nanometer range cease working due to the small dimensions. In order to obtain functional materials novel strategies had to be developed. Self-assembly is the method of choice for colloidal particles, which can be conducted by a range of techniques in two and three dimensions. Due to the spherical shape of the particles one typically obtains

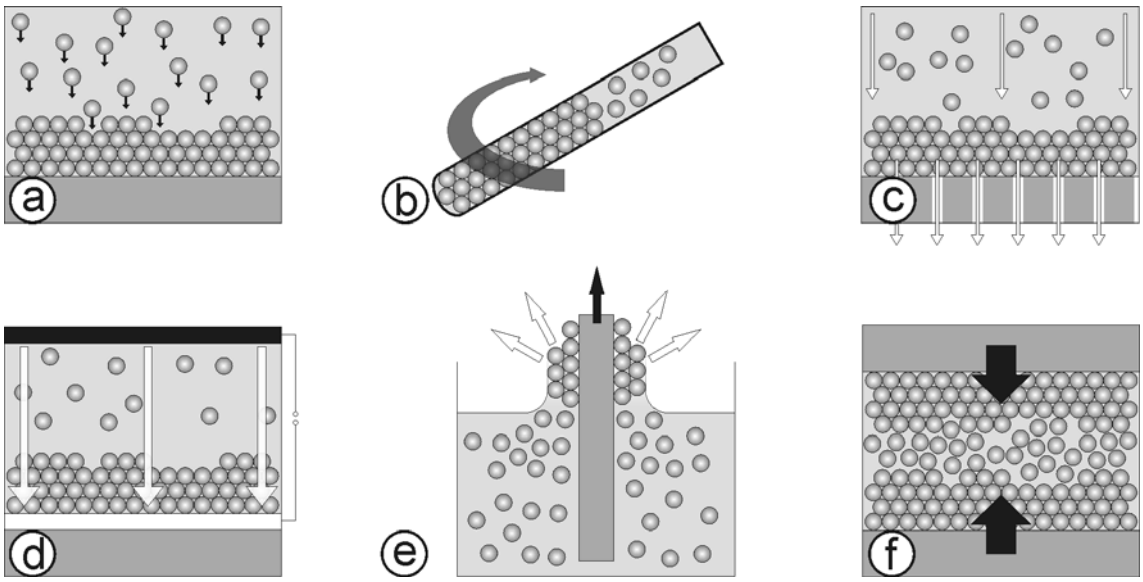

Figure 1.3. *Formation of colloidal crystals via a) sedimentation, b) centrifugation, c) filtering, d) electrodeposition, e) vertical deposition, or f) compression molding.*[32]

hexagonally ordered arrays and face centred cubic (fcc) crystals. Figure 1.3 gives an overview of the various methods to fabricate 3D colloidal crystals.

The simplest technique is sedimentation, where under the influence of gravity monodisperse particles slowly settle down and arrange into a hexagonal pattern. Drying of the supernatant solution yields the dry colloidal crystal. This method is time consuming and strongly dependent on the diameter and density of the constituting spheres.[33, 34] Settling of the colloidal particles can be greatly accelerated by applying the enhanced gravitational field in a centrifuge.[35, 36] Another technique is to assemble the particles under the influence of a liquid flow field, as achieved by filtering the dispersion. A membrane with pore sizes smaller than the particle diameter is used while continuously drawing the dispersion through a funnel, while the colloidal particles are retained at the membrane surface and accumulate.[37] Simultaneous application of an oscillating shear field during the filtration process improves the quality of particle ordering.[38]

Since colloidal particles such as PS latex and silica nanoparticles are stabilized by electrostatic repulsion, their charged state can also be exploited for the assembly process. Either a constant (dc) or alternating (ac) electric field is applied perpendicular to the receiving substrate, above which the dispersion is confined. By adjusting the direction of the electric field the particle assembly can either be accelerated under the simultaneously acting gravitational field or it can be slowed down. It was further shown that single monolayer formation is possible by the controlled application of an ac-field, which results in the continuous formation and dissolution of a close packed particle layer.[39] Additionally, the influence of an simultaneously acting hydrodynamic flow field was

investigated, showing that the domains of crystalline order grow with increasing flow rate.[40]

Another widespread technique is the assembly of particles under convective flow. In contrast to the filtration method, the liquid flow in this approach is generated by the evaporation of the dispersion medium. In order to avoid uncontrolled aggregation at the drying front, the so-called coffee ring effect,[41] the particles are not assembled on a horizontal substrate, but on a tilted or vertically standing specimen. The onset of crystallization occurs along the meniscus line (the contact line between the liquid, the substrate and the air), while enhanced medium evaporation at this line leads to a solvent flux, which drags the particles from the suspension bulk towards this crystallization edge.[42] As the evaporation continues, the contact line slowly migrates down the substrate and assembly of the particles takes place in a homogeneous film. The thickness of the resulting crystal is determined by the particle concentration in the suspension and increases along the substrate as the concentration increases continuously with evaporation. The rate of evaporation, which is controllable by the environmental humidity and temperature, governs the quality and domain size of the crystal.[43] Simultaneous lifting of the substrate, as outlined by Dimitrov *et al.*,[44] allows a further degree of control, with the thickness of the colloidal crystal being uniform over the entire substrate and depending on the speed of substrate lifting. The application of widespread standard polymer processing techniques such as extrusion to the formation of colloidal crystal was introduced by Ruhl *et al.*[45]

A brief review of a variety of techniques to fabricate 2D ordered monolayers of colloidal particles will be given in chapter 4.1.

Colloidal crystals are widely used to template porous network materials. Such porous networks with interconnected voids have fundamental properties, advantageous in adsorption, mass- and heat transport, and spatial confinement, which result in a myriad of practical applications ranging from oil recovery, water purification, to tissue engineering.[46] Moreover, when the porous networks possess a well-defined, highly-ordered structure with periodicities around the wavelength of light, they may exhibit exquisite optical properties.[47-49]

In general the colloidal crystal template is infiltrated with the desired network material by one of three fundamental methods: a) non-reactive or b) reactive infiltration, and c) codeposition. Non-reactive infiltration has been shown by the use of particles smaller than the channels of the free voids, such as CdSe quantum dots[50], silica or titania parti-

cles[51] and gold as metallic nanoparticles.[52] Also the usage of molten metals[53] and the precipitation of inorganic salts[54] has been demonstrated.

A lot of research has also been devoted to the infiltration of macroporous templates by reactive components. Porous polymer material was synthesized by infiltration of a monomer-initiator mixture with subsequent polymerization.[55, 56] A quite common route for the fabrication of metal oxide networks is to infiltrate the template structure with its corresponding sol gel solution, which eventually hydrolyses and solidifies in the desired porous shape.[2, 57, 58] Materials such as silica,[37] titania,[35, 59] zirconia,[59] or alumina[59] were obtained.

Various electrochemical approaches have been used to infiltrate colloidal templates with a great variety of metals, semiconductors and conducting polymers. Both, electroless deposition by chemical reduction[60] and electrodeposition under the influence of an electric current[61, 62] were demonstrated.

In general, the successful formation of inverse opals greatly depends on the degree and quality of the void filling procedure. Therefore, some requirements have to be met and some compromises have to be faced. Firstly, the infiltrating liquid has to be compatible with the solubility and surface properties of the constituting spheres. Otherwise the liquid may dissolve or swell the template, or it will not properly wet the nanochannels and -cavities, leaving them unfilled. Especially when using polymer solutions for the infiltration process optimization of the experimental conditions may be tedious, since the maximum polymer concentration at the lowest possible viscosity is required to ensure full void filling in a reasonable time frame. Too low concentrations might lead to thin, fragile networks, while too concentrated samples might not replicate all voids. Possible improvements for difficult sample infiltration processes are for instance repeated infiltration and drying cycles using a more dilute sample, or application of vacuum during the template filling process to prevent entrapment of air-bubbles.

The last step in the process of porous network preparation requires template removal. This is normally achieved by particle dissolution or combustion. In case of polymer particle templates both methods, dissolution in organic solvents (like toluene or tetrahydrofuran), or combustion (often at temperatures > 350 °C) are available. The combustion temperature has to be adjusted with regard to the polymer template as well as to the network material. In the case of inorganic particles this step is often accompanied by sintering of the nanoparticles, leading to a stronger porous network matrix. On the other hand, inorganic silica particle templates can not be pyrolized and are usually removed by etching with hydrofluoric acid. Depending on the volume filling factor of the matrix

material, substantial shrinkage of the porous network accompanied by crack formation may occur for low filling fractions during template removal. Furthermore, annealing the replica material at elevated temperatures may lead to a transformation from one modification or crystal phase to another one, which is thermodynamically more stable at these temperatures, as shown for the thermal conversion of amorphous titania or its anatas phase to the rutil structure.[63]

1.3. Colloidal Crystals and their Interaction with Light and Sound

A key feature of colloidal crystals is their periodic undulation of the refractive index, the elastic constants, and the material density. These variations are responsible for modulations of electromagnetic and mechanical waves of similar wavelength as the lattice spacing. The lattice spacing for colloidal crystals under consideration here falls typically in the few 100 nm range. As a consequence light in the visible range (400 nm - 750 nm) is hindered to travel through such an ordered material. The periodic alteration of the dielectric constant can be regarded as a grating at which the light is refracted. Destructive interference leads to stop bands in the continuous spectrum of white light. Yablonovitch[49] and John[48] predicted the existence of full photonic band gaps in materials structured on the length scale of light. Full photonic band gap means that light of a certain frequency can not pass through such a material, regardless of the direction of propagation. In such a case the photonic band gap extends over the entire Brillouin zone (BZ), which is represented by a truncated octahedron for an fcc crystal (Figure 1.4 b).[64, 65] However, a full photonic band gap in the visible range is not achievable with fcc colloidal crystals. Materials with higher contrast and lower symmetry are required for full band gaps.[66] Blanco *et al.* were the first to demonstrate a complete band gap between the 8th and 9th BZ in the near infrared range by the fabrication of an inverse silicon opal (Figure 1.4 a).[67]

Even though the realization of full photonic band gaps in the visible range have not been shown experimentally so far, colloidal crystals have started to emerge into some interesting applications due to their stop band. Among these are sensors,[30, 68-72] sieves,[73, 74] photonic papers and inks,[75, 76] solar cells,[77-79] optical fibers,[80] lasers,[81-83] and integrated optical circuits and telecommunication devices.[84, 85]

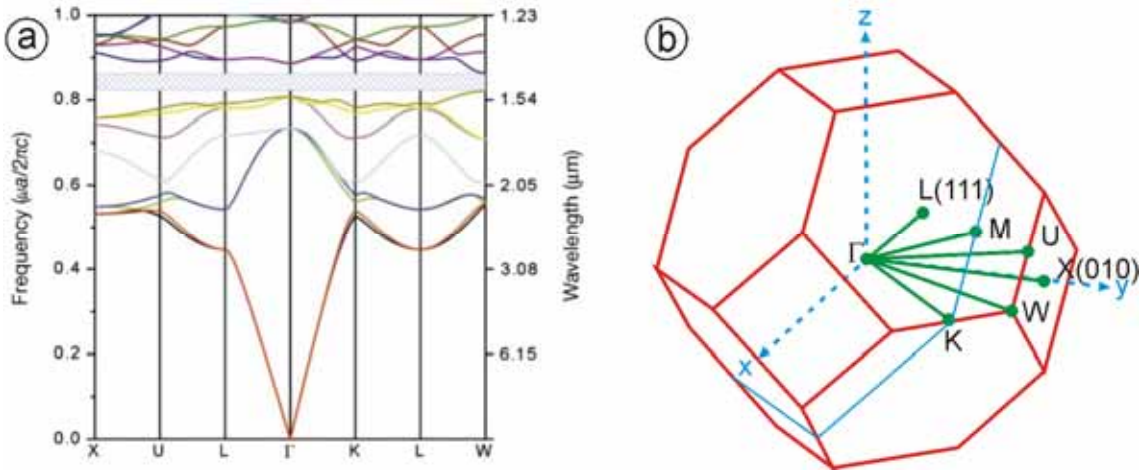

Figure 1.4. *a) Band structure of an inverse silicon opal. The complete photonic band gap is highlighted by the crosshatched region. b) Truncated octahedron representing the first BZ of a fcc crystal.*[65, 67]

With further improvements still to be made, photonic crystals might find manifold applications in every day products as well as high performance technologies. A vision of future use of colloidal crystals resembles the photonic crystal micropolis from Joannopoulos (Figure 1.5).[47, 85]

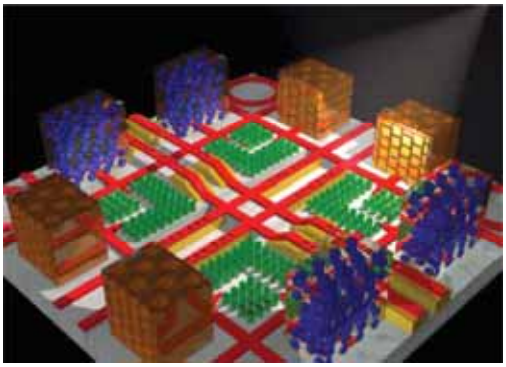

Figure 1.5. *Joannopoulos photonic crystal micropolis, a futuristic all optical chip.*[85]

Interaction of sound waves with colloidal crystals can be regarded as the mechanical analogue to the interaction with light. Mechanical waves with a wavelength of several 100 nm fall into the hypersonic range (GHz), which is assigned to phonons. Therefore, when looking at the interaction with mechanical waves one speaks of phononic-[86] instead of photonic crystals. Phononic properties of nanostructured materials are far less well understood as their photonic analogue. Most realized systems deal so far with sonic and ultrasonic phononic crystals with periodicity in the millimeter range.[87-95] Soon after the first experimental observation of ultrasonic band gaps,[89-92, 96] peculiar phenomena with potential applications dealing with the propagation of elastic waves in periodic composite materials such as tunneling,[93] negative refraction, focusing,[94, 95] and enhanced transmission through one-dimensional gratings[97] have been discovered.

Due to the difficulty to prepare appropriate samples in the nanometer range and special demands on the methods to actually measure phonons in such materials, only recently the existence of a phononic band gap in the hypersonic range was proven.[98] The band gap could be adjusted in its width by altering the mechanical contrast between colloidal particles and the surrounding medium. Decreasing the sound velocity of the medium by infiltration of glycerol, silicon oil, or polydimethylsiloxane broadens the band gap due to the higher contrast (Figure 1.6).

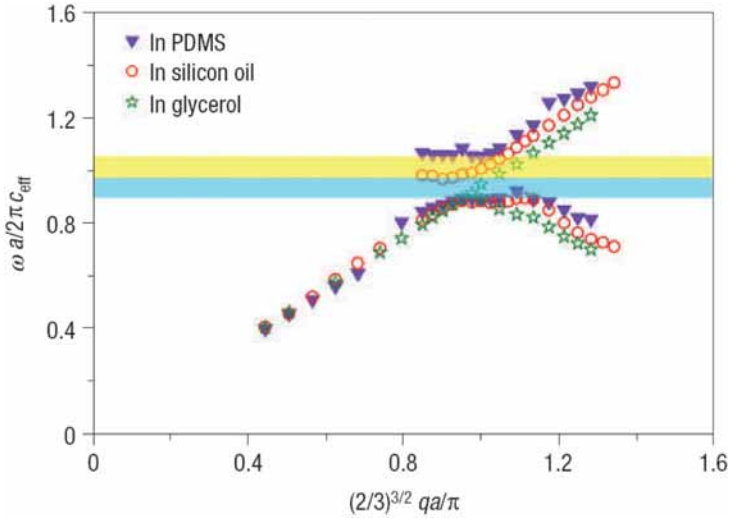

Figure 1.6. *Dispersion relation in a reduced plot with c_{eff} being the effective sound velocity of the PDMS infiltrated PS crystal, and a being the lattice parameter. Whereas no band gap is discernible in glycerol, a gap opens up in silicon oil and increases for PDMS.*[98]

A detailed understanding of how to mold the flow of sound in nanostructured materials is highly desirable for many applications, which range from acoustic filters for the telecommunication industry to heat management. Phonons control the heat capacity of a material and thus, hindering their movement through a specific material might lead to efficient thermoelectric[99] or thermooptic materials.[100]

Furthermore, simultaneous occurrence of photonic and phononic band gaps in colloidal crystals can path the way to optoacoustic devices.

1.4. Nanosphere Lithography

Besides the popularity of 3D colloidal crystals for fundamental research and various applications, also their 2D analogues attract high interest. In the quest of fabricating smaller and smaller feature sizes on a target substrate single layers consisting of colloidal particles exhibit some advantages over conventional techniques such as UV- or e-beam lithography. On the one hand colloidal monolayers can easily template nanostructures well below 100 nm, on the other hand they provide a parallel method to struc-

ture surfaces. Details of various methods for the fabrication of colloidal monolayers will be given in chapter 4.1.

The first to use colloidal monolayers as shadow mask were Deckmann and Dunsmuir in 1982, who termed this method "natural lithography".[101] Ever since, this method has gained increasingly attention and a large range of various particles can now be fabricated by evaporating gold through this shadow mask. Besides triangles,[102] which directly replicate the opens voids, also more complex structures such as rings, rods, and frames can be obtained (Figure 1.7).[102, 103]

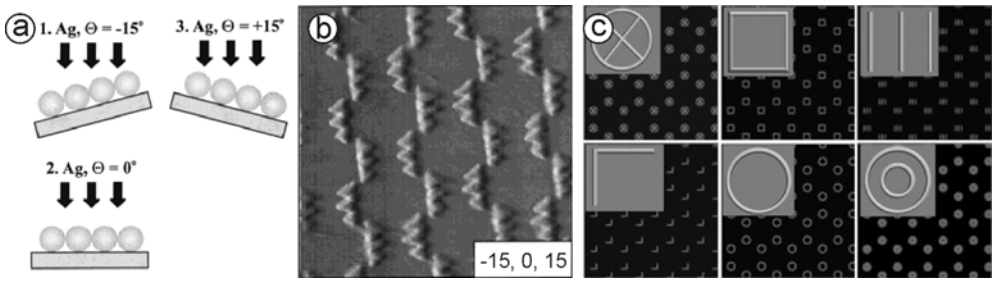

Figure 1.7. *a) Schematic illustration and b) contact mode AFM image of three laterally displaced Ag triangles. Diameter of templating particles was 542 nm. c) Computer simulation of structures that should be possible by evaporation through annealed PS masks.*[103, 104]

A major interest for the fabrication of nanostructured materials stems from the optical properties of such metallic nanoparticles. They feature localized surface plasmon resonances with rich optical field enhancements at their sharp tips and edges.[105] Therefore, such materials have gained interest in highly sensitive sensing devices; a characteristic shift in the absorption maximum indicates a change in the dielectric environment.[106, 107] Furthermore, the optical properties of such nanoscale particles could open the way to obtain metamaterials in the visible range.[108, 109]

However, colloidal lithography is not only limited to the deposition of material onto a substrate. By appropriate coverage of the first monolayer with a second top layer and ensuing reactive ion etching regularly nano-drilled particles can be obtained, as demonstrate by Choi *et al.*[110] (compare Figure 1.8).

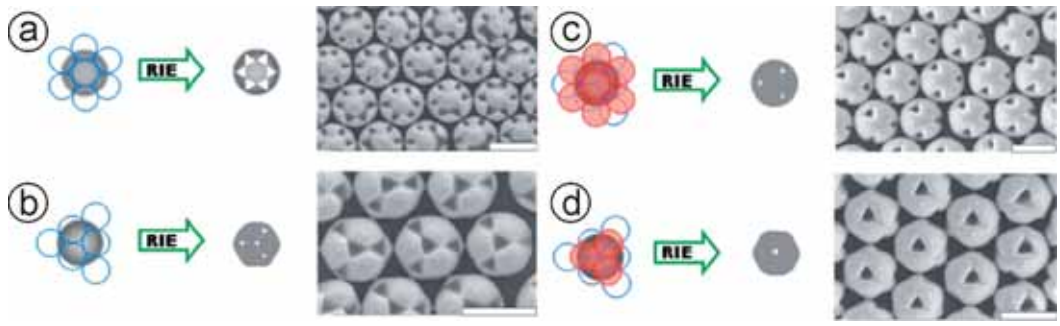

Figure 1.8. *Schematics of binary colloidal-stacking sequences and the resulting SEM images of the sculpted PS beads produced via oxygen reactive ion etching (RIE). SiO_2 spheres were coated onto a preformed monolayer of spherical PS beads. a – d) Schematics of binary colloidal-stacking sequences for a fixed size ratio of SiO2 spheres/PS beads of 0.574. Scale bars 1 µm.*[110]

Finally, a colloidal monolayer can be modified by reducing its size by plasma etching.[111] Depending on the etching parameters the underlying substrate may remain unaffected, which opens novel possibilities to fabricate non-close packed hexagonal structures by established nanosphere lithography techniques. The conditions can also be tuned in a way to affect the underlying substrate, for instance by CF_4 in a plasma reaction.[112] The supporting glass substrate will then be selectively etched, where the protection from the colloidal monolayer is missing. Such materials might find applications in ultrahydrophobic and ultrahydrophilic surfaces.

1.5. Aim and Motivation

The aim of this thesis is split into two parts. One part is devoted to the fabrication of nanostructured materials with highly crystalline order, structural hierarchy, and/or composite material combinations, which can be employed for future applications such as sensing, filtering, catalysis, or in optical circuits. The other part is dedicated to fundamental research in the field of phononic properties of colloidal particles and films.

In the first case the fabrication of monomodal colloidal- and micrometer-patterned hetero-monolayers and their importance for surface structuring by nanosphere lithography is investigated. Several improvements to existing technologies are introduced with respect to the versatility and simplicity of the monolayer fabrication process and to the quality of the resulting monolayer. Furthermore, a method, which is amenable to structure colloidal monolayers on a tens-of-micrometer scale in a simple and technologically feasible manner with particles of various sizes and materials, is proposed. The improved monolayer fabrication method is used further on in several projects to exploit its advantages. Nanostructured surfaces, which span the range from sensors to metamaterials are synthesized and characterized. However, nanostructured materials are not only fabricated in two dimensions, but also an approach to introduce three-dimensional hierarchy into mesoporous inverse opals is discussed. This methodology allows the combination of various materials, which finally might give rise to advanced optical, storage, or catalytic properties.

In case of the phononic properties a more detailed understanding of the vibrational modes of colloidal particles - so called eigenmodes - is set up. Previous results on monodisperse polystyrene particles are reviewed and the influence of the local environment is examined. The colloidal particles under investigation become gradually more complex (from copolymer latexes to core-shell particles) and the power of Brillouin light scattering to measure the individual mechanical properties on a nanometer

scale is evidenced. Finally, the phonon dispersion relations in liquid infiltrated samples were investigated. These dispersion relations can be split into two regimes, the purely acoustic branch at low **q** and more complex distributions of phonons at high **q**. These two regimes are treated individually to gain insight into the effective medium of such a composite film, and to learn more about phononic band gaps and their origin in such samples.

The unifying foundation of these diverse projects, questions, and interests is the underlying material. Everything is built on the well controlled synthesis of monodisperse colloidal particles of specifically designed size and function. Self-assembly is the method of choice to arrange these particles into useful and interesting materials, which are partially on the step to find broader applications and yet still need more fundamental understanding.

Thus, in the course of this thesis it will become clear that interesting and complex materials can still be made from relatively simple building blocks by colloidal crystallization.

1.6. Bibliography

1. Everett, D. H., *Basic Principles of Colloid Science*. London 1988.
2. Xia, Y. N.; Gates, B.; Yin, Y. D.; Lu, Y. *Adv. Mater.* **2000,** 12, (10), 693-713.
3. Gilbert, R. G., *Emulsion Polymerization: A Mechanistic Approach*. Academic: London, 1995.
4. Pavel, F. M. *J. Dispersion Sci. Technol.* **2004,** 25, (1), 1-16.
5. Chow, P. Y.; Gan, L. M., Microemulsion polymerizations and reactions. In *Polymer Particles*, 2005; Vol. 175, pp 257-298.
6. Schork, F. J.; Luo, Y. W.; Smulders, W.; Russum, J. P.; Butte, A.; Fontenot, K., Miniemulsion polymerization. In *Polymer Particles*, 2005; Vol. 175, pp 129-255.
7. Landfester, K., Miniemulsions for nanoparticle synthesis. In *Colloid Chemistry Ii*, 2003; Vol. 227, pp 75-123.
8. Egen, M.; Zentel, R. *Macromol. Chem. Phys.* **2004,** 205, (11), 1479-1488.
9. Shouldice, G. T. D.; Vandezande, G. A.; Rudin, A. *Eur. Polym. J.* **1994,** 30, (2), 179-183.
10. Goodwin, J. W.; Hearn, J.; Ho, C. C.; Ottewill, R. H. *Colloid. Polym. Sci.* **1974,** 252, 464-471.
11. Kawaguchi, S.; Ito, K. *Polymer Particles* **2005,** 175, 299-328.
12. Nomura, M.; Tobita, H.; Suzuki, K. *Polymer Particles* **2005,** 175, 1-128.
13. Arshady, R. *Colloid. Polym. Sci.* **1992,** 270, (8), 717-732.
14. Fitch, R. M., *Polymer Colloids : A Comprehensive Introduction*. Academic: London, 1995.
15. Vollmert, B., *Polymer Chemistry*. Springer Verlag: New York, 1973.
16. Smith, W. V.; Ewart, R. H. *J. Chem. Phys.* **1948,** 16, 592.

17. Chung-li, Y.; Goodwin, J. W.; Ottewill, R. H. *Prog. Coll. Polym. Sci.* **1976,** 60, 163-165.
18. Cushing, B. L.; Kolesnichenko, V. L.; O'Connor, C. J. *Chem. Rev.* **2004,** 104, (9), 3893-3946.
19. Lamer, V. K.; Dinegar, R. H. *J. Am. Chem. Soc.* **1950,** 72, (11), 4847-4854.
20. Stöber, W.; Fink, A.; Bohn, E. *J. Colloid Interface Sci.* **1968,** 26, (1), 62-69.
21. Giesche, H. *J. Eur. Ceram. Soc.* **1994,** 14, (3), 189-204.
22. Zhang, J. H.; Zhan, P.; Wang, Z. L.; Zhang, W. Y.; Ming, N. B. *J. Mater. Res.* **2003,** 18, (3), 649-653.
23. Hartlen, K. D.; Athanasopoulos, A. P. T.; Kitaev, V. *Langmuir* **2008,** 24, (5), 1714-1720.
24. Bogush, G. H.; Tracy, M. A.; Zukoski, C. F. *J. Non-Cryst. Solids* **1988,** 104, (1), 95-106.
25. Giesche, H. *J. Eur. Ceram. Soc.* **1994,** 14, (3), 205-214.
26. Verhaegh, N. A. M.; Vanblaaderen, A. *Langmuir* **1994,** 10, (5), 1427-1438.
27. Zou, H.; Wu, S. S.; Shen, J. *Chem. Rev.* **2008,** 108, (9), 3893-3957.
28. Lange, B.; Metz, N.; Tahir, M. N.; Fleischhaker, F.; Theato, P.; Schroder, H. C.; Muller, W. E. G.; Tremel, W.; Zentel, R. *Macromol. Rapid Commun.* **2007,** 28, (20), 1987-1994.
29. Luna-Xavier, J.-L.; Guyot, A.; Bourgeat-Lami, E. *J. Colloid and Interface Sci ence* **2002,** 250, (1), 82-92.
30. Wohlleben, W.; Bartels, F. W.; Altmann, S.; Leyrer, R. J. *Langmuir* **2007,** 23, (6), 2961-2969.
31. Spahn, P. Kolloidale Kristalle aus monodispersen Silika-Polymer Hybridpar tikeln. PhD thesis, Technische Universität Darmstadt, Darmstadt, 2008.
32. Li, Q.; Retsch, M.; Wang, J.; Knoll, W.; Jonas, U. *Top. Curr. Chem.* **2008,** DOI 10.1007/128_2008_3.
33. Mayoral, R.; Requena, J.; Moya, J. S.; Lopez, C.; Cintas, A.; Miguez, H.; Mese guer, F.; Vazquez, L.; Holgado, M.; Blanco, A. *Adv. Mater.* **1997,** 9, (3), 257-260.
34. Davis, K. E.; Russel, W. B.; Glantschnig, W. J. *Journal of the Chemical Society-Faraday Transactions* **1991,** 87, (3), 411-424.
35. Wijnhoven, J.; Vos, W. L. *Science* **1998,** 281, (5378), 802-804.
36. Vos, W. L.; Megens, M.; vanKats, C. M.; Bösecke, P. *Langmuir* **1997,** 13, (23), 6004-6008.
37. Velev, O. D.; Jede, T. A.; Lobo, R. F.; Lenhoff, A. M. *Nature* **1997,** 389, (6650), 447-448.
38. Vickreva, O.; Kalinina, O.; Kumacheva, E. *Adv. Mater.* **2000,** 12, (2), 110-112.
39. Trau, M.; Saville, D. A.; Aksay, I. A. *Science* **1996,** 272, (5262), 706-709.
40. Yoldi, M.; Gonzalez-Vinas, W.; Arcos, M. C.; Sirera, R. *Journal of Materials Science* **2006,** 41, (10), 2965-2969.
41. Deegan, R. D.; Bakajin, O.; Dupont, T. F.; Huber, G.; Nagel, S. R.; Witten, T. A. *Nature* **1997,** 389, (6653), 827-829.
42. Denkov, N. D.; Velev, O. D.; Kralchevsky, P. A.; Ivanov, I. B.; Yoshimura, H.; Nagayama, K. *Langmuir* **1992,** 8, (12), 3183-3190.
43. Cong, H.; Cao, W. X. *Langmuir* **2003,** 19, (20), 8177-8181.
44. Dimitrov, A. S.; Nagayama, K. *Langmuir* **1996,** 12, (5), 1303-1311.
45. Ruhl, T.; Spahn, P.; Hellmann, G. P. *Polymer* **2003,** 44, (25), 7625-7634.
46. Hollister, S. J. *Nat. Mater.* **2005,** 4, (7), 518-524.
47. Joannopoulos, J. D.; Villeneuve, P. R.; Fan, S. *Nature* **1997,** 386, (6621), 143-149.
48. John, S. *Phys. Rev. Lett.* **1987,** 58, (23), 2486-2489.

49. Yablonovitch, E. *Phys. Rev. Lett.* **1987,** 58, (20), 2059-2062.
50. Vlasov, Y. A.; Yao, N.; Norris, D. J. *Adv. Mater.* **1999,** 11, (2), 165-169.
51. Gu, Z. Z.; Kubo, S.; Fujishima, A.; Sato, O. *Appl Phys A-Mater* **2002,** 74, (1), 127-129.
52. Velev, O. D.; Tessier, P. M.; Lenhoff, A. M.; Kaler, E. W. *Nature* **1999,** 401, (6753), 548-548.
53. Bogomolov, V. N.; Sorokin, L. M.; Kurdyukov, D. A.; Pavlova, T. M.; Hutchi son, J. L. *Phys. Solid State* **1997,** 39, (11), 1869-1874.
54. Yan, H. W.; Blanford, C. F.; Holland, B. T.; Smyrl, W. H.; Stein, A. *Chem. Ma ter.* **2000,** 12, (4), 1134-1141.
55. Johnson, S. A.; Ollivier, P. J.; Mallouk, T. E. *Science* **1999,** 283, (5404), 963-965.
56. Park, S. H.; Xia, Y. N. *Chem. Mater.* **1998,** 10, (7), 1745-1747.
57. Velev, O. D.; Kaler, E. W. *Adv. Mater.* **2000,** 12, (7), 531-534.
58. Hoa, M. L. K.; Lu, M. H.; Zhang, Y. *Adv. Colloid Interface Sci.* **2006,** 121, (1-3), 9-23.
59. Holland, B. T.; Blanford, C. F.; Stein, A. *Science* **1998,** 281, (5376), 538-540.
60. Jiang, P.; Cizeron, J.; Bertone, J. F.; Colvin, V. L. *J. Am. Chem. Soc.* **1999,** 121, (34), 7957-7958.
61. Braun, P. V.; Wiltzius, P. *Nature* **1999,** 402, (6762), 603-604.
62. Tian, S. J.; Wang, J. J.; Jonas, U.; Knoll, W. *Chem. Mater.* **2005,** 17, (23), 5726-5730.
63. Holland, B. T.; Blanford, C. F.; Do, T.; Stein, A. *Chem. Mater.* **1999,** 11, (3), 795-805.
64. Kittel, C., *Einführung in die Festkörperphysik*. 14. Auflage ed.; Oldenburg Ver lag: München, 2005.
65. Lopez, C. *Adv. Mater.* **2003,** 15, (20), 1679-1704.
66. Hynninen, A. P.; Thijssen, J. H. J.; Vermolen, E. C. M.; Dijkstra, M.; Van Blaaderen, A. *Nat. Mater.* **2007,** 6, (3), 202-205.
67. Blanco, A.; Chomski, E.; Grabtchak, S.; Ibisate, M.; John, S.; Leonard, S. W.; Lopez, C.; Meseguer, F.; Miguez, H.; Mondia, J. P.; Ozin, G. A.; Toader, O.; van Driel, H. M. *Nature* **2000,** 405, (6785), 437-440.
68. Tian, E. T.; Wang, J. X.; Zheng, Y. M.; Song, Y. L.; Jiang, L.; Zhu, D. B. *J. Ma ter. Chem.* **2008,** 18, (10), 1116-1122.
69. Nishijima, Y.; Ueno, K.; Juodkazis, S.; Mizeikis, V.; Misawa, H.; Tanimura, T.; Maeda, K. *Opt. Express* **2007,** 15, (20), 12979-12988.
70. Fujishima, M.; Sakata, S.; Iwasaki, T.; Uchida, K. *Journal of Materials Science* **2008,** 43, (6), 1890-1896.
71. Fleischhaker, F.; Arsenault, A. C.; Kitaev, V.; Peiris, F. C.; von Freymann, G.; Manners, I.; Zentel, R.; Ozin, G. A. *J. Am. Chem. Soc.* **2005,** 127, (26), 9318-9319.
72. Holtz, J. H.; Asher, S. A. *Nature* **1997,** 389, (6653), 829-832.
73. Zeng, Y.; Harrison, D. J. *Anal. Chem.* **2007,** 79, (6), 2289-2295.
74. Han, J. Y.; Fu, J. P.; Schoch, R. B. *Lab on a Chip* **2008,** 8, (1), 23-33.
75. Fudouzi, H.; Xia, Y. N. *Langmuir* **2003,** 19, (23), 9653-9660.
76. Arsenault, A. C.; Miguez, H.; Kitaev, V.; Ozin, G. A.; Manners, I. *Adv. Mater.* **2003,** 15, (6), 503-507.
77. Florescu, M.; Lee, H.; Puscasu, I.; Pralle, M.; Florescu, L.; Ting, D. Z.; Dowling, J. P. *Sol. Energy Mater. Sol. Cells* **2007,** 91, (17), 1599-1610.
78. Colodrero, S.; Mihi, A.; Häggman, L.; Ocaña, M.; Boschloo, G.; Hagfeldt, A.; Míguez, H. *Adv. Mater.* **2009,** 21, (7), 764-770.

79. O'Brien, P. G.; Kherani, N. P.; Chutinan, A.; Ozin, G. A.; John, S.; Zukotynski, S. *Adv. Mater.* **2008,** 20, (8), 1577-1582.
80. Russell, P. *Science* **2003,** 299, (5605), 358-362.
81. Englund, D.; Atlug, H.; Ellis, B.; Vuckovic, J. *Laser Photonics Rev.* **2008,** 2, (4), 264-274.
82. Painter, O.; Lee, R. K.; Scherer, A.; Yariv, A.; O'Brien, J. D.; Dapkus, P. D.; Kim, I. *Science* **1999,** 284, (5421), 1819-1821.
83. Furumi, S.; Fudouzi, H.; Miyazaki, H. T.; Sakka, Y. *Adv. Mater.* **2007,** 19, (16), 2067-2072.
84. Lourtioz, J. M.; Benisty, H.; Chelnokov, A.; David, S.; Olivier, S. *Annales Des Telecommunications-Annals of Telecommunications* **2003,** 58, (9-10), 1197-1237.
85. Arsenault, A.; Fournier-Bidoz, S. B.; Hatton, B.; Miguez, H.; Tetrault, N.; Vek ris, E.; Wong, S.; Yang, S. M.; Kitaev, V.; Ozin, G. A. *Journal of Materials Chemistry* **2004,** 14, (5), 781-794.
86. Gorishnyy, T.; Maldovan, M.; Ullal, C.; Thomas, E. *Phys. World* **2005,** 18, (12), 24-29.
87. Liu, Z. Y.; Zhang, X. X.; Mao, Y. W.; Zhu, Y. Y.; Yang, Z. Y.; Chan, C. T.; Sheng, P. *Science* **2000,** 289, (5485), 1734-1736.
88. Goffaux, C.; Sanchez-Dehesa, J.; Yeyati, A. L.; Lambin, P.; Khelif, A.; Vasseur, J. O.; Djafari-Rouhani, B. *Phys. Rev. Lett.* **2002,** 88, (22), 225502.
89. Montero de Espinosa, F. R.; Jiménez, E.; Torres, M. *Phys. Rev. Lett.* **1998,** 80, (6), 1208-1211.
90. Sanchez-Perez, J. V.; Caballero, D.; Martinez-Sala, R.; Rubio, C.; Sanchez-Dehesa, J.; Meseguer, F.; Llinares, J.; Galvez, F. *Phys. Rev. Lett.* **1998,** 80, (24), 5325-5328.
91. Liu, Z. Y.; Chan, C. T.; Sheng, P.; Goertzen, A. L.; Page, J. H. *Phys. Rev. B* **2000,** 62, (4), 2446-2457.
92. Vasseur, J. O.; Deymier, P. A.; Chenni, B.; Djafari-Rouhani, B.; Dobrzynski, L.; Prevost, D. *Phys. Rev. Lett.* **2001,** 86, (14), 3012-3015.
93. Yang, S. X.; Page, J. H.; Liu, Z. Y.; Cowan, M. L.; Chan, C. T.; Sheng, P. *Phys. Rev. Lett.* **2002,** 88, (10), 104301.
94. Zhang, X. D.; Liu, Z. Y. *Appl. Phys. Lett.* **2004,** 85, (2), 341-343.
95. Yang, S. X.; Page, J. H.; Liu, Z. Y.; Cowan, M. L.; Chan, C. T.; Sheng, P. *Phys. Rev. Lett.* **2004,** 93, (2), 024301.
96. Martinez-Salazar, R.; Sancho, J.; Sanchez, J. V.; Gomez, V.; Llinares, J.; Mese guer, F. *Nature* **1995,** 378, (6554), 241-241.
97. Lu, M.-H.; Liu, X.-K.; Feng, L.; Li, J.; Huang, C.-P.; Chen, Y.-F.; Zhu, Y.-Y.; Zhu, S.-N.; Ming, N.-B. *Phys. Rev. Lett.* **2007,** 99, (17), 174301-4.
98. Cheng, W.; Wang, J.; Jonas, U.; Fytas, G.; Stefanou, N. *Nat. Mater.* **2006,** 5, 830-836.
99. Mingo, N.; Hauser, D.; Kobayashi, N. P.; Plissonnier, M.; Shakouri, A. *Nano Lett.* **2009,** 9, (2), 711-715.
100. Chong, H. M. H.; De La Rue, R. M. *IEEE Photonics Technol. Lett.* **2004,** 16, (6), 1528-1530.
101. Deckman, H. W.; Dunsmuir, J. H. *Appl. Phys. Lett.* **1982,** 41, (4), 377-379.
102. Hulteen, J. C.; Vanduyne, R. P. *J Vac Sci Technol A* **1995,** 13, (3), 1553-1558.
103. Haynes, C. L.; Van Duyne, R. P. *J. Phys. Chem. B* **2001,** 105, (24), 5599-5611.
104. Kosiorek, A.; Kandulski, W.; Glaczynska, H.; Giersig, M. *Small* **2005,** 1, (4), 439-444.
105. Murray, W. A.; Barnes, W. L. *Adv. Mater.* **2007,** 19, (22), 3771-3782.
106. Haes, A. J.; Van Duyne, R. P. *J. Am. Chem. Soc.* **2002,** 124, (35), 10596-10604.

107. Bocchio, N. L.; Unger, A.; Alvarez, M.; Kreiter, M. *J. Phys. Chem. C* **2008,** 112, (37), 14355-14359.
108. Liu, N.; Guo, H. C.; Fu, L. W.; Kaiser, S.; Schweizer, H.; Giessen, H. *Nat. Ma ter.* **2008,** 7, (1), 31-37.
109. Valentine, J.; Zhang, S.; Zentgraf, T.; Ulin-Avila, E.; Genov, D. A.; Bartal, G.; Zhang, X. *Nature* **2008,** 455, (7211), 376-U32.
110. Choi, D. G.; Jang, S. G.; Kim, S.; Lee, E.; Han, C. S.; Yang, S. M. *Adv. Funct. Mater.* **2006,** 16, (1), 33-40.
111. Haginoya, C.; Ishibashi, M.; Koike, K. *Appl. Phys. Lett.* **1997,** 71, (20), 2934-2936.
112. Tan, B. J. Y.; Sow, C. H.; Lim, K. Y.; Cheong, F. C.; Chong, G. L.; Wee, A. T. S.; Ong, C. K. *J. Phys. Chem. B* **2004,** 108, (48), 18575-18579.

2. Methods

2.1. Optical Microscopy

Detailed optical images of the samples were recorded with an optical microscope using magnifications from 5x to 100x. The microscope used in this work was an Axioscope Zeiss, which could be operated in bright field, dark field, or differential interference contrast (DIC) mode. Images were recorded either with an Axiocam Zeiss color (1300x1030 pixels) or with a μeye UI 1540SE CMOS (1280x1024 pixels) camera. Calibration of the images was conducted measuring μm-sized gratings of known spacing. Image processing was conducted by Photoshop CS3 or CorelDraw X4.

2.2. Scanning Electron Microscopy

Scanning electron microscopy (SEM) is a standard technique to characterize nanostructured materials microscopically. The smaller wavelength λ of accelerated electrons as compared to visible light provides the possibility to resolve structures down to the nanometer range. The maximum resolution of two individual points with a distance *d* is given by the Abbé criterion, with *NA* being the numerical aperture.

$$d = \frac{\lambda}{2 \cdot NA} \qquad \text{Equation 2.1}$$

The contrast in SEM is given by the intensity of electrons at the detector while the focused electron beam is scanning over the sample surface. Thus one obtains a 2D resolved picture, which displays the x, y-position dependent electron intensity at the detector. In low-voltage (LV) SEM electron beams with an acceleration voltage < 5 kV are used.[1-3] The electron beam interacts with the sample surface in several ways. The different electrons, which are generated by the primary electron beam (PE), are depicted in Figure 2.1.[4]

Secondary electrons (SE) have low energies (< 50 eV). Therefore they can only leave the sample surface within a very thin film (λ_{SE} = 1-10 nm), which results in a high resolution, both laterally and in depth. Detection of SE gives therefore topographic pictures of the sample surface. Backscattered electrons (BSE) have much higher energies and are measured with a different detector. BSE contain information about the sample's material composition, since the scattering length (and thus intensity at the detector) is a function of the atomic number. However, the resolution is inferior as compared to SE. Detection of Auger electrons (AE) or X-rays (X) allows the precise identification of atoms

in the sample region of interest. In order to excite x-rays from the sample elements the acceleration voltage is usually increased to tens of kV; the mode of detection is termed energy dispersive x-ray spectroscopy (EDX).

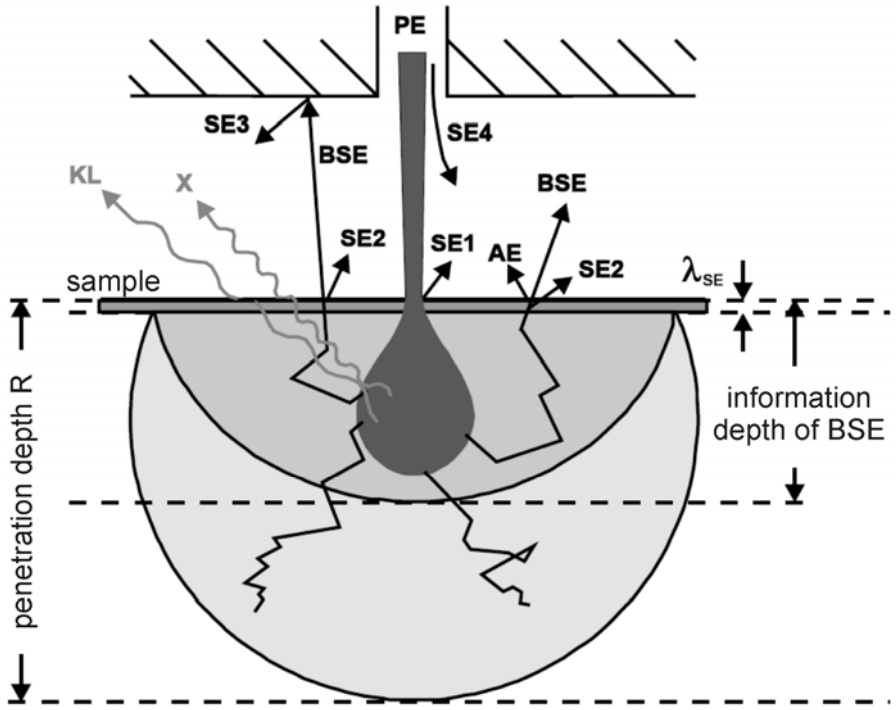

Figure 2.1. *A primary electron beam (PE) hits the sample surface. Secondary electrons (SE), backscattered electrons (BSE), and Auger electrons (AE) are generated by interaction with the sample. Cathode luminescence (KL) and X-rays (X) are also present. The secondary electrons probe only a very thin layer of the sample (λ_{SE}).*[4]

SEM images were recorded on a LEO Gemini 1530 with an In-Lens SE detection system. Native, non-sputtered samples were used in all cases. The acceleration voltage ranged from 0.4 kV to 5 kV.

SEM was used to determine the particle diameter by manual evaluation of the pictures using the software ImageJ. At least 50 particles were measured before averaging. Particle surface coverage was determined by image processing using ImagePro. Photoshop CS3 and CorelDraw X4 were used for image compositions.

2.3. Atomic Force Microscopy

Atomic force microscopy (AFM) is a technique, which images the topography of surfaces via the interaction between a sharp cantilever tip and the sample interface.[5-7] The force acting between the tip and the surface leads to a deflection of the cantilever, which is read out by a laser hitting a photodetector. The sample surface is scanned line by line, analogous to SEM, therefore AFM is also termed scanning force microscopy (SFM). The topographic image is obtained by plotting the cantilever deflection against the position on the sample. A typical AFM setup is shown in Figure 2.2.[8]

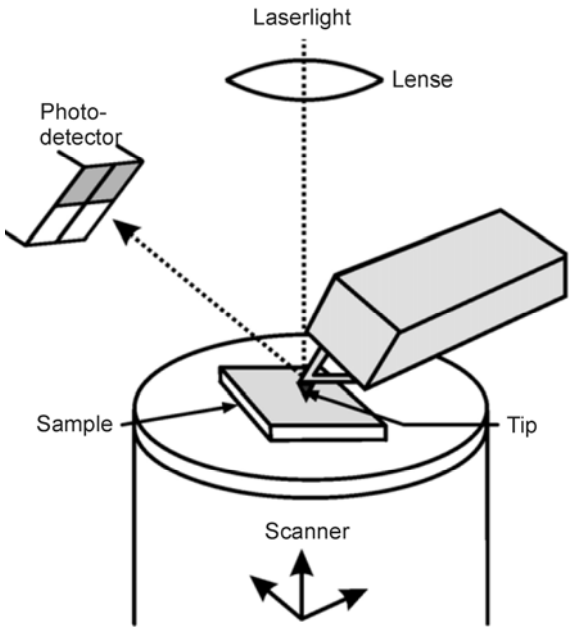

Figure 2.2. *Important components of an AFM setup. Laser light from top hits the cantilever (tip) and the deflection is measured by the photodetector. The sample is mounted on a scanner, which can move in x, y, and z direction by piezo crystals.*[8]

A major advantage of AFM compared to SEM is the measurement of 3D resolved pictures, since the sample scanner can be moved in all three directions in space. Typically AFM images are recorded in "contact mode", where the tip is in physical contact with the sample surface, or in "non-contact mode", which operates at a given tip-sample separation under oscillation of the cantilever at its resonance frequency. In case of the non-contact mode (tapping mode) the interaction between sample and tip alter the amplitude and phase of the oscillation. In tapping mode the simultaneous measurement of height and phase images is possible. The height image displays the topography, whereas the phase image provides information about the mechanical properties of the sample. A phase shift can be caused for example by differences in the samples hardness like in phase separated block copolymers[9] or by attractive or repulsive forces, which act between tip and substrate.

Another advantage of AFM is the possibility to measure force-distance curves. In a special application of that it is possible to measure the contact angle of single colloidal particles.[10] Briefly, a single colloidal particle is glued to a cantilever and is used as colloidal probe. The measurement is conducted under water (or in another liquid of interest), where the colloidal probe approaches an air bubble, which is held at the bottom of the measurement cell. The force acting on the colloidal probe is recorded as a function of the position. A schematic of the measurement setup is shown in Figure 2.3.

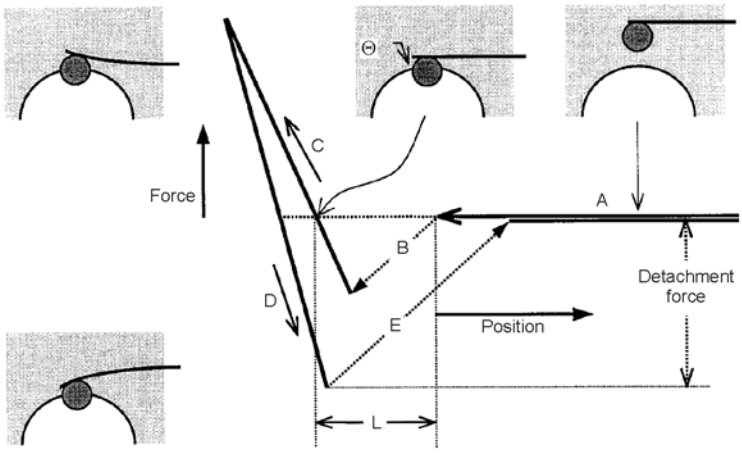

Figure 2.3. *Force versus position curve of a colloidal probe and a bubble. (A) The cantilever approaches the bubble. (B) The colloidal particle jumps into the bubble, a three-phase-contact line is formed. (C) The particle is further pushed into the bubble; the three-phase-contact line is shifted over the particle. (D) The particle is retracted. (E) At a certain point the force is high enough to overcome the capillary force and the particle is pulled off the air-water interface.*[10]

The colloidal particle snaps into the air-water interface (B) and is further pushed into the air bubble (C). At a certain point no force is acting on the particle. From this distance, L, and the radius of the sphere, R, the contact angle Θ can be calculated by

$$\cos\Theta_r^{sphere} = \frac{R-L}{R} \qquad \text{Equation 2.2}$$

This is the receding contact angle, since the liquid on the particle interface is displaced by air. Upon retraction of the particle (D) the advancing contact angle can be determined. Finally a point is reached at which the force is high enough (E) to overcome the capillary force and the particle jumps off the three-phase-contact line.

AFM measurements were conducted on a Nanoscope III MultiMode (Veeco, USA) or on a Dimension 3100 (Veeco, USA) atomic force microscope. Cantilevers were used from Olympus (OMCLAC 160 TS-W2). Modifications to the cantilevers are outlined in the respective chapter.

2.4. UV/Vis/NIR Spectroscopy

Stop bands due to destructive interference:

Colloidal crystals inherently possess a periodic pattern of the dielectric constant, which derives from the difference of the refractive index of the constituent spheres and the surrounding medium, in most cases air. Light is diffracted at this periodic grating leading to constructive and destructive interference. Therefore electromagnetic waves of certain wavelength can not pass the colloidal crystal, depending on the lattice spacing and the materials contrast. This is referred to as the Bragg gap, since this particular

wavelength λ_{Bragg} is filtered from the continuous spectrum according to the Bragg condition of diffraction at a periodic lattice for a given wavelength and angle of incidence. For fcc colloidal crystal the first order Bragg gap can be calculated as[11]

$$\lambda_{Bragg} = 2d_{111}\mathrm{n}_{\mathrm{eff}} \sin\Theta = 1.63D\mathrm{n}_{\mathrm{eff}} \sin\Theta \qquad \text{Equation 2.3}$$

d_{111} is the lattice spacing between (111) planes of the fcc crystal, D is the particle diameter, and $\mathrm{n}_{\mathrm{eff}}$ is the effective refractive index of the opal, which depends on the refractive index of the spheres and the medium. Θ is the angle between the incident light and the (111) plane of the crystal. For transmission spectra, which were recorded throughout this work sin Θ equals 1. $\mathrm{n}_{\mathrm{eff}}$ calculates according to

$$n_{eff} = (\Phi_{sphere}\mathrm{n}^2_{sphere} + \Phi_{medium}\mathrm{n}^2_{medium})^{0.5} \qquad \text{Equation 2.4}$$

Φ_{sphere}, Φ_{medium} are volume fractions of the spheres and the surrounding medium, and n_{sphere} and n_{medium} the corresponding refractive indices.
The Bragg gap is measured as a peak in the extinction spectrum.

Plasmon absorption:
Plasmons are resonant modes that involve the interaction between mobile charge carriers in metals and light.[12] Mobile charge carriers of noble metal nanoparticles can be excited by electromagnetic waves of the right wavelength, which leads to collective oscillations. Resonant modes evolve in the metal nanoparticle, which are referred to as local surface plasmon resonances (LSPR). The position and width of the LSPR is greatly governed by the metal, shape and size of the nanoparticle. Furthermore, depending on the shape the resonances can depend on the polarization of the incident light. The particular LSPR modes of many gold nanoparticles in the several tens and hundreds nanometer range can be measured by UV/Vis/NIR extinction spectra.
Extinction spectra of all samples were recorded in transmission mode, using a conventional UV/Vis/NIR spectrometer (*Lambda 900, Perkin-Elmer*), operating in the 300 – 2500 nm range.

2.5. Brillouin Light Scattering

Light scattering probes local dielectric constant fluctuations, which can be caused by processes like diffusion or thermal fluctuations. Light scattering can be divided in elastic (the wavelength/energy of the incident light is not changed) and inelastic scattering techniques (the scattered light energy is modulated).[13] Brillouin light scattering is an inelastic light scattering technique, which allows the measurement of phonons with fre-

quencies in the hypersonic range (GHz). Scattering takes place due to thermally excited sound waves in the material, called thermal phonons.

One might best understand the principals of BLS by regarding it as constructive interference of multiply reflected light beams at a density grating, which is caused by a plane sound wave of wavelength Λ propagating through the material. Due to the large difference in speed of light and speed of sound, the light wave experiences the grating as a quasi-static one. This simple picture is sketched in Figure 2.4.

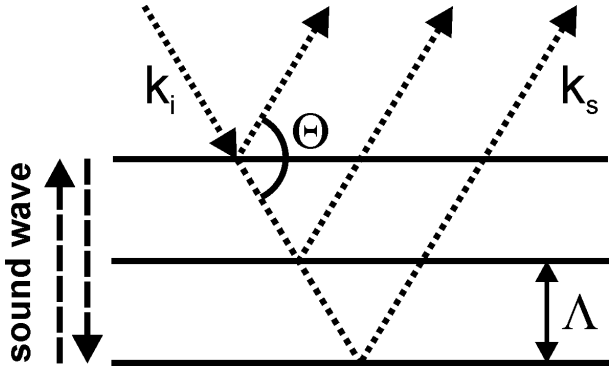

Figure 2.4. *Brillouin light scattering as constructive interference of multiply scattered beams at a dielectric grating with wavelength Λ caused by sound waves.*[14]

Due to the Bragg condition one finds that the wavevector **k** of the sound wave ($k = 2\pi/\Lambda$) is equivalent to the scattering wavevector **q** ($\mathbf{q} = \mathbf{k}_s - \mathbf{k}_i$).

$$q = \frac{2\pi}{\Lambda} = \frac{4\pi n}{\lambda_i} \sin\frac{\Theta}{2} \qquad \text{Equation 2.5}$$

n is the refractive index of the medium, λ_i is the wavelength of the incident light. Thus by changing the scattering geometry different sound waves are probed. An exchange of momentum between the sound wave and the light takes place, which can happen in an additive or subtractive way, since the sound wave can travel in two directions, relative away from or towards the detector. This leads to the characteristic Brillouin doublets,[15] analogous to Stokes and Anti-Stokes peaks in Raman light scattering, caused by a Doppler shift.

$$f = f_s - f_i = \pm\frac{vq}{2\pi} \qquad \text{Equation 2.6}$$

f_s and f_i are the scattered and incident light frequency, respectively. v is the phase velocity of the travelling sound wave. Thus in the scattering spectrum $I_{is}(\mathbf{q},f)$ the doublet centred at the frequency f represents the energy exchange between the sound wave and the light.[14]

The experimental setup for BLS measurements is shown in Figure 2.5. Also the scattering geometry in the sample of a colloidal crystal is envisioned.

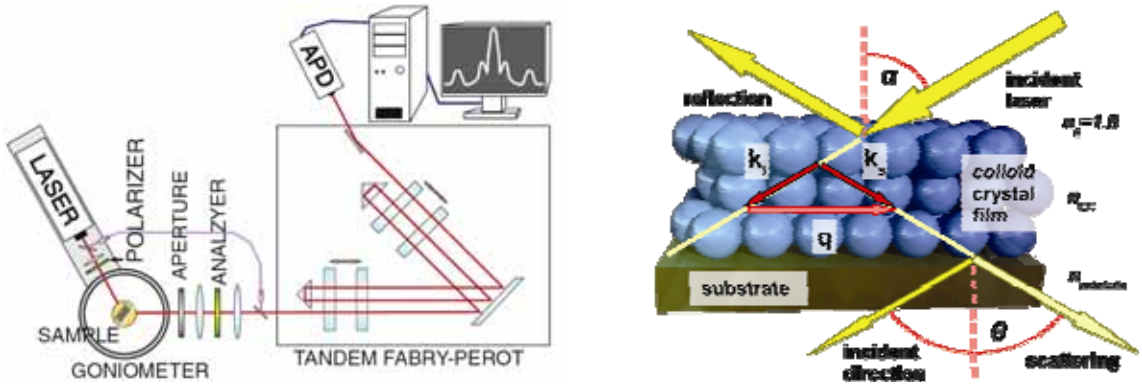

Figure 2.5. *Left: BLS measurement setup, the Tandem-Fabry-Perot interferometer provides the high resolution. Right: Scattering geometry of the incident (k_i) and scattered (k_s) wavevectors in a colloid crystal film.*[16, 17]

The heart of the BLS setup is the six pass Tandem-Fabry-Perot interferometer, which is crucial to reach the high resolution. Laser and sample are placed on a goniometer to adjust the scattering angle.

Two types of measurement modes will be considered within this work. One is the measurement of dry, opaque colloidal films. Due to multiple scattering the wavevector is no longer well defined. Thus only **q**-independent spectra can be recorded. The rich spectra obtained by this approach can be assigned to the particle eigenfrequencies and will be discussed in detail in the Results and Discussion section.

The other type of measurement is conducted on liquid-infiltrated, index-matched colloidal films. On these transparent films **q**-dependent measurements can be conducted, which ultimately give the phonon dispersion relation of the material of interest. Phononic bandgaps can be identified by the analysis of such dispersion relations.

Infiltration of the colloidal films was achieved by dropping a few 100 µl of polydimethylsiloxane (PDMS, made in-house, Mw ~ 800 g/mol) on the sample. Excessive liquid on top of the crystal was blown away by pressurized air or nitrogen streams.

2.6. Bibliography

1. Pawley, J. *Journal of Microscopy-Oxford* **1984,** 136, (OCT), 45-68.
2. Butler, J. H.; Joy, D. C.; Bradley, G. F.; Krause, S. J. *Polymer* **1995,** 36, (9), 1781-1790.
3. Joy, D. C.; Joy, C. S. *Micron* **1996,** 27, (3-4), 247-263.
4. Schindler, B. Untersuchungen zur energiegefilterten Abbildung und Spektrosko pie in einem Feldemissions-Rasterelektronenmikroskop. PhD thesis, Westfäli sche Wilhelms-Universität Münster, Münster, 1999.
5. Binnig, G.; Quate, C. F.; Gerber, C. *Phys. Rev. Lett.* **1986,** 56, (9), 930.
6. Martin, Y.; Williams, C. C.; Wickramasinghe, H. K. *J. Appl. Phys.* **1987,** 61, (10), 4723-4729.
7. Albrecht, T. R.; Grutter, P.; Horne, D.; Rugar, D. *J. Appl. Phys.* **1991,** 69, (2), 668-673.
8. Butt, H. J.; Berger, R.; Bonaccurso, E.; Chen, Y.; Wang, J. *Adv. Colloid Inter face Sci.* **2007,** 133, (2), 91-104.
9. Knoll, A.; Magerle, R.; Krausch, G. *Macromolecules* **2001,** 34, (12), 4159-4165.
10. Preuss, M.; Butt, H. J. *Langmuir* **1998,** 14, (12), 3164-3174.
11. Gaillot, D. P.; Graugnard, E.; King, J. S.; Summers, C. J. *Journal of the Optical Society of America B-Optical Physics* **2007,** 24, (4), 990-996.
12. Murray, W. A.; Barnes, W. L. *Adv. Mater.* **2007,** 19, (22), 3771-3782.
13. Berne, B. J.; Pecora, R., *Dynamic Light Scattering: with Applications to Chemis try, Biology, and Physics*. Wiley: New York, 1975.
14. Wei, C. Hpyersonic Elastic Excitations in Soft Mesoscopic Structures. Phd the sis, Universität Mainz, Mainz, 2007.
15. Brillouin, L. *Ann. de Physique (Paris)* **1922,** 17, 88.
16. Still, T.; Cheng, W.; Retsch, M.; Jonas, U.; Fytas, G. *J. Phys.: Condens. Matter* **2008,** 20, (40), 404203.
17. Cheng, W.; Wang, J.; Jonas, U.; Fytas, G.; Stefanou, N. *Nat. Mater.* **2006,** 5, 830-836.

3. Materials

Monodisperse colloidal particles are prerequisite for the successful fabrication of ordered nanostructures via self-assembly. Even though there are a great variety of nanoparticles available on the market, the in-house synthesis has some striking advantages. Amongst these advantages one has to mention the precise control of the particles surface functionalization, the knowledge of any additives or impurities, and the cheap production.

This section will provide recipes for the preparation of monodisperse polystyrene (PS) and polymethylmethacrylate (PMMA) latex particles of various sizes, surface functionalities and compositions, which will be routinely used in the later chapters. All syntheses were carried out in an emulsifier-free emulsion polymerization fashion as outlined in the introduction chapter. The recipes used here were adapted from literature.[1-4]

Styrene (> 99 %, Aldrich), methylmethacrylate (MMA, 99 %, Acros) and allylmethacrylate (AllylMA, 98 %, Aldrich) were washed three times with a 10 % KOH solution and three times with MilliQ water. Finally the monomers were distilled under reduced pressure; acrylic acid (AA, 99 %, Aldrich) was distilled without washing with KOH. n-butylacrylate (nBA, > 99 %, Aldrich) was run over a basic alumina column. After removal of the inhibitor all monomers were stored in the freezer. Tetraethyl orthosilicate (TEOS, 98 %, Acros) was distilled under reduced pressure and stored under argon atmosphere at RT. Potassium persulfate (KPS, 99+ %, Acros), sodium 4-vinylbenzenesulfonic acid (NaPSS, 90 %, Aldrich), 2,2′-azobis(2-methylpropionamidine) dihydrochloride (ABA.2HCl, 97 %, Aldrich), and [2-(Methacryloyloxy)ethyl]trimethylammonium chloride solution (METAC, 80 wt% in H_2O, Aldrich), LUDOX SM 30 wt%, LUDOX HS 40 wt%, LUDOX AS 30 wt% (all Aldrich), aluminum oxide (30 wt%, 10 nm), and titanium oxide dispersion (anatase, 15 wt%, 5-30 nm) (both NanoAmor Materials Inc., Houston, USA) were used as received. 4-metharyloyloxybenzophenon (MABP) was synthesized by Robert Roskamp.[5]

The polymerization reactions were carried out either in a ~ 300 ml reactor with a thermostat jacket or a 500 ml three necked flask. At first water was heated to the reaction temperature. Then all additives, monomers, and co-monomers were added; solid chemicals were dissolved in water prior to addition. Strong magnet stirring was used and the chemicals were allowed to equilibrate for five min. Finally, the initiator was added as aqueous solution. The reactor was flushed with N_2 or Ar during charging with the

chemicals and a slight inert gas flow was maintained throughout the reaction. Reaction times were typically between 12 and 20 h.

In case of semibatch synthesis mechanical stirring (300 rpm) was used. The seed dispersion was diluted and heated to the reaction temperature. Co-monomers were added at once and allowed to equilibrate for five minutes. After addition of the initiator (as aqueous solution) the monomer feed was started by a syringe pump. The reactions were conducted under nitrogen atmosphere.

Silica nanoparticles were synthesized without any inert atmosphere in a thermostat jacketed ca. 350 ml flask. Only magnetic stirring was used. A mixture of water, EtOH, and ammonia was heated to the reaction temperature. TEOS was diluted 1:4 in EtOH and warmed to the reaction temperature before addition. Stirring was maintained throughout the reaction, which typically took 12 to 24 h.

For the step-by-step experiments, a three necked flask was charged with the seed dispersion. The desired amounts of TEOS (diluted with EtOH) and ammonia (diluted with water) were added by disposable syringes.

For the continuous growth experiments, a three necked flask was charged with the seed dispersion. TEOS (diluted with EtOH) and ammonia (diluted with water) were added by two peristaltic pumps at an adjusted feed rate.

Latex and silica nanoparticles were either purified by several cycles of centrifugation and redispersion, by ultrafiltration, or dialysis. In all cases the purification protocol was adjusted to the particles size and composition by means of centrifugation speed and duration, or filtration and dialysis membrane molecular weight cut-off.

All glass and silicon substrates were sonicated twice with a 2 % aqueous solution of Hellmanex (Hellma GmbH, Mühlheim, Germany) for 15 minutes and extensively rinsed with MilliQ water and ethanol. Plasma cleaning (10 % O_2, 90 % Ar, 300 W, 5 minutes) was used to hydrophilize the substrates.

3.1. Size adjustment of polymer nanoparticles

The syntheses described in this section are all “batch” syntheses. This means that all components were added to the reaction vessel in the beginning at once. The reaction finished after consumption of the provided components. In chapter 3.3 “semibatch” syntheses will be discussed, which start from a seed particle solution and continuous monomer feed is maintained throughout the reaction.

3.1.1. Polystyrene nanoparticles

As it has been pointed out by Ottewill[1, 2] and Shouldice[3] several parameters can be tuned in order to adjust a desired particle size. The parameters are monomer, co-monomer and initiator concentration, temperature, agitation rate and ionic strength. In the cases shown here, the particle size was mainly adjusted by the addition of co-monomers such as NaPSS or AA. Table 3.1 summarizes two sets of experiments, in which the concentration of NaPSS was altered. Monodisperse samples with size distributions of less than 5 % were obtained in all cases.

Table 3.1. Polymerization of styrene carried out in 250 ml MQ water.

entry	styrene, g	KPS, g	temperature, °C	NaPSS, g	diameter, nm
1	15	0.1	70	0.06	179 ± 6
2	15	0.1	70	0.03	219 ± 3
3	15	0.1	70	0.02	260 ± 3
4	15	0.1	70	0.02	234 ± 3
5	15	0.1	70	0.01	297 ± 6
6	15	0.1	70	0.01	300 ± 6
7	15	0.1	70	0.005	360 ± 5
8	7.5	0.2	80	0.05	110 ± 4
9	7.5	0.2	80	0.03	131 ± 7
10	7.5	0.2	80	0.01	199 ± 2

The dependence of final particle diameter and co-monomer concentration follows the reported trends from literature. The dependence is also depicted in Figure 3.1.

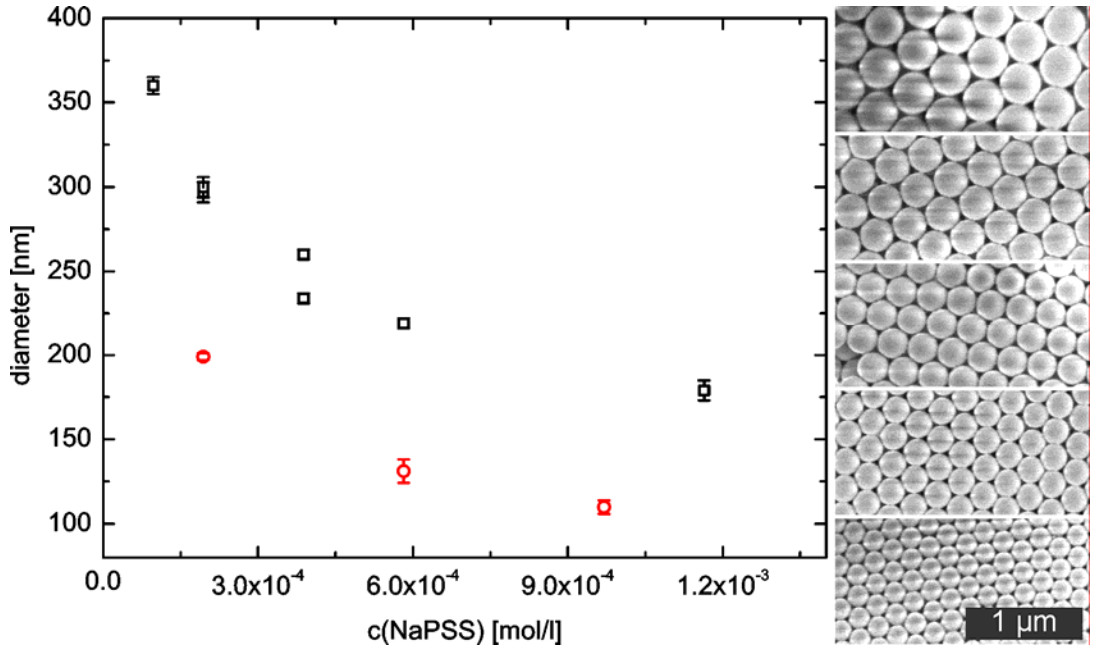

Figure 3.1. *Adjustment of the latex particle diameter by changing of the co-monomer concentration. Open square represent entries 1-7 from Table 3.1. Open circle represent entries 8-10. The right column shows SEM measurements of the corresponding particles.*

From Table 3.1 and Figure 3.1 it becomes clear that the particle size is greatly affected by the co-monomer concentration. The higher the co-monomer concentration, the smaller the particle diameter. According to Ottewill the particle diameter should decrease upon increase of initiator concentration and temperature and reduction of initial monomer concentration. This dependency can also be seen in Figure 3.1, which shows a drastic size reduction for the second set of experiments (open circles).

Initiators and co-monomers are conveniently used to tailor specific properties, like surface charges, of the particle surface. Experiments to synthesize negatively charged PS particles with a weak acid such as AA were carried out. The summarized results in Table 3.2 show the same tendency as for the strong acidic NaPSS co-monomer. However, the particle size is changing less sensitively, which could be caused by the high pKa of AA (~ 4.3)[6] compared to more polar sulfonic acid (< 0).[6]

Table 3.2. Change of the particle size in dependence of the amount of AA as co-monomer for the reaction of 15 ml Styrene and 0.2 g KPS in 250 ml H_2O at 80 °C.

entry	AA, ml	diameter, nm
1	0.1	363 ± 6
2	0.2	356 ± 13
3	0.3	314 ± 13

The size can also be addressed by variation of the monomer concentration relative to the initiator concentration. These results are compiled in Table 3.3.

Table 3.3. Change of the particle size in dependence of the monomer concentration for the reaction of 0.1 ml AA and 0.2 g KPS in 250 ml H_2O at 80 °C.

entry	styrene, ml	diameter, nm
1	15	363 ± 6
2	10	311 ± 4
3	5	225 ± 9

As expected the diameter drops with decreasing styrene concentration. A comparison of entry 1 and 2 assuming a constant number of nucleating particles for each reaction fulfills the cubic root dependency ($r_2 = r_1 \cdot \sqrt[3]{V_2/V_1}$)[4] ($r_2$ is the radius of the sphere after polymerization, V_1 is the initial monomer volume). Entry 2 and 3 slightly mismatch, which might be due to subtle differences during the nucleation period, possibly arising from the different monomer to initiator ratio.

3.1.2. Polymethylmethacrylate nanoparticles

In contrast to PS particles the size of PMMA latexes is less sensitive to variations of initiator or co-monomer concentration. This behavior was found for PMMA particles with positive charge and is summarized in Table 3.4, but was also reported for the KPS analogous case, leading to negatively charged particles.[4] A possible reason for this behavior could be the higher polarity of MMA compared to styrene, which severely influences the particle nucleation as well as monomer and micelle droplet size and number.

Table 3.4. Change of the particle size in dependence of the initiator and co-monomer concentration for the reaction of 10 ml MMA in 250 ml H_2O at 80 °C.

entry	ABA.2HCl, g	10% METAC, ml	diameter, nm
1	0.05	0.094[a]	334 ± 9
2	0.10	0.094[a]	361 ± 8
3	0.15	0.094[a]	333 ± 11
4	0.20	0.094[a]	362 ± 14
5	0.10	0.094	283 ± 13
6	0.10	0.200	277 ± 10
7	0.10	0.300	281 ± 7

[a] *METAC was added after 2 h of reaction.*

Thus, the particle size is best adjusted by varying the monomer concentration. Two examples for PMMA particles with positive and negative charge are shown in Table 3.5 and 3.6, respectively.

Table 3.5. Change of the particle size in dependence of the monomer concentration for the reaction of 0.1 g ABA.2HCl in 250 ml H_2O at 80 °C. No co-monomer was added.

entry	MMA, ml	diameter, nm
1	10	347 ± 5
2	7.5	288 ± 13
3	5	274 ± 9
4	2.5	164 ± 8

Table 3.6. Change of the particle size in dependence of the monomer concentration for the reaction 0.2 g KPS and 0.02 g NaPSS in 250 ml H_2O at 80 °C.

entry	MMA, ml	diameter, nm
1	15	284 ± 9
2	10	231 ± 7
3	8	220 ± 20
4	6	181 ± 5

The results are plotted in Figure 3.2 in order to show the trend more clearly. Additionally, results, which were reported in literature,[4] are also given. Interestingly, the results

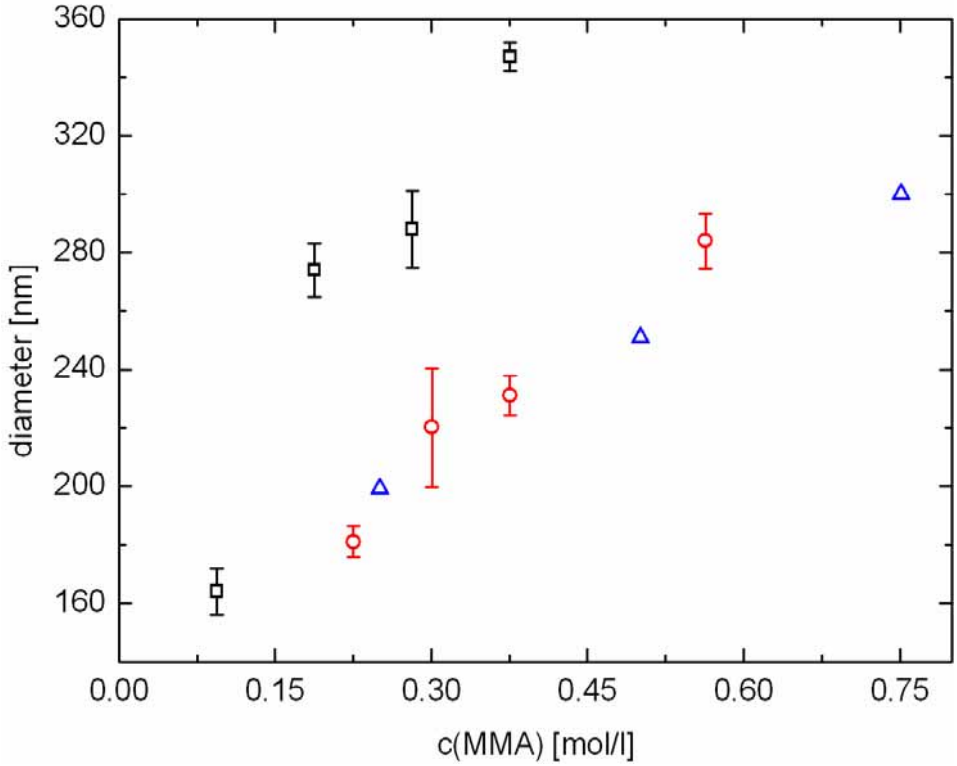

Figure 3.2. *Dependence of the PMMA particle diameter on the MMA monomer concentration. Open squares were initiated by ABA.2HCl (see Table 3.5), open circles are negatively charged particles comprising of KPS and NaPSS (see Table 3.6), and open triangles are values from literature for initiation with KPS.*[4]

shown here match perfectly with the reported values, even though no co-monomer (NaPSS) was used in this case.

Since the slope of the cationic initiator (ABA.2HCl, open squares) is much steeper as compared to the anionic system (KPS and NaPSS, open circles), it is evident that the cationic case reacts more sensitive on the monomer concentration. Concomitantly, the reproducibility of cationic latex fabrication is poorer than the anionic one.

3.2. Synthesis of Monodisperse Polymer Particles with Different Functionality and Composition

Not only the size of colloidal particles is an important parameter. For many experiments the surface functionality (positively or negatively charged; tuneable degree of polarization) plays an important role and needs to be controlled. Covalent introduction of functional groups to a colloidal particle can be achieved by rational selection of initiator and co-monomer. Table 3.7 lists experiments, which were designed in a way to give particles of almost identical size, but with various charges on the surface.

Table 3.7. Recipes used to synthesize PMMA particles of similar size but different surface functionality. All reactions were carried out in 250 ml H_2O at 80 °C.

entry	MMA, ml	comonomer	initiator, g	diameter, nm	ς, mV[a]
1	7.5	-	0.1 ABA.2HCl	288 ± 13	+42.5 ± 2.0
2	10	0.094 ml 10%METAC	0.1 ABA.2HCl	283 ± 13	+38.4 ± 0.8
3	7	0.1 ml AA	0.2 KPS	267 ± 7	-45.7 ± 1.6
4	15	0.02 g NaPSS	0.2 KPS	284 ± 9	-46.6 ± 1.6

[a] *Zeta potential measured in MQ water.*

Four different particles were obtained: two being positively and two being negatively charged. They differ in their degree of ionization upon change of pH. Entry 1 with only amidinium entities is a soft base, whereas the use of a quaternary amine (METAC) introduces a permanent positive potential (entry 2). The same concept applies for entries 3 and 4 with acrylic acid being a weak, and styrene sulfonic acid being a strong negative charge carrier.

Another method to introduce function to a specific particle is by changing the constituent polymer itself. Synthesis of PS or PMMA particles was already shown in Chapter 3.1.1 and 3.1.2. Copolymerization of two distinct monomers permits the combination of their individual properties and hence, allows control over various features such as the glass transition temperature, Tg. Random copolymerizations of MMA and nBA were conducted in order to tune the Tg of the resulting colloid.[7, 8] Table 3.8 summarizes the experimental details for the fabrication of PMMA/nBA colloids with similar size but different monomer composition.

Table 3.8. Recipes used to synthesize PMMA/nBA copolymer particles of similar size. All reactions were carried out with 0.2 g KPS and 0.02 g NaPSS in 250 ml H_2O at 80 °C.

entry	MMA, ml	nBA, ml	diameter, nm	Tg, °C[a]
1	10	-	231 ± 7	112
2	9	1	215 ± 6	92
3	8	2	197 ± 6	70
4	7	3	205 ± 4	47

[a] *determined by the 3rd heating cycle in DSC.*

3.3. Synthesis of Core-Shell Particles and Semibatch Synthesis

Using batch processes as described above one can obtain monodisperse polymeric nanoparticles in a size range from about 100 nm to 800 nm.[2] However, for various applications particles in the low micrometer size range with narrow size distribution are necessary. To achieve that, a seeded growth emulsion polymerization is the method of choice. In order to avoid secondary nucleation, which would lead to a bimodal distribu-

tion, one has to control the seed concentration, the amount and feed rate of the added monomer, and the initiator and co-monomer concentration.

With no secondary nucleation occurring, one can calculate the final particle diameter, r_2, using equation 3.7.[9]

$$r_2 = r_1 \cdot \sqrt[3]{1 + \frac{m_{m2} \cdot C_2}{x_{SC1} \cdot m_{D1}}} \qquad \text{Equation 3.7}$$

r_1 is the initial particle diameter, x_{SC1} the solid content, and m_{D1} the mass of the seed particle dispersion used in the semibatch synthesis. m_{m2} is the weight of the added monomer and C_2 the expected conversion, typically larger than 0.9, for the emulsion polymerization.

Table 3.9 shows the synthesis of PS particles with diameters larger than 1 μm via two ensuing seeded growth steps.

Table 3.9. Semibatch synthesis for PS particles larger than 1μm. All syntheses were carried out with a mechanical stirrer (300 rpm) and at 70 °C.

entry	styrene, ml	seed dispersion	KPS, g	NaPSS, g	rate, ml/h[d]	solid content, %[e]	diameter, nm
seed[a]	39	-	0.2	-	-	8.6	566 ± 14
1[b]	22	100 ml of seed	0.5	0.02	2.89	16	1137 ± 33[f]
2[c]	22	50 ml of (1)	0.5	0.02	2.89	14.7	1686 ± 58[f]

[a] *with 0.2 g NaCl in 300 ml H_2O according to literature.*[2]
[b] *50 ml H_2O added.*
[c] *100 ml H_2O added.*
[d] *monomer feed rate.*
[e] *assuming 90 % conversion.*
[f] *some minor second nucleation occurred.*

The diameter of the particles of entry 1 in Table 3.9 is a lot larger than one would expect from equation 3.7 that calculates to about 820 nm diameter. The reason for that is not clear, especially since second nucleation or other side reactions would rather result in smaller diameters. Possibly a mistake happened when weighing the reactants. However, the second seeded growth step (entry 2) matches perfectly with the expected size, which was predicted to be 1677 nm.

Instead of using the same monomer as for the seed particle, one can also use a different monomer, or a mixture of various monomers in the feed step. This approach opens the way to fabricate core-shell particles, which comprise of different physical properties in core and shell. Here, the synthesis of core-shell particles, with a rigid core and a soft shell, which could also be crosslinked, is shown. Table 3.10 gives the experimental details.

Table 3.10. Semibatch synthesis of hard-core, soft-shell nanoparticles. All reactions were carried out with 0.02 g NaPSS and mechanical stirring (300 rpm) at 70 °C.

entry	monomer[a]	seed dispersion, ml	KPS, g	water, ml	rate, ml/h[b]	diameter, nm[c]	PDI[c]
seed	15 g styrene	-	0.1	250	-	255	0.026
1	12 g nBA 4 g MMA 0.1 g AllylMA	100	0.3	100	2.89	379	0.036
2	16 g nBA 0.3 g MABP	100	0.3	100	2.89	342	0.049

[a] *monomers were mixed and added via a single syringe pump.*
[b] *monomer feed rate.*
[c] *particle size was measured with a Malvern Zetasizer 3000HS. PDI: polydispersity index.*

In both cases the expected particle diameter matches well with the calculated size, which should be 355 nm for dry particles. Entry 1 has a slightly larger diameter, which can be explained by the fact that the Zetasizer only measures the hydrodynamic radius, R_h. The shell of these particles is slightly crosslinked by the addition of AllylMA. The particles of entry 2 have a slightly smaller radius than expected, maybe due to some minor second nucleation or a not complete conversion. They have a very soft shell, which can be crosslinked under UV irradiation due to the co-monomer MABP.

3.4. Synthesis of Monodisperse Silica Nanoparticles

Another important class of colloidal nanoparticles are inorganic particles consisting of metals or metal oxides. They feature a manifold of physical properties, which in many cases are complementary to their polymeric counterparts. Important differences are for example the heat resistance and insolubility in organic solvents in case of metal oxide nanoparticles. Silica nanoparticles are widespread, since their monodisperse synthesis is fairly easy and their surface functionality can be tuned over a wide range by the well known silane chemistry. In principal two synthetic strategies are feasible to synthesize monodisperse silica nanoparticles. The first one is a one-step batch process, also termed "Stöber" process.[10, 11] The other one is a seeded growth process; this can either be conducted in a step-by-step manner,[12] or by continuous addition of the reaction components.[13, 14]

Whereas the one-step Stöber process is the simplest and fastest process, it can be rather difficult to get highly monodisperse particles especially in the case of < 400 nm particles. The particle size and polydispersity is governed by the interplay of TEOS-, water-, and ammonia concentration and the reaction temperature. One-step syntheses, which gave moderately monodisperse silica nanoparticles, are put together in Table 3.11.

Table 3.11. One-step synthesis of silica nanoparticles. TEOS was preheated and added as a 1:4 diluted ethanolic solution to the reaction mixture. Strong magnetic stirring was used.

entry	TEOS, ml	NH_3 (32%), ml	H_2O, ml	EtOH, ml	temperature, °C	diameter, nm
1	5	10	-	145	60	45 ± 6
2	5	10	-	145	40	104 ± 8
3	6.7	18.3	10.7	64.4	60	255 ± 15
4	8.9	18.3	10.7	62.2	60	385 ± 18
5	4.5	18.3	1.64	76.6	RT	641 ± 21

General trends, which were already reported, could also be observed in the experiments shown here. Comparing entry (1) and (2) shows that an increase in reaction temperature leads to a reduction in particles size; in many cases it also leads to a reduction in particle size distribution. Increasing the amount of TEOS also increases the final particle diameter (entry (3) and (4)).

In order to gain more control over the particle size and their distribution, seeded growth approaches were conducted. Firstly, a step-by-step growth was investigated.[12] For this purpose 25 ml of (2) from table 3.11 were stirred with a magnetic stirrer at room temperature. TEOS (1:3 dilute with EtOH) and $NH_{3,\ conc}$ (5.25 ml + 0.4 ml H2O) were added in portions of 4 ml and 0.28 ml, respectively. After 15 addition steps over a period of ten days (with the shortest interval being 3.5 h) the reaction was finished. Using the cubic root dependency, the expected and experimental particle diameters could be compared.[13] The results for the single addition steps are summarized in Figure 3.3.

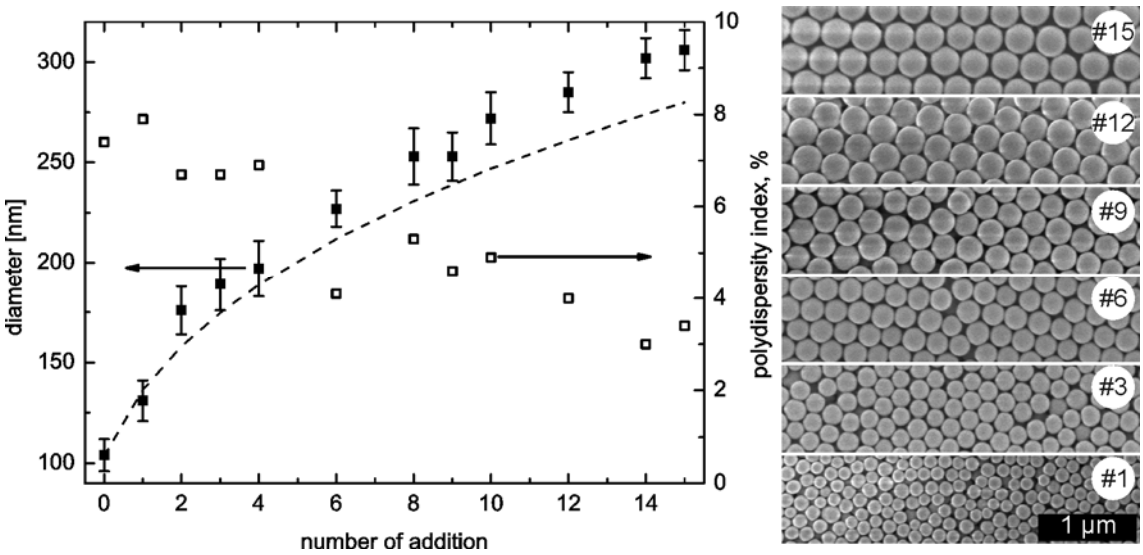

Figure 3.3. *Step-by-step growth of silica nanoparticles. Full squares are the experimental diameters, determined by SEM images. The dotted line shows the theoretically expected diameter, assuming a cubic root dependency. The open squares give the corresponding polydispersity index The right panel shows SEM images of the silica nanoparticles at various stages.*

As can be seen from Figure 3.3 the step-by-step growth can be predicted by the cubic-root dependency. The theoretical underestimation of the experimental diameter at later stages of the synthesis can be explained by the inherent porosity of the silica nanoparticles fabricated by this method, which leads to an overall larger particle size with lower silica density. The polydispersity index of the particles decreases with the number of addition steps.

Finally, continuous growth experiments were conducted.[14] The experiments were conducted in a three necked flask with magnetic stirring, the controlled feed was provided by two peristaltic pumps for TEOS and NH_3, respectively. Three particles were synthesized by continuous growth, where each growth step also served as seed particle in the following experiment. Table 3.12 and Figure 3.4 summarize the reaction conditions and results.

Table 3.12. Continuous growth of silica nanoparticles. All reactions were carried out at room temperature and with vigorous magnetic stirring.

entry	seed	feed 1	rate 1, µl/min	feed 2	rate 2, µl/min	diameter, nm
seed, see (1) from table 2.11						45 ± 6
1	50 ml of seed	14.8 ml NH_3 + 1.1 ml H_2O	11.1	57,7 ml TEOS + 173,1 ml EtOH	160.3	136 ± 6
2	50 ml of (1)	18.6 ml NH_3 + 1,4 ml H_2O	11.1	72.1 ml TEOS + 216,4 ml EtOH	160.3	285 ± 7
3	50 ml of (2)	10.8 ml NH_3	20	50 ml TEOS + 200 ml EtOH	464	378 ± 9

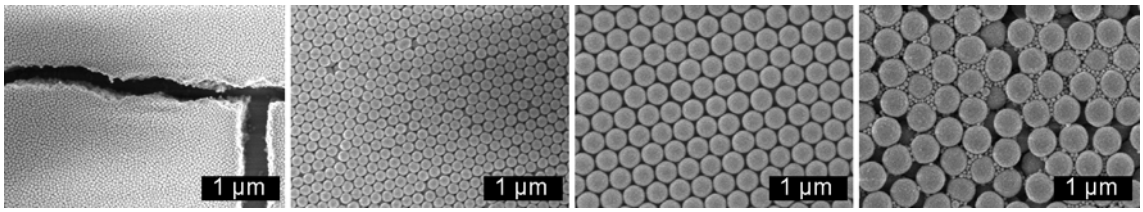

Figure 3.4. *SEM images of the seed particles (left) and the final particles after each step of continuous growth (1, 2, and 3 from middle left to right).*

Similar to the step-by-step growth a good control over particle size and distribution could be observed. Highly monodisperse silica nanoparticles in a size range from 100 nm to 400 nm could be synthesized by this method. The higher addition rate in the last case (entry 3) might be the reason for some minor secondary nucleation, which can be seen on the right side in Figure 3.4. However, the big difference in sizes makes it possible to separate the secondary seeds by centrifugation.

The major advantage of the continuous particle growth is the automation, which produces the desired particle size faster and with less experimental effort, as compared to

the step-by-step addition. Both methods give equally monodisperse, spherical silica particles.

3.5. Fabrication of Colloidal Crystals

The synthesis of monodisperse nanoparticles is the first step to successfully fabricate colloidal crystals (CC). The second step is the assembly of the nanoparticles in a highly ordered ensemble. This can be done by a variety of methods such as sedimentation,[15] centrifugation,[16] filtration,[17] or vertical deposition.[18] The method of choice in the work presented here was vertical lifting deposition (VLD),[19] and was used for the fabrication for all three-dimensionally ordered crystals or glasses. Parameters, which influence the quality and thickness of the resulting crystal, are lifting speed, particle concentration, substrate surface functionality, temperature, and humidity. Two VLD setups were used throughout the work. One, with an automatic z-stage with adjustable speed in a vibration isolated Perspex box, which did not allow controlling the environmental humidity, but ensured a constant climate during the experiment. The other one is shown in Figure 3.5.

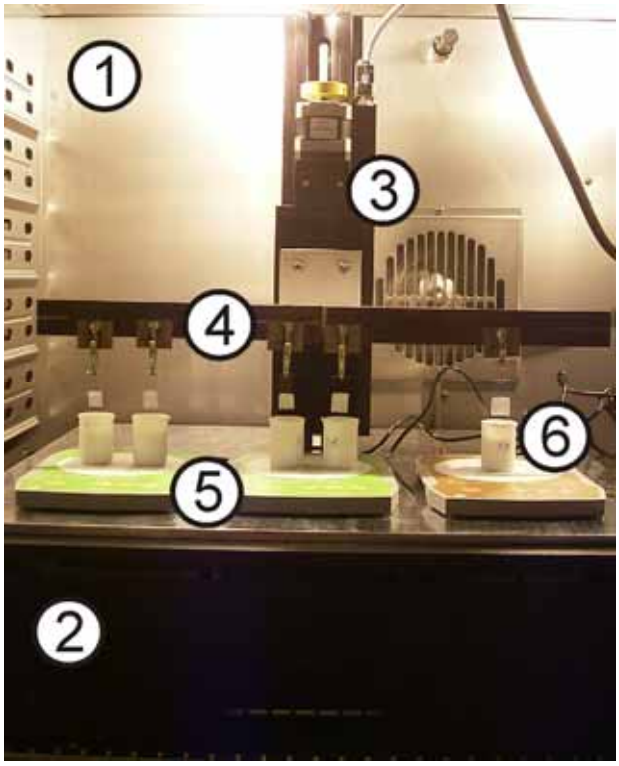

Figure 3.5. *Photograph of the vertical lifting setup used in this work. Important parts are indicated by numbers, please refer to the text for more details.*

The setup shown in Figure 3.5 was self-built and consists of several parts. (1) Constant clima chamber KBF 240 from Binder, with a temperature range from -10 °C to 100 °C, and relative humidity from 10 % to 90 %. (2) MinusK vibration isolation table BM-6.

(3) OWIS high precision z-stage Limes 60 in combination with a home-built control unit. The speed is adjustable from 50 nm/s to 10 µm/s at a step size of 600 nm. (4) Magnetic stripe to easily "click in" the clamps, which hold the samples. (5) Magnetic stirrers to ensure convection in case of heavy or large particles. (6) Teflon beakers for the colloidal dispersion, which prevent crystallization of particles to the beaker.

Typical parameters ranged from 0.5 wt% to 4 wt% dispersion concentrations, 20 °C – 30 °C environmental temperature, 30 % - 80 % RH environmental humidity, and 100 nm/s to 1 µm/s lifting speed.

Detailed results of the colloidal crystals and films, which were fabricated using these setups and parameters will be discussed in the respective chapter in the Results and Discussion section.

3.6. Inverse Opals via Codeposition

Inverse opals are the 3D negative of a colloid crystal; that means that a continuous skeleton of a certain material encloses spherical air bubbles. The attractiveness of inverse opals stems from the high internal interface with yet continuously connected and ordered pores. A variety of materials, as well as a vast range of methods to generate inverse opals has been investigated in the past.[20] Codeposition of large colloidal particles simultaneously with small nanoparticles as filling and finally skeleton material is one of the easiest methods. However, the right particle ratio from colloids to nanoparticles has to be found in order to obtain fully filled and simultaneously highly ordered mesostructured materials. A systematic study of the influence of nanoparticle concentration on the crystalline order of the inverse opal was conducted.

PS particles with a diameter of 300 nm in aqueous suspension were used at a concentration of 1 wt% and the concentration of the silica nanoparticles (LUDOX SM) was adjusted to be 0.3 wt%, 0.5 wt%, 0.8 wt%, and 1.1 wt%. VLD was conducted at 20 °C, 50 % RH at a lifting speed of 400 nm/s. The films were deposited on plasma treated glass. After VLD the PS particles were removed by calcination for a few hours in a tube oven at 450 °C in air. The quality of the resulting inverse opal was characterized by SEM and UV/Vis measurements; the results are compiled in Figure 3.6.

Both, SEM and UV/Vis, show an increase in order with a decrease of silica nanoparticle concentration. Whereas in the case of 1.1 wt% silica nanoparticles no crystallinity can be observed in the SEM side view images, some ordered domains start growing from the top and bottom interface in case of 0.8 wt% and 0.5 wt% samples, respectively. A completely crystallized inverse opal was obtained in the case of only 0.3 wt% silica

nanoparticles in the dispersion, which is confirmed by the UV/Vis measurement, where a sharp peak evolves at 488 nm. Only slight bumps were measured around the Bragg peak position for the higher concentrated samples, no feature could be resolved in the highest concentration case.

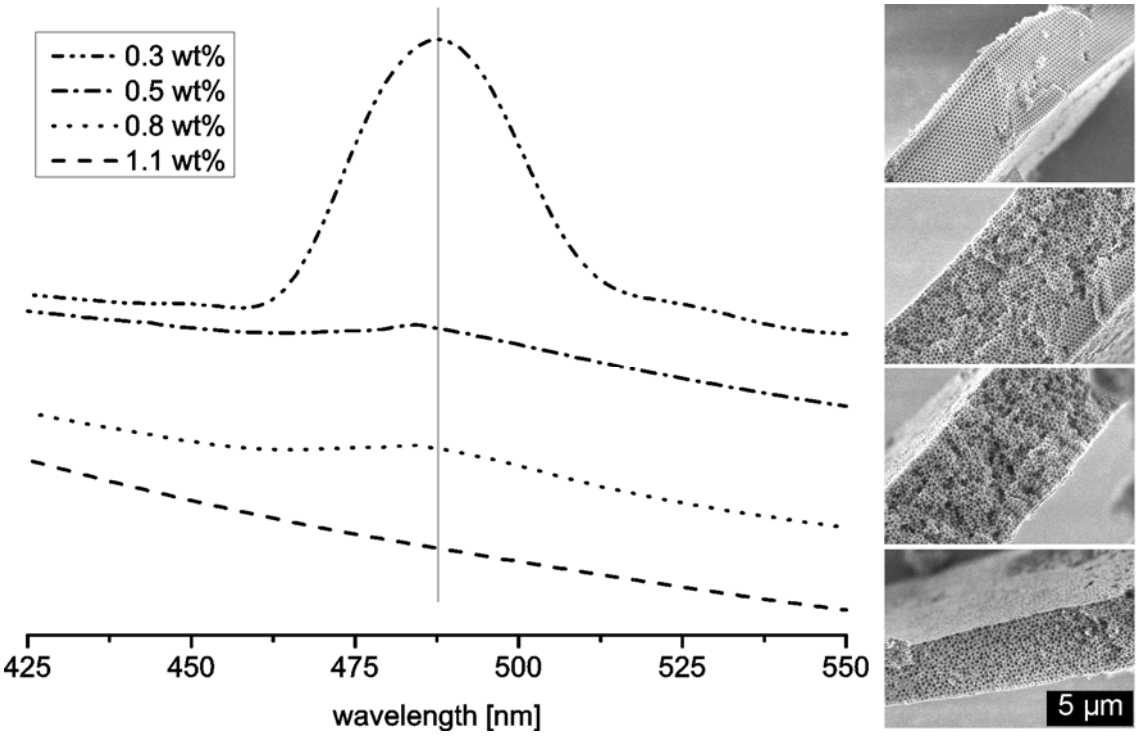

Figure 3.6. *Left: Background corrected UV/Vis transmission spectra of inverse opals with various silica nanoparticle content during the codeposition process (y-axis is absorption). The individual curves were offset for reason of clarity. Right: Correlating SEM measurements of the inverse opals, 0.3 wt% to 1.1 wt% from top to bottom.*

Based on these findings a series of inverse opals with various void sizes was set up. Particles of 180 nm (1 wt%, 0.3 wt% LUDOX SM), 300 nm (1 wt%, 0.3 wt% LUDOX SM), and 400 nm (2.3 wt%, 0.3 wt% LUDOX SM) were used. VLD parameters were 20 °C, 50 % RH and 400 nm/s. Calcination was conducted at 450 °C in air.

The inverse opals are shown in Figure 3.7.

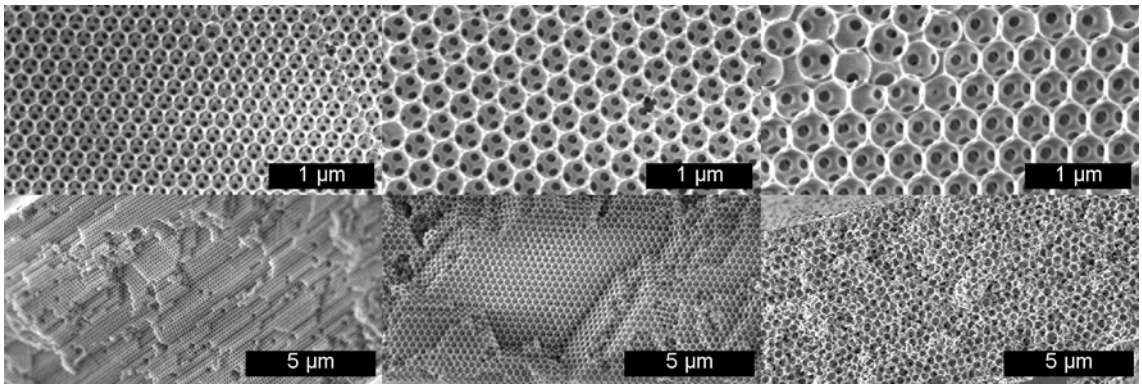

Figure 3.7. *Inverse opals, which were fabricated by the use of 180 nm, 300 nm, and 400 nm PS particles as templates (from left to right). The top row shows top view images, the bottom row side view cuts.*

Porous silica replica of high quality were obtained in all cases. The absence of crystalline order within the layer bulk in case of the 400 nm particles (Figure 3.7 right) must be attributed to the higher polydispersity of the templating PS particles.

In principal this methodology can be applied to a great range of metaloxide nanoparticles, which paves the way to fabricate inverse opals consisting of various materials.

3.7. Bibliography

1. Goodwin, J. W.; Hearn, J.; Ho, C. C.; Ottewill, R. H. *Colloid. Polym. Sci.* **1974,** 252, 464-471.
2. Chung-li, Y.; Goodwin, J. W.; Ottewill, R. H. *Prog. Coll. Polym. Sci.* **1976,** 60, 163-165.
3. Shouldice, G. T. D.; Vandezande, G. A.; Rudin, A. *Eur. Polym. J.* **1994,** 30, (2), 179-183.
4. Egen, M.; Zentel, R. *Macromol. Chem. Phys.* **2004,** 205, (11), 1479-1488.
5. Beines, P. Synthese und Charakterisierung einer Hydrogelmatrix für die Multia nalyt-Sensorik. PhD thesis, Universität Mainz, Mainz, 2007.
6. March, J., *Advanced Organic Chemistry*. 2nd Edition ed.; McGraw-Hill Book Company: New York, 1977.
7. Penzel, E.; Rieger, J.; Schneider, H. A. *Polymer* **1997,** 38, (2), 325-337.
8. Gordon, M.; Taylor, J. S. *Journal of Applied Chemistry* **1952,** 2, (9), 493-500.
9. Krüger, C. Kolloidale Organisation auf lithographisch hergestellten Silanschich ten: Neue Möglichkeiten der Strukturbildung auf Oberflächen. PhD thesis, Jo hannes Gutenberg Universität Mainz, Mainz, 2001.
10. Stöber, W.; Fink, A.; Bohn, E. *J. Colloid Interface Sci.* **1968,** 26, (1), 62-69.
11. Giesche, H. *J. Eur. Ceram. Soc.* **1994,** 14, (3), 189-204.
12. Bogush, G. H.; Tracy, M. A.; Zukoski, C. F. *J. Non-Cryst. Solids* **1988,** 104, (1), 95-106.
13. Zhang, J. H.; Zhan, P.; Wang, Z. L.; Zhang, W. Y.; Ming, N. B. *J. Mater. Res.* **2003,** 18, (3), 649-653.
14. Giesche, H. *J. Eur. Ceram. Soc.* **1994,** 14, (3), 205-214.
15. Mayoral, R.; Requena, J.; Moya, J. S.; Lopez, C.; Cintas, A.; Miguez, H.; Meseguer, F.; Vazquez, L.; Holgado, M.; Blanco, A. *Adv. Mater.* **1997,** 9, (3), 257-260.
16. Vos, W. L.; Megens, M.; vanKats, C. M.; Bösecke, P. *Langmuir* **1997,** 13, (23), 6004-6008.
17. Velev, O. D.; Jede, T. A.; Lobo, R. F.; Lenhoff, A. M. *Nature* **1997,** 389, (6650), 447-448.
18. Denkov, N. D.; Velev, O. D.; Kralchevsky, P. A.; Ivanov, I. B.; Yoshimura, H.; Nagayama, K. *Langmuir* **1992,** 8, (12), 3183-3190.
19. Dimitrov, A. S.; Nagayama, K. *Langmuir* **1996,** 12, (5), 1303-1311.
20. Li, Q.; Retsch, M.; Wang, J.; Knoll, W.; Jonas, U. *Top. Curr. Chem.* **2008,** DOI 10.1007/128_2008_3.

4. Results and Discussion

The work presented in this chapter is organized in two parts. The first part outlines the fabrication of colloidal monolayers and their usage as mask for nanosphere lithography. After a detailed description of the monolayer fabrication process, the possibility to structure colloidal monolayers without the necessity of a template is envisioned. Finally, the established system is used for two applications in the field of nanosphere lithography. A methodology to generate ultraflat, laterally nanostructured surfaces will be shown. Furthermore, densely ordered arrays of golden split-ring resonators will be synthesized in three dimensions.

In an approach to fabricate hierarchically three-dimensionally structured materials, the synthesis of inverse opals in inverse opaline materials comprising of various materials will be introduced.

The second part deals with the phononic properties of colloidal crystals and films. At first, the vibrational properties of colloidal particles and their mechanical properties in the dry state will be outlined. Then measurements on liquid infiltrated samples will be discussed, with the focus being laid on the effective sound velocity and the existence of band gaps in such nanostructured materials. Different regions in the phonon dispersion relation diagram will be assessed to address these questions.

4.1. Fabrication of Large Area, Transferable Colloidal Monolayers Utilizing Self-Assembly at the Air-Water Interface

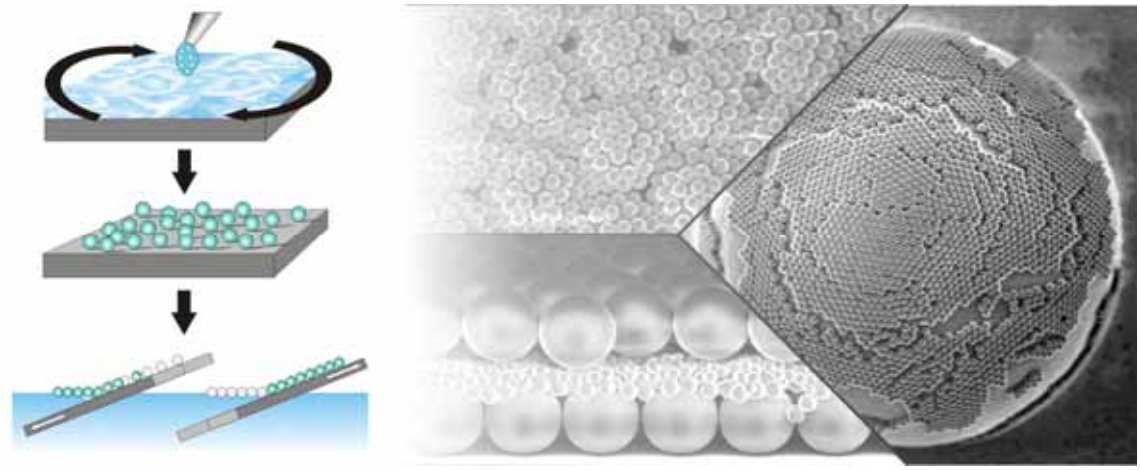

Close-packed colloidal 2D crystals can serve as templates for various surface patterning- and structuring methods. A versatile and simple method for the rapid fabrication of close-packed colloidal 2D crystals with large domain sizes by floating and redeposition of colloidal monolayers at the air-water interface is presented here. A detailed analysis of changes on the particle surface during the individual steps of the monolayer fabrication process has been conducted. It was found that the quality of the monolayer depends on various parameters like colloidal particle distribution on the initial parent substrate, pH adjustment of the subphase, and addition of surfactants. The floating monolayer can be transferred onto many substrate types, regardless of surface polarity, roughness, or curvature.

4.1.1. Introduction

Two dimensional (2D) colloidal crystals, or colloidal monolayers, are of particular importance to nanoscale surface patterning, which is a key platform for a variety of applications such as high density data storage,[1, 2] photonic crystals,[3] and biosensors.[4] Furthermore, colloidal monolayer-based surface patterning, i.e. nanosphere lithography,[5, 6] presents a simple and cost effective method to produce repetitive symmetric patterns with structural features down to the sub-100 nm regime.[7-11] A key technical component of nanosphere lithography is the deposition of a layer of colloidal particles serving as a sacrificial mask, which is removed after the patterning process. The morphology and function of the resultant nanostructures depend on the colloidal particle size, interparticle separation distance, ordering, and the overall colloidal film size. Moreover, colloidal monolayers have also found promising applications in microoptics[12] and surface modifications.[10] In practice, a major obstacle to the broader application of colloidal monolayers is the difficulty in fabricating and processing large areas with minimum defect density.

Different methods have been developed to assemble nanospheres with high order on various substrate types. The 2D colloidal crystal self-assembly can be divided into two categories: 1) direct assembly on the target substrate and 2) pre-assembly on an intermediate surface followed by a transfer onto the target. In the first case (1) monolayer deposition was often achieved by drying the colloidal suspension on a vertical substrate or by vertical lifting deposition.[13, 14] Thickness control was mainly achieved by adjusting the dispersion concentration and substrate lifting speed. However, the formation of stripes due to pinning of the meniscus limits the vertical lifting deposition for large area samples.[15] Monolayer formation on tilted substrates was demonstrated by Micheletto *et al.*[16] by using a closed chamber and a Peltier element to control the rate of evaporation in order to improve the quality of the final monolayer. Furthermore, spin coating was employed as a rapid method to form colloidal monolayers.[17] Although spin-coating is an extremely rapid and simple fabrication method, the strong rotational force and its radial gradient hinders the formation of large, single crystalline domains. Additionally, careful adjustments of concentration, rotational speed, and surface functionality have to be carried out for each single type of particle. More elaborated equipment has been designed by Picard *et al.*[18] They employed a dynamic thin laminar flow, controlled by a rotating glass rod, to deposit colloidal monolayers on hydrophilic and hydrophobic substrate. Nevertheless, the methods reported so far provide colloidal monolayers of only limited quality in terms of sample area size, defect density, and controllability; in many cases

free voids or multilayered regions are formed alongside with the monolayer areas. Thus indirect fabrication methods were formulated which provide the required particle mobility for defect free packing. In these indirect methods, high quality monolayers are first formed on an intermediate surface (like water) that allows for better particle ordering, and then transferred to the target substrate.[19] In a typical procedure, colloidal particles are dispersed in an organic liquid and slowly pipetted onto a water surface. After evaporation of the solvent the mobile colloidal spheres form highly ordered floating films over a large area that can be transferred to the desired substrate.[7, 20-22] These approaches often employ the well established Langmuir-Blodgett technique, with which the floating particles are first compressed by a barrier to a dense monolayer and then deposited on the receiving substrate.[23]

The procedure introduced here represents a simple and rapid method to utilize the air-water interface for self-assembling large area, high quality, and transferable monolayers. It comprises the sparse, disordered distribution of individual, dry latex particles on a solid support (the parent substrate), followed by an immersion step, during which the ordered colloidal monolayer is formed by self-assembly, and finally the transfer of the floating film to a target substrate.

4.1.2. Monolayer formation by dry, sparsely distributed particles

It has been previously reported that colloidal polystyrene particles can be trapped at the air-water interface to form highly ordered 2D crystals,[24] and various methods have been described for the deposition of single colloidal particles onto the air-water interface. Dispersing particles in a volatile, water-immiscible, organic non-solvent for the latex particles and spreading the organic suspension onto the air-water interface is a common practice.[25, 26] Barriers of a Langmuir-Blodgett trough are used to push the particles into a hexagonally close-packed monolayer, which is then transferred onto a solid substrate. With the novel approach presented here, a close-packed monolayer is fabricated by floating and self-aggregation of a sparse particle sub-monolayer without the necessity of using the Langmuir-Blodgett technique. Figure 4.1.1 presents the basic principle of this method, which will be referred to as “dry, sparsely distributed particles” (*DSDP*) method.

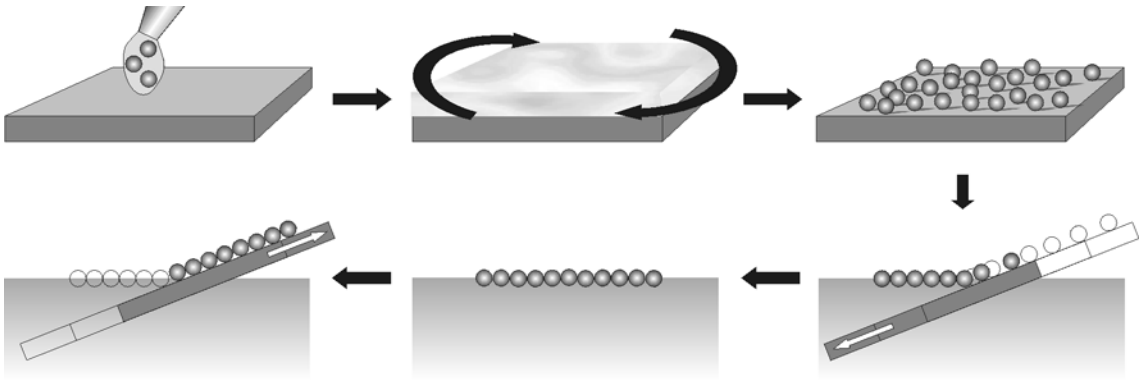

Figure 4.1.1. *Monolayer formation at the air-water interface from a spin coated parent substrate by the DSDP-method.*

The fundamental prerequisite of the *DSDP*-method is that colloidal particles are deposited on a first substrate (denoted as parent substrate) as sparsely distributed spheres (optimally the particles should not touch each other). When the parent substrate is slowly immersed into the water phase, the colloids that reach the three-phase-contact line detach from the substrate surface and float on the water interface. At this point the particles do not diffuse away but remain at the three-phase-contact line and are pushed forward by the following colloids. Thus the single particles self-assemble into a highly ordered monolayer without further treatment. This 2D crystallization can be regarded as a quasi-epitactic crystal growth, as single particles are individually incorporated into the edge of the hexagonal closed-packed floating monolayer. Finally, the floating monolayer is transferred to a second substrate (denoted as receiving substrate). Figure 4.1.2 demonstrates the effectiveness of this self-assembly process at the air-water interface in the *DSDP*-method. The sparse particle distribution on the parent substrate is shown in Figure 4.1.2 a) and c) for particles of 1116 nm and 182 nm in diameter, respectively. In order to optimize the 182 nm particles separation, the substrates were chemically modified beforehand by a cationic silane, NR_4^+. This treatment greatly enhances the electrostatic adsorption of the negatively charged colloids onto the substrate with high particle coverage. While maintaining the particle separation, the quaternary silane layer is hydrophilic enough to be easily spin-coated with the particle dispersion, and the electrostatic adsorption is sufficiently reversible, for the adsorbed colloids to detach from the substrate during the floating step.

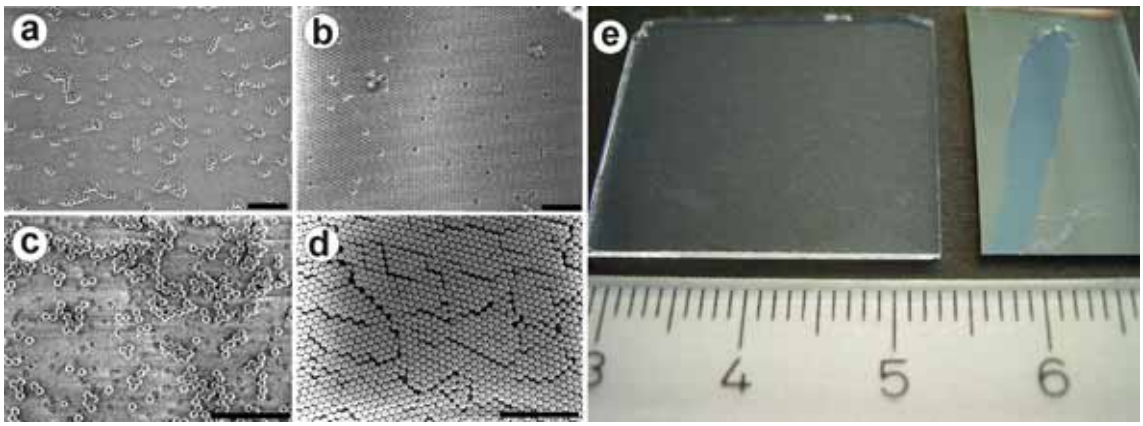

Figure 4.1.2. *Formation of highly ordered, hexagonally close-packed monolayers (b and d) by floatation of sparsely distributed colloids of 1116 nm (a) and 182 nm (c), respectively, with the DSDP-method. (e) shows a comparison of the 182 nm particles distribution on the parent substrate (left) versus a resultant close packed monolayer after floating (right, dark blue patch). Scale bars are 10 µm for figures (a) and (b), and 2 µm for figures (c) and (d).*

As seen in Figure 4.1.2 a) and c), the individual separation of the colloids is not perfectly achieved by the spin coating procedure, as some small clusters coexist with the individually isolated particles. Cluster formation is enhanced with decreasing particle diameter and increasing particle concentration. During the immersion of the parent substrate the hexagonally close-packed arrays form instantaneously at the three-phase-contact line. This can be observed by naked eye by the evolution of strong iridescent colors in the case of the 1116 nm particles. A qualitative analysis of the correlation between the particle distribution on the parent substrate and the homogeneity of the monolayer on the receiving substrate reveals that the presence of particle clusters inhibits the formation of a monocrystalline film. It is reasonable to assume that those clusters either serve as independent nucleation centres for single-crystalline domains, which subsequently reduce the domain size with increasing cluster number, or that cluster incorporation with random orientation causes defect-formation. This behaviour is apparent in Figure 4.1.2, where the relative crystal domain size in the dense monolayer of the 182 nm particles (Figure 4.1.2 d) is much smaller compared to the 1116 nm particles (Figure 4.1.2 b). Nevertheless, in both cases, some systematic defects are inevitably introduced as the substrate was immersed by hand. When using fully coated substrates of about 2.5 cm x 2.5 cm, the sparse particle layer collapses down to a monolayer with dimensions of about 2.5 cm x 0.5 cm, as shown in Figure 4.1.2 e. The *DSDP*-method proved to be applicable to PS and PMMA particles; successful monolayers were fabricated with sizes ranging from 90 nm to 1.2 µm. However, monolayers exceeding this size range should in principal be possible, too. A key feature of all samples prepared by the *DSDP*-method is that the width of the parent sparse particle layer is preserved in the

compact monolayer and that shrinkage takes place only along the immersion direction. The significant advantage of this method is that only few parameters need to be controlled to obtain a high quality, large area monolayer. Two critical parameters are the concentration and the volume of the dispersion, which need to be optimized to yield a sparse distribution of the particles on the parent substrate by spin coating. Chemical modification of the substrates may facilitate the sparse particle distribution, as it was shown for quarternization of the parent substrate (particle-substrate Coulomb attraction).

4.1.3. Parameters affecting the monolayer quality

The *DSDP*-method provides the possibility to tune the interactions between the individually isolated particles floating at the air-water interface, since they separately detach from the parent substrate at the three-phase contact line and are individually incorporated into the growing monolayer.

The formation of large area, high quality colloidal monolayers is the result of an intricate interplay of different mechanisms and colloidal forces, which act during the different steps of the monolayer preparation. Firstly, electrostatic attraction between oppositely charged colloidal particles and the parent substrate surface yield a homogenous coverage of the parent substrate with separated particles. Secondly, the liquid dispersion medium is removed by spin coating. The particles dry, rendering their surface more hydrophobic as compared to the dispersed colloids (this change was characterized by AFM measurements on dry and water immersed colloids, as shown below in Figure 4.1.3 and 4.1.4). Thirdly, long-range capillary attraction and short range electrostatic repulsion act simultaneously during particle self-assembly at the air-water interface, yielding highly ordered colloidal monolayers (pH dependent monolayer assembly gave insight into this dependency, Figure 4.1.5). The hydrophobicity of the colloidal particles allows them to float at the air-water interface, as it has been pointed out by Pieranski.[24] However, purely hydrophobic, uncharged particles would not crystallize in a hexagonally close packed geometry, but would directly aggregate in a disordered layer upon contact due to the attractive capillary force. The electrostatic repulsion provides the required mobility for order formation before particle aggregation takes place.

To investigate the surface chemical and physical properties of the dried PS particles, height and phase AFM images on various colloidal particles with modified cantilever tips were measured. The results are given in Figure 4.1.3 for 1.1 μm sulfate-stabilized polystyrene colloids.

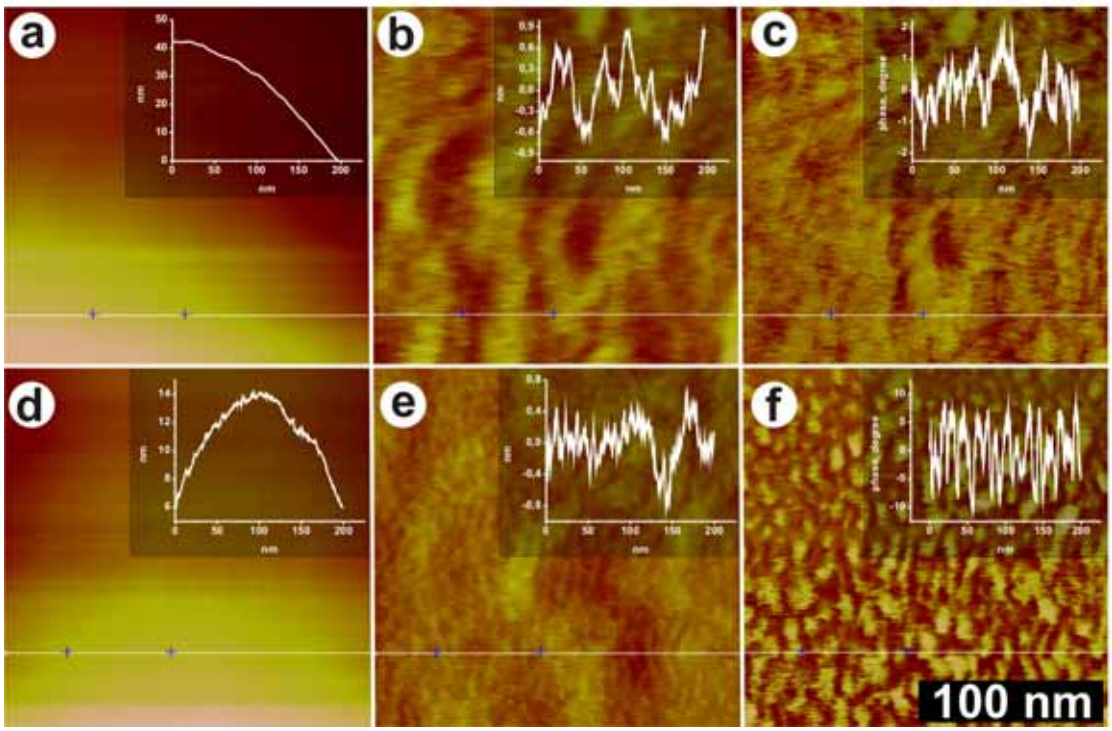

Figure 4.1.3. *top row: Tapping mode AFM measurements with an Ar/O_2 Plasma activated tip. Bottom row: Measurements conducted with an ODTS modified tip. a) and d) raw height image. b) and e) show the topography on the single particle after a second order flattening. c) and f) represent the corresponding phase images. Whereas no specific interaction can be seen in c), some distinct phase shifts are clearly discernible in f). The insets show cross sections along the white lines as indicated in the AFM pictures.*

The height images were 2nd order flattened to reveal the nanoscale topography on top of the spherical particle, potentially coinciding with patterns in the phase image. Differences in the phase images can be used for tracing heterogeneous interactions between the cantilever tip and the particle surface, and could possibly probe hydrophilic and hydrophobic patches.[27] When employing a negatively charged cantilever tip (by Ar/O_2 plasma treatment), only slight variations can be observed, which were partly correlated with the wavy topography on a ~100 nm scale. In the case of the hydrophobic, octadecyltriethoxysilane (ODTS) modified tip a strong phase contrast was visible, which correlated with small topographic substructures at the ~10 nm scale. This contrast may be attributed to differences in the viscoelastic properties and chemical composition of the particle surface, as a result of surface group segregation. Control measurements with the ODTS tip on a bulk polystyrene film without hydrophilic moieties did not reveal any surface structure. Measurements with a positively charged tip (by modification with a quaternary aminosilane) were difficult to realize and did not reveal any phase separation. The opposite charge attraction of the positive tip and the negative particle severely hindered the measurement of clear phase images.

The question of the reversibility of such surface segregations was investigated by water contact angle measurements on single colloidal particles. These measurements and data

evaluation were conducted by Sergio Rivera. The first measurement was conducted after the particles underwent a drying step required by the preparation (gluing) of the colloidal probes, which reflects the drying step on the parent substrate in the particle monolayer fabrication. Subsequently, the colloidal probes were immersed in MilliQ water, and contact angle measurements were conducted immediately and after 1, 2, 3, and 4 weeks of immersion. For each data point in the figure, more than 100 force curves were drawn for averaging. Although the measurements show a strong variation of the exact values for the water contact angles, a general trend can be clearly deduced as shown in Figure 4.1.4.

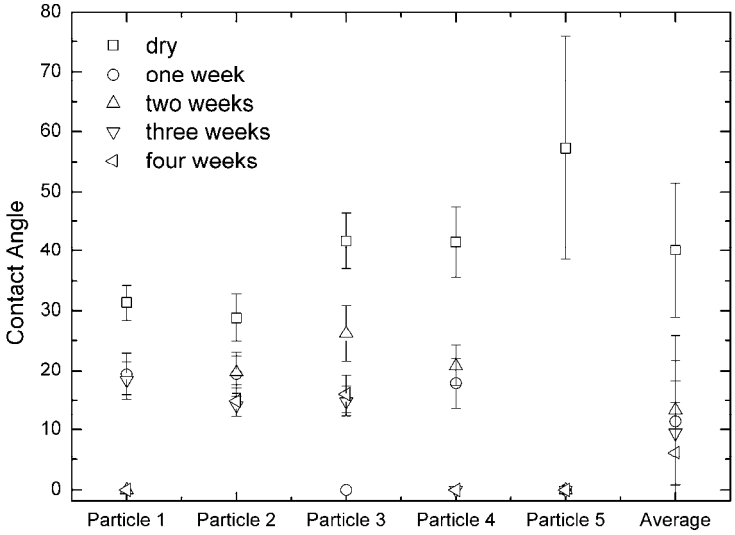

Figure 4.1.4. *Water contact angle measurement by AFM on 5 different colloidal particles of 1116 nm diameter. Measurements on dry particles (open square) and particles which were immersed in water for one (open circle), two (triangle tip up), three (triangle tip down) and four weeks (triangle tip left), are shown.*

After the initial drying step, the PS particles first showed a larger contact angle, with the average values ranging from 29º to 57º among the 5 samples. The subsequent prolonged immersion of the particles into water lead to a noticeable reduction of the contact angles (on average, a reduction of more than 10 degrees after the first week). After an immersion period of three to four weeks, the contact angles had significantly dropped to values below 15 degrees.

The contact angle measurements suggest that after the first drying step, a restructuring of the hydrophilic particle surface takes place, which leads to the noticeable increase in the water contact angle. This observation is corroborated by the fact that after drying the particles float on the water surface, which requires a certain degree of hydrophobicity. The large spread between the different colloidal probes, as well as the partially undefined time evolution of the surface polarity during water exposure may either suggest a very heterogeneous surface structure of the particles on a length scale sensitive to the

contact angle measurements, or a large variation in the surface restructuring process. Two fundamental scenarios may be envisioned during restructuring:

1.) Upon exchange of the particle environment (air or water) surface segregation of different moieties in the constituting polymer (polar moieties introduced by the initiator or co-monomer and the apolar polymer backbone) takes place to accommodate changes in the interfacial energy. While in aqueous environment the polar groups are located on the particle surface, in air these polar groups may rearrange and the less polar polymer backbone faces towards the air. This reconstitution does not happen homogeneously, but gives a patchy surface of varying hydrophobicity, as it could be deduced from AFM measurements on single colloids.

2.) Another possibility might be the absorption of mobile, surface active components onto the particle surface and modifying its polarity. This behavior is well known for freshly prepared gold surfaces, which are initially very hydrophilic, but soon turn hydrophobic within hours due to adsorbate layer formation from volatile impurities in the air. Due to the simplicity of the proposed benchtop process, such low level impurities, which are omnipresent and very difficult to control, can not be excluded. An experimental clue to such a scenario is provided by the use of surfactants, as described further below.

Either of these mechanisms or a combination of both may be responsible for the change of particle polarity upon change of the environment.

Overall, the experiments suggest that the colloids possess an ambivalent behavior. On the one hand they have hydrophobic properties, which keep the particles trapped at the air-water interface; on the other hand they still possess surface charges, which induce electrostatic repulsion. An experiment, which addresses directly the electrostatic interaction, is summarized in Figure 4.1.5. For two types of particles (one stabilized by sulfate groups (Figure 4.1.5 a - c), the other stabilized by carboxylic groups (Figure 4.1.5 e - d) the pH of the floating medium was varied.

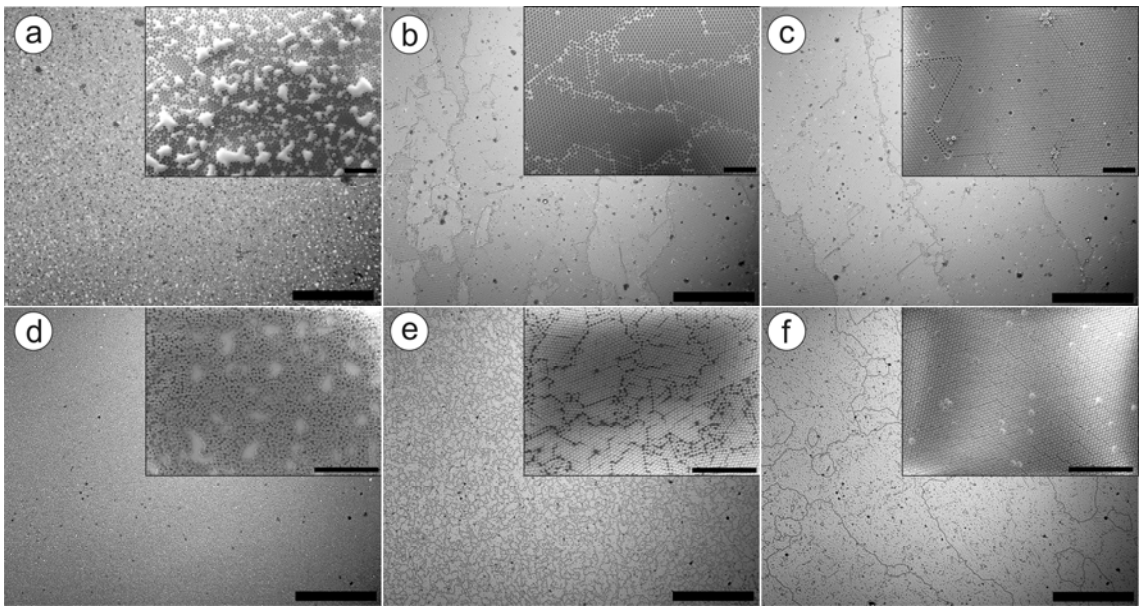

Figure 4.1.5. *Influence of the floatation medium pH on monolayer formation for sulfate functionalized (1116 nm, upper row) and carboxylic acid functionalized particles (538 nm, lower row). The pH was adjusted to 0 (a, d), 5.5 (b, e) and 10.5 (c, f). Scale bars are 100 µm in the optical microscope pictures and 10 µm in the SEM insets.*

The quality of the obtained monolayer unambiguously depends on the pH of the aqueous subphase. When the negative charges of the colloidal particles are screened at low pH, e.g. pH 0, the electrostatic short range repulsion is "switched" off and the resulting disordered colloidal monolayer resembles a spontaneous aggregation of single particles. Under these conditions the particles experience mainly attractive interactions by capillary forces, van der Waals attraction, and possibly in the contact region between two adjacent particles hydrogen bonding of the protonated acid groups. Upon increase of the pH the colloidal spheres are increasingly negatively charged. The short-range repulsive force introduced by this charge seems to provide the required mobility to assemble the particles with high order by long-range attractive capillary forces.[28]

In addition to the pH of the floatation medium, surfactants like SDS also exert a noticeable influence, especially on the handling of the floating monolayer. The surfactant molecules accumulate at the air-water interface and constitute a soft barrier in the monolayer formation process, which facilitates the packing of the single colloidal particles into a hexagonal crystal lattice. On the molecular scale the detaching colloids are pushing against the floating surfactant layer, which in turn pushes the particles together and thus facilitates the nucleation of the 2D crystal. Dunsmuir *et al.*[19] described this feature as 'piston oil' effect. Monolayers, which were floated in the presence of surfactants exhibit a higher mechanical stability and fracture less easily at the edges. As a result, the addition of SDS also improves the monolayer transfer.

Applying concentrations of SDS higher than the CMC resulted in redispersion of the dry colloids into the bulk liquid upon immersion of the parent substrate. Also, small monolayer rafts, which floated at the air-water interface, redispersed after a few hours. This suggests that the excessive SDS amphiphilic molecules adsorb onto the hydrophobic PS particles and render them hydrophilic.

4.1.4. Transfer of monolayers

With the *DSDP*-method it is possible to deposit the robust free-floating monolayers onto a wide variety of substrates, which may not be suited for other techniques due to their surface roughness and/or their wetting behavior with aqueous suspensions. In analogy to the reports in the literature[29] the floating monolayers have been transferred to a large variety of substrates like glass, untreated silicon, functionalized glass with amines or quaternary ammonium salts, hydrophobic (hexamethyldisilazane (HMDS) functionalized glass) and ultrahydrophobic (fluorinated glass) substrates, and metals such as gold. In some cases (like HMDS functionalized glass) the adjustment of the contact angle at the receiving substrate by the addition of minimal amounts of surfactant such as SDS to the floatation subphase facilitates the transfer. In case of gold a one minute treatment with UV ozon decreased the contact angle and subsequently improved the transfer.

In general two types of transfer to a receiving substrate are possible, as depicted in Figure 4.1.6. In the first case (upper row in Figure 4.1.6) the floating monolayer is transferred on top of the hydrophilic surface of a withdrawn receiving substrate. In the second case (lower row in Figure 4.1.6) the monolayer is deposited onto the underside of the hydrophobic substrate upon immersion.

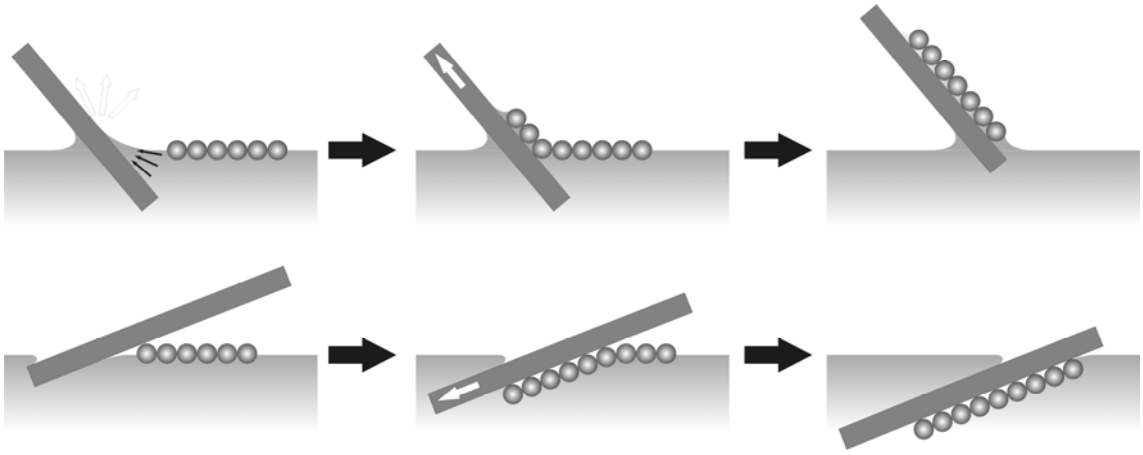

Figure 4.1.6. *Transfer of a floating monolayer onto a hydrophilic (top row) and hydrophobic (bottom row) substrate.*

In both cases sufficient adhesion of the monolayer to the receiving substrate is crucial for a successful transfer. In the first case the floating monolayer attaches to the hydrophilic substrate by capillary forces when the substrate has a low contact angle with water (Figure 4.1.6 top). Evaporation takes place at the meniscus, which results in a net flux of solvent to the contact line. This flux transports the floating monolayer towards the contact line where it attaches by the immersion capillary forces.[28, 30] After the initial attachment the monolayer can be fully transferred by slow withdrawal of the substrate. This route works for a wide range of substrates as long as the receding contact angle is sufficiently low.

The second case is relevant for hydrophobic substrates with high water contact angles (Figure 4.1.6 bottom). The attachment of the monolayer occurs then via effective attraction between the hydrophobic underside of the substrate and the floating particle monolayer. As one edge of the monolayer is brought into contact with the hydrophobic surface the monolayer adheres and can be fully transferred by slowly pushing the substrate into the water. The transfer also works by simply putting the receiving substrate on top of the floating layer. The adhesion of the monolayer to the substrate is so strong that it does not detach when taken out of the water. This strong adhesion is due to the hydrophobic attraction by van der Waals forces between the hydrophobic substrate and the PS or PMMA particles. It further corroborates the hydrophobic attribute of the floating colloids.

After thermally annealing the first colloidal monolayer, further layers with particles of different diameters can be consecutively stacked by the same method. This method provides a convenient route for the preparation of colloidal materials with structural hierarchies and heterogeneity via colloidal monolayer-by-monolayer deposition. These hetero-multilayer architectures may provide novel functional materials, for example porous structure with a defined porosity gradient, which is desirable in controlled adsorption and desorption. Up to now, functional hetero-multilayer colloidal crystals have mostly been prepared by stacking a multilayer 3D crystal on top of another multilayer 3D crystal with emphasis on tuning their optical properties.[31-36] However, no hetero multilayer crystals constituting of single, highly ordered 2D colloidal films have been shown so far. In Figure 4.1.7 two examples of such colloidal hetero-multilayer stacks are presented.

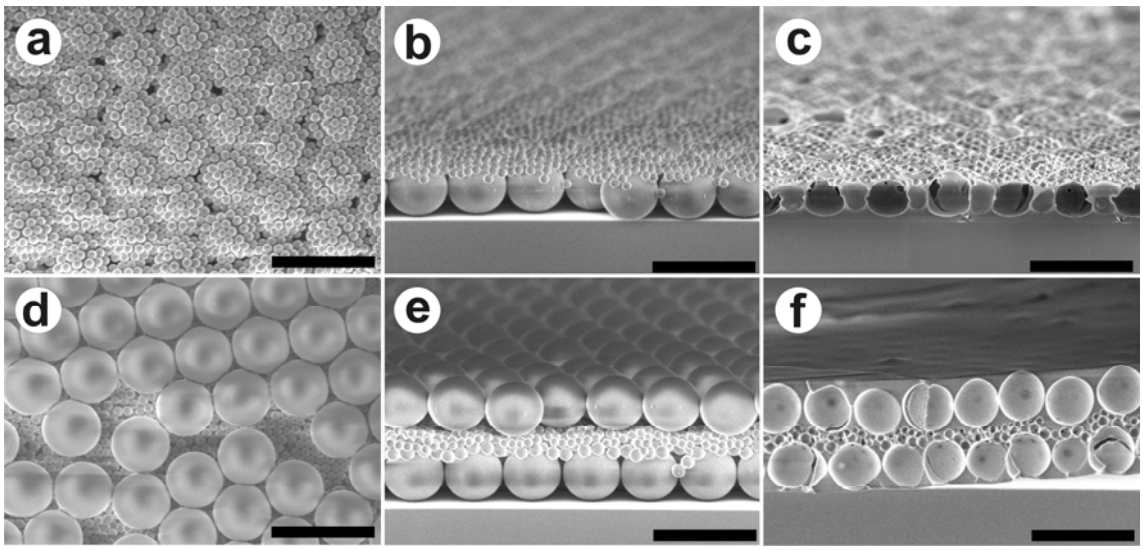

Figure 4.1.7. *Stacking of different particle monolayers to yield hierarchically structured hetero-multilayers. Top view (a) and side view (b) SEM images of a 182 nm particle monolayer on top of a 1116 nm particle monolayer. Top view (d) and side view (e) SEM images of a stack of 1116, 262, 182 and 1116 nm particle monolayers. (c) and (f) shows the corresponding inverse hetero-multilayer replicas made of silica by a sol gel infiltration process. Scale bars are 2 µm.*

The SEM of Figure 4.1.7 a) (top view) and b) (side view) show a stack of a 182 nm particle monolayer on top of an 1116 nm particle monolayer. The underlying 1116 nm monolayer was annealed at elevated temperatures on the receiving hydrophilic substrate to prevent it from floating off the substrate during transfer of the second layer. The order in this bottom layer was unchanged by the stacking procedure. As clearly visible in the top and side view (Fig. 4.1.7 a and b), the small particle monolayer is undulated vertically and replicates the topography of the underlying large particle monolayer without apparent rupture. The small particles residing at the centre of the underlying large colloids are pushed upwards, while the remaining small particle layer adapts to the curvature of the large colloids and spans over the triangular void among three adjacent large spheres. The cohesive forces between neighbouring particles in a close-packed monolayer are apparently strong enough to prevent layer rupturing or substantial displacement of individual particles.

In the SEM of Figure 4.1.7 d) (top view) and e) (side view) a hetero-multilayer stack of a sequence of 1116-262-182-1116 nm particles was prepared by monolayer-by-monolayer transfer. The top view has been selected for a region with some defects in order to see the underlying small particle layer. The small particle film is homogeneously packed and from inspection of the large particle crystalline regions it is evident that the large particles are not affected by the fine undulation in the underlying layers. Even the third layer, constituting of 182 nm particles, exhibits well ordered regions on

top of the 262 nm particle layer. Thus the topographic influence of a rough surface is healed out efficiently by only a few particle layers.

The hetero-multilayer crystals could be replicated as inverse network structures by the application of a silica sol gel process. Figure 4.1.7 c) and f) show the corresponding inverted structures of the double and four-layer stack, respectively, consisting of silica after removal of the templating PS particles. These interconnected network structures of the inverted hierarchical multilayer replicas might find potential applications for sieving or catalytic applications, which require a high surface area, a good transport of analytes, and a well defined and uniform pore size. The hierarchical order of the macropores would be beneficial for an efficient analyte transport from the outside with large pores to the center region with simultaneous size selection.

As the robust particle monolayers can adapt well to topographic features of the underlying substrate, the deposition of a 182 nm particle monolayer on curved samples was investigated in more detail. For this purpose the monolayer was coated on top of very large receiving spheres of 1.1 µm, 10.3 µm and 16.4 µm diameter. The top view SEM images are provided in Figure 4.1.8. A high degree of order among the transferred small colloids is preserved even on the smallest receiving sphere of 1.1 µm diameter with the highest bending curvature. With increasing size of the underlying receiving spheres fewer cracks are introduced into the deposited monolayer and complete domains of hexagonally close-packed arrays are transferred. On the 10.3 µm sphere some uncovered regions close to the sphere's equator remain, whereas full coverage of the upper hemisphere is achieved on the 16.4 µm receiving sphere.

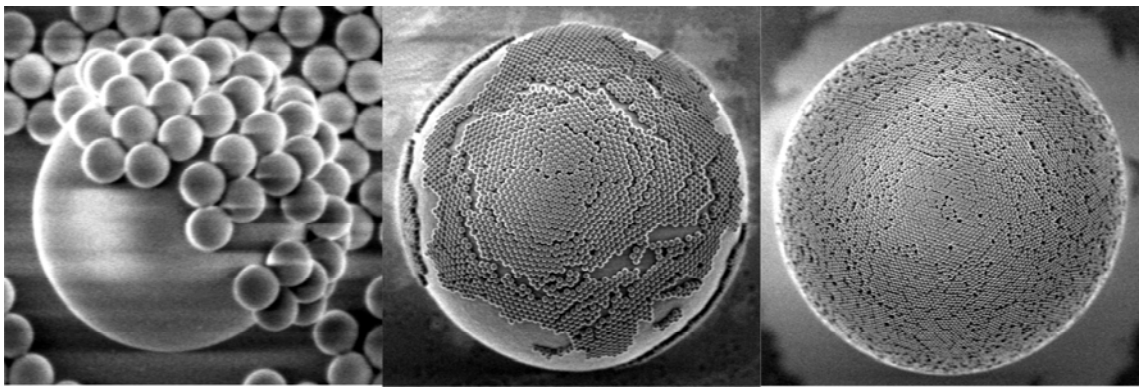

Figure 4.1.8. *Coating of a 182 nm particle monolayer on receiving spheres of 1.1 µm, 10.3 µm and 16.4 µm diameter. The particles within a monolayer show strong cohesion with each other, as indicated by the preservation of the hexagonal order in all cases. The bending radius of the 16.4 µm receiving sphere is already large enough to allow a complete covering of the upper hemisphere by the 182 nm monolayer.*

A special challenge is the transfer of colloidal monolayers onto a single side of a multi array micromechanical cantilever. This research was conducted in collaboration with Ting Liu.

Micromechanical cantilever arrays have attracted increasing interest throughout the last decade, since they can be widely used as extremely sensitive sensors for chemical and biological applications.[37-39] One of their major advantage is the tiny probe volume, which is confined on the cantilever of typically only several hundred μm^2. At the same time this small probe surface challenges the essay fabrication, since standard techniques for surface modification like spin coating can not be used any more. Deposition of well defined colloidal monolayers on one side of the cantilever could overcome this difficult and path the way to study colloidal particle interactions or thin polymer films after annealing of the colloidal monolayer on such a micromechanical device.

A typical multi array micromechanical cantilever as used in this work is shown in Figure 4.1.9.

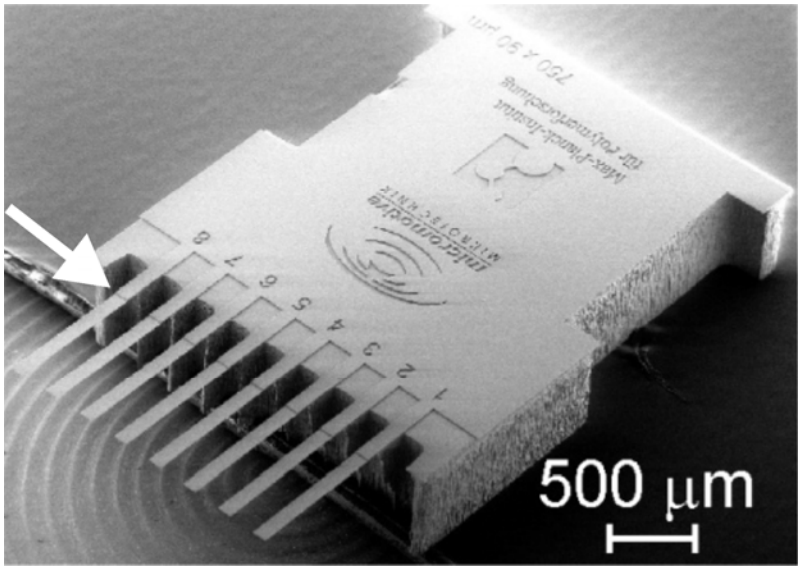

Figure 4.1.9. *SEM image of a multi array micromechanical cantilever with eight arms of a size of 750x50 µm. The white arrow points to a step, which is located at the junction of the cantilever to its support.*

The major challenge was to avoid monolayer deposition on the underside of the cantilevers, which inevitably and irreproducibly happens, if the monolayer was transferred on a hydrophilic array according to Figure 4.1.6 top row. In this case the monolayer film spans the free space between the single arms. During withdrawal from the water interface rafts of the "free-hanging" monolayer rupture and are put on the underside of the cantilever due to the meniscus, which formed between the tip and the water surface. Thus the hydrophobic pick up methodology had to be used and is sketched in Figure 4.1.10.

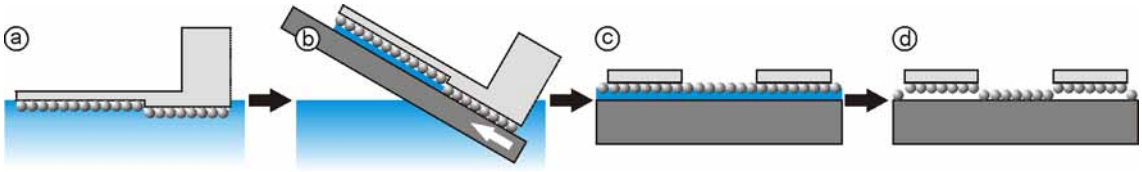

Figure 4.1.10. *Method to deposit colloidal monolayers on a single side of a multiarray cantilever. a) and b) are side view, c) and d) show front view. a) The hydrophobic cantilever is put on top of a floating monolayer. b) Monolayer and cantilever are transferred on a hydrophilic substrate. c) The monolayer is dried on the receiving substrate. d) The free-hanging monolayer is deposited on the hydrophilic substrate, whereas the hydrophobic cantilevers remain coated with a single monolayer only on one side.*

The cantilevers were turned hydrophobic by chemical vapour deposition (CVD) of a perfluorsilane. After putting the strongly hydrophobic cantilever on top of a floating monolayer (a) both, cantilever and monolayer, are transferred onto a hydrophilic substrate such as glass or metal (b). The monolayer is allowed to dry on the receiving substrate (c). The clue of this method is the fact that the "free hanging" monolayer between the tips can not fold back on the deposited first layer, since it only dries onto the receiving substrate (d). The hydrophobic adhesion between the tip and the colloidal monolayer is strong enough to remain unchanged during the drying step. Furthermore, due to a little step in the cantilever tip, the top side is not in physical contact with the receiving substrate. The backside of the cantilever remains free of any particles, as it always faces to the air.

The feasibility of this concept is shown in Figure 4.1.11.

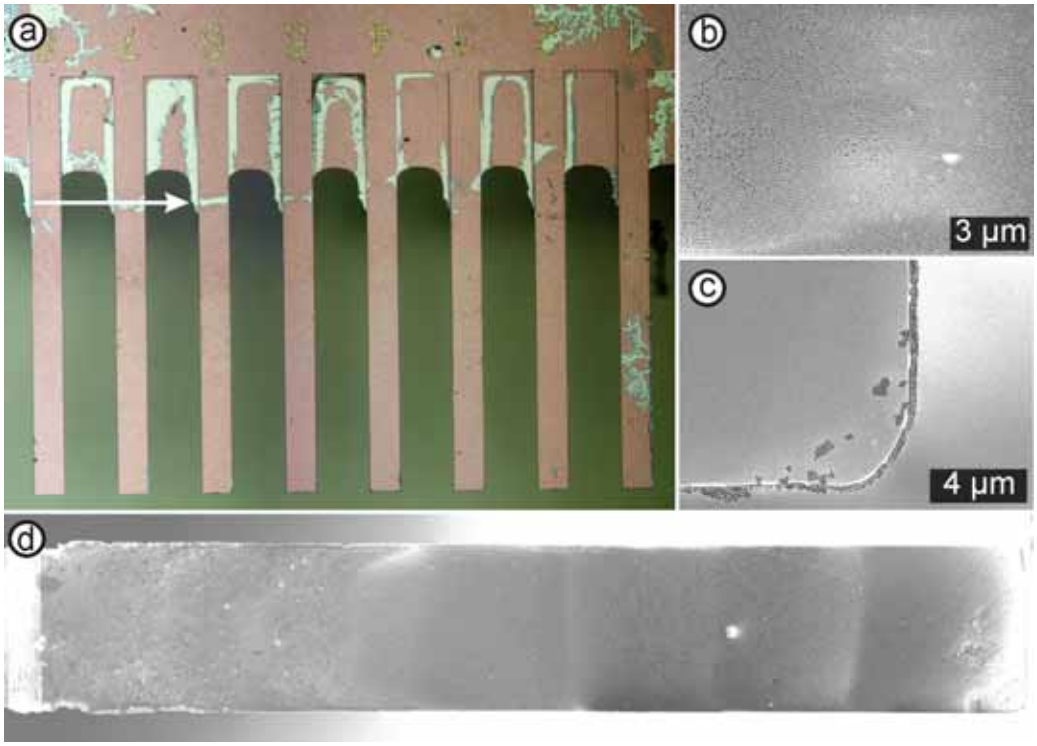

Figure 4.1.11. *a) Optical microscope image of the entire cantilever array. Red parts are covered by a colloidal monolayer, green parts are not covered. The cantilevers have a width of ~ 80 µm. b) Higher magnification SEM image of the monolayer on d). c) The backside of the cantilever remains free of colloids, some particles also adhere to the side of the tip. d) SEM image of an entire single cantilever tip.*

The characterization of the successful monolayer deposition can be conducted by optical microscopy, as shown in Figure 4.1.11 a). The homogenous color on all cantilevers indicates the deposition of a highly ordered monolayer, double or multiple layers as well as free parts would appear differently. This finding is backed by the SEM measurement (d), which confirmed the formation of a highly ordered monolayer (b). Close inspection of Figure 4.1.11 d) reveals a higher density of cracks, voids, and dislocations in the upper third of the cantilever, which is caused by the step at the junction with the cantilever support (indicated by an arrow in Figure 4.1.11 a). This leads to the formation of a meniscus and hinders the particle deposition. No particles could be detected on the backside of the tip, but some particles were deposited on the thin edge of the cantilever (c).

4.1.5. Conclusion and outlook

The *DSDP*-method produces high quality colloidal monolayers without the necessity of elaborate equipment. The single colloidal particles or small clusters float off the parent substrate only at the air-water-substrate contact line and insert with high mobility into the floating monolayer crystal, preserving the existing lattice orientation with low defect density. In this sense it is a one-dimensional quasi-epitaxial growth mechanism taking place at the edge of the already formed, crystalline monolayer.

From the experiments discussed here various factors have been identified that contribute to the formation of the highly ordered particle monolayers at the air-water interface:

- Surface polarity: A change of the particle surface polarity takes place during drying from hydrophilic (wet) to hydrophobic (dry). The change is happening inhomogenously, resulting in patches of various hydrophilicity, and reversibly, as indicated by the change of the water contact angle of single colloids.
- Particle separation: Floating of single particles provides maximal particle mobility for optimal ordering during the parent substrate immersion. Silanization of the parent substrate in order to introduce oppositely charged particle-substrate attraction facilitates sparse particle distribution.
- pH of the subphase: For negatively charged particles the ordering of the monolayer increases with increasing pH due to mutual particle repulsion. An interplay of long range attractive capillary and short range repulsive electrostatic forces is prerequisite for the self-assembly in hexagonally ordered monolayers.
- Amphiphilic mobile species: Surfactants at the air-water interface favor dense monolayer packing by acting as a compressing barrier (referred to as "piston oil effect")

and by modifying the particle surface polarity. Furthermore the transfer of the floating monolayer is facilitated.

In comparison with existing technologies, like the Langmuir-Blodgett techniques, several major advantages can be pointed out:

1) Ordering occurs only at the three-phase contact line (air-water-substrate, one dimensional), which substantially reduces the number of nucleation centers (compared to the compression of a floating layer by barriers, two dimensional), thus reducing the polycrystallinity and favoring large monodomains.

2) The anisotropic shrinkage of the sparse distributed particle film during the floating step can be exploited to directly pattern colloidal monolayer films by dispersing the particles in a patterned way on the parent substrate. Patterning of the individual particle film can, for instance, be achieved by printing. This possibility will be discussed in detail in the following chapter.

3) The initial particle films can be formed on the parent substrates by simple spin coating and the floating crystalline monolayers are easily prepared by parent substrate immersion into a water bath without tedious control of environmental parameters, like temperature and humidity. Thus the *DSDP*-method is a very simple method, which can be conducted just on the benchtop without complicated or expensive equipment.

Further optimization of this simple monolayer fabrication process may be achieved by automatic control of parent- and receiving substrate immersion and withdrawal (to allow for precise immersion and transfer speed) and detailed investigation of the influence of surfactant type and concentration. The method has been used for PS and PMMA particles of sizes ranging from 90 nm to 1.2 µm, but it should also be applicable to particle sizes below 90 nm and above 1200 nm, as long as the particles float at the air-water interface upon parent substrate immersion. The floating monolayer can be transferred to a wide range of substrates. The deposition on hydrophobic surface is of special importance for single sided coating of multiarray cantilevers.

The method introduced here represents a platform for the fabrication of a variety of new materials, exploiting the distinctive advantages, such as the mechanical stability of the macroscopic films, the large area of monocrystalline patches, and the possibility to transfer the monolayer onto hydrophilic or hydrophobic, and flat or rough substrates.

In the following chapters various applications and modifications of colloidal monolayers prepared by the *DSDP*-method will de discussed.

4.1.6. Experimental part

Materials. PS particles with diameters of: 182 nm ± 4 nm (0.8 wt%) and 261 nm ± 3.4 nm (2.7 wt%), functionalized by styrene sulfonic acid as co-monomer, and 1116 nm ± 12 nm (7.0, 3.5 and 4.4 wt%) (synthesized by Zuocheng Zhou) polystyrene particles, stabilized by sulfate terminal moieties, were used. Another type of particle was functionalized by acrylic acid as co-monomer during the polymerization and had a diameter of 538 nm ± 21 nm (2.0 wt%). Large colloids of 10 µm and 16 µm in diameter were received from Bayer and used without further purification.
Some glass substrates were functionalized by liquid phase silanization of *N*-trimethoxysilylpropyl-*N*,*N*,*N*-trimethylammonium chloride (NR_4^+, 50 % in methanol) (ABCR/Gelest, Karlsruhe, Germany).[40] Strongly hydrophobic substrates and multiarray cantilevers were prepared by chemical vapor deposition of 1H,1H,2H,2H-Perfluorodecyltrichlorosilane (97 %, ABCR, Karlsruhe). For the floating experiments MilliQ water, $5x10^{-4}$ M or $5x10^{-3}$ M sodium dodecylsulfate (SDS) solutions, and MilliQ water adjusted to pH 0 or 5.5 by addition of concentrated HCl (37 %, VWR Normapur) or adjusted to pH 10.5 with ammonia solution (25 %, WTL Laborbedarf, Kastellau) were used.
Fabrication of Colloidal Monolayers. The generic approach to produce PS colloidal monolayers, as outlined in Figure 4.1.1, starts with the deposition of a colloidal dispersion drop on the parent substrate. In order to facilitate the sparse distribution by a stronger, electrostatic particle-substrate interaction, NR_4^+ functionalized glass slides with a permanent positive charge and dimensions of 2.5 cm x 2.5 cm were employed. 40 µl dispersion was spread over the glass slide and spin coated at 4000 rpm for 20 sec. When using particles of 1116 nm a sparse distribution was already achieved on plasma cleaned glass slides.
Functionalization of Cantilevers. AFM cantilevers from Olympus (OMCLAC 160 TS-W2) were activated in an oxygen/argon plasma (1:9) at a power of 100 W for 10 sec. The tips were modified by immersion into a 1 vol% solution of NR_4^+ in H_2O and 1 vol% of n-octadecyltriethoxysilane (ODTS, 94 %, ABCR) in EtOH for 30 min, respectively. Both solutions were pre-hydrolysed for 30 min. The cantilevers were blown dry with N_2 after rinsing with EtOH.
Multilayer Stacking and Inverse Structure Formation. For the stacking of several monolayers it was necessary to anneal the first layer of 1116 nm particles, which was deposited on a silicon wafer, over night at 60 °C. Consecutively, monolayers consisting of various particle sizes were picked up by the pre-coated substrate. After drying of the top layer no further annealing was necessary. The substrate could be used immediately to add the next layer.
Analogously, sparsely distributed colloids of 1.1 µm, 10 µm and 16 µm were annealed on glass substrates in an oven overnight at 80 °C before coating with a top monolayer of 182 nm particles.
In order to prepare an inverse replica of the stacked colloid layers, the colloidal film was dipped twice into a prehydrolized sol gel solution of tetraethyl orthosilicate (5.5 ml), EtOH (8 ml), 0.1 M HCl (8.1 ml) and water (16.3 ml) and blown dry with nitrogen. The templating PS latex was removed by solvent extraction with tetrahydrofuran (THF) in the case of the double layer film, while the four layer stack was calcinated at 450 °C over night in air (heating rate ~10 K/min).

4.1.7. Bibliography

1. Krauss, P. R.; Chou, S. Y. *Appl. Phys. Lett.* **1997,** 71, (21), 3174-3176.
2. Born, A.; Wiesendanger, R. *Appl Phys A-Mater* **1999,** 68, (2), 131-135.
3. Poborchii, V. V.; Tada, T.; Kanayama, T. *Appl. Phys. Lett.* **1999,** 75, (21), 3276-3278.
4. Haes, A. J.; Van Duyne, R. P. *J. Am. Chem. Soc.* **2002,** 124, (35), 10596-10604.
5. Deckman, H. W.; Dunsmuir, J. H. *Appl. Phys. Lett.* **1982,** 41, (4), 377-379.
6. Hulteen, J. C.; Vanduyne, R. P. *J Vac Sci Technol A* **1995,** 13, (3), 1553-1558.
7. Kosiorek, A.; Kandulski, W.; Glaczynska, H.; Giersig, M. *Small* **2005,** 1, (4), 439-444.
8. Haynes, C. L.; Van Duyne, R. P. *J. Phys. Chem. B* **2001,** 105, (24), 5599-5611.
9. Boneberg, J.; Burmeister, F.; Schafle, C.; Leiderer, P.; Reim, D.; Fery, A.; Her minghaus, S. *Langmuir* **1997,** 13, (26), 7080-7084.
10. Li, Y.; Cai, W.; Duan, G. *Chem. Mater.* **2008,** 20, (3), 615-624.
11. Yang, S. M.; Jang, S. G.; Choi, D. G.; Kim, S.; Yu, H. K. *Small* **2006,** 2, (4), 458-475.
12. Wu, M. H.; Whitesides, G. M. *Appl. Phys. Lett.* **2001,** 78, (16), 2273-2275.
13. Dimitrov, A. S.; Nagayama, K. *Langmuir* **1996,** 12, 1303-1311.
14. Denkov, N. D.; Velev, D.; Kralchevsky, P. A.; Ivanov, I. B.; Yoshimura, H.; Nagayama, K. *Nature* **1993,** 361, 26.
15. Teh, L. K.; Tan, N. K.; Wong, C. C.; Li, S. *Appl Phys A-Mater* **2005,** 81, (7), 1399-1404.
16. Micheletto, R.; Fukuda, H.; Ohtsu, M. *Langmuir* **1995,** 11, (9), 3333-3336.
17. Winzer, M.; Kleiber, M.; Dix, N.; Wiesendanger, R. *Appl Phys A-Mater* **1996,** 63, (6), 617-619.
18. Picard, G. *Langmuir* **1998,** 14, (13), 3710-3715.
19. Dunsmuir, J. H.; Deckman, H. W.; McHenry, J. A. Production of close packed colloidal particle coatings. EP 0 270 212 A1, 1987.
20. Lenzmann, F.; Li, K.; Kitai, A. H.; Stöver, H. D. H. *Chem. Mater.* **1994,** 6, (2), 156-159.
21. Wang, W.; Gu, B. H. *J. Phys. Chem. B* **2005,** 109, (47), 22175-22180.
22. Zhang, Y. J.; Li, W.; Chen, K. J. *J. Alloys Compd.* **2008,** 450, (1-2), 512-516.
23. Fulda, K. U.; Tieke, B. *Adv. Mater.* **1994,** 6, (4), 288-290.
24. Pieranski, P. *Phys. Rev. Lett.* **1980,** 45, (7), 569-572.
25. Reculusa, S.; Ravaine, S. *Chem. Mater.* **2003,** 15, 598-605.
26. Chen, W.; Tan, S. S.; Huang, Z. S.; Ng, T. K.; Ford, W. T.; Tong, P. *Phys. Rev. E* **2006,** 74, 021406.
27. Magonov, S. N.; Reneker, D. H. *Annu. Rev. Mater. Sci.* **1997,** 27, 175-222.
28. Li, Q.; Jonas, U.; Zhao, X. S.; Kapp, M. *Asia Pac. J. Chem. Eng.* **2008,** 3, (3), 255-268.
29. Burmeister, F.; Schafle, C.; Matthes, T.; Bohmisch, M.; Boneberg, J.; Leiderer, P. *Langmuir* **1997,** 13, (11), 2983-2987.
30. Kralchevsky, P. A.; Nagayama, K. *Langmuir* **1994,** 10, (1), 23-36.
31. Ye, J. High Quality Colloidal Crystal with Different Architecture and their Opti cal Properties. Johannes Gutenberg Universität Mainz, Mainz, 2006.
32. Romanov, S. G.; Torres, C. M. S.; Ye, J.; Zentel, R. *Prog. Solid State Chem.* **2005,** 33, (2-4), 279-286.
33. Fleischhaker, F.; Arsenault, A. C.; Kitaev, V.; Peiris, F. C.; von Freymann, G.; Manners, I.; Zentel, R.; Ozin, G. A. *J. Am. Chem. Soc.* **2005,** 127, (26), 9318-9319.

34. Jiang, P.; Ostojic, G. N.; Narat, R.; Mittleman, D. M.; Colvin, V. L. *Adv. Mater.* **2001,** 13, (6), 389-393.
35. Rengarajan, R.; Jiang, P.; Larrabee, D. C.; Colvin, V. L.; Mittleman, D. M. *Phys. Rev. B* **2001,** 6420, 205103.
36. Wong, S.; Kitaev, V.; Ozin, G. A. *J. Am. Chem. Soc.* **2003,** 125, (50), 15589-15598.
37. Lang, H. P.; Baller, M. K.; Berger, R.; Gerber, C.; Gimzewski, J. K.; Battiston, F. M.; Fornaro, P.; Ramseyer, J. P.; Meyer, E.; Guntherodt, H. J. *Anal. Chim. Acta* **1998,** 393, 59-65.
38. Bumbu, G. G.; Wolkenhauer, M.; Kircher, G.; Gutmann, J. S.; Berger, D. *Lang muir* **2007,** 23, (4), 2203-2207.
39. Lang, H. P.; Berger, R.; Battiston, F.; Ramseyer, J. P.; Meyer, E.; Andreoli, C.; Brugger, J.; Vettiger, P.; Despont, M.; Mezzacasa, T.; Scandella, L.; Guntherodt, H. J.; Gerber, C.; Gimzewski, J. K. *Appl. Phys. A* **1997,** 66, S61-S64.
40. Jonas, U.; del Campo, A.; Krüger, C.; Glasser, G.; Boos, D. *P Natl Acad Sci USA* **2002,** 99, (8), 5034-5039.

4.2. Template Free Structuring of Colloidal Monolayers using Inkjet Printing

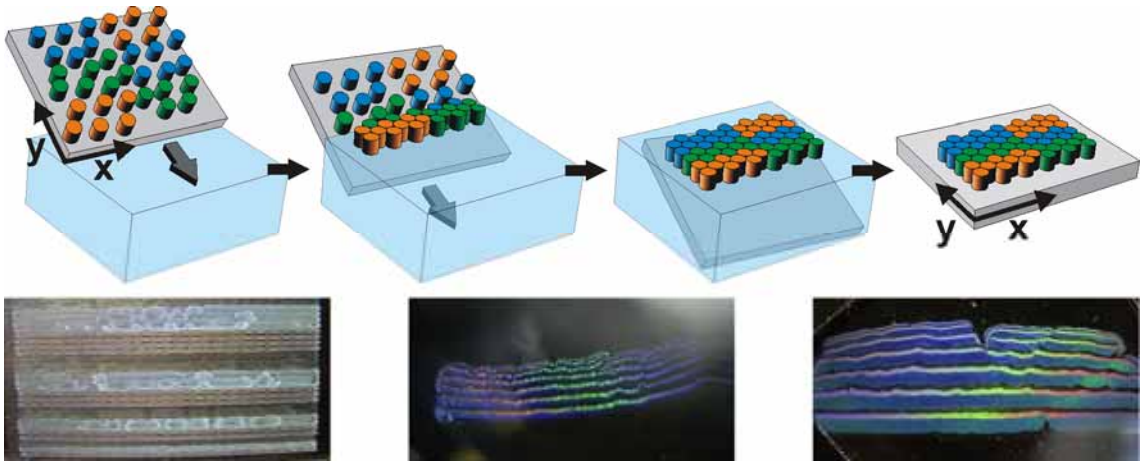

Colloidal monolayers are versatile masks, which are widely used in nanosphere lithography. Structuring monolayers on a µm-scale with different particle sizes of various materials has so far only been possible by the combination of various techniques and multiple steps. Here, a novel approach is introduced, which yields patterned colloidal monolayers with varying particle sizes and materials in a single process. The essential step is the anisotropic shrinkage of a dry sub-monolayer and self-assembly of latex particles upon floating at the air-water interface. The pattern of the sub-monolayer is defined by inkjet printing and is preserved during the self-assembly step. Various sizes and types of particles can be employed in this procedure, giving a versatile toolbox to specifically pattern surfaces.

4.2.1. Introduction

Patterning is of great importance in many areas of current research and technology. Applications are spanning from integrated circuits, information storage devices, and display units to miniaturized sensors, microfluidic devices, photonic crystals, and micro-optical components.[1] Throughout the last 20 years a huge toolbox of various patterning techniques has been established to generate 2D patterns on any desired substrate. They can be mainly divided into two categories, these being serial or parallel processes. In the first case the pattern is generated feature by feature, giving a good control over geometry and position, but paying off by being a slow sequential process, which is often only used on a small area. Examples for this are 2-photon polymerization,[2] e-beam,[3, 4] or dip-pen lithography.[5, 6] The parallel approach uses a mask, which transfers its predefined pattern onto a substrate or another intermediate matrix (like a photo resist), thus generating the desired pattern in a single step. Photo-lithography,[7] widely used in the chip industry, or nanosphere lithography[8, 9] are examples of such parallel methods. Photo-lithography can create any desired geometry with any pattern; however, it is limited in its minimum feature size due to the diffraction of light. Nanosphere lithography on the opposite, can easily fabricate structures in the sub-100 nm regime, but mostly in a repetitive pattern usually with hexagonal arrangement. One is also limited to objects like triangles, rings, stripes,[10] even though more complex architectures have been shown.[11, 12] For many applications homogenous structuring of a complete substrate does not give the desired function, which is why patterning on several length scales, for example in a hierarchical way, is of key importance. Hierarchical structures have been investigated for 3D materials,[13] but they are also of great importance for two-dimensional patterns.[14] In principal three general approaches can be undertaken to structure colloidal monolayers on several length scales. The first starts with a homogeneously coated substrate and stamps the pattern by usage of a mask in the second step. The second method employs a mask to directly arrange the particles in the desired pattern, whereas the third strategy uses a mask to modify the substrate such that the particles specifically accumulate or avoid certain regions.

A direct combination of colloidal monolayer and μ-pattern fabrication was shown by Moon et al.[15, 16] In a two step process they first deposited a colloidal monolayer of photocrosslinkable particles. These were successively crosslinked by UV-irradiation through a standard lithographic mask, which rendered certain patches stable towards thermal annealing. Silica was finally only deposited through the patches with open voids. Similarly Jiang *et al.* pre-assembled a non-close packed monolayer on a silicon

wafer, and successively patterned it with standard photolithography techniques.[17] It has also been demonstrated that a second layer of colloidal particles can serve as mask. During a reactive ion etching process the larger particles protect the underlying layer of smaller colloids, resulting in hexagonally arranged patches.[14] Instead of putting a monolayer of larger colloids on top of a pre-assembled film, one can also infiltrate a colloidal template with smaller particles. The particles can only assemble in the interstices of the larger particles, which replicates their hexagonal order.[18] A single step method was employed by Harris *et al.*, who used a mask to control the evaporation of the dispersion liquid locally.[19] Depending on the particle concentration discrete particle spots were obtained. Inversely, it has been shown that confined dewetting under a patterned mask can also generate μ-structures. In this case no particles are deposited under the open pores, but accumulate in the meniscus spanning from mask to substrate.[20] Another combined photolithographic technique was used by Hayward *et al*. They created colloidal monolayers by electrophoretic deposition, with the pattern formation being achieved by covalent particle bonding via illuminating the ITO electrode through a mask.[21] The ITO electrode can also be covered by a photoresist, opening the way to combine standard photolithography with electrophoretic particle deposition.[22]

The other approach is to tailor the particle-substrate interaction in a way that selective film formation occurs. Forces, which are employed to arrange the particles in the desired way are either capillary,[23] or electrostatic forces,[24, 25] or an interplay of both. A lithography free approach to structure by capillary forces was introduced by Lu *et al.*, who deposited particles in the grooves of wrinkled substrates.[26]

Another lithography-free way of patterning particle assemblies is to use inkjet printing or plotting of colloidal suspensions.[27, 28] Depending on the surface functionality and the particle concentration hemi-spherical colloidal crystals were deposited on the desired substrate.[29-31] A problem severely obstructing the formation of homogenous spots is the so called coffee-stain effect.[32] This effect is most pronounced on surfaces, which have a low water contact angle. Solvent evaporation and pinning of the meniscus cause a net flux of solvent to the meniscus line, which results in the accumulation of colloidal particles. In order to obtain well ordered colloidal monolayers one has to overcome this phenomenon. Precise adjustment of the dispersion solvent and particle concentration is necessary, as it has been pointed out by Park and Moon, who used a mixture of high and low boiling point solvents.[33]

In the method presented here several problems of the afore mentioned strategies are overcome. Key point is the self-assembly of various particles in different regions of a

well defined pattern. It is a template and lithography-free method, with the pattern being generated by inkjet printing. Only a few parameters need to be adjusted to obtain high quality colloidal monolayers, since the particle self-assembly is separated from the pattern printing. The usefulness of this approach to generate nano- and microstructured materials in a parallel process will be shown.

4.2.2. Single step patterning with multiple particles

The principal idea of the concept introduced here is the possibility to print any desired structure on a parent substrate, which can be transferred first onto an air-water interface and finally onto a target substrate. Following the *DSDP*-method introduced in chapter 4.1 the printing of the particle dispersion should give patterns, which consist of sparsely distributed particles. The concept of this novel method is shown in Figure 4.2.1 (colloids are presented as colored cylinders).

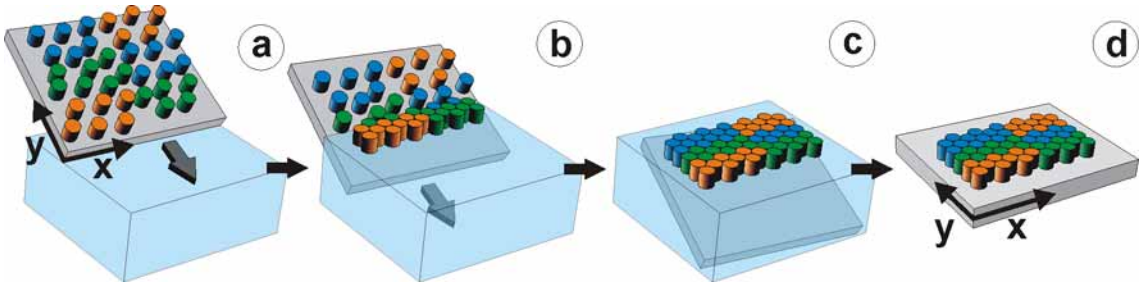

Figure 4.2.1. *Concept of printing structured colloidal monolayers consisting of various particles in a single step. a) A pattern of sparsely distributed particles is printed on the parent substrate. b) The particles are floated off the parent substrate at the air-water interface. c) The printed structure shrinks anisotropically along the immersion-direction (y), giving a compressed replica. d) The floating colloidal monolayer is transferred to a target substrate.*

Sparsely distributed particle patterns are printed on a parent substrate (Figure 4.2.1 a). Similarly to the formation of single particle monolayers (Chapter 4.1), only a few parameters like particle concentration and surface functionality need to be adjusted. In analogy to the *DSDP*-method, the goal is to avoid clusters of particles during drying of the dispensed particle dispersion, as this would deteriorate the quality of the final monolayer. Additionally, one has to minimize the particle flux towards the solid-liquid-air contact line of the dispensed drop, a phenomena known as the "coffee-stain" effect.[32] This effect would lead to ridges of multilayers. The key step is sketched in Figure 4.2.1 b), where the sparse pattern is floated onto an air/water interface. Shrinkage occurs only perpendicular to the three-phase-contact line (along the y-axis), whereas the width is preserved. Thus the printed pattern is compressed by a factor, which is given by the particle surface coverage on the parent substrate. In order to obtain the desired pattern, this compression has already to be taken into account during the printing step. This,

however, can be an advantage of the proposed method, as structure features, which are smaller than the sparse particle pattern (below the y-resolution of the printing process), can be accessed. The structured monolayer (Figure 4.2.1 c) can finally be transferred to a target substrate, where it may be used for novel device applications (Figure 4.2.1 d).
In principal any desired pattern could be printed by this method in a single step with a manifold of specifically application-tuned designed particles. Furthermore, one can expect that this approach can be easily translated to a continuous process, which makes it attractive for technological applications.

4.2.3. Printing of sub-monolayer lines

In order to demonstrate the fundamental principle, discrete lines were printed on glass slides with various particles using a Nanoplotter 2.1. Two sets of particles were used, the first one comprising of PS-COOH particles with varying diameter (225 nm, 356 nm, and 538 nm), the other set featuring particles of almost the same diameter (~ 200 nm) but of different copolymer composition (90 % PMMA/ 10 % nBA, Tg = 92 °C; 80 % PMMA/ 20 % nBA, Tg = 70 °C; 70 % PMMA/ 30 % nBA, Tg = 47 °C), which determines the respective particle Tg. The practical resolution limit of this nanoplotter system with a dispensing droplet volume of 0.4 nl was determined by printing of single drops onto a cationically functionalized glass substrate. The spread droplets were found to cover circular areas of 250 - 320 µm in diameter, which represents the minimum accessible feature size. The fabrication of individual lines comprising of three different, sparsely distributed particles was realized (Figure 4.2.2, only the PS-COOH particles are shown here, due to the better optical contrast stemming from the differences in particle size).
The line patterns were designed such that at first single lines of each particle type were placed next to each other. The width of a stripe of a specific particle was gradually increased, which can be seen in Figure 4.2.2 d. At the very right a single stripe of 538 nm particles was printed, followed by single lines of the other two particles. Then a double stripe was deposited and so on. In the end seven lines of a single particle were printed next to each other in case of the parallel stripes, and five in case of the perpendicular ones. A spacing of 380 µm was found to be sufficiently large to yield separate lines without overlapping particle regions, but small enough to leave only a minimum space uncovered. One should note that a small overlap of stripes occurs in the perpendicular case between particle 1 and 3 (Figure 4.2.2 d).

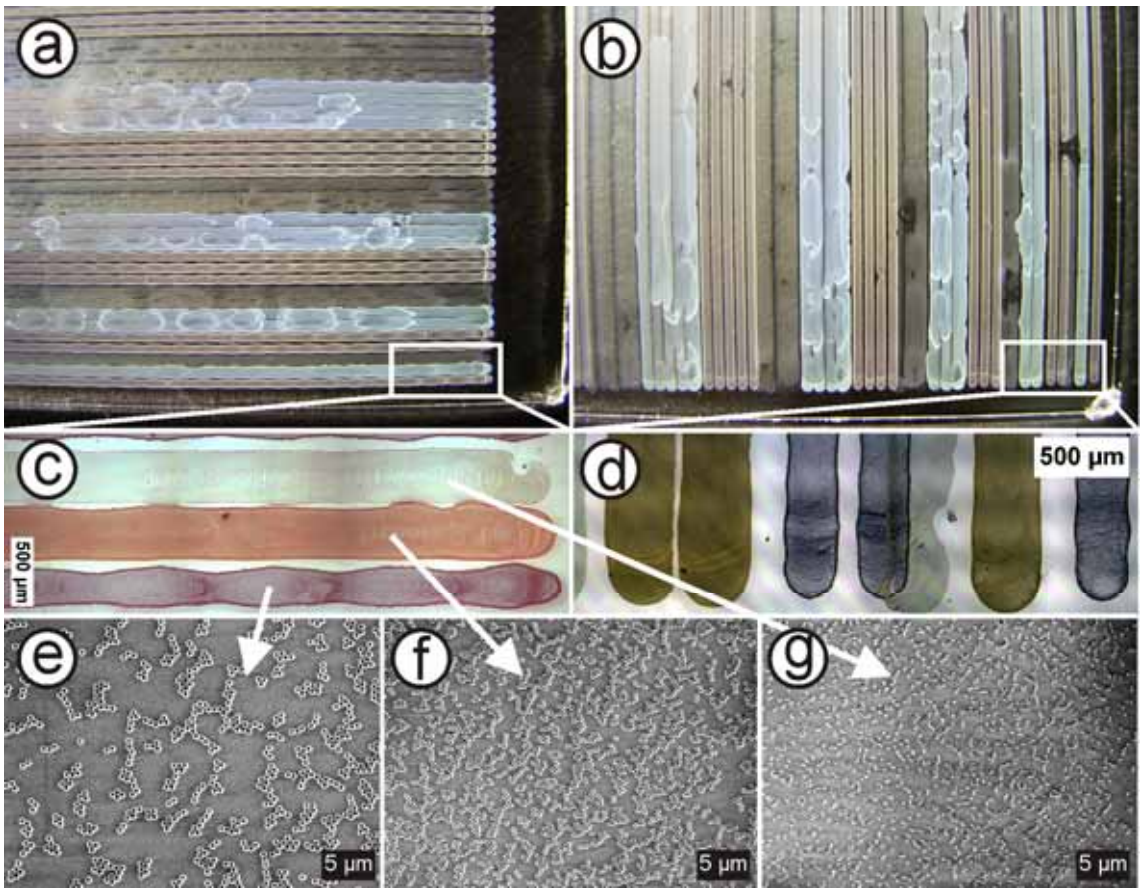

Figure 4.2.2. *Printing of sparse distributed particles of 225 nm, 356 nm, and 538 nm. a) Lines with a spacing of 380 µm were printed parallel (a) and perpendicular (b) to the three-phase-contact line during floating. c) and d) show optical micrographs at a 5x magnification of the parallel and perpendicular stripes, respectively. The different colors derive from the different monolayer thicknesses, given by the various particle diameters. SEM images demonstrate the sparse particle distribution (e: 538 nm, f: 356 nm, and g: 225 nm).*

Close inspection of the photo- and micrographs in Figure 4.2.2 reveals a wavy character of the dispensed lines, which derives from the pulsed pipetting of the particle dispersion in the Nanoplotter. Additionally, some coffee-staining can be seen by the slightly darker edges of the lines. Quarternization of the substrate with NR_4^+ was used to mitigate this effect. It was found that decreasing particle concentrations also decrease the extent of coffee-staining. However, this phenomenon had to be compromised with the particle surface coverage, which also depends on the concentration. The particle surface coverage had to be sufficiently high, in order to obtain large enough floating monolayer areas to be manageable (i.e. samples of several millimeters in width) after floating.

In a detailed analysis the width of the printed lines and the corresponding particle surface coverage ratio were extracted from the optical microscope and SEM images, and are summarized in Table 4.2.1. The particle surface coverage in this context denotes the relative area, which is covered by sparsely distributed particles. It is not a number-particle coverage and is therefore particles size independent.

Table 4.2.1. Surface coverage of sparsely distributed PS and PMMA/nBA particles, and their line width after printing on NR_4^+ glass. Also the widths of the expected and the floated monolayers are given.

			line width, µm				
particle	diameter, nm	surface coverage, %	printed line	floated, expected	single floated	double floated	triple floated
PS	225	16.3 ± 1.3	262 ± 28	47	41 ± 5	91 ± 4	147 ± 12
PS	356	33.7 ± 3.2	363 ± 17	134	117 ± 9	256 ± 17	375 ± 26
PS	538	19.3 ± 4.4	367 ± 13	78	61 ± 11	127 ± 10	194 ± 25
PMMA/nBA 10%	215	21.4 ± 1.4	272 ± 24	64	57 ± 3	125 ± 4	186 ± 5
PMMA/nBA 20%	197	30.1 ± 2.0	340 ± 22	112	70 ± 8	153 ± 3	227 ± 6
PMMA/nBA 30%	205	24.4 ± 4.6	328 ± 19	88	77 ± 12	149 ± 8	243 ± 10

A particle surface coverage ranging from 15 % to 35 % was measured. Thus, with a printed substrate of about 2 x 2.5 cm one can expect to obtain structured monolayers of 2 x 0.5 cm in size. The reproducibility of the surface coverage was within an error of about 5 % between sample to sample. The printed lines range from 260 µm to 370 µm; the reason for the large deviation of the first stripe in both cases (PS and PMMA/nBA) is not clear.

4.2.4. Floating of printed lines

The next step of the procedure was floating of the printed sparse patterns at the air/water interface, compare Figure 4.2.1 b). The substrate immersion was done automatically using a motorized z-stage, whereas the transfer to the target substrate was conducted manually. The printed glass slides were fixed at a shallow angle relative to the water surface and slowly submersed. Highly ordered monolayers form immediately at the three-phase-contact line. Stripes parallel to the meniscus (as shown in Figure 4.2.2 a, c) yield highly ordered monolayers as shown in Figure 4.2.3.

It was possible to assemble and transfer the entire printed substrate down to the smallest feature size, which was given in this case by the width of a single particle line. Even though the transfer of the floating monolayer to the target substrate was conducted by hand, the smallest structure sizes (~ 40 µm) could be preserved. Figure 4.2.3 a) evinces the high quality hetero-monolayer in several ways. The sparse particle lines are homogenously compressed resulting in discrete, straight lines with a sharp border to each neighboring line. The presence of strong opalescent colors upon illumination demonstrates the exceptional quality of the hexagonally ordered monolayers. The dark stripes in Figure 4.2.3 a) can be assigned to the 225 nm spheres, which are too small to show Bragg diffraction from a particle monolayer in the visible range. The smallest feature, which was resolved in the experiments shown here was 40 µm. The width of the first

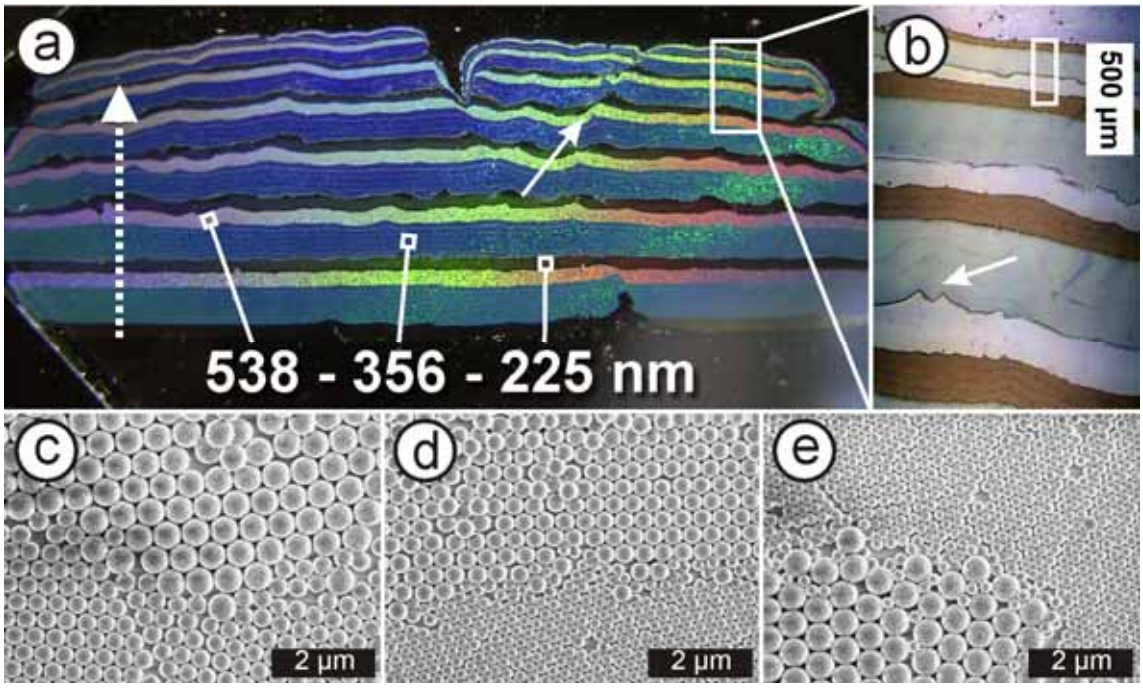

Figure 4.2.3. *Floated monolayer resulting from parallel stripe patterns. a) Photograph showing strong opalescent colors. The regions of the single particles are indicated. The dotted white arrow represents the direction of substrate immersion. b) Optical microscope (OM) image with differential interference contrast (DIC) of the white boxed region from a). The different colors derive from the different monolayer thicknesses, given by the various particles: brown: 538 nm, light blue: 356 nm, and white: 225 nm. c, d, and f) SEM images of the boundaries from one assembled stripe to the other as indicated by the white box from b).*

three particle rows are summarized in Table 4.2.1 and compared to their expected width, based on the sparse particle line width and the corresponding surface coverage.

In all cases (except for the 80 % PMMA / 20% nBA particles) the obtained layer width is only slightly slimmer than expected. A possible explanation for this finding could be that not all printed particles are floated off the substrate or trapped at the air/water interface. Only a few percent of such particles being stuck at the parent substrate or submerse into the subphase could be responsible for this deviation. Within the experimental error, a homogenous increase in stripe width could be observed with increasing number of sparse particle lines, corroborating the good control over the assembly process. Nevertheless, some deviations from an ideal behavior are present in Figure 4.2.3 a). The most obvious is a crack in the middle, which spans over three particle lines. This derives from meniscus pinning either on the parent or the target substrate during floating or drying, respectively. Meniscus pinning can also lead to a displacement of the floated layers, as indicated by the solid white arrow (Figure 4.2.3 a) or to undulations of the straight contact line between neighboring regions (white arrow in Figure 4.2.3 b). The SEM images prove that remarkably sharp transition regions among the distinct particle types evolved. For all cases only a minimum intermixing of the two adjacent species takes place. With the particle concentrations used here, also the problems arising from the

coffee-stain effect could be minimized, but not excluded. Thus one can see in Figure 4.2.3 c) and d) some particles or particle clusters residing on top of the ordered layer.

The presented method can be equivalently applied to PMMA/nBA latex particles. The results of stripes comprising of PMMA/nBA particles are also listed in Table 4.2.1.

The result of floating stripes, which were printed perpendicular to the three-phase-contact line, is shown in Figure 4.2.4.

It evidences that also structures perpendicular to the three-phase-contact line can be successfully assembled and transferred. The quality of the monolayer is again excellent as envisioned by the opalescent colors. However, due to the adjacent particle border-lines being parallel to the direction of motion (as indicated by the dotted white arrow in Figure 4.2.4 a) such structures are more amenable to bend or even break. For this reason the block of single stripes broke apart during the transfer process and only the double stripes (~ 600 – 700 µm) and larger features are shown in Figure 4.2.4 a) and b). However, in case of the PMMA/nBA particles the full layer could be transferred with the thinnest stripes being 275 µm to 425 µm wide (Figure 4.2.4 c).

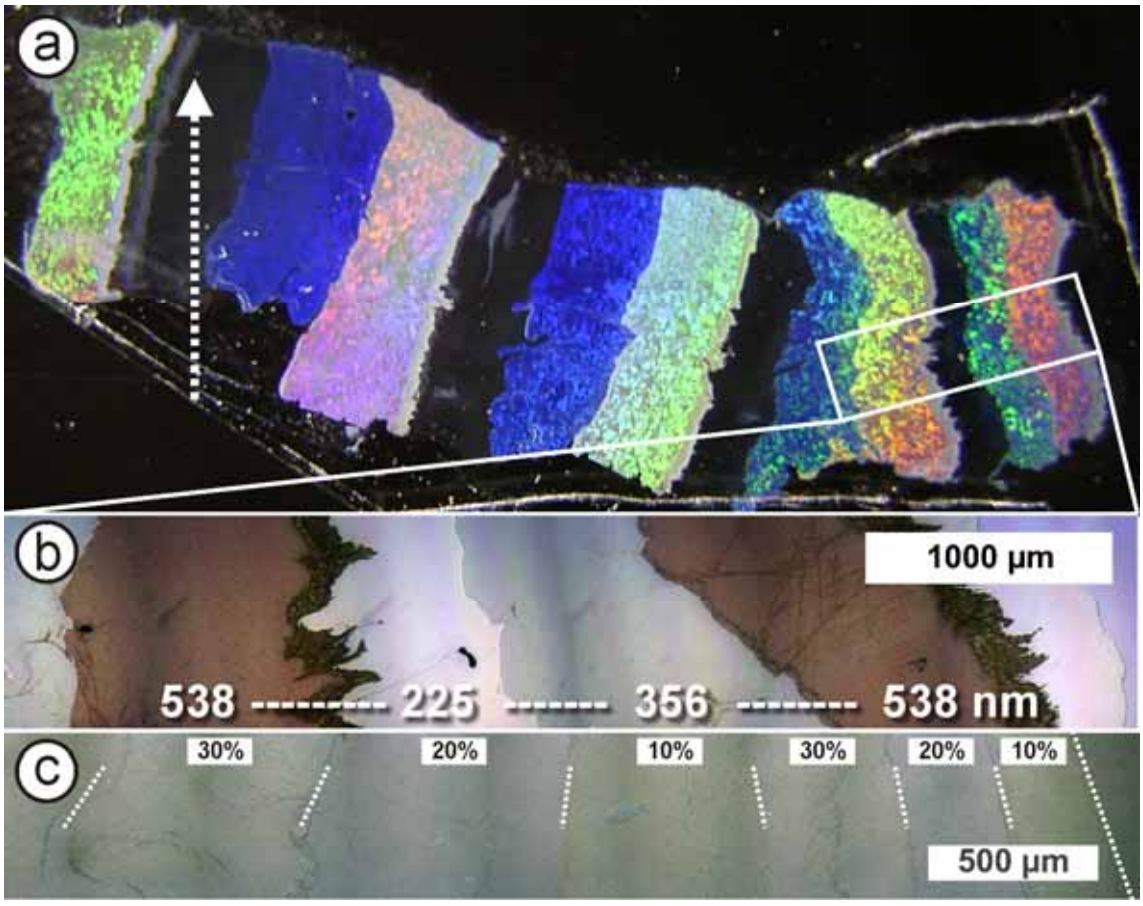

Figure 4.2.4. *Floated monolayer resulting from perpendicular stripe patterns. a) Photograph showing strong iridescent colors. b) OM-DIC image of the white boxed region from a), with the particle diameter attributed to the individual monolayers. c) OM-DIC image of an equivalently structured monolayer of PMMA/nBA particles. The numbers indicate the nBA-content of the PMMA/nBA copolymer particles. White dotted lines indicate the boundaries.*

A crucial point to control in such an experiment is the homogenous growth of each individual particle stripe, which necessitates adjusting the particle surface coverage. Regions having higher or lower particle concentrations than their neighboring regions induce a bending of the adjacent stripe (due to the mismatch of the length of the assembled stripe) and ultimately lead to a failure of the whole film.

When taking a close look at Figure 4.2.4 one finds whitish (a) and dark (b) regions between the stripes of 225 nm and 538 nm particles. These originate from the slight intersection of the printed lines, as shown in Figure 4.2.1 b). Furthermore, pinning of the meniscus upon floating results in fringes, which can be seen by perpendicular irregularities between two adjacent particle layers.

4.2.5. Fabrication of arbitrary patterns

Being able to preserve printed, sparsely distributed patterns parallel and perpendicular to the floating direction, one should also be able to print any desired shape, taking into account the anisotropic shrinkage parallel to the immersion direction. In order to demonstrate this possibility and to go a step further to potential technological applications, the method was transferred to a regular HP inkjet printer. On the expense of precisely controlling the single deposited drops (due to multiple nozzles per print head with 20 µm diameter), fabrication of patterns on a complete DIN A4 sized aluminium foil, glued to a transparency foil could be realized (details in the experimental part 4.2.9). As an arbitrary pattern the MPIP logo was chosen and printed in a stretched way onto the aluminium foil. The results after transfer to silicon wafers are shown in Figure 4.2.5.

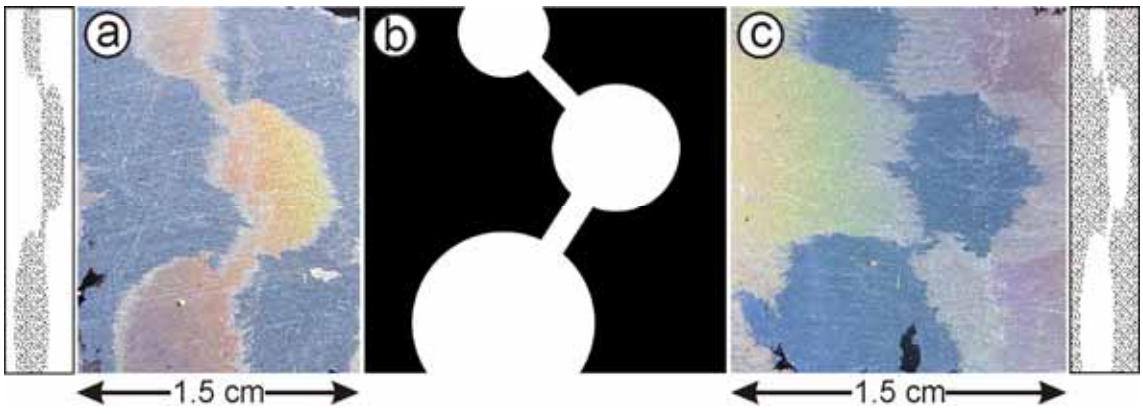

Figure 4.2.5. *Printing of structured monolayers of arbitrary shape, here the MPIP logo (b). a) Particles of 1.1 µm diameter make up the interior (hatched part in the left panel), surrounded by 356 nm particles. c) Inverse structure of a), with 356 nm in the interior, surrounded by 1.1 µm particles (hatched part in the right panel).*

Complex structures like circles or diagonal ridges can be reproducibly printed on a several millimeter scale and transferred, but some distortion of the macroscopic shape takes

place. The reasons for this are turbulences at the air/water interface and inhomogenities on the aluminium foil leading to meniscus pinning. Furthermore, these monolayers were floated and transferred by hand, which additionally promotes irregularities. The good quality of the assembled monolayer can deduced from the opalescent colors of the 1.1 µm parts. Similar to Figure 4.2.4 some whitish parts at the boundary of the two monolayer regions are visible. These stem from a poor registration of the printer when printing several times on the same sheet, which was necessary to adjust the particle surface coverage. An equal particle surface coverage in both parts of the printed pattern is mandatory to successfully retain the desired shape, analogous to the case of the perpendicular stripes.

Some technical shortcomings of the HP system used here are briefly discussed, as they are believed to be avoided when using a state-of-the-art piezo printer. The cartridges of HP 970CXI work thermally, which means that the ink is rapidly heated in order evaporate explosively. This shoots the ink through a perforated membrane with pores of 20 µm diameter. When using a latex dispersion this heating leads to a gradual and irreversible accumulation of polymer around the heating unit, eventually clogging the cartridges of the thermoprinter, and making it difficult to deposit an adjusted amount of material on the substrate. Another problem was that only the black cartridge, which does not feature a sponge to store the ink, could be used. Thus in order to pattern two types of particles, the same substrate had to be printed at least twice for changing the cartridges between the printing runs. Slight differences in the feeder reflected directly in an intersection of the printed patterns. However, these problems do not limit the general applicability of the method described. Clogging of the nozzle was not found to be a problem for the Nanoplotter (which works piezoelectrically), thus a piezo-inkjet printer can be used, and simultaneous use of several cartridges (black and multi-color) will immediately circumvent the registration issue.

4.2.6. Selective surface patterning

So far it has been demonstrated that colloidal monolayers can be patterned on a several 10 µm scale with a variety of particles. Colloidal monolayers are widely used as lithographic mask for nanosphere lithography (NSL).[8] Now, being able to structure a colloidal monolayer with the technique presented here, one might also want to preserve this pattern during the NSL process. Therefore, a method to selectively close the pores between three neighboring particles in a structured array has to be used. This property can readily be implemented into the printed particles from the beginning. Using particles

with a different film forming temperature (which can be adjusted by the Tg) opens the possibility to selectively close single regions, whereas the rest remains unaffected during the annealing step. Method and experiment are shown in Figure 4.2.6.

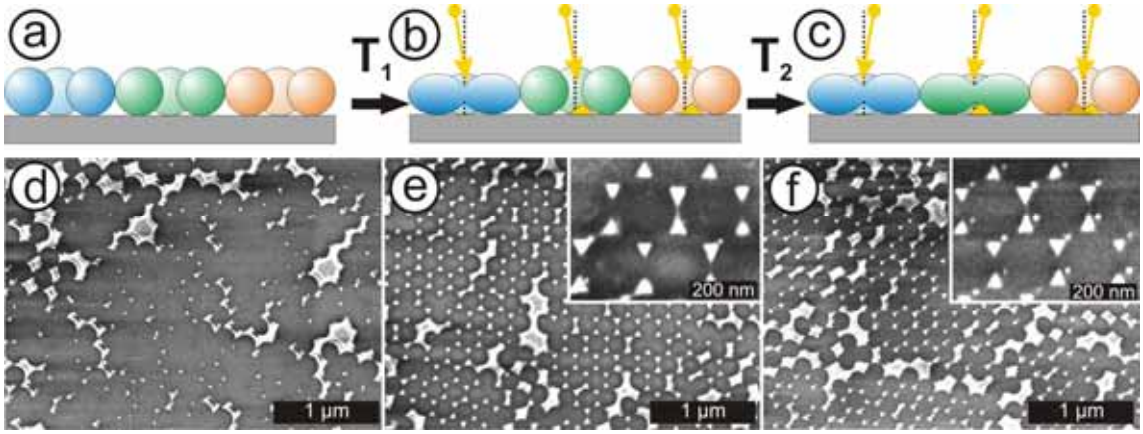

Figure 4.2.6. *a) A structured monolayer comprising of three particle types with same diameter, but different Tg is transferred to a target substrate (blue, green, and orange having the lowest, medium, and highest Tg, respectively). b) After closing the voids of the softest particles gold is evaporated at an angle of 5° relative to the substrate normal. c) After a second annealing step to close the medium-Tg particles voids, gold is evaporated under the opposite angle as before. This leads to a displacement of the evaporated structure and makes it possible to identify the different regions by SEM. c), d), and e) are SEM images of regions corresponding to the blue, green, or orange particle, respectively, after Au evaporation and monolayer removal.*

In order to prove the principal feasibility of this method, monolayer patterns by particles of three different Tg were fabricated. Precisely, PMMA/nBA copolymer nanoparticles with increasing amount of nBA were used. The Tg of the respective PMMA/nBA statistical copolymers was measured to be ~ 47 °C, 70 °C, and 92 °C (for a content of 30 %, 20 %, and 10 % of nBA in the copolymer). Due to these differences in Tg the individual areas should be selectively addressable by annealing at different temperatures T_1 and T_2 (Figure 4.2.6 b and c). When evaporating gold under different angles after each annealing step one should obtain displaced nanostructures after monolayer removal, which can be characterized by SEM.[34] The experimental results are summarized in the bottom row of Figure 4.2.6. From left to right, the Tg of the masking particle increased. The free voids were almost completely closed for the softest particle after the first tempering at 45 °C. This can be seen by the deposition of only tiny Au dots in a few places of the previous mask (Figure 4.2.6 d). Only at defect positions (point and line defects), which are always present in a colloidal monolayer, major gold structures were deposited in the otherwise closed film. The other two particles were mainly unaffected by this first annealing step. For both regular Au triangles of a size of about 40 nm edge length were obtained. In the second annealing step the pores of the medium-Tg particle were closed, and no further Au features could be added next to the first triangles (Figure 4.2.6 e). In this case also the third particle type started to fuse together, but at a lower rate, which

left tiny holes that could still be used to evaporate gold dots of ~ 10 nm diameter (some closure of the free voids due to the previously deposited gold might also lead to smaller feature sizes). Due to the different angles of evaporation these gold dots lay just next to the Au triangles (Figure 4.2.6 f).

Thus, it is possible to specifically structure surfaces by using particles with different Tg. Some improvements can still be made to increase the control over this process. One step would be to use even softer particles that could already fuse together on the (slightly heated) water interface. Another way would be to employ tougher particles, for instance by using crosslinked latexes, crosslinkable particles,[15] or higher melting monomers.

4.2.7. Multiple plasmonic properties

Since it is possible to create patterns with a combination of various particles one can deposit particles of various sizes in a single step. Using those monolayers as mask for NSL it is clear that also a range of nanoparticles with different sizes can be easily obtained. The compartmentalized arrangement of the nanostructures can be designed at will, based on the results already presented. In order to give a proof of the concept simple Au nano triangles were evaporated through a structured monolayer comprising of 225 nm, 356 nm, and 538 nm particles in one case, and 356 nm, 538 nm, and 850 nm particles in the other case. The resulting structures were characterized by SEM and the local surface plasmon resonances (LSPR) were probed with Vis/NIR spectrometry.[34] The results for both are summarized in Figure 4.2.7.

The SEM images show that Au nano triangles of sizes ranging from 255 nm, 133 nm, 82 nm, to 47 nm could be simultaneously deposited on the glass substrate.

The corresponding plasmonic behavior is very rich due to the superposition of the resonances of three independent resonators over the area covered by the measuring light beam. In Figure 4.2.7 e) a stripe pattern of Au triangle of 255 nm, 133 nm, and 82 nm were measured, in Figure 4.2.7 f) the individual stripes consisted of 133 nm, 82 nm, and 47 nm nanoparticles. The solid black lines in Figure 4.2.7 e) and f) represent the averaged absorption over all three layers and were measured perpendicular to the individual Au triangle stripes. The inset in Figure 4.2.7 f) emphasizes the measurement setup. The incident spot of the Vis/NIR spectrometer was about 3x5 mm in size, thus hitting several particle type regions at the same time. The resulting spectra show very broad resonances, which are convoluted by the nanoparticle surface coverage and the absorption efficiency of each particular structure. The peak at ~ 1300 nm stemming from the 255 nm triangles is missing in spectrum f). Therefore, those spectra were only recorded

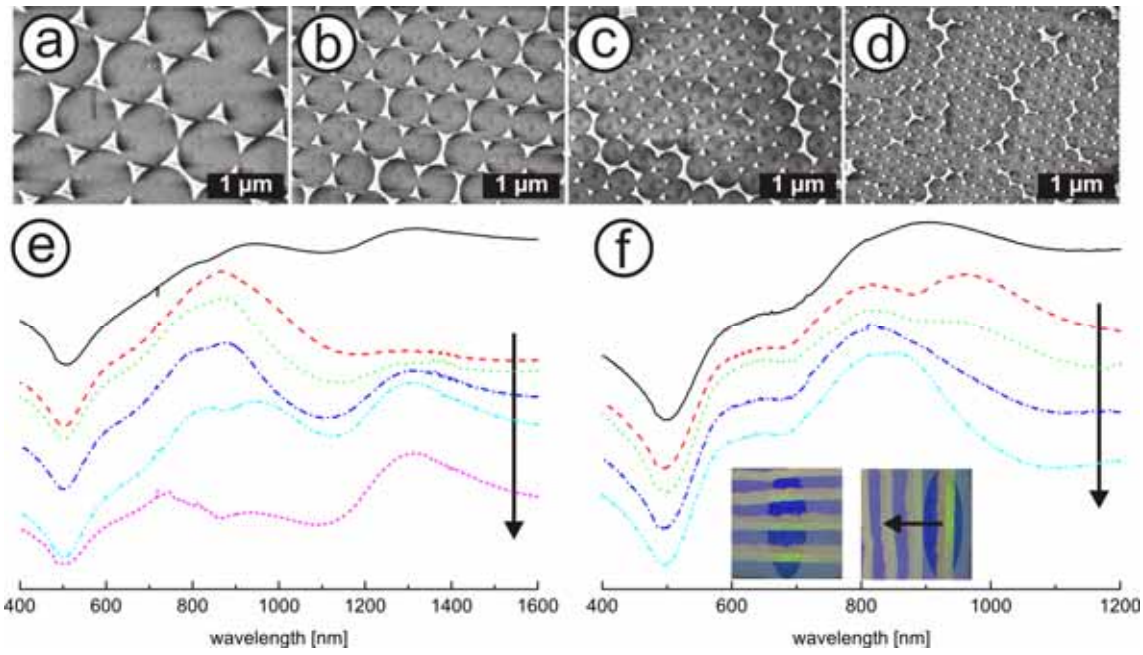

Figure 4.2.7. *a) to d) SEM images of Au triangles of different sizes: 255 nm, 133 nm, 82 nm, and 47 nm (from left to right). e) Corresponding Vis/NIR spectra measured on a substrate with 255 nm, 133 nm, and 82 nm gold triangles. f) Spectra measured on a substrate with 133 nm, 82 nm, and 47 nm gold triangles. The inset indicates the measurement geometry of the light beam (ellipse) with respect to the line pattern. The solid curve shows the spectrum measured perpendicular to the stripes. The dashed/dotted curves show the evolution of the spectra, when moving the beam parallel to the nanoparticle stripes and thus measures at various spots.*

up to 1200 nm.

By orienting the structured stripes parallel to the Vis/NIR beam, individual peaks in the spectra became more pronounced and it was possible to roughly address individual regions with a particular type of nano-triangle resonators. This can be followed by the relative change of the peak intensities, when the structured substrate was gradually moved through the Vis/NIR beam as schematically shown in the inset. For both material combinations one finds a decrease for one particle resonance, whereas at the same time the other peaks increase. For instance, when illuminating on the stripe of 255 nm particles the LSPR peak (~ 1300 nm) becomes highest, relative to the resonances stemming from the 133 nm and 82 nm particles (short dashed line, magenta); moving the layer towards the 133 nm resonators their intensity increases (~ 950 nm, dash double-dotted line, turquoise). Going further to the smallest nanostructures the peak at 1300 nm almost vanishes, whereas a broad peak covering both resonances of the smaller particles (~ 950 nm and 800 nm, dashed line, red) evolves. Since the UV/Vis beam is not focused down to a single stripe width one always probes several nanoparticle stripes and gets therefore superpositioned spectra. This makes it particularly difficult to identify the LSPR from the 82 nm triangles, since their maximum (~ 780 nm) falls in the range of additional absorption bands from the larger particles. Qualitatively, the same behavior

can be deduced from Figure 4.2.7 f), too, where the largest resonators were exchanged with 47 nm triangles. However, the UV/Vis spectrum of these tiniest structures did not show a distinct peak, but a broad absorption spanning from ~ 650 nm to 900 nm and can not be individually identified in the presented spectra.

The measurements shown here evidence that parallel fabrication of nanostructures with different sizes by NSL is possible and that the properties of the single arrays can be individually addressed.

4.2.8. Conclusion and outlook

A new methodology has been introduced to fabricate structured colloidal monolayers. By printing sparsely distributed particle patterns, which only requires a minimum of parameter optimization, one can easily obtain heterogeneous monolayers, which not only possess a pattern in the tens of μm range, but can also comprise of several particle types, a feature, which is not possible with other methods so far. The desired pattern, which can be of any shape, is printed onto a first substrate taking into account the anisotropic shrinkage during the self-assembly process. This method makes the use of masks redundant and is therefore a lithography-free process. Additionally, printing, floating, and transfer can be straightforwardly translated into continuous processes, making this method technically relevant. The heterogeneous monolayers can be used as mask to generate nanostructures, which are accessible by NSL. Proper particle design allows selective closing of open inter-particle voids by simply annealing the entire film. Combination of particles with various sizes and film forming temperatures paves the way to design novel multiarray sensors. These could consist of patches with different particle sizes, corralled by a low film formation temperature matrix. After annealing, gold evaporation, and mask removal as the only processing steps, multiple arrays of plasmonic resonators could be obtained.

Further improvements of this method point to a fully automation of printing, floating, and transfer, which could lead to an improved reproducibility and reduction of the minimum feature size, which can be accessed. Concomitant, the use of state-of-the-art piezoelectric printers with only picoliters of drop volume could enable printing of finer structures.

4.2.9. Experimental part

Printing via Nanoplotter 2: Printing was undertaken in collaboration with Sebastian Nett. A nanoplotter NP2.1 from GeSim (Groperkmannsdorf, Germany) equipped with a pipette NanoTip 15255 (0.4 nl/drop) was used to print stripes of sub-monolayer latex particles on NR_4^+ functionalized glass substrates (35 x 26 x 1 mm). PS-COOH latex dispersions consisting of the following particles and concentrations were used: 225 nm (0.14 wt%), 356 nm (0.57 wt% and 0.21 wt%), 538 nm (0.66 wt%). A PS-SO_4H latex dispersion of 850 nm (0.69 wt%) was used. PMMA/nBA copolymer latex particles of the following size and composition were used: 215 nm (10 % nBA, 0.18 wt%), 197 nm (20 % nBA, 0.19 wt%), and 205 nm (30 % nBA, 0.19 wt%). All dispersions were filtered through 1.2 µm syringe filter prior to use. The 850 nm particle dispersion was filtered through a paper filter. Lines with a periodicity of 380 µm among each other were printed over the entire substrate using speed "9" (corresponding to ~ 3 - 5 mm/s) of the NP2.1 control software. The glass substrates were functionalized by liquid phase silanization of *N*-trimethoxysilylpropyl-*N*,*N*,*N*-trimethylammonium chloride (NR_4^+, 50 % in methanol) (ABCR/Gelest, Karlsruhe, Germany).[25] The lines were printed parallel and perpendicular to the immersion direction. The layout was designed such that first a single line of each particle is dispensed, then a double line, then a triple line and so on. In case of the parallel lines up to seven lines of each particle were printed, in case of the perpendicular stripes up to five lines were deposited. All lines of a specific particle were printed in one run.

Floating of glass substrates: Floating of the printed sub-monolayers on glass slides was conducted automatically. The printed glass slide was fixed at a shallow angle (10°-20°) to a z-stage. Immersion of the slide was conducted by a speed of 20 mm/min of the z-stage, corresponding to a speed of the water meniscus on the substrate of about 1 -2 mm/s. The immersion liquid was MQ water at pH 11 (by addition of $NH_{3\ conc}$) and with $5x10^{-4}$ M SDS. The floating layer was picked up with a clean glass slide by hand and dried at an angle of 30°.

Printing via HP Deskjet 970cxi: Printing was undertaken in collaboration with Karl-Heinz Dostert. The black cartridge of a commercial HP Deskjet printer was cleaned by several washing cycles with MQ water until clear lines of water could be printed. It was then filled with an adjusted ink containing PS-SO_3H latex particles of either 360 nm or 1150 nm. Explicitly the following dispersions were used: A 0.6 wt% aqueous solution of 1150 nm particles, a 0.4 wt% 1150 nm particles in a 95 vol% water/5 vol% isopropanol dispersion, and a 0.3 wt% 360 nm particles in a 95 vol% water/5 vol% isopropanol dispersion. Each particle was printed with its own cartridge. Due to gradual jamming of the cartridge nozzle the desired pattern was printed several times on the same substrate to ensure a sufficiently high surface coverage; this was adjusted individually for each run. Aluminum foil glued to a laser transparency foil with spray glue (3M) served as DIN A4 substrate. The miniaturized pattern shown below was printed on the entire aluminum foil (DIN A4), once as shown below with one particle type, once the inverted pattern was printed with the other particle type. Standard monochrome printing settings were used in all cases.

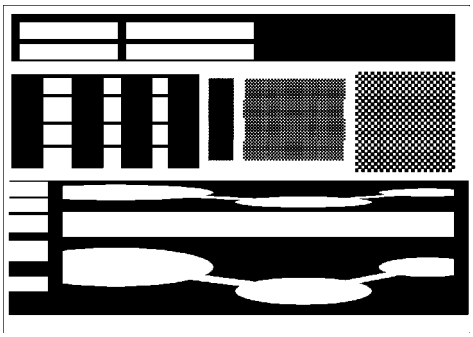

Floating of Aluminum Foil: The aluminum foil was immersed in a home-built tray made of Teflon with milled guide rails (see the photograph below). The left side shows a side view with an aluminum foil in place. The right side shows a top view with a floating monolayer (reddish and greenish patches). The black background facilitates to capture the floating monolayer.

The tray was filled with MQ water at pH 11 by addition of $NH_{3\ conc}$. Usually the printed film was immersed at an angle of 40° (as shown in the photograph above). Immersion speed varied and was in the order of 30 sec for the entire DIN A4 page. The floating monolayers were transferred to silicon wafers, which were previously cleaned with acetone. The transferred layers were dried at an angle of 30°.
Photographs of printed, floating and transferred monolayers were taken with a RICOH Caplio RR30.
Monolayer annealing and Au evaporation: Annealing of monolayers consisting of particles with different Tg was performed in a glass beaker immersed in an oil bath. The first annealing step was performed at 45 °C for 30 min. Then 1.5 nm Cr and 30 nm Au were sequentially evaporated (*Auto 306, Edwards, Sussex UK*) on the colloidal template, with the samples being tilted relative to the metal source by Θ=5°. The second annealing step was performed at 69 °C for 30 min. A second evaporation step was conducted, with 1.5 nm Cr and 30 nm Au, but with the sample being tilted in the opposite direction by Θ=-5°.
Samples consisting of PS particles with various sizes were perpendicularly evaporated with 1.5 nm Cr and 30 nm Au.
The colloidal mask was removed by stripping with an adhesive tape (Tesa), and brief rinsing with THF.

4.2.10. Bibliography

1. Geissler, M.; Xia, Y. N. *Adv. Mater.* **2004,** 16, (15), 1249-1269.
2. Lee, K. S.; Kim, R. H.; Yang, D. Y.; Park, S. H. *Prog. Polym. Sci.* **2008,** 33, (6), 631-681.
3. Saitou, N. *Int. J. Jpn Soc. Precis. Eng.* **1996,** 30, (2), 107-111.
4. Mendes, P. M.; Preece, J. A. *Current Opinion in Colloid & Interface Science* **2004,** 9, (3-4), 236-248.
5. Piner, R. D.; Zhu, J.; Xu, F.; Hong, S. H.; Mirkin, C. A. *Science* **1999,** 283, (5402), 661-663.
6. Hong, S.; Zhu, J.; Mirkin, C. A. *Science (Washington, D. C.)* **1999,** 286, (5439), 523-525.
7. Bratton, D.; Yang, D.; Dai, J. Y.; Ober, C. K. *Polym. Adv. Technol.* **2006,** 17, (2), 94-103.

8. Yang, S. M.; Jang, S. G.; Choi, D. G.; Kim, S.; Yu, H. K. *Small* **2006,** 2, (4), 458-475.
9. Hulteen, J. C.; Vanduyne, R. P. *J Vac Sci Technol A* **1995,** 13, (3), 1553-1558.
10. Kosiorek, A.; Kandulski, W.; Glaczynska, H.; Giersig, M. *Small* **2005,** 1, (4), 439-444.
11. Zhang, G.; Wang, D. Y.; Mohwald, H. *Nano Lett.* **2007,** 7, (11), 3410-3413.
12. Shumaker-Parry, J. S.; Rochholz, H.; Kreiter, M. *Adv. Mater.* **2005,** 17, (17), 2131-2134.
13. Yang, P. D.; Deng, T.; Zhao, D. Y.; Feng, P. Y.; Pine, D.; Chmelka, B. F.; Whi tesides, G. M.; Stucky, G. D. *Science* **1998,** 282, (5397), 2244-2246.
14. Xia, D. Y.; Ku, Z. Y.; Li, D.; Brueck, S. R. J. *Chem. Mater.* **2008,** 20, (5), 1847-1854.
15. Moon, J. H.; Jang, S. G.; Lim, J. M.; Yang, S. M. *Adv. Mater.* **2005,** 17, (21), 2559-2562.
16. Moon, J. H.; Kim, W. S.; Ha, J. W.; Jang, S. G.; Yang, S. M.; Park, J. K. *Chem. Commun.* **2005**, (32), 4107-4109.
17. Jiang, P.; Prasad, T.; McFarland, M. J.; Colvin, V. L. *Appl. Phys. Lett.* **2006,** 89, 011908.
18. Nagao, D.; Kameyama, R.; Matsumoto, H.; Kobayashi, Y.; Konno, M. *Colloids and Surfaces a-Physicochemical and Engineering Aspects* **2008,** 317, (1-3), 722-729.
19. Harris, D. J.; Hu, H.; Conrad, J. C.; Lewis, J. A. *Phys. Rev. Lett.* **2007,** 98, 148301.
20. Celio, H.; Barton, E.; Stevenson, K. J. *Langmuir* **2006,** 22, (26), 11426-11435.
21. Hayward, R. C.; Saville, D. A.; Aksay, I. A. *Nature* **2000,** 404, (6773), 56-59.
22. Xie, R. G.; Liu, X. Y. *Adv. Funct. Mater.* **2008,** 18, (5), 802-809.
23. Maury, P. A.; Reinhoudt, D. N.; Huskens, J. *Current Opinion in Colloid & Inter face Science* **2008,** 13, (1-2), 74-80.
24. Aizenberg, J.; Braun, P. V.; Wiltzius, P. *Phys. Rev. Lett.* **2000,** 84, (13), 2997-3000.
25. Jonas, U.; del Campo, A.; Krüger, C.; Glasser, G.; Boos, D. *P Natl Acad Sci USA* **2002,** 99, (8), 5034-5039.
26. Lu, C. H.; Mohwald, H.; Fery, A. *Soft Matter* **2007,** 3, (12), 1530-1536.
27. de Gans, B. J.; Duineveld, P. C.; Schubert, U. S. *Adv. Mater.* **2004,** 16, (3), 203-213.
28. Tekin, E.; Smith, P. J.; Schubert, U. S. *Soft Matter* **2008,** 4, (4), 703-713.
29. Ko, H. Y.; Park, J.; Shin, H.; Moon, J. *Chem. Mater.* **2004,** 16, (22), 4212-4215.
30. Park, J.; Moon, J.; Shin, H.; Wang, D.; Park, M. *J. Colloid Interface Sci.* **2006,** 298, (2), 713-719.
31. Burkert, K.; Neumann, T.; Wang, J. J.; Jonas, U.; Knoll, W.; Ottleben, H. *Lang muir* **2007,** 23, (6), 3478-3484.
32. Deegan, R. D.; Bakajin, O.; Dupont, T. F.; Huber, G.; Nagel, S. R.; Witten, T. A. *Nature* **1997,** 389, (6653), 827-829.
33. Park, J.; Moon, J. *Langmuir* **2006,** 22, (8), 3506-3513.
34. Haynes, C. L.; Van Duyne, R. P. *J. Phys. Chem. B* **2001,** 105, (24), 5599-5611.

4.3. Parallel Preparation of Densely Packed Arrays of 150 nm Split-Ring Resonators in Three Dimensions

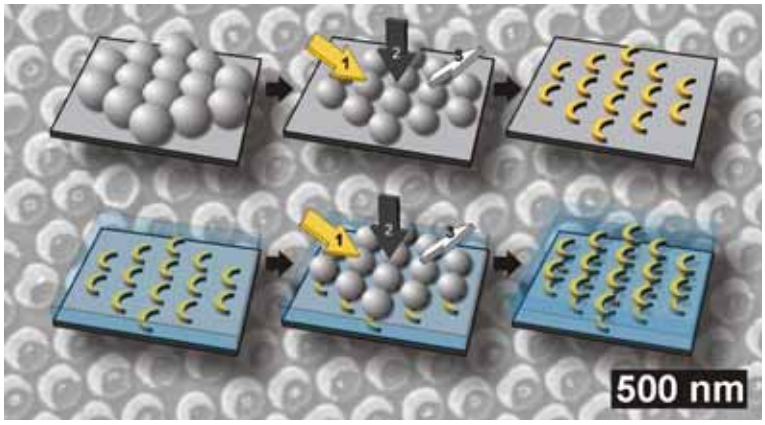

A parallel method to fabricate densely packed, ordered arrays of gold split-ring or crescent-shaped nanostructures supporting plasmonic resonances in the near infrared spectral range will be presented. Hexagonally ordered monolayers of monodisperse polystyrene colloids were size-reduced in a plasma process and used as a shadow mask. The resulting two-dimensional array of plasmonic resonators could be coated with a transparent silica layer, which served as support for a second layer prepared in an identical manner. The mutual orientation of the nanostructures in the individual layers could be adjusted at will. This opened the possibility to introduce chirality in this type of 3D metamaterial. This methodology may pave the way to high-quality optical metamaterials at affordable production cost for the discovery of novel optical effects and their technological application.

4.3.1. Introduction

The interaction of metallic objects with electromagnetic radiation depends critically on their size and geometry. For frequencies at which the metal is a good conductor, one may assign capacitances, resistances and inductance to these structures. Such passive electrical circuits can be realized with object dimensions below the wavelength of the incident radiation, which exhibit resonances at particular wavelengths.[1] A three-dimensional assembly of such objects can approximately be described by an effective homogenous refractive index.[2] The refractive index of these metamaterials may be tailored to exhibit unique values that are not found for naturally occurring materials. For example, negative refraction and perfect lenses,[3] i.e. formation of optical images well below the diffraction limit have been proposed for these metamaterials. More recently, the concept of "cloaking", the formation of a structure that may be put around any object and then completely prevents this object from interacting with incident electromagnetic waves, has been discussed.[4-6] While metamaterials with these properties have been demonstrated successfully in the microwave regime soon after their first proposal,[1] their implementation at frequencies corresponding to visible light is still under investigation.

Since individual resonators must be smaller than the wavelength under consideration, any methodology for the preparation of metamaterials at visible frequencies must be able to produce individual resonators with a total structure size well below 1 µm, exhibiting geometrical features on the length scale of 10 nanometers. This has been demonstrated to be possible by electron-beam lithography, which is a comparably slow and expensive process due to sequential writing. With this technique, two dimensional arrays of split-ring resonators, with a total size of 200 nm have been prepared.[7] They possess a loop with a large geometrical cross section and therefore interact with the magnetic component of an electromagnetic field, for this reason they are regarded as the optical analogue of an LC-circuit.

Recently, nanofabrication of true 3-dimensional arrangements of such resonator structures has been achieved, both for split-ring resonators[8] and for a mesh ("fish-net") structure.[9] In the latter case, negative refraction has been shown.

An alternative method for the preparation of nanosized structures uses colloids as shadow mask. This approach sacrifices the possibility to generate any wanted object shape, but in return, macroscopic areas are structured quickly in a parallel process. Structure sizes of 10 nm are routinely achieved. Moreover, the optical response of structures made by colloidal lithography can be described based on the tabulated optical response of the pure metal under consideration. In contrast, modelling of the structures

produced by the sequential methods mentioned above requires the assumption of additional damping mechanisms.[7] This damping is attributed to contaminations like residues of resist and amorphous carbon, which represent a problem in electron-beam writing, or heavy doping by the ions that form a focused ion beam.

When a close-packed monolayer of colloids is used as mask, regular arrays of triangular structures can be achieved.[10, 11] Several geometrical variations of these structures by adjustment of the experimental parameters[12] have been demonstrated. Isolated, free standing colloid particles, allow for the preparation of different structures such as disks[13] or rings.[14] In particular, crescent-shaped structures[15] can be made, which support several multipolar resonances and are equivalent to the 'split ring resonators' discussed in the context of metamaterials.[16] However, for the assembly of a material with an average response, a regular arrangement in a lattice and a high packing density are mandatory. At the same time, a minimum separation between the masking colloids must be guaranteed to provide geometric access to the individual particle as required by the structuring process.

A possible strategy to prepare ordered arrays of colloids with defined spacing utilizes plasma-etching of colloidal monolayers.[17] Plasma-etched colloids have previously been shown as masks for the preparation of gold disks with random[13, 18] and regular[19] arrangement. They have been used for the preparation of "Nano-Shuttlecocks"[20] and quasi-three-dimensional grids.[21]

Here, the use of plasma-etched colloidal monolayers for the preparation of crescent-shaped structures with a high array density and defined orientation is demonstrated. The particle array can be covered in such a way that a second layer can be deposited on top. The mutual in-plane rotational orientation between stacked layers can be freely chosen allowing for the introduction of chirality as an extra important[22] degree of freedom to tailor the effective optical response.

4.3.2. Concept of the fabrication process

The experimental concept for the preparation of macroscopic areas of crescent-shaped plasmonic resonators is sketched in Figure 4.3.1. A hexagonally close-packed array of polystyrene colloids was prepared on a glass substrate (a). The colloids were reduced in size by exposure to plasma. These size-reduced colloids were then used as shadow mask for the preparation of nanocrescents. First, gold was evaporated at an angle Θ (b1). Subsequently, the sample was exposed to an argon ion beam perpendicular to the substrate to remove all gold except in the area of the geometrical shadow under the colloids (Fig-

ure 4.3.1 b2). Finally, the masking particles were removed (Figure 4.3.1 b3), leading to a surface, which is covered by a densely packed array of metal crescents (Figure 4.3.1 c). The structures are covered by a transparent film (Figure 4.3.1 d) and the process was repeated (Figure 4.3.1 e, f). In principle, these steps may be repeated several times leading to a thick three-dimensional structure.

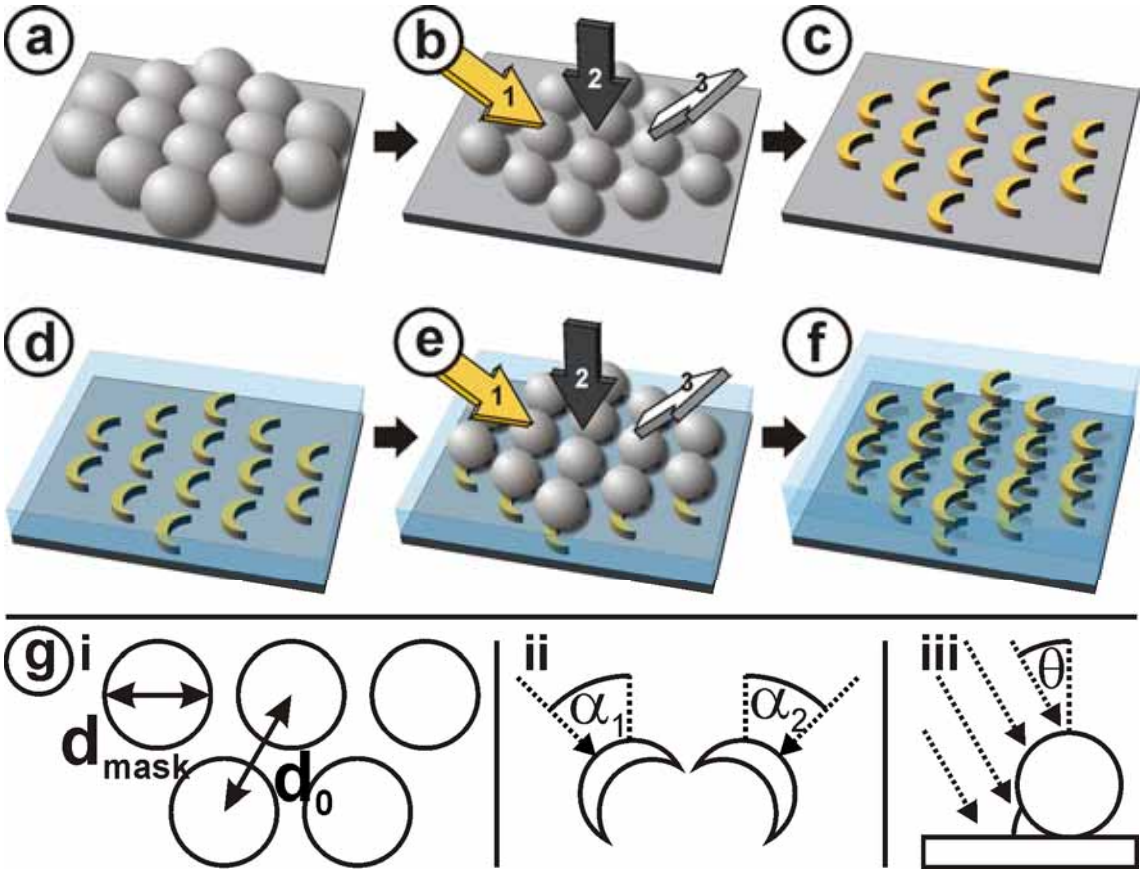

Figure 4.3.1. *Sketch of the process used to prepare multilayers of densely packed crescent-shaped resonators. a) hexagonally close-packed layer of polymer beads. b) After plasma treatment the colloid diameter is reduced. Inclined gold deposition (1), perpendicular reactive ion beam etching (2), and particle removal (3) are indicated as arrows. c) An ordered assembly of metal crescents is obtained. d) The surface is coated by a silica film. e) Repetition of step a) – c) gives the second layer on top of the first. f) After coverage with a second silica layer. g) Geometrical parameters of an etched monolayer. i) interparticle spacing d_0 and d_{mask}, the colloid diameter after size reduction. ii) in-plane orientation α of individual crescent layers. iii) evaporation angle Θ.*

Central geometrical parameters describing the resulting structure are shown in Figure 4.3.1 g. The lattice constant d_0 is defined by the diameter of the colloids used initially. After size reduction their diameter is reduced to d_{mask}. Different orientations for the individual crescent layers are achieved by a variation of the azimuthal direction of the gold deposition, described by the angle α. A final free parameter is the polar evaporation angle θ (g iii).

This process leaves ample degrees of freedom to tune the resulting structure. In particular, by varying α for each individual layer, a defined chirality can be given to the final

material. Since etching time and size of the initial colloids can be chosen independently, both size and density of the resulting crescents can be tuned. As a result, the resonance frequency of the individual resonator, which is mainly defined by its size, can be adjusted. At the same time, tuning the inter particle distance allows for a fine tuning of the inter-particle coupling.

4.3.3. Crescents array fabrication

As outlined, the first step involved a controlled size reduction of colloidal monolayers of a certain diameter, d_0, to the desired size of d_{mask}. This was conducted by Matthias Tamm via plasma etching. At a given set of parameters the size reduction of polymeric nanoparticles is a function of time. Important parameters to control during plasma etching are the gas type and -flow, and the power. The shrinkage of 1.1 µm PS particles for two sets of etching conditions is shown in Figure 4.3.2.

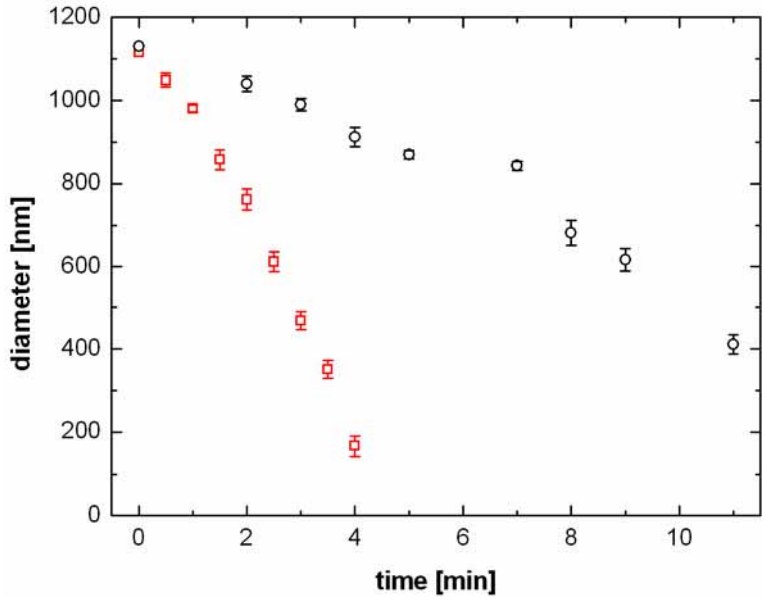

Figure 4.3.2. *Size reduction of 1.1 µm PS particles via plasma etching. Etching conditions were Ar:O_2 @ 9:3 sccm (open squares) and pure Ar @ 5 sccm (open circles) at a power of 190 W.*

The size of the colloids could be adjusted over a wide range. The plasma etching shrinks the particles homogeneously, which preserves the narrow particle size distribution. Addition of oxygen to the plasma mixture greatly accelerates the PS particle decomposition. Assuming a linear size reduction one finds a rate of ~ 60 nm/min for the pure Ar case, and about the fourfold for the Ar/O_2 mixture.

In Figure 4.3.3 a - c) SEM images illustrating the manipulation of an ordered colloidal mask are shown. In this case smaller particles of 180 nm diameter were used; the size reduction was at about the same rate as shown in case of the 1.1 µm particles. Figure 4.3.3 a) shows the close-packed colloidal monolayer before etching. In the overall

high quality layer, the common defects are seen, like some missing colloids which can be regarded as point defects, as well as dislocations that appear as cracks. Figure 4.3.3 b) shows a monolayer with the same initial particle size after etching for 60 sec. While the colloids keep their initial position accurately, they are reduced in diameter by roughly 30 nm. From the electron micrographs, no increase in polydispersity can be deduced. The particles appear now slightly oblate as seen in the side view. This anisotropic etching is due to the plasma, which predominantly attacks the upper surface of the almost close-packed monolayer.[23] No significant etching of the glass substrate takes place while a defined spacing between neighboring colloids is established. These two properties are required for the use of the etched colloidal layer as a shadow mask for crescent preparation.

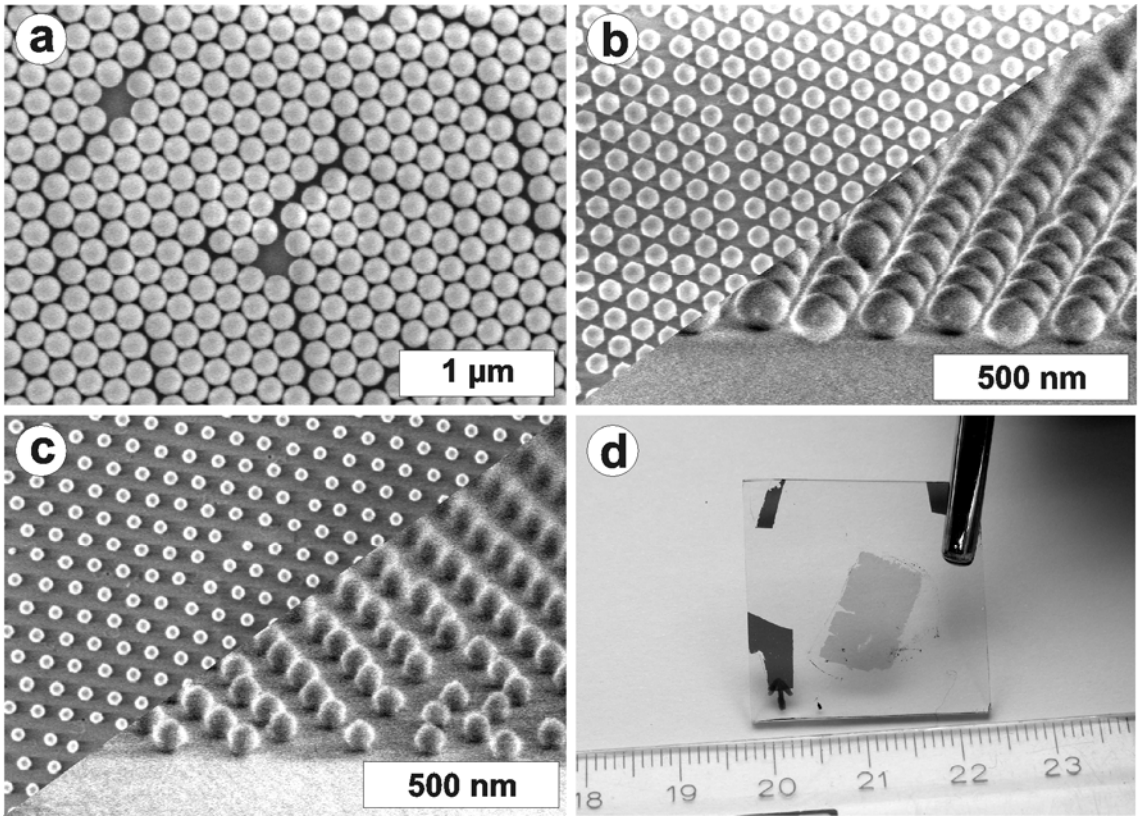

Figure 4.3.3. *Plasma etching of a colloidal monolayer of 180 nm spheres with 5 sccm Ar @ 190 W for different periods of time. a) Pristine close-packed monolayer of surface-attached colloids. b) After 60 sec, and after c) 90 sec etching. The top view is scaled identically to a). d) Photograph of as-prepared crescent layer, showing the size of the covered area.*

A mask with the same d_0 and longer plasma treatment (90 sec) is shown in Figure 4.3.3 c). The colloids have been reduced significantly ($d_{mask} < d_0/2$). They are still approximately spherical and thus remain suitable as masks. Figure 4.3.3 d) shows a photograph of a final as-prepared crescent layer on a macroscopic scale. It demonstrates that a homogenous coating of an area of the order of cm^2 is feasible. This size is not an intrinsic limitation of the process but represents a reasonable choice for handling under

standard laboratory conditions. In principle, upscaling to larger substrate areas is straightforward.

Using these structures as colloidal mask for the crescent fabrication, one obtains highly ordered and densely packed arrays of crescent nanoparticles (fabricated by Matthias Tamm). Such particles of various sizes and inter-particle spacing are shown in Figure 4.3.4.

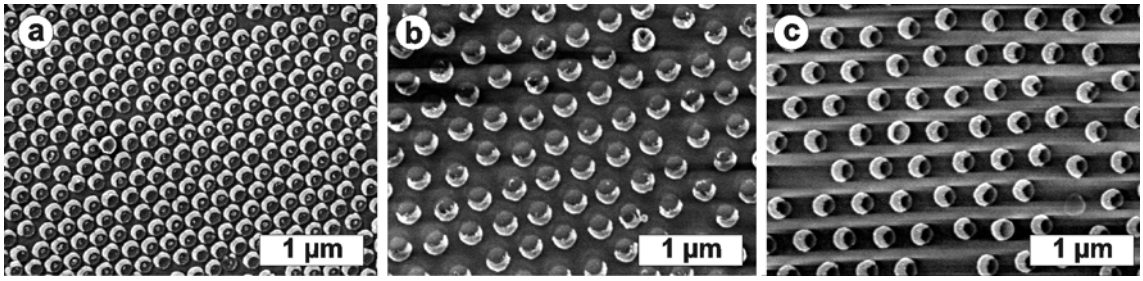

Figure 4.3.4. *Crescent monolayers obtained via colloid monolayers of various size d_0 and plasma etching conditions. a) Monolayer of d_0=180 nm etched with Ar:O_2 = 5:1 sccm @ 130 W for 30 sec, Θ = 30°. b) Monolayer of d_0 = 360 nm etched with a two step process: I) 5 sccm Ar @ 190 W for 1.5 min + II) Ar:O_2 = 5:1 @ 190 W for 1 min Θ = 30°. c) Monolayer of d_0=360 nm etched with Ar:O_2=5:1 @ 190 W for 1.5 min Θ = 40°.*

Crescent monolayers with very small distances between individual crescents as prepared by this technique are shown in Figure 4.3.4 a). Inter-particle distances of the order of 20 - 30 nm are achieved over a large area. Small deviations from the perfect crescent shape are seen where the shadow of a neighboring colloid prevents gold deposition. A sample with larger distances of about 100 nm between individual crescents is displayed in Figure 4.3.4 b). The size-reduced masks still lead to well-defined crescents. The sample shown in Figure 4.3.4 c) consists of crescents with large spacing. It furthermore demonstrates that gold evaporation at a higher angle (θ is increased from 30° to 40°) leads to different, thicker crescent shapes. The well-preserved size homogeneity of the masks yields an equally well-defined monodispersity of the resulting crescents. A detailed analysis of the electron micrographs shows a polydispersity below 5 %. Some angular variation of the crescent orientation of about $\Delta\alpha$ = 5-10° is seen. A limitation of this process is the lack of orientation of the crescent orientation relative to the lattice axis of the monolayer. The reason for that are the multiple single-crystalline domains, which are randomly distributed in the colloidal monolayer.

4.3.4. Stacking and twisting of crescent arrays

The next step towards a three-dimensional structure is the coating of the first particle layer. A silica layer which was prepared by a sol gel route served as a transparent, robust coating. Being chemically similar to the supporting glass, this material proves to be

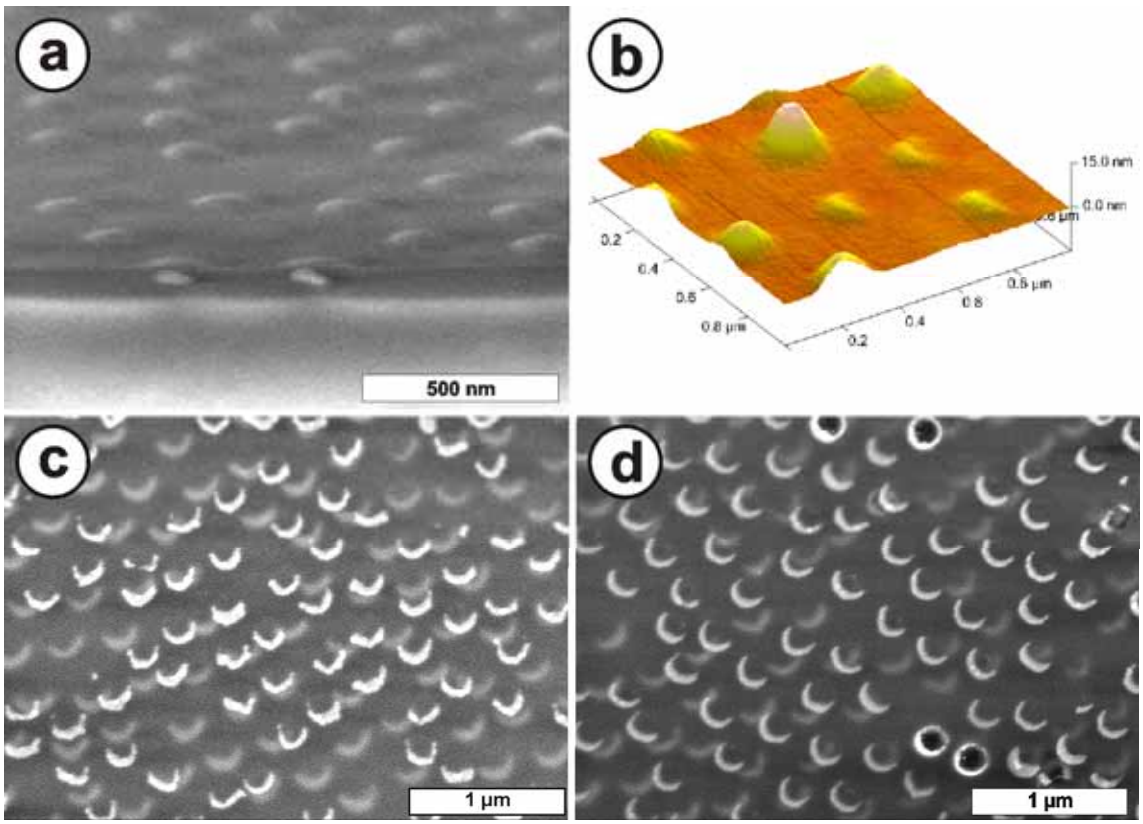

Figure 4.3.5. *a) SEM side view image after coating with the first SiO_2 layer. b) Topography of the sample shown in a) measured by AFM. c, d) SEM top view images of crescent double layers with different relative orientation (c: $\Delta\alpha = 0°$, d: $\Delta\alpha = 70°$). Both layers are covered with ~ 50 nm SiO_2.*

suitable for the deposition of a second layer, in terms of surface chemistry, mechanical hardness, and etch resistance. Figure 4.3.5 a) shows the first layer after coating.

The silica film has a thickness of approximately 50 nm. In order to provide a suitable substrate for the next crescent layer, the resulting surface should be as flat as possible. The surface topography as determined by atomic force microscopy is shown in Figure 4.3.5 b). Above the metal crescents some protrusions of the order of 5 nm are seen on the silica surface. This height variation is much smaller than the crescents which have a height of 30 nm. Figure 4.3.5 c, d) show scanning electron micrographs of crescent double layers, coated with a second silica layer, see schematics in Fig. 4.3.1 f). The crescents forming the bottom layer appear as faint features, in the top layer they are brighter. By variation of α for the two samples, identically oriented layers as shown in Figure 4.3.5 c) as well as other defined relative orientations of the constituents of the different layers can be achieved. In particular, the structure shown in Figure 4.3.5 d) has a defined chirality.

Finally the optical response of ordered crescent in distinct layers with a defined relative orientation among each other was measured. UV/Vis extinction spectra for three double layer samples with different $\Delta\alpha = \alpha_1 - \alpha_2$ are shown in Figure 4.3.6.

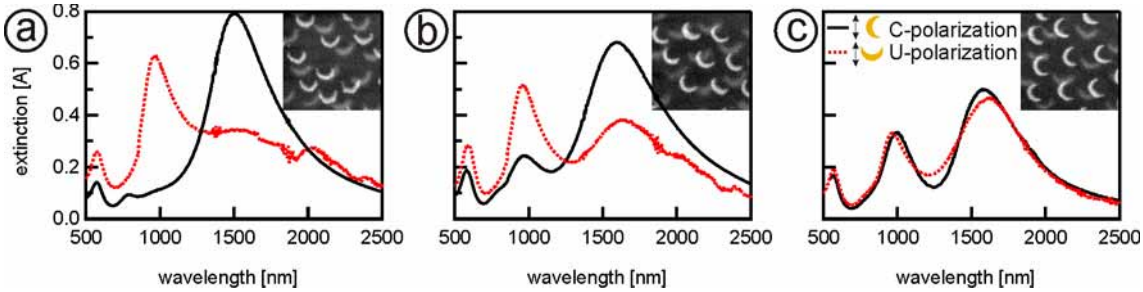

Figure 4.3.6. *Polarized extinction spectra of double layers of crescents with different relative orientation Δα (a) 0°, (b) 45°, (c) 70°. Electron micrographs of the samples are shown in the inset. For each sample, datasets corresponding to linear polarization of the incident light perpendicular (solid line) and parallel (dotted line) to the symmetry plane of the lower crescent layer are shown.*

In Figure 4.3.6 a) the orientation of the first and second layer are identical, compare Figure 4.3.5 c). A strong maximum around 1500 nm is observed for a polarization of the electrical field perpendicular to the vertical crescents symmetry plane (C-polarization).[15, 24] For the orthogonal (U-) polarization a maximum around 1000 nm is found. Apart from the significantly increased overall signal, no difference to dispersed, single layers of crescents is observed. The resonances are assigned to the fundamental and first harmonic standing wave along the crescents contour. They have been termed C1 and U1 resonance[15, 24] according to the polarization of their net electrical dipole moment. In Figure 4.3.6 b) the two layers show orientations with a relative angle of roughly $\Delta\alpha = 45°$. A U1 maximum appears upon excitation with a linear polarization corresponding to C-polarization for the first layer. This is expected since this polarization is neither pure U nor C for the second layer such that both resonances may be excited. Illumination with U polarization relative to the first layer shows a corresponding signature of a C1 resonance. The response for an almost perpendicular orientation of the two layers ($\Delta\alpha = 70°$) is shown in Figure 4.3.6 c). Each linear polarization corresponds to U or C excitation of one of the two layers, leading to an almost polarization independent optical response. This response of double layer arrangements corresponds to an addition of the effects of the two individual layers with equal optical response. At sufficient inter-crescent and inter-layer spacing, the spectral features are as sharp as for individual crescents, proving the high degree of control over crescent shape and orientation in a macroscopic process.

4.3.5. Conclusions and outlook

In summary, the fabrication of densely packed two-dimensional arrangements of crescent-shaped metal nanoparticles prepared by nanosphere lithography was shown. These layers can be embedded in a silica matrix, allowing for a repetition of the process to

fabricate three-dimensional arrangements of crescents with full control over the relative orientation between two layers. This versatile and parallel approach yields nanostructures with total sizes of some 100 nm and feature sizes in the range of 10 nm over macroscopic areas. The precise control of each part of this multiple step process yields crescents of equal size, which is mandatory to study their rich plasmonic features. The deposition and embedding of two separate layers of nanoparticles with large interparticle distances and different mutual angles, shows an additive response of the LSPR signal of each single layer.

Further developments of this method aim towards a control of the lattice orientation by macroscopic pre-structuring or epitaxial registry of neighboring layers, potentially exploiting the small residual protrusions after silica coating or the local field enhancement of the deposited crescents. Decreasing the interparticle distance, both in one plane (x, y direction) and to the next layer (z direction) could lead to interaction of the individual optical near fields, which could result in novel optical properties ultimately resulting in negative refractive index materials.

4.3.6. Experimental part

Fabrication of a mask of ordered colloids*:* Large area colloidal masks of evenly spaced polystyrene spheres were prepared by combining two procedures: the formation of a close packed colloidal monolayer on a flat glass substrate, and the controlled size reduction of the colloids by plasma etching. The method used here to fabricate a colloidal monolayer has been described in chapter 4.1.

Controlled size reduction: The surface-assembled colloids were placed in the centre of a tubular 13.56 MHz plasma reactor described elsewhere.[25] Etching of the particles was carried out by Matthias Tamm using mixtures of Ar:O_2 as well as pure Ar or O_2 at rf power settings between 130 W and 180 W. Typical gas flows were set between 1 and 5 sccm (standard cubic centimeters per minute). Precise etching parameters are specified for each sample.

Fabrication of the crescent shaped structures: 1 nm chromium and a 40 nm thick gold film were sequentially evaporated (*Auto 306, Edwards, Sussex UK*) on the colloidal template, with the samples being tilted relative to the metal source by $\theta = 30°$ unless otherwise specified.[15, 24] Then, they were etched by a normally incident argon ion beam (*RR-I SQ76, Roth & Rau, Wüstenbrand, Germany*). Finally, the colloidal mask was removed mechanically by applying an adhesive tape (*Scotch Magic Tape 810: 19mm × 33m, 3M France*) which was pulled off. A second ion-beam etching step was applied in order to remove residual sputtered material. Crescent fabrication was undertaken by Matthias Tamm and Noelia Bocchio.

Embedding of the layer: The crescent-covered substrate was rendered hydrophilic by plasma treatment (Ar:O_2 9:1, 200 W, 15 s). A 1:1:10 vol% tetraethyl orthosilicate (TEOS, Acros, 98%):1 M HCl:EtOH p.a. sol, was pre-hydrolyzed for 30 min and spin coated (3000 rpm, 60 s) on the first particle layer. The resulting sol gel layer was baked at 100 °C in air for one hour. Subsequently, the process for nanoparticle fabrication was repeated.

Characterization: SEM images were taken on a LEO Gemini 1530 machine with acceleration voltages ranging from 1 kV to 5 kV. AFM images were recorded by Uwe Rietzler on a Dimension 3100. Vis/NIR measurements were conducted by Natalie Horn.

4.3.7. Bibliography

1. Shelby, R. A.; Smith, D. R.; Schultz, S. *Science* **2001,** 292, (5514), 77-79.
2. Pendry, J. B. *Contemporary Physics* **2004,** 45, (3), 191-202.
3. Pendry, J. B. *Phys. Rev. Lett.* **2000,** 85, (18), 3966-3969.
4. Pendry, J. B.; Schurig, D.; Smith, D. R. *Science* **2006,** 312, (5781), 1780-1782.
5. Schurig, D.; Mock, J. J.; Justice, B. J.; Cummer, S. A.; Pendry, J. B.; Starr, A. F.; Smith, D. R. *Science* **2006,** 314, (5801), 977-980.
6. Liu, R.; Ji, C.; Mock, J. J.; Chin, J. Y.; Cui, T. J.; Smith, D. R. *Science* **2009,** 323, (5912), 366-369.
7. Linden, S.; Enkrich, C.; Wegener, M.; Zhou, J. F.; Koschny, T.; Soukoulis, C. M. *Science* **2004,** 306, (5700), 1351-1353.
8. Liu, N.; Guo, H. C.; Fu, L. W.; Kaiser, S.; Schweizer, H.; Giessen, H. *Nat. Ma ter.* **2008,** 7, (1), 31-37.
9. Valentine, J.; Zhang, S.; Zentgraf, T.; Ulin-Avila, E.; Genov, D. A.; Bartal, G.; Zhang, X. *Nature* **2008,** 455, (7211), 376-U32.
10. Fischer, U. C.; Zingsheim, H. P. *Journal Of Vacuum Science & Technology* **1981,** 19, (4), 881-885.
11. Deckman, H. W.; Dunsmuir, J. H. *Appl. Phys. Lett.* **1982,** 41, (4), 377-379.
12. Zhang, X. Y.; Whitney, A. V.; Zhao, J.; Hicks, E. M.; Van Duyne, R. P. *Journal Of Nanoscience And Nanotechnology* **2006,** 6, (7), 1920-1934.
13. Hanarp, P.; Kall, M.; Sutherland, D. S. *J. Phys. Chem. B* **2003,** 107, (24), 5768-5772.
14. Aizpurua, J.; Hanarp, P.; Sutherland, D. S.; Kall, M.; Bryant, G. W.; de Abajo, F. J. G. *Phys. Rev. Lett.* **2003,** 90, (5), 057401.
15. Shumaker-Parry, J. S.; Rochholz, H.; Kreiter, M. *Adv. Mater.* **2005,** 17, (17), 2131-2134.
16. Gwinner, M. C.; Koroknay, E.; Fu, L.; Patoka, P.; Kandulski, W.; Giersig, M.; Giessen, H. *Small* **2009,** 5, (3), 400-406.
17. Haginoya, C.; Ishibashi, M.; Koike, K. *Appl. Phys. Lett.* **1997,** 71, (20), 2934-2936.
18. Hanarp, P.; Sutherland, D. S.; Gold, J.; Kasemo, B. *Colloids Surf., A* **2003,** 214, (1-3), 23-36.
19. Zheng, Y. B.; Juluri, B. K.; Mao, X. L.; Walker, T. R.; Huang, T. J. *J. Appl. Phys.* **2008,** 103, (1), 014308.
20. Zhang, G.; Wang, D. Y.; Mohwald, H. *Nano Lett.* **2007,** 7, (1), 127-132.
21. Zhang, G.; Wang, D. Y.; Mohwald, H. *Nano Lett.* **2007,** 7, (11), 3410-3413.
22. Pendry, J. B. *Science* **2004,** 306, (5700), 1353-1355.
23. Tan, B. J. Y.; Sow, C. H.; Lim, K. Y.; Cheong, F. C.; Chong, G. L.; Wee, A. T. S.; Ong, C. K. *J. Phys. Chem. B* **2004,** 108, (48), 18575-18579.
24. Rochholz, H.; Bocchio, N.; Kreiter, M. *New J. Phys.* **2007,** 9, (53).
25. van Os, M. T.; Menges, B.; Foerch, R.; Vancso, G. J.; Knoll, W. *Chem. Mater.* **1999,** 11, (11), 3252-3257.

4.4. Laterally Patterned Ultraflat Surfaces for Reusable Surface Plasmon Sensors

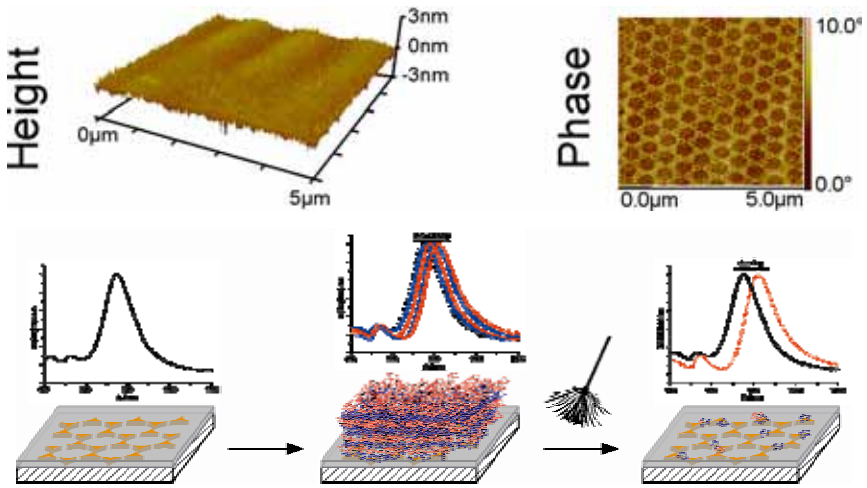

Laterally patterned, ultraflat surfaces are prepared by a modified template-stripping procedure. While the surfaces do not show any topographic features, the heterogeneous nature is revealed by an AFM phase contrast between gold and silicon dioxide areas. Straightforward assembly of patterned, multifunctional monolayers, paired with their inherent ultralow surface roughness, renders these surfaces attractive substrates for any monolayer-based devices. Due to the embedding of the plasmonic resonators, these materials can be employed as mechanically stable, reusable sensors.

4.4.1. Introduction

Novel devices in information technology, opto-electronics, or for sensing applications require complex architectures with small features. In principle, such devices combine conductive and insulating materials together with organic and inorganic layers to functional structures. The use of micro-engineered substrates together with the self-assembly of molecules or nanoscopic objects with tailored properties is a promising approach towards smart interfaces with nanoscale resolution. Self–assembled monolayers (SAMs) provide an elegant and flexible way to selectively functionalize surfaces and create desired surface properties, e.g. binding sites, chemical reactivity, and hydrophobic or hydrophilic character.

Extensive work has been reported on SAMs on gold or silicon substrates using thiol- or silane-chemistry, respectively.[1-6] For a self-assembled multi-functional coating, several challenges have to be addressed. First, the SAM needs to be dense and defect-free to guarantee reliable device performances. Second, the SAMs have to be patterned with nanometer precision to achieve a valuable surface functionalization with different chemical or physical behavior.

The formation of a SAM is known to be greatly influenced by surface roughness and surface chemistry of the underlying substrate.[7-11] While polished silicon wafers or mica are nearly atomically flat by nature, thermally evaporated gold surfaces are typically relatively rough (root mean square (RMS) roughness values above 1.0 nm). Gold substrates with a roughness in the sub-nanometer range can be obtained using a "template-stripping" procedure.[11-16]

The original template stripping process leads to homogeneous substrates, while certain applications require heterogeneously structured samples. This can be achieved by structuring the SAM itself. Various approaches have been proposed in literature including microcontact printing[17, 18] or lithographic patterning of photosensitive silane molecules.[19-21] Additionally, metal nanostructures can be used to intermediately block parts of the surface. After a first silanization step and removal of the metal structures, bifunctional monolayers can then be created by a second silanization step.[22, 23] However, if different parts of the substrates should be addressed individually, the substrate itself has to be structured.

Two examples of heterogeneously structured substrates using a template stripping procedure have been reported previously.[24, 25] First, mica was proposed as the template material.[24] A major drawback of this process is the lack of reliability to uncover large structured areas. The sheet-like structure of mica tends to break upon removal, thus

leaving parts of the surface covered with very thin films of the template material that are then not addressable for any further functionalization. In a second attempt, a sacrificial layer of carbon was introduced to reduce adhesion between template and evaporated structures, thus reducing the risk of incomplete separation.[25] However, several problems arise from this procedure, as thermally evaporated carbon does not show the flatness of mica or silicon wafers, and upon separation the substrate can not be directly used as carbon remains on its surface (which has to be removed in a separate cleaning step).

In this chapter a new method for the fabrication of laterally structured substrates based on nanopshere lithography (NSL) with an extremely low surface roughness will be discussed. The approach is versatile as it allows using a wide range of patterning materials. Macroscopic arrays comprising of nanoparticle features of only several tens of nanometers can be produced with great reliability by using colloidal monolayers as masks for successive Cr and Au evaporation. Additionally, no further cleaning steps are necessary and the substrates can be functionalized straightforward using self-assembly techniques.

Structuring surfaces in the nanometer range with noble metals gives raise to local surface plasmon resonators (LSPR), which can be used as sensors since their resonances sensitively depend on the dielectric environment. Among various methods NSL proved to be a particular simple method to fabricate metallic nanostructures on a solid substrate in a parallel fashion. Extended fundamental work has been focused on the detailed examination and tuning of the optical properties of particles produced by NSL and other methods.[26-28] Furthermore, their response to changes in refractive index of their direct environment upon binding events[29-31] has been investigated, and significant improvements towards low detection limits, high sensitivity, and spatial resolution in multiplexed assays have been made.[32]

However, a major drawback of conventional fabrication methods is the lack of stability.[33] Upon submersion in liquids like buffer solutions the nanostructures tend to get washed off the solid support. This decreases their sensitivity by time and also hampers their reusability. Some efforts have been undertaken in recent time to recover plasmonic sensors for repeated usage.[34, 35]

Besides the interest in using the ultraflat substrates presented here for membrane applications, they were also found to be extremely robust sensor platforms. Their sensing power will be demonstrated by layer-by-layer self-assembly of polyelectrolytes as a model system. The high stability of these embedded nanostructures will be investigated and their reusability without loss of sensitivity will be shown.

4.4.2. Fabrication of ultraflat, nanostructured surfaces

For the fabrication of structured substrates, the template-stripping process as described by Hegner has been modified by Nicolas Vogel and Mathieu Jung (Figure 4.4.1). A silicon wafer was chosen as template material, being as flat as mica but without the typical terrace-like defects arising from its sheet-like structure. Passivation of the silicon surface with an inert alkylsiloxane monolayer was necessary to successfully cleave the nanostructured array. After transfer of a colloidal monolayer onto the passivated silicon wafer (a), gold and chromium were successively evaporated through the mask (b). The colloidal particles were then carefully removed (c) and a layer of silicon dioxide was evaporated over the gold-chromium structures and in the holes formerly protected by the colloids (d). Finally, the prepared films were glued onto a glass substrate, cured, and mechanically stripped (e) to reveal the laterally structured, ultraflat surface (f).

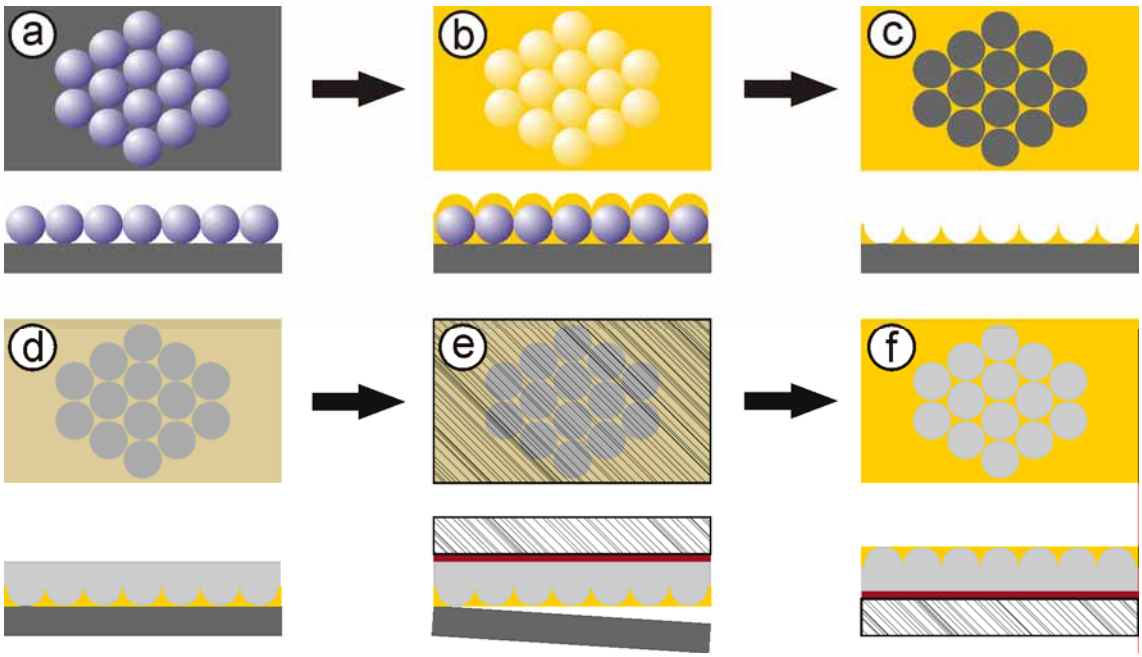

Figure 4.4.1. *Top view and side view images of the ultraflat substrate preparation process. a) Transfer of a colloidal monolayer onto a passivated silicon wafer. b) Evaporation of gold and chromium through the mask. c) Removal of the colloidal template. d) Evaporation of SiO_2 over the metallic nanoparticles. e) Gluing of a glass substrate on top of the SiO_2 covering layer via an epoxy resin. f) Ultraflat, nanostructured surface after mechanical cleavage of the silicon wafer.*

Successful rupture in the predetermined plane was achieved with hexamethyldisilazane (HDMS) modified silicon-wafer templates. Their water contact angle was low enough to use the transfer method on hydrophilic substrates for colloidal monolayer deposition, as outlined in chapter 4.1.

In order to monitor the substrate topography, freshly cleaved surfaces were characterized by tapping mode AFM and SEM (Figure 4.4.2). The AFM height image (Fig-

ure 4.4.2 a) underlines the smoothness of the surface while the phase image (Figure 4.4.2 b) reveals the heterogeneity of the patterned substrate. At a z-scale of 3 nm in the height image no surface topography is apparent. The complete absence of topographic features proves a smooth transition between the gold structures and silicon dioxide matrix without signs of rupture, defects or irregularities at the surface. The contrast in the phase image is produced by the different hardness of silicon dioxide and gold. A similar picture is obtained by the SEM measurement, in which the contrast is given by the different electron scattering efficiency of SiO_2 and gold.

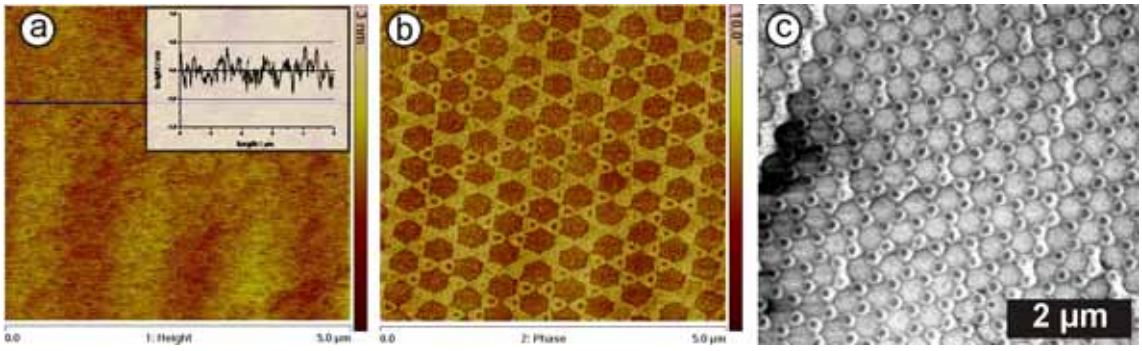

Figure 4.4.2. *a) AFM height image of the smooth surface of gold triangles produced by a mask of 550 nm PS particles embedded in a SiO_2 matrix. The inset shows the line scan along the black line. b) The gold triangles can be clearly seen in the phase image. c) SEM measurement of a sample, prepared by 550 nm PS particles as mask. The gold triangles appear brighter.*

A root means square (RMS) surface roughness of 2 Å was measured. The linescan analysis (Figure 4.4.2 a, inset) only shows fluctuations of the surface topography in the sub-nanometer range. The peak to valley distance over the complete linescan is determined to be 0.8 nm and underlines the extraordinary smoothness with a maximal difference of only few atomic layers on a length scale of 5 µm.

This method is not only restricted to the material combination Au/SiO_2; also Au/ITO materials have been fabricated accordingly (however, not using colloidal monolayers as mask, but single µm-sized particles).[36]

4.4.3. Selective functionalization of patterned surfaces

Independent surface functionalization of the nanopatterned structure was demonstrated by selective monolayer formation of hexadecanethiol. AFM images after incubation of the freshly cleaved substrate in a hexadecanethiol solution are shown in Figure 4.4.3.

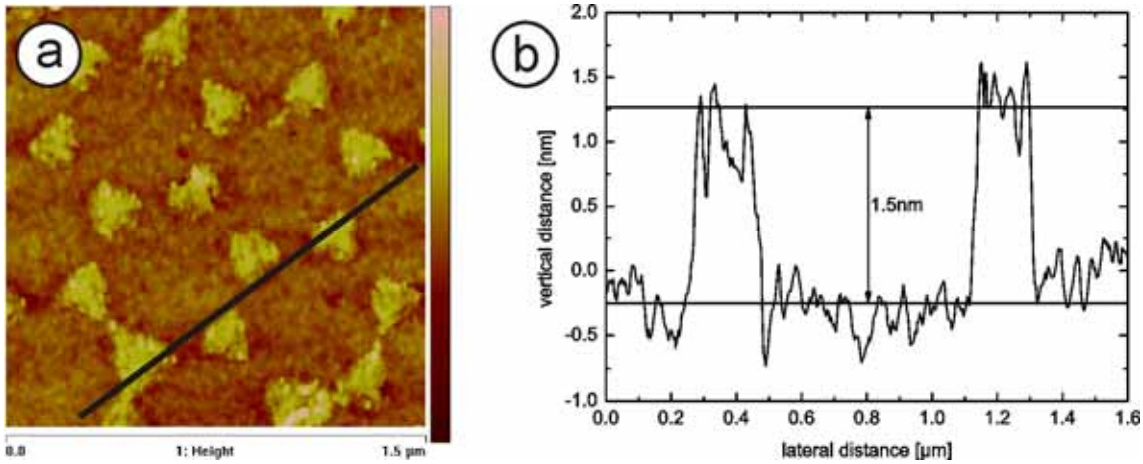

Figure 4.4.3. *a) AFM height image of gold nanotriangles with a SAM of hexadecanethiol. b) Linescan along the black line indicated in a), showing the selective formation of a monolayer on the gold parts.*

The nanotriangles of about 140 nm side-length are selectively covered with the thiol monolayer. The SiO_2 matrix was left unaffected by the thiol. The height of the monolayer was determined by the cross-section (Figure 4.4.3 b) to be 1.5 nm. This height matches with the theoretical value for an all-trans conformation tilted by 30° with respect to the surface normal, the typical conformation of alkane monolayers.[5, 7, 9] Furthermore, the lateral distance between plain surface and the monolayer plateau, known as line edge roughness, was deduced. The value averaged over the four edges present in the linescan was calculated to be 43 nm. Taking into account the artificial enlargement of the edge due to tip convolution (tip diameter 10 nm as specified by the manufacturer), the resolution for monolayer patterning by this method extends to only several tens of nanometers, a value that greatly exceeds the diffraction limits of light as the maximal resolution for conventional lithography.

4.4.4. Embedded nanostructures as reusable sensing platform

Gold nanotriangles of a few 100 nm in size show LSPR signals in the visible (Vis) and near infrared (NIR) range. The stability of the embedded particle arrays in aqueous environments has been investigated by immersion of the substrates in PBS buffer solution under a constant flow rate of 1.5 ml/min. The samples were studied at several time intervals upon exposure to the buffer via Vis/NIR spectroscopy. In order to evaluate the resistance of the surface embedded particles to the buffer environment, the extinction of the LSPR in each case was divided by the original value ($I_{0,\,LSPR}$) of the sample before exposure to liquid. For comparison, two samples of conventionally produced nanoparticles (one being pure Au, the other having Cr as an adhesive interlayer) were exposed to similar conditions. Figure 4.4.4 presents the result of the stability test. Conventionally produced particles on a glass substrate showed a strong decay in signal intensity; after

20 hours of immersion, the extinction decreased to 7.5 % of its original value (dashed lines in Figure 4.4.4 a). The use of chromium (Cr) as an adhesive interlayer significantly increases the stability of conventionally produced nanoparticles. Their signal intensity drops to only ~85 % after 115 h rinsing (open circles in Figure 4.4.4 b). The embedded particles however, did not show any loss in signal intensity even after 5 days of incubation (open squares in Figure 4.4.4 b).

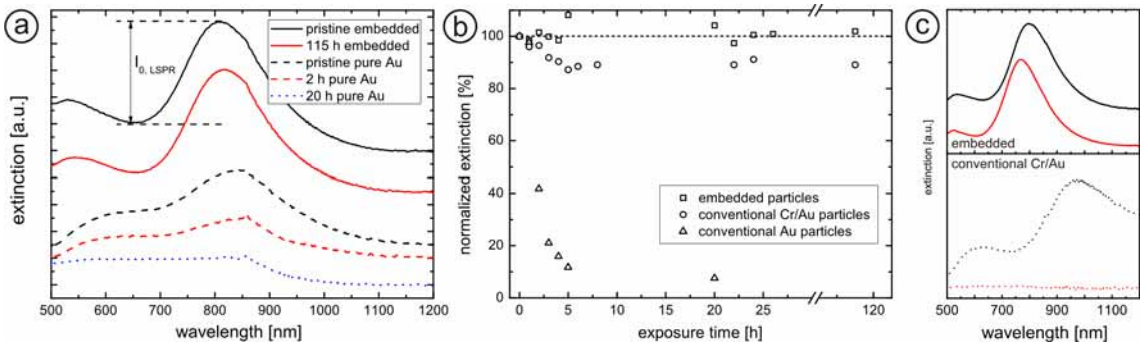

Figure 4.4.4. *a) Vis/NIR spectra of embedded gold nanoparticles (solid lines) and conventional gold triangles on glass (dashed lines) for various exposure times to PBS buffer. b) Normalized LSPR peak height of embedded (open squares), conventional Cr/Au (open circles), and conventional Au (open triangles) nanotriangles during exposure to a PBS buffer solution. c) Effect of mechanical wiping (red lines) on the LSPR signal of embedded (solid lines) and conventional Cr/Au (dotted lines) nanotriangles.*

A major difference between conventionally produced particles (with Cr interlayer) and embedded structures was found upon mechanically cleaning the substrates. For this purpose a tissue soaked in water was gently wiped over the substrate surface. Whereas the embedded particles did not show any drop in the LSPR signal intensity, no absorption could be detected any more in case of the conventional particles (Figure 4.4.4 c) indicating a complete loss of the nanoparticles on the surface. This stresses the superior stability of embedded nanoparticles compared to conventional ones. The blue shift of the plasmon absorption of the embedded nanoparticles after wiping will be addressed later.

In order to probe the sensitivity of embedded particles to thin dielectric films, a layer-by-layer (LBL) deposition[37] of polyelectrolytes has been applied to an array produced by using a monolayer of 550 nm polystyrene colloids as mask. In order to functionalize the surface, the samples were immersed for 90 minutes in an aqueous cysteamine hydrochloride solution. Afterwards, layers of negatively (polystyrene sulfonate *PSS*) and positively (polyallylamine hydrochloride, *PAH*) charged polyelectrolytes were deposited and Vis/NIR spectra were recorded. The typical plasmonic resonances were observed and a red shift of the extinction maximum was induced upon increasing thickness of the deposited polyelectrolyte layers. The Vis/NIR spectra for the native sample and two, four, six, and eight adsorbed double layers are shown in Figure 4.4.5 a.

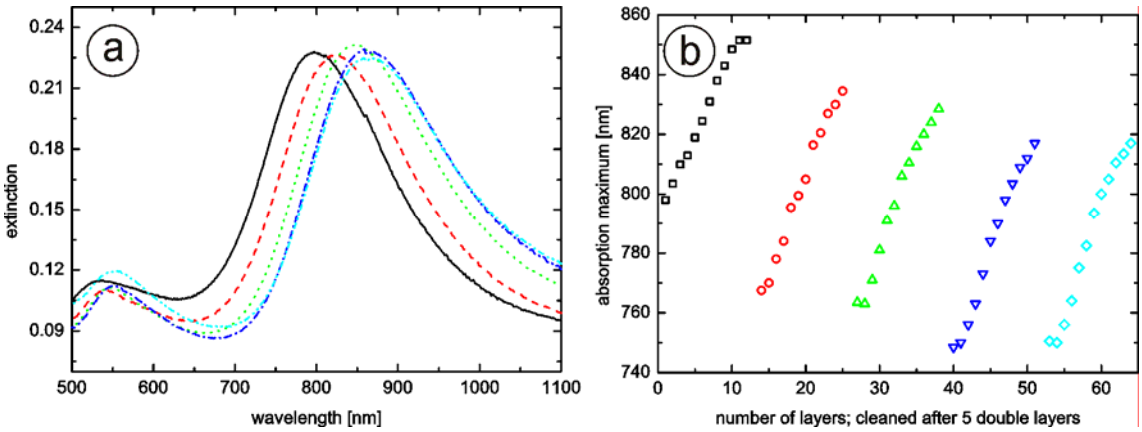

Figure 4.4.5. *a) Red-shift of the LSPR peak position upon addition of PE layers on top of the surface. Results are shown for the native substrate (solid line), and two (dashed line), four (dotted line), six (dash-dotted line), and eight (dash-double dotted line) double layers. b) Repeated LBL formation on the substrate, followed by cleaning of the surface; five cycles of five double layer depositions are shown.*

The plasmon peak shifts linearly with increasing layer deposition and reaches a saturation plateau after about six double layer depositions, which correlates to a thickness of roughly 50 nm.[28] The saturation regime can be deduced from Figure 4.4.5 a, where the spectra of six and eight double layers coincide. A shift of ca. 5 nm per deposited layer and a maximum peak displacement of 6 nm were measured, which agrees with plasmon shifts of conventional particles already reported.[31] The reusability was examined by five cycles of deposition and cleaning (Figure 4.4.5 b). Cleaning was undertaken by repeatedly wiping the substrate with a tissue soaked in EtOH and water. Only in the first cycle (open squares) the formation of the cysteamine SAM can be seen by a LSPR shift, while no shift is detected for the other cycles. Thus, one has to assume that this SAM is not completely removed from the surface during the mild cleaning with a tissue soaked in ethanol and water. All five cycles show the characteristic red shift with a peak displacement of about 65 nm, indicating the preservation of sensitivity. Deposition cycles four and five were done after storing the substrate for four months at lab conditions. The striking difference between the individual measurement cycles is the blue shift of the plasmon resonance after cleaning, which is especially pronounced after the first cleaning step and then decreases until reaching stable values after the fourth cleaning cycle. The origin of this shift is not yet completely clear. Probably two factors are responsible for it. First, changes in the silicone dioxide layer can cause this shift as the sample is prepared with a thermal evaporation process of silicone dioxide leading to poor bonding coordination.[38, 39] Traces of the silicon monoxide precursor or silicone dioxide crystallites that are not fully connected to the matrix might be washed out during the cleaning processes and hence, decrease the refractive index of the matrix material, which in turn leads to a blue-shift of the plasmon resonances. The saturation of the shift to a stable

wavelength of 750 nm for the plain nanoparticles after three cleaning cycles support this model as after several washing steps, all debris in the matrix is removed and no further changes lead to a stable extinction maximum. Second, solvent annealing, known to be able to cause blueshifts in the resonances,[29] is at least partly responsible for the shift detected in the first measurement cycles. To investigate such annealing effects, pristine samples were incubated for one hour in the polyelectrolyte buffer solutions in absence of the polyelectrolyte. Incubation into the negative polyelectrolyte buffer led to a blue-shift in the resonances of about 30 nm, while the positive polyelectrolyte solution did not further alter the resonances. Immersion of a pristine sample in ethanol induced a minor blueshift of about 5 nm after one hour of incubation. No further changes in the resonances were detected after 23 hours of incubation time.

Hence, apart from an initial blueshift of the particles' resonances Vis/NIR characterisation of the plasmonic resonances confirmed that the embedded nanoparticle arrays can be reused multiple times without any changes in signal intensity or sensitivity.

4.4.5. Conclusion and outlook

A novel platform of ultraflat, highly stable nanostructured surfaces and their suitability to sensing applications was demonstrated.

Ultraflat substrates were produced by a modified template stripping method, which at first created the desired pattern on a passivated silicon wafer. Due to the passivation it was possible to mechanically cleave the wafer without any residues on the substrate, yielding the pristine sample. The advantages of this procedure are fourfold: i) Once prepared, the template-protected substrates can be stored for months and stripped free just before usage, thus providing a clean surface whenever needed. ii) The patterning of the substrate material itself allows the selective and independent assembly of functional monolayers, e.g. on the gold- or silicon dioxide regions without affecting each other. iii) The template stripping procedure leads to very flat surfaces with an RMS-roughness below 3 Å and without any gaps or steps between both evaporated materials. iv) Embedding of the metallic nanostructures into a solid matrix greatly increases their stability towards buffer solutions. Therefore they can be repeatedly used for sensing applications exploiting their plasmonic resonances.

The last point was elucidated by several cycles of polyelectrolyte LBL deposition and cleaning, without loss of device sensitivity or signal intensity.

Future challenges are the exploration and designed fabrication of further material combinations. The nanoparticle shape is not limited to triangles, but the whole range of NSL

can be employed to create the desired shape, as long as the passivated wafer remains unaffected. For the use of electrochemical experiments the fabrication of electrically conducting nanoelectrodes would be appealing. Concomitant, conducting samples could further facilitate the pristine sample recovery by electro-desorption of thiols and therefore improve their sensor performance.

4.4.6. Experimental part

Hexamethyldisilazane was purchased from ABCR Speciality Chemicals (Karlsruhe, Germany) and used without further purification. Pre-cut silicon wafers were obtained from CrysTec Kristalltechnologie (Berlin, Germany). Gold, chromium and silicon monoxide were purchased from Balzers AG (Balzers, Liechtenstein). The epoxy glue used was the two components EPO-TEK 353ND4 (Epoxy Technologies, Billerica, USA).
Colloidal monolayers were prepared as outlined in chapter 4.1. All solvents were HPLC grade and used as received. Sample preparation and characterization was carried out by Nicolas Vogel and Mathieu Jung.
Silanization. For the silanization reactions, a procedure from Jonas[40] was adapted. To passivate the template, the silicon wafer was carefully cleaned and activated by ultrasonication for 10 min in ethanol followed by treatment with a 5:1:1 water : 25 % ammonia solution : 33 % hydrogen peroxide mixture for 45 minutes at 80 °C. Afterwards, the wafer was carefully washed with ultrapure water (milli-Q, Millipore, Molsheim, France) and ethanol and stored in ethanol until silanization. Embedded SiO_x parts of the surface were activated using a mild plasma treatment with a gas mixture of argon and oxygen (0.9 and 0.1 mbar partial pressure respectively) for 2 min at 200 W prior to silanization.
The HMDS reaction was conducted in gas phase at room temperature with ambient pressure. Incubation time was 30 min.
Evaporation. All evaporations were carried out in a Balzers PLS500 evaporation chamber with a Pfeiffer vacuum pump. The pressure in the evaporation chamber was always below $5*10^{-6}$ mbar before start of the evaporation process. Gold and chromium were evaporated at a rate of approx. 0.02 nm/s, silicon monoxide was evaporated at a rate of approx. 0.1 nm/s with an oxygen partial pressure of $1*10^{-4}$ mbar.
Gluing was performed as suggested by the manufacturer. The two component glue was cured at 150 °C for 60 min. Before gluing, all glass slides were cleaned by consecutive ultrasonic treatment in 2 % Hellmanex solution, milli-Q water and ethanol.
The template-stripping step was performed by carefully scratching on the edges of the silicon wafer glued to the glass slide with a scalpel until the wafer could be lifted off the substrate.
Layer-by-layer deposition. The initial cysteamine monolayer was assembled by immersion of the substrate in a 2 mg/ml solution of the thiol (cysteamine hydrochloride, Sigma Aldrich, Seelze, Germany) in ultrapure water.
Subsequent layer-by-layer deposition was performed by immersion for 20 min in solutions of positively- and negatively charged polyelectrolytes. The solution contained the following substances. Positively charged polyelectrolyte: 50 ml ultra pure water (milli-Q, milli-Pore, Moslheim, France), 0,0935 g polyallylamine hydrochloride (PA, M_W = 15000 g/mol, Sigma Aldrich, Seelze, Germany), 10,29 g NaBr (Sigma Aldrich, Seelze, Germany), 0.5 ml HCl (0.1 mol/l; Sigma Aldrich, Seelze, Germany). Negatively charged polyelectrolyte: 50 ml ultra pure water (milli-Q, milli-Pore, Moslheim, France), 0,2070 g sodium polystyrene sulfonate, (PSS, M_W = 70000 g/mol, Sigma Aldrich,

Seelze, Germany), 4.049 g MnCl2 (Sigma Aldrich, Seelze, Germany), 0.5 ml HCl (0.1 mol/l; Sigma Aldrich, Seelze, Germany).

4.4.7. Bibliography

1. Sagiv, J. *J. Am. Chem. Soc.* **1980,** 102, (1), 92-98.
2. Ulman, A. *Chem. Rev.* **1996,** 96, (4), 1533-1554.
3. Nuzzo, R. G.; Allara, D. L. *J. Am. Chem. Soc.* **1983,** 105, (13), 4481-4483.
4. Bain, C. D.; Whitesides, G. M. *Angewandte Chemie-International Edition in English* **1989,** 28, (4), 506-512.
5. Nuzzo, R. G.; Dubois, L. H.; Allara, D. L. *J. Am. Chem. Soc.* **1990,** 112, (2), 558-569.
6. Delamarche, E.; Michel, B.; Biebuyck, H. A.; Gerber, C. *Adv. Mater.* **1996,** 8, (9), 719-729.
7. Bryant, M. A.; Pemberton, J. E. *J. Am. Chem. Soc.* **1991,** 113, (22), 8284-8293.
8. Lee, M. T.; Hsueh, C. C.; Freund, M. S.; Ferguson, G. S. *Langmuir* **1998,** 14, (22), 6419-6423.
9. Naumann, R.; Schiller, S. M.; Giess, F.; Grohe, B.; Hartman, K. B.; Karcher, I.; Koper, I.; Lubben, J.; Vasilev, K.; Knoll, W. *Langmuir* **2003,** 19, (13), 5435-5443.
10. Losic, D.; Shapter, J. G.; Gooding, J. J. *Langmuir* **2001,** 17, (11), 3307-3316.
11. Gupta, P.; Loos, K.; Korniakov, A.; Spagnoli, C.; Cowman, M.; Ulman, A. *An gewandte Chemie-International Edition* **2004,** 43, (4), 520-523.
12. Butt, H. J.; Wang, D. N.; Hansma, P. K.; Kuhlbrandt, W. *Ultramicroscopy* **1991,** 36, (4), 307-318.
13. Butt, H. J.; Muller, T.; Gross, H. *Journal of Structural Biology* **1993,** 110, (2), 127-132.
14. Hegner, M.; Wagner, P.; Semenza, G. *Surf. Sci.* **1993,** 291, (1-2), 39-46.
15. Wagner, P.; Hegner, M.; Guntherodt, H. J.; Semenza, G. *Langmuir* **1995,** 11, (10), 3867-3875.
16. Stamou, D.; Gourdon, D.; Liley, M.; Burnham, N. A.; Kulik, A.; Vogel, H.; Duschl, C. *Langmuir* **1997,** 13, (9), 2425-2428.
17. Kumar, A.; Whitesides, G. M. *Appl. Phys. Lett.* **1993,** 63, (14), 2002-2004.
18. Wilbur, J. L.; Kumar, A.; Kim, E.; Whitesides, G. M. *Adv. Mater.* **1994,** 6, (7-8), 600-604.
19. Jonas, U.; del Campo, A.; Krüger, C.; Glasser, G.; Boos, D. *P Natl Acad Sci USA* **2002,** 99, (8), 5034-5039.
20. del Campo, A.; Boos, D.; Spiess, H. W.; Jonas, U. *Angewandte Chemie- Inter national Edition* **2005,** 44, (30), 4707-4712.
21. Alvarez, M.; Best, A.; Pradhan-Kadam, S.; Koynov, K.; Jonas, U.; Kreiter, M. *Adv. Mater.* **2008,** 20, (23), 4563-4567.
22. Herzer, N.; Hoeppener, S.; Schubert, U. S.; Fuchs, H.; Fischer, U. C. *Adv. Ma ter.* **2008,** 20, (2), 346-351.
23. Gotesman, G.; Naaman, R. *Langmuir* **2008,** 24, (12), 5981-5983.
24. Frey, W.; Woods, C. K.; Chilkoti, A. *Adv. Mater.* **2000,** 12, (20), 1515-1519.
25. Jung, B.; Frey, W. *Nanotechnology* **2008,** 19, (14), 145303.
26. Murray, W. A.; Barnes, W. L. *Adv. Mater.* **2007,** 19, (22), 3771-3782.
27. Jensen, T. R.; Duval, M. L.; Kelly, K. L.; Lazarides, A. A.; Schatz, G. C.; Van Duyne, R. P. *J. Phys. Chem. B* **1999,** 103, (45), 9846-9853.
28. Bocchio, N. L.; Unger, A.; Alvarez, M.; Kreiter, M. *J. Phys. Chem. C* **2008,** 112, (37), 14355-14359.
29. Haes, A. J.; Van Duyne, R. P. *J. Am. Chem. Soc.* **2002,** 124, (35), 10596-10604.

30. Haes, A. J.; Zou, S. L.; Schatz, G. C.; Van Duyne, R. P. *J. Phys. Chem. B* **2004,** 108, (22), 6961-6968.
31. Haes, A. J.; Zou, S. L.; Schatz, G. C.; Van Duyne, R. P. *J. Phys. Chem. B* **2004,** 108, (1), 109-116.
32. Anker, J. N.; Hall, W. P.; Lyandres, O.; Shah, N. C.; Zhao, J.; Van Duyne, R. P. *Nat. Mater.* **2008,** 7, (6), 442-453.
33. Rindzevicius, T.; Alaverdyan, Y.; Kall, M.; Murray, W. A.; Barnes, W. L. *J. Phys. Chem. C* **2007,** 111, (32), 11806-11810.
34. Riboh, J. C.; Haes, A. J.; McFarland, A. D.; Yonzon, C. R.; Van Duyne, R. P. *J. Phys. Chem. B* **2003,** 107, (8), 1772-1780.
35. Sato, A.; Menges, B.; Knoll, W. *J. Appl. Phys.* **2009,** 105, (1), 014701.
36. Vogel, N.; Jung, M.; Retsch, M.; Jonas, U.; Knoll, W.; Köper, I. *Small* **2009,** http://dx.doi.org/10.1002/smll.200801583.
37. Decher, G. *Science (Washington, D. C.)* **1997,** 277, (5330), 1232-1237.
38. Aikawa, K.; Sakata, H.; Furuuchi, S. *Journal of Materials Science* **1978,** 13, (1), 37-42.
39. Soh, M. T. K.; Savvides, N.; Martin, P. J.; Musca, C. A. *Thin Solid Films* **2006,** 515, (4), 2284-2290.
40. Jonas, U.; Krüger, C. *J. Supramolecular Chemistry* **2002,** 2, (1-3), 255-270.

4.5. Composite Inverse Opals in Inverse Opals

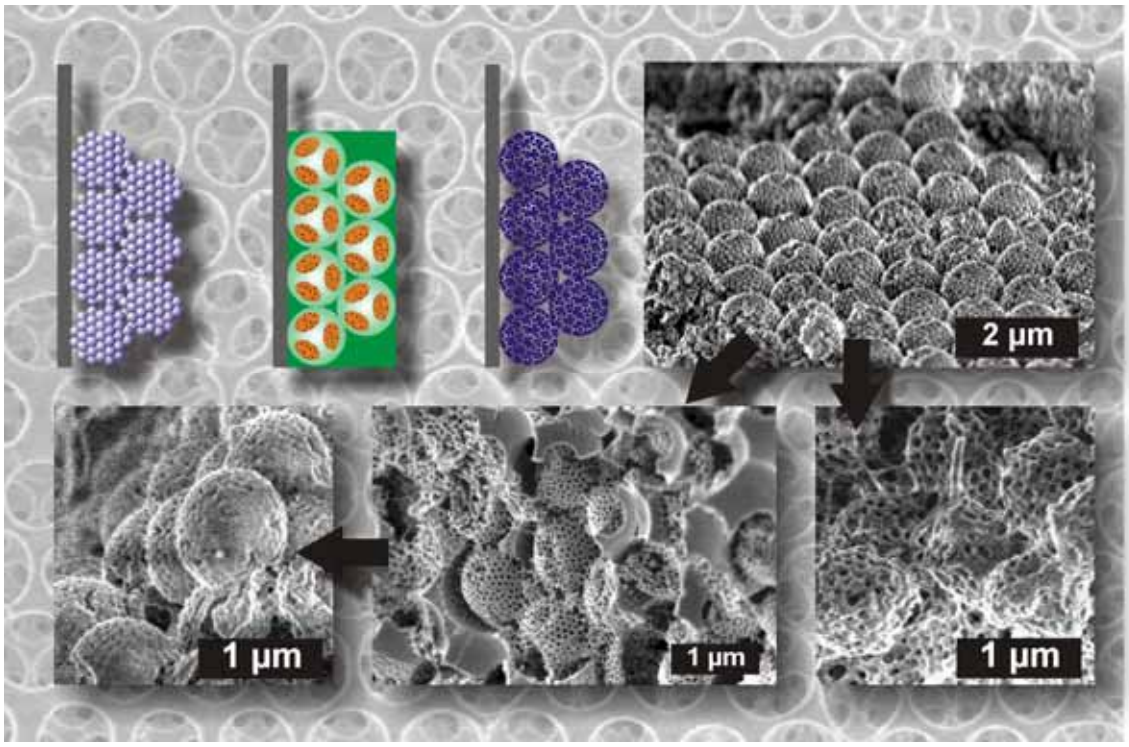

A methodology is introduced to fabricate hierarchically structured, interpenetrating inverse opal networks on the length scales of micrometer and 100 nm. Multiple infiltrations of template substrates with metal oxide nanoparticles and polystyrene or silica colloids were used. The stepwise construction of an inverse opal in an inverse opal host allows the combination of various materials, such as SiO_2, TiO_2, or Al_2O_3. Finally, the complex hierarchical material can be inverted to its polymer replica. The materials introduced here might prove useful for advanced storage-, filtering-, or sensing applications.

4.5.1. Introduction

Porous materials can be classified into materials, which consist of microporous (below 2 nm), mesoporous (2 – 50 nm) and macroporous (larger than 50 nm) channels and voids. Networks, which comprise various classes of pores with characteristically different dimensions, are termed "hierarchical". By introducing a hierarchy of interconnected cavities at different length scales, the surface-to-volume ratio can be dramatically increased and the materials properties accordingly tailored. Furthermore, in such complex pore hierarchies the transport phenomena of penetrating liquid or gaseous media, as well as the diffusion of dispersed species is fundamentally altered compared to uniform pore architectures. The controlled synthesis of hierarchically ordered porous materials is highly desirable and has attracted a lot of attention during the last decade. The search for such synthesis strategies is motivated by the superior material properties, which are the basis for a large range of possible applications, like catalysis, sensing, selective filtering, chromatography, or as wave guides and photonic crystals with a tuneable band gap. For the purpose of catalysis and sensing, an efficient mass transport can be provided by interconnected macropores that allow large molecules like proteins to efficiently diffuse to the reaction- or detection sites, which are commonly located in the meso- and micropores of such hierarchical materials. Due to this pore hierarchy these materials possess a very large surface area and can thus expose maximal amounts of catalysts or receptors to the penetrating medium. The fabrication of hierarchically porous materials has been covered by several reviews.[1-5]

The practical synthesis of hierarchical networks can be achieved in various ways: quite commonly, colloid particles are used for templating the macropores, while meso- and micropores can be introduced by phase separation of block copolymers[6] or surfactants.[7]

The combination of colloidal templating and phase separation represents a bottom up approach to hierarchical materials. Also top down techniques were demonstrated, which introduce material shaping from macroscopic dimensions down to the µm scale. This was demonstrated by deposition within confined space,[6, 8, 9] plotting of discrete drops,[10] or by post-modification of a homogenous crystal.[11-13]

Whereas a lot of work has been devoted to the combination of macro-, meso-, and micropores, only little work has been devoted to the combination of various macropores in one material. As Wang *et al.* showed, the tetrahedral voids of a colloidal crystal can be filled with smaller particles in a single vertical deposition step, which resulted in a porous interconnected network after replication.[14, 15] The aim of the work presented here is to close the gap between structuring macroporous materials either with micropores or

on a µm scale. An inverse opal comprising of µm sized voids will therefore be filled with colloids, which are one order of magnitude smaller. This two-step process allows the combination of various materials and one can expect novel material properties deriving from material choice and structural hierarchy. One could expect the existence of a double photonic band gap and the precise tuning of materials and pores could make these structures attractive for sensing, sieving, or storage applications. (At this stage no UV/Vis data will be shown, since the expected Bragg peaks for inverse silica opals of the sizes under consideration (> 1000 nm and < 100 nm) are out of the range (> 2000 nm and < 200 nm) of the available spectrometers).

4.5.2. Inverse opal in inverse opal fabrication by multiple vertical lifting deposition

The methodology of inverse opal in inverse opal (IOIO) fabrication is outlined below in Figure 4.5.1.

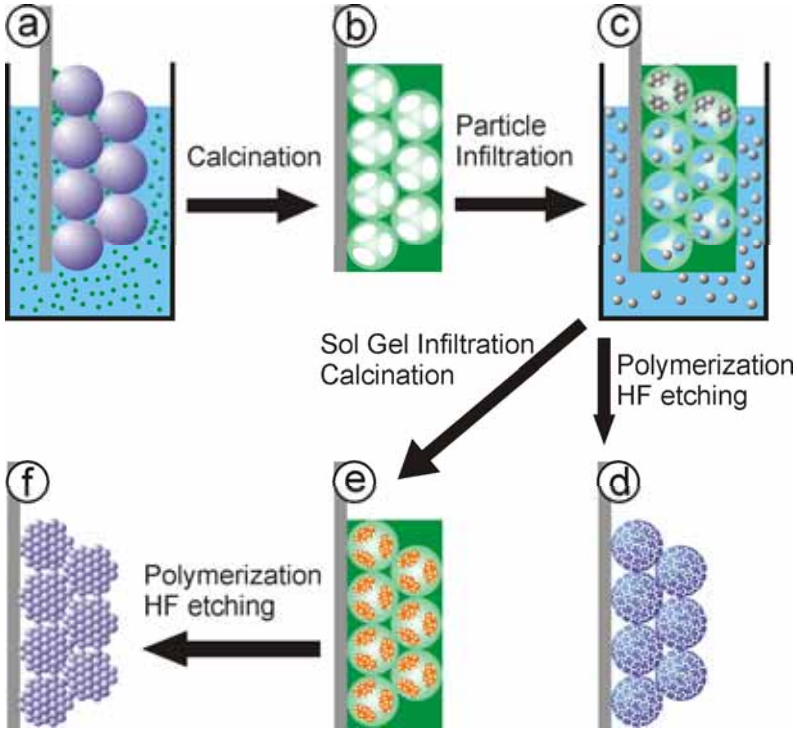

Figure 4.5.1. *a) An annealed colloidal crystal template is infiltrated with metal oxide nanoparticles. b) After calcination an inverse opal with large pores is obtained. c) The free voids can be filled with smaller PS or SiO_2 colloids. d) In case of a silica host matrix and silica colloidal particles, one can directly obtain hierarchically structured polymer particles by photopolymerization and silica removal. e) Sol gel infiltration and calcination leads to an inverse opal in an inverse opal (IOIO) comprising of composite materials. f) The IOIO can be inverted again to give 3D structured, raspberry-like particles. Dark blue represents polymer, green and orange symbolize metal oxides.*

A colloidal crystal constituting of large PS particles was chosen as template structure. The possibility to increase the interconnecting area between adjacent particles allows tailoring of the pore size in the inverse structure, which is important for further particle

deposition. Infiltration with metal oxide nanoparticles similar to Gu *et al.*[16] was chosen, as this approach leads to a minimum shrinkage during calcination (Figure 4.5.1 a and b). Furthermore, this is a very versatile approach, since in principal any metal oxide nanoparticle or metal oxide mixture should be applicable to this infiltration. In a second vertical lifting step another colloidal crystal consisting of smaller colloidal particles is deposited in the free voids of the host matrix, c). One can fabricate colloidal crystals of both, polymer and silica particles inside the first inverse opal. Depending on the material combination chosen, one can either infiltrate the composite material with monomer and ensuing polymerization, or with a sol gel of another metal oxide precursor. This leads either to mesoporous, interconnected polymer particles (Figure 4.5.1 d) or to an inverse-opal-in-inverse-opal. Since this replica is additionally shaped by the host matrix, one can also speak of a double inverse opal in this case (Figure 4.5.1 e). Finally this structure could be inverted once more by photopolymerization of a monomer and removal of the templating matrix. One obtains raspberry-like, 3D structured particles (Figure 4.5.1 f).

4.5.3. Inverse opals by infiltration with metal oxide nanoparticles

At first, the annealing time needs to be adjusted to give a maximum diameter of the open pores, but also to leave large enough ridges for the inverse opal to form a stable network. Thus a colloidal crystal consisting of PS particles of 1137 nm was chosen and the pore widening in dependence of the annealing time was studied, Figure 4.5.2.

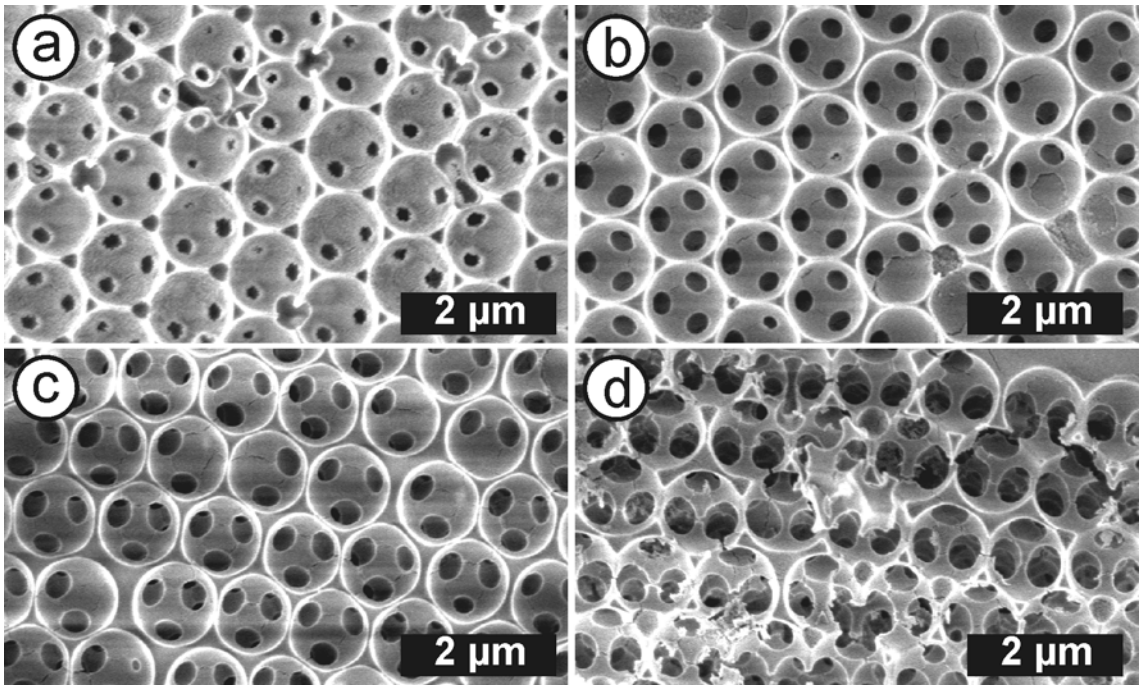

Figure 4.5.2. *Widening of the pores between adjacent spheres by annealing in an oven. a) 15 min at 93 °C; b) 10 min, c) 15 min, and d) 30 min annealing at 104 °C.*

The efficiency of this annealing step can be followed in Figure 4.5.2. Exposure to low temperatures (93 °C) even for prolonged times (15 min) has a minimum effect on the interconnecting pores, which are about 180 nm in diameter. This temperature is slightly below the Tg of the constituting PS polymer, which was found to be 95 °C by DSC measurements. For comparison, the diameter of the pores obtained by codeposition of PS and silica nanoparticles was also found to be ~ 180 nm. Going to higher temperatures (104 °C) the polymer particles are getting softer and wider pores of ~ 300 nm can readily be found after 5 and 10 min. Longer annealing times (15 min and 30 min) increase the contact point between neighboring spheres and thus lead to larger pores of 360 nm (Figure 4.5.2 c) and 490 nm (Figure 4.5.2 d) between the free voids. This is accompanied by the evolution of macroscopic cracks, which start to evolve in rectangular blocks in the homogenous crystal film. In any sample the final diameter of the open void was found to be 1050 – 1080 nm, which corresponds to a shrinkage of less than 8 %. As one can deduce from Figure 4.5.2 d) a compromise between large pores and a stable host matrix structure has to be established. Too long annealing times or too high temperatures lead to gradual closure of the interconnecting ridges. They ultimate become too small to be penetrated by the nanoparticles, which are used for infiltration (ranging from 5 nm to 30 nm in the cases shown here). Additionally, the probability of clogging is increasing, which also leads to defects in the replica. As an optimum, a pore opening of about 400 nm was deduced for the particles used here.

Thus the parameter to control at this stage is the temperature during the annealing step. For a successful and complete infiltration of the colloidal template, the nanoparticle concentration and the lifting speed of the substrate need to be adjusted. Good results could be obtained with dispersions of 5 wt% to 10 wt% silica nanoparticles and lifting speeds of 1 to 2 µm/s. 20 vol% ethanol was added to the dispersion in order to decrease the surface tension and thus facilitate complete infiltration into the free voids of the template. However, some regions showing a complete closure of the template surface by an excess layer could not be avoided. The evolution of cracks happens inevitably with this method during drying of the dispersion. For samples with no excess layer, blocks of typically several tens of µm in width and a few hundred µm in length were found. Usage of higher particle concentrations or lower lifting speeds increases the risk of excess layers and ultimately leads to disintegration of the template from the supporting substrate by pronounced cracks (blocks of only tens of µm).

The versatility of the nanoparticle infiltration procedure was further examined by usage of TiO_2 and Al_2O_3 nanoparticles. 10 wt% dispersions were used in both cases and the

lifting speed was set to 2 µm/sec. A comparison of all three host matrix systems examined in this work is compiled in Figure 4.5.3. Top view and side view SEM images are given.

In Figure 4.5.3 a) and d) the good hexagonal ordering of the SiO_2 matrix can be seen. The side view image reveals a thin excess layer of silica particles (the measurement was conducted on a flake of the inverse opal, which is the reason why the excess layer is at the bottom right corner and not on top).

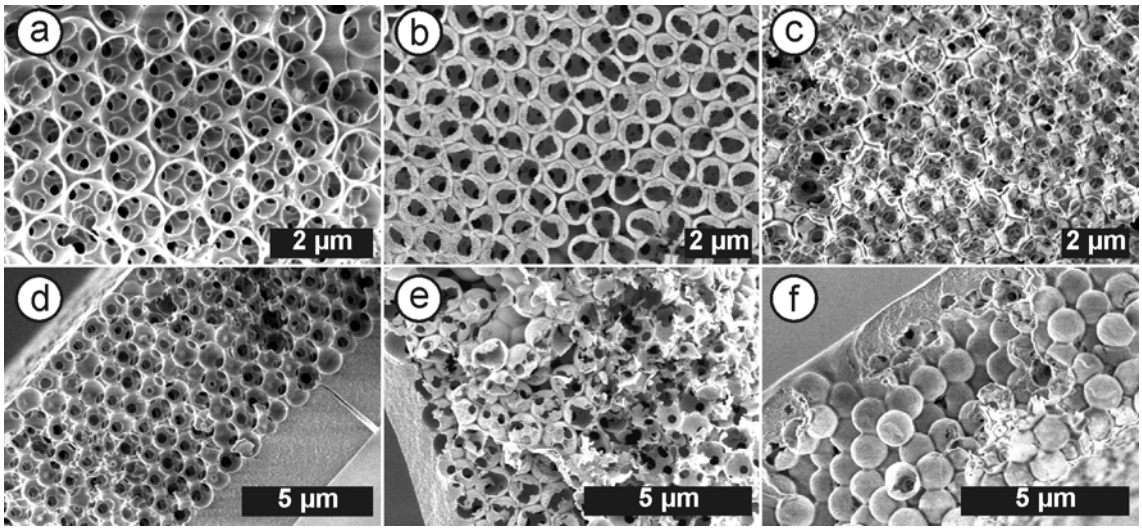

Figure 4.5.3. *Top view and side view SEM images of inverse host matrices consisting of different materials. a) and d) SiO_2, b) and e) TiO_2 (anatas), and c) and f) Al_2O_3 (γ aluminium oxide).*

A remarkable difference to the other two nanoparticles is the filling factor of the SiO_2 matrix. Whereas the SiO_2 nanoparticles completely fill the free space, open parts and merely just a covering of the polymer particles interface was observed in the other two cases. This difference in infiltration was already pointed out by Zakhidov *et al.*,[3, 17] who differentiated between volume-templating and surface-templating. The surface-templating behavior of the TiO_2 and Al_2O_3 nanoparticles may best be seen in Figure 4.5.3 b) and f). In the first case the thin shells, which wrap around the particles are clearly seen, in the second case the inverse opal looks like being constituted of hollow Al_2O_3 shells. The reason for this surface-templating is not quite clear. It looks like there is an attractive interaction between the negatively charge PS particle interface and the metal oxide nanoparticles. After fully covering the PS particle surface the nanoparticles repel each other, which even overcomes the capillary and convective forces during the vertical lifting deposition.

Due to the thin walls of the resulting host matrix, the inverse opals constituting of TiO_2 and Al_2O_3 are expected to be more fragile as compared to their SiO_2 analogue. Never-

theless, they also replicate the template structure with only a minimum of shrinkage. 18 % size reduction was measured for the TiO_2 matrix, and 7 % for the Al_2O_3 case.

4.5.4. Infiltration of colloidal particles into inverse opals

The next step is to infiltrate the host matrix with another set of colloidal particles (compare Figure 4.5.1 c). Clearly, the particles, which can possibly be used for filling the free voids of the inverse opal, have to be smaller than the interconnecting pores. A systematic study on the filling efficiency in dependence on the particle diameter was conducted; the results are given by top view and side view SEM images in Figure 4.5.4.

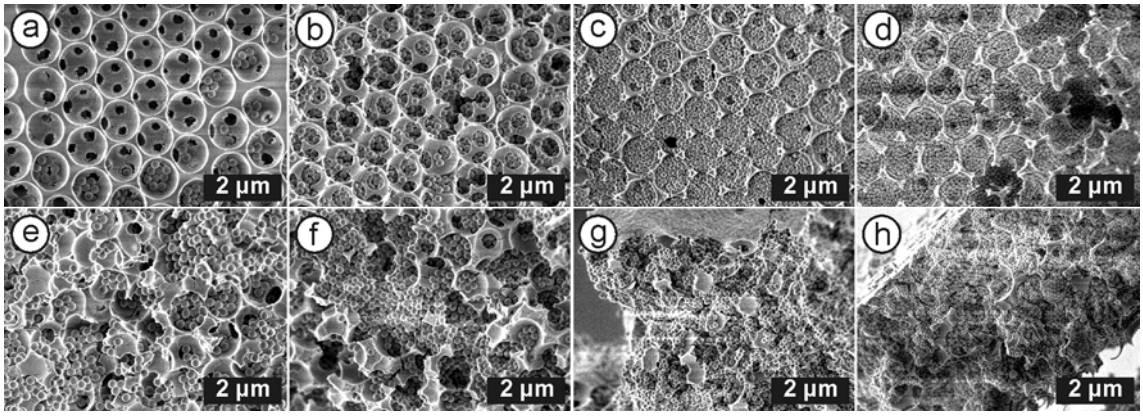

Figure 4.5.4. *Infiltration of a host inverse opal consisting of SiO_2 by PS particles of various diameters. a), e) 220 nm, b), f) 180 nm, c), g) 130 nm, and d), h) 93 nm. All dispersions were adjusted to 0.25 wt%. Top row shows top view and bottom row side view SEM images. The host inverse opal had voids of about 1 µm and pores ranging from 380 nm to 470 nm.*

One finds that all particles infiltrate into the host inverse opal. However, a complete filling of the free voids is only achieved with particles of 130 nm in diameter or smaller. This corresponds roughly to a third of the pore diameter. A complete filling of the host matrix is mandatory in order to obtain a second continuous network after the next replication step. However, this is not only dependent on the particle size, but can also be influenced by the particle concentration and lifting speed, analogous to the nanoparticle infiltration step. Concomitantly, an over infiltration of the inverse host should be avoided. Due to defect sites in the host material and an increased material roughness, meniscus pinning can not be totally avoided, which results in undesired material deposition on top of the host opal at some regions.

Infiltration of TiO_2 and Al_2O_3 inverse opals was conducted in the same way. The ordered porous network was mainly maintained during this step, even though the matrix was constituted of thinner ridges, as pointed out above. The filling was not as complete and homogenous as in the SiO_2 case. Especially regions with singly adsorbed particles

were found in the TiO_2 case; a similar behavior as it was already seen by the surface-templating of the TiO_2 nanoparticles onto the PS template.

In order to broaden the range of materials, which can be accessed by this multi step process, the infiltration with SiO_2 particles of 135 nm diameter was studied. The results are given in Figure 4.5.5 and are compared to PS particles of 93 nm. The complete infiltration of a SiO_2 template on a large scale is shown in Figure 4.5.5 a). The host matrix is completely filled from top to bottom without the formation of an excessive layer. The complete filling is corroborated by Figure 4.5.5 b), which shows the hierarchical arrangement of the PS particles by the voids. The picture was taken on an accidentally exposed lattice.

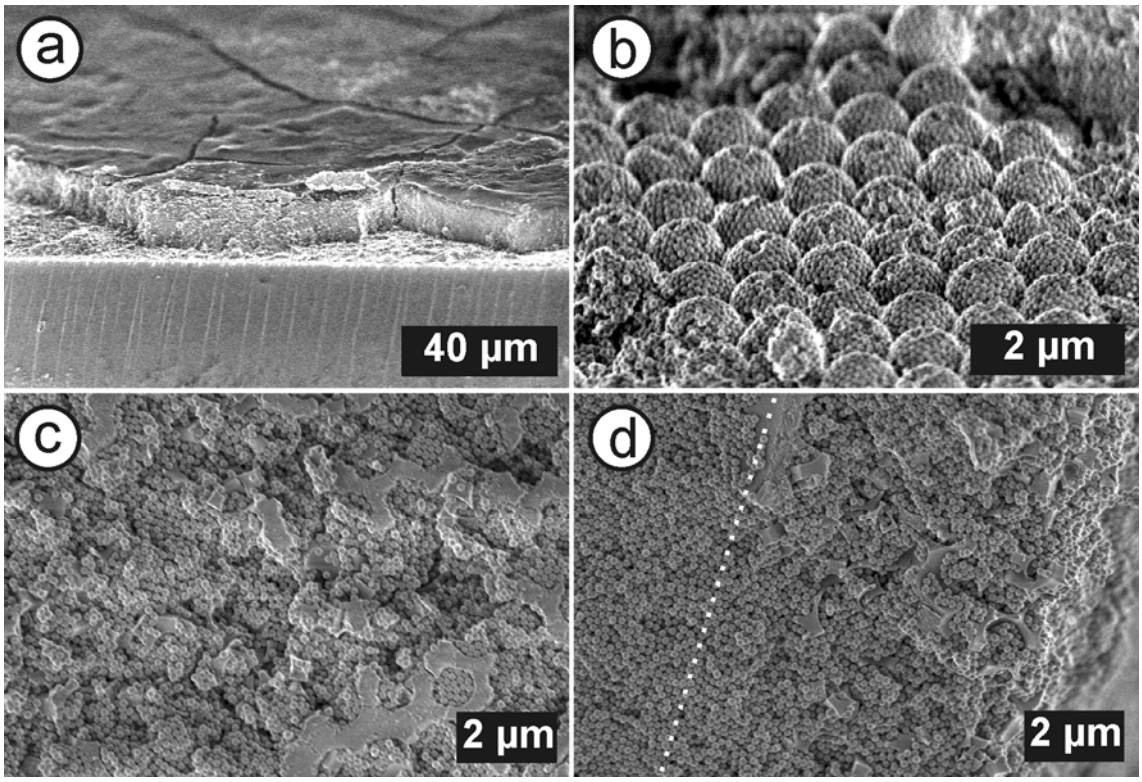

Figure 4.5.5. *a) Large side view of an inverse opal infiltrated with 93 nm PS. b) Hierarchically ordered PS particles after full infiltration of the host matrix. c) View on the underside of an inverse opal infiltrated with SiO_2 particles. d) The side view image proofs the full infiltration of the template, however, some excessive layer formed on top. The interface is highlighted by the dotted line.*

One finds that the PS particles perfectly adept to the spherical void and readily start to arrange in a close-packed lattice. It is straightforward to assume that hexagonal ordering will increase with decreasing particle diameter, as those smaller particles can more easily accommodate the stress imposed by the confined geometry (the key geometry parameters are particle radius versus void radius). Figure 4.5.5 c) and d) evidence that the infiltration is equally possible with SiO_2 particles. The view to the underside of the template and the side view both indicate a complete filling. Even though the sample was ruptured from the support before measurement, one still finds hexagonally ordered

patches in Figure 4.5.5 c. However, an excess layer of silica particles formed on top of the host matrix. The interface between these two phases is indicated by the dotted line.

4.5.5. IOIO comprising of various materials

After filling the host inverse opal with another set of PS particles one can infiltrate the colloidal template with a sol gel solution containing the desired metal oxide precursor. Due to the small particle sizes (93 nm) employed here, a codeposition of PS and nanoparticles would not be feasible for host matrix filling, as the metal oxide nanoparticles are too large to effectively fit into the free voids. Two types of sol gel precursors were chosen, tetraethyl orthosilicate (TEOS) and titanium(IV) ethoxide, and combined with all matrix materials to give composite macroporous materials on different length scales, Figure 4.5.6.

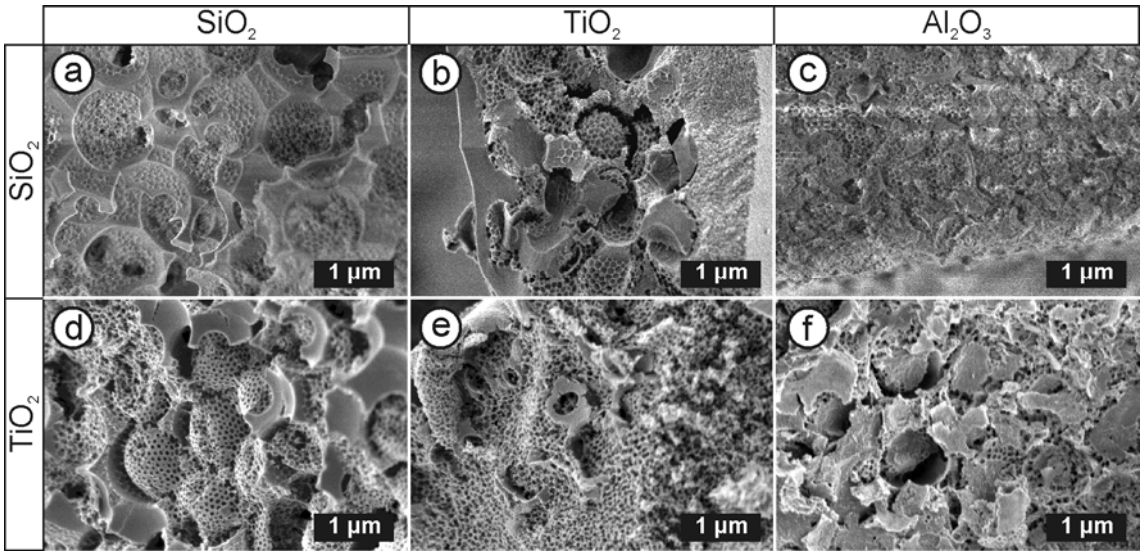

Figure 4.5.6. *SEM images of composite IOIO's. The top row is composed of SiO_2 as the inner matrix, the bottom row consists of TiO_2. The corresponding host opal material is indicated on top of each column.*

In all cases the structural hierarchy can be identified. Tiny macroporous networks are embedded in the larger host matrix. Material combinations of SiO_2, TiO_2, and Al_2O_3 as host matrix with SiO_2 and TiO_2 as second inverse structure are shown. However, the method is not limited to these materials, but any combination of metal oxide nanoparticles and sol gel precursor should be accessible. The presence of the desired elements was confirmed by EDX measurements. The relative ratios of the individual elements in the entire material are listed in Table 4.5.1. A comparison of the experimentally determined and the theoretically expected relative element ratios is given in Table 4.5.2.
The EDX measurements evidence the presence of all individual elements as expected. Only a semi-quantitative analysis was conducted, since the atomic ratios already mismatch for the pure SiO_2 case by about 5 %. When comparing the expected element ra-

tios to the experimental results, one finds that in all cases a significantly lower amount of Ti and Al was incorporated. This corroborates the earlier finding of surface templating of TiO_2 and Al_2O_3 nanoparticles in the host opal formation step. The thin shell does not efficiently fill the free space and therefore leads to less material deposition than expected.

Table 4.5.1. Total element ratios in the composite IOIO as determined by EDX measurements.

atomic %	SiO_2-SiO_2[a]	SiO_2-TiO_2[a]	TiO_2-SiO_2[a]	TiO_2-TiO_2[a]	Al_2O_3-SiO_2[b]	Al_2O_3-TiO_2[a]
Ti L	-	9.7	7.6	18.8	-	8.8
Ti K	-	14.0	18.1	32.7	-	29.2
Si K	38.4	22.7	31.7	-	21.3	-
Al K	-	-	-	-	18.7	15.6
O K	61.6	53.6	42.6	48.5	60.0	46.4

L and K denote the respective atomic orbitals.
[a] *measured with 20 kV.*
[b] *measured with 10 kV.*

Table 4.5.2. Comparison of measured and theoretical relative element ratios in completely filled composite IOIO. The theoretical values are given in brackets.

relative ratio, %	SiO_2-TiO_2	TiO_2-SiO_2	Al_2O_3-SiO_2	Al_2O_3-TiO_2
Si	61.8 (45.8)	63.7 (31.1)	53.3 (25.1)	
Ti	38.2 (54.2)	36.4 (68.9)		65.2 (35.2)
Al			46.8 (74.9)	34.8 (64.8)

An efficient and complete filling of the template structure with the sol gel solution is the key step to successfully replicate the hierarchical structure, but concomitantly a larger shrinkage has then to be taken into account. Shrinkage can further contribute to deviations from the expected element ratio as determined by EDX. This effect can be seen in SEM images in Figure 4.5.6. b) and d), where complete voids were replicated. Macroporous spheres, which are embedded in the larger host voids, are discernible but due to the shrinkage they do not fully fill the larger inverse opal structure after calcination. The opaline structure is better maintained in the case of the SiO_2 network. The surface-templating of the TiO_2 and Al_2O_3 nanoparticles is prone to dislocations and cracks after the second calcination step. Additionally, the necessity to break the IOIO for examination by SEM can introduce further defects.

When fabricating an all SiO_2 hierarchical macroporous material one can invert the final structure by polymerization of a monomer inside the template. The SiO_2 can be gently removed by treatment with diluted hydrofluoric acid (HF). This possibility was conducted with samples having air holes (Figure 4.5.6 a) and silica particles

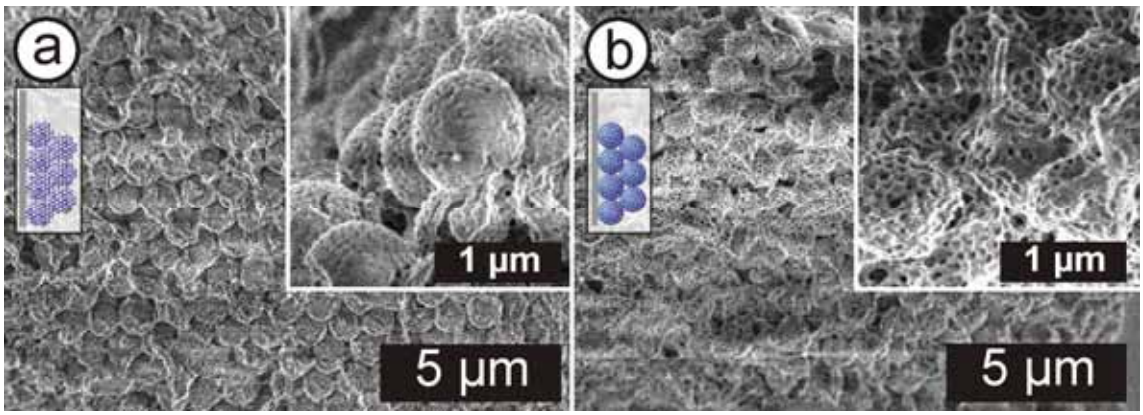

Figure 4.5.7. *a) Hierarchical PMMA particles consisting of interconnected spheres templated by a IOIO (compare Figure 4.5.1 f). b) Hierarchical PMMA particles consisting of interconnected air holes, which were templated by 130 nm SiO_2 particles in a silica host matrix (compare Figure 4.5.1 d).*

(Figure 4.5.5 c and d) inside the host matrix. MMA was photopolymerized inside these structures (Figure 4.5.7).

The successful formation of mesostructured PMMA particles can be seen in Figure 4.5.7 a) and b). These particles are showing complementary structures, as one consists of PMMA nanoparticles, whereas the other represents the inverse case and shows a continuous network of air holes, corralled by a PMMA matrix. Thus, even though it is a multiple step process to fabricate those structures, one can conclude that the repeated filling of the silica host matrix gave reasonably good materials, which can be replicated under conservation of their hierarchical architecture.

The SEM images in Figure 4.5.7 appear partially blurred. The reason for this is the nature of PMMA, which is easily damaged by the electron beam. This leads to an immediate collapse of the fine structures and ends in a featureless, continuous film. Thus the pictures had to be taken with low integration times.

4.5.6. Conclusions and outlook

A methodology was introduced to structure macroporous inverse opals on two length scales, these being 1 µm and 100 nm in size. The repeated infiltration of a colloidal crystal and its replica by vertical lifting deposition gave composite hierarchically structures. The combination of SiO_2, TiO_2, and Al_2O_3 with SiO_2 and TiO_2 was demonstrated. The crucial step to optimize is the filling fraction in each step, which should avoid the deposition of an excessive layer. In order to efficiently deposit colloidal particles in a larger host matrix, the interconnecting pores had to be widened, which was conducted by thermal annealing. Particles of up to a third of the pore diameter effectively filled the voids. However, this was not only a matter of geometric constraints, but also the material itself influenced this step, which equally holds for the fabrication of the host opal by

infiltration with nanoparticles. Namely, surface-templating of TiO_2 and Al_2O_3 nanoparticles hints to an attractive interaction with the polymer template, whereas the SiO_2 particles were found to infiltrate the entire volume. The hierarchical architecture of only-silica materials could be well inverted to their polymer replica, giving µm sized spheres either consisting of PMMA nanoparticles or air-holes corralled by PMMA.

Due to the manifold of processing steps the bottleneck to investigate the physical properties of the composite materials is their homogeneity on a macroscopic scale. In order to improve that one might use codeposition for generating the host matrix with an ensuing selective etching step to open the pores. The use of larger colloidal templates would also allow depositing the second particle type in a codeposition manner, which would overcome the shrinkage problems deriving from sol gel infiltration. On the other hand, combination of the sol gel process with well established surfactant or copolymer templating techniques, could introduce a third level of structural hierarchy.

Exchange of PMMA to more functional polymers such as hydrogels could pave the way to biomedical scaffolds or sensors.

4.5.7. Experimental part

Colloidal Crystal Fabrication and Annealing. 1137 nm PS colloidal particles were used to fabricate colloidal crystals, which served as template for the inverse opals. Colloidal crystals were fabricated by vertical lifting deposition of a 2 wt% aqueous solution of the PS particles onto plasma cleaned glass slides at a speed of 600 nm/s. Temperature and humidity were set to 20 °C and 50 %, respectively. Annealing of the colloidal template was conducted in a Heraeus vacuum oven. The temperature was set to 115 °C, which corresponded to a temperature of 104 °C at the sample. Due to the poor temperature control among different experiments the annealing time ranged from 15 min to 25 min. The evolution of tiny cracks in the homogenous colloidal crystal was taken as an indication of the onset of particle fusion.

Infiltration with Metal Oxide Nanoparticles. Three different metal oxide nanoparticle dispersions were employed to infiltrate the annealed colloidal crystals to give the host inverse opal.[16] In most cases a 5 wt% solution of LUDOX SM silica nanoparticles, a 10 wt% solution of TiO_2 nanoparticles (NanoAmor, 5-30 nm, Anatas), and a 10 wt% solution of γ Al_2O_3 nanoparticles (NanoAmor, 10 nm) was used. The nanoparticle dispersion was mixed with EtOH in a 8:2 (nanoparticle:EtOH) ratio. Subsequently the template colloidal crystal was immersed in the nanoparticle dispersion and slowly withdrawn at RT and humidity ranging from 30 % - 60 %. The withdrawal speed was set to 1 or 2 µm/s. The PS template was removed by calcination in air at 450 °C for several hours. A fast heating rate (~10 K/min) was applied.

Infiltration with Polymer and Silica Colloids. Infiltration of the host inverse opal was conducted with aqueous dispersions of PS and silica colloids by vertical lifting deposition. PS dispersions were used at a concentration of 0.25 wt% (220 nm, 180 nm, 130 nm, 93 nm), or 0.5 wt% (93 nm), and stirred silica dispersions were used at 2.5 wt% (130 nm). The deposition speed was in all cases 400 nm/s at 20 °C and 50 % RH.

Sol Gel Infiltration and Photopolymerization. The samples, which were infiltrated with PS particles into the host inverse opal, were infiltrated with a sol gel solution of the desired final metal oxide in order to generate the second inverse opal matrix. For a silica matrix a sol gel consisting of 2 ml TEOS, 2 ml EtOH, and 0.1 ml HCl was dropped several times onto an inclined sample after 10 min of prehydrolysis. The substrate was left standing upright in the sol gel solution for 45 min. Infiltration with TiO_2 was conducted by placing the substrates upright in a vial containing a titanium ethoxide (Aldrich, 75 %, used as received) solution, which was diluted 3:1 with EtOH. A few drops of the sol gel were dropped onto the sample. Condensation was allowed for 30 min. Finally the PS template was removed by calcination at 450 °C in air. The samples, which were infiltrated with colloidal silica particles, were subjected to photopolymerization of MMA. A 15 wt% solution of Irgacure 907 in MMA was dropped several times onto the substrate and UV polymerized using a UV LED (365 nm) for 5 min. This procedure was repeated several times until a clear, yellowish film was obtained. The same procedure was applied to a IOIO only consisting of SiO_2 matrices. The silica was removed by etching with hydrofluoric acid (HF). The samples were immersed for about 2 min into a 4 vol% solution of HF and rinsed twice with MQ water.

Characterization. SEM images were taken on flakes of the film, which were scratched off the supporting substrate with a scalpel (measurements partially conducted on a LEO Gemini machine in Bayreuth, Germany). EDX measurements were conducted by Maren Müller on a FEI Nova 600 Nanolab.

4.5.8. Bibliography

1. Li, Q.; Retsch, M.; Wang, J.; Knoll, W.; Jonas, U. *Top. Curr. Chem.* **2008,** DOI 10.1007/128_2008_3.
2. Stein, A.; Li, F.; Denny, N. R. *Chem. Mater.* **2008,** 20, (3), 649-666.
3. Stein, A. *Microporous Mesoporous Mater.* **2001,** 44, 227-239.
4. Holland, B. T.; Blanford, C. F.; Do, T.; Stein, A. *Chem. Mater.* **1999,** 11, (3), 795-805.
5. Velev, O. D.; Kaler, E. W. *Adv. Mater.* **2000,** 12, (7), 531-534.
6. Yang, P. D.; Deng, T.; Zhao, D. Y.; Feng, P. Y.; Pine, D.; Chmelka, B. F.; Whitesides, G. M.; Stucky, G. D. *Science* **1998,** 282, (5397), 2244-2246.
7. Fujita, S.; Nakano, H.; Ishii, M.; Nakamura, H.; Inagaki, S. *Microporous Mesoporous Mater.* **2006,** 96, (1-3), 205-209.
8. Wijnhoven, J.; Vos, W. L. *Science* **1998,** 281, (5378), 802-804.
9. Gates, B.; Yin, Y. D.; Xia, Y. N. *Chem. Mater.* **1999,** 11, (10), 2827-2836.
10. Burkert, K.; Neumann, T.; Wang, J. J.; Jonas, U.; Knoll, W.; Ottleben, H. *Lang muir* **2007,** 23, (6), 3478-3484.
11. Lee, W. M.; Pruzinsky, S. A.; Braun, P. V. *Adv. Mater.* **2002,** 14, (4), 271-274.
12. Taton, T. A.; Norris, D. J. *Nature* **2002,** 416, (6882), 685-686.
13. Muller, M.; Zentel, R.; Maka, T.; Romanov, S. G.; Torres, C. M. S. *Chem. Ma ter.* **2000,** 12, (8), 2508-2512.
14. Wang, J.; Ahl, S.; Li, Q.; Kreiter, M.; Neumann, T.; Burkert, K.; Knoll, W.; Jo nas, U. *J. Mater. Chem.* **2008,** 18, (9), 981-988.
15. Wang, J. J.; Li, Q.; Knoll, W.; Jonas, U. *J. Am. Chem. Soc.* **2006,** 128, (49), 15606-15607.
16. Gu, Z. Z.; Kubo, S.; Fujishima, A.; Sato, O. *Appl Phys A-Mater* **2002,** 74, (1), 127-129.
17. Zakhidov, A. A.; Baughman, R. H.; Iqbal, Z.; Cui, C. X.; Khayrullin, I.; Dantas, S. O.; Marti, I.; Ralchenko, V. G. *Science* **1998,** 282, (5390), 897-901.

4.6. Elastic Properties of Individual Colloidal Particles

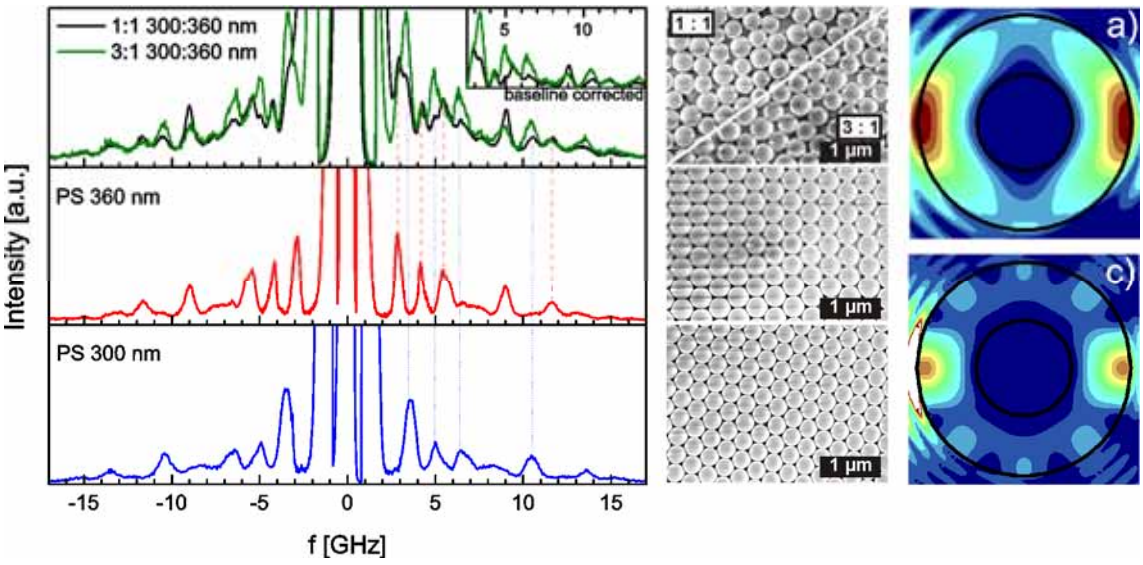

Brillouin light scattering (BLS) is an inelastic, non-invasive, non-destructive technique to probe phonons in the GHz range in soft matter. Colloidal particles possess due to their small dimensions resonant modes, which lie in the GHz range. Thus determination of these resonant modes by BLS allows insight into the mechanical properties of individual colloidal particles. Therefore, influence of changes in the architecture and composition on the mechanical properties of colloidal particles can be determined on a nm scale. Here, colloidal particles consisting of PS homopolymers and PMMA/nBA copolymers will be investigated, and the influence of core-shell architectures on the materials mechanical properties will be shown.

4.6.1. Introduction

Nowadays, colloidal nano- and mesoscale particles with dimensions from few nanometers up to one micrometer are used in a growing number of applications, e.g., as fillers in polymer thin films[1] to enhance thermo-mechanical properties, to improve coatings performance, and as components in nanocomposites operating as photonic,[2] plasmonic,[3] and phononic structures.[4]

For a wide range of such applications, information on the mechanical properties and the stability of these colloidal composite materials are of paramount importance. Conventional rheological measurements on the macroscopic system are often not sufficient to elucidate the specific contributions of the nanostructured components. At the nanoscale, forces negligible in macroscopic systems, such as depletion, interfacial, and confinement effects often become significant and the behavior of the same materials in nanoscopic systems can considerably deviate from the bulk. A fundamental understanding of transport and thermomechanical properties of nanostructured materials is a precondition to address a specific need by structural engineering. In the case of colloidal composite materials, the vibration modes confined to the individual particles result from the elastic motion at the nanoscale and should sensitively depend on the geometrical, architectural, interfacial, and mechanical characteristics of the particles. However, there is a paucity of non-destructive experimental techniques to probe this "music" of particle vibrations since both high frequency resolution and sensitivity are required to detect the numerous eigenmodes. Raman scattering[5, 6] has been utilized to measure few eigenfrequencies of nanoparticles with dimension below 10 nm, whereas Brillouin light scattering (BLS)[7-9] and optical pulse-probe techniques[10, 11] can probe respectively the spontaneous and stimulated vibrations confined in sub-micrometer particles. In BLS, light is scattered inelastically by the density fluctuations (phonons) associated with these particle localized modes at thermal equilibrium as outlined in chapter 2.5. Due to the strong elastic form factor of the individual spheres and the large elastic contrast with the surrounding medium air, the colloidal particle films show strong multiple scattering. In such samples the inelastic scattering from localized modes leads to incoherent BLS in analogy to the Raman scattering. Thus BLS can be utilized to analyse the particle eigenfrequencies, describing the spheroidal (i, l) modes, with i as the i^{th} mode of the l^{th} spherical harmonic.

As it has been pointed out by Lamb,[12] the frequencies associated with a distinct set of spheroidal modes can be calculated by

$$\mathrm{f}(il) = x(il) \cdot \sqrt{\frac{R(c_\mathrm{l}, c_\mathrm{t})}{\rho}} \cdot d^{-1} \qquad \text{Equation 4.6.1}$$

With $x(il)$ being a temperature independent constant for each individual mode, $R(c_\mathrm{l}, c_\mathrm{t})$ the rigidity, ρ the mass density, and d the particle diameter. The rigidity is a function of the longitudinal (c_l) and transversal (c_t) sound velocity. Thus, the single resonant modes of a certain type of particle depend inverse linearly on the particle diameter. Changes made to the rigidity of the particle will also shift the eigenmode frequency.

From the c_l and c_t the elastic constants are directly accessible.[13] These are the Poisson ratio

$$\sigma = \frac{c_\mathrm{l}^2 - 2c_\mathrm{t}^2}{2(c_\mathrm{l}^2 - c_\mathrm{t}^2)} \qquad \text{Equation 4.6.2}$$

the Young modulus

$$E = (1+\sigma)(1-2\sigma)\frac{\rho c_\mathrm{l}^2}{1-\sigma} \qquad \text{Equation 4.6.3}$$

and the shear modulus

$$G = \rho c_\mathrm{t}^2 \qquad \text{Equation 4.6.4}$$

Colloid science can create novel materials that possess spatial variation of density and elastic constants at the nanoscale but their mechanical characterization remains difficult. Similarly, the influence of the particle architecture (polymer composition, core-shell spheres, or hollow capsules), size, and shape on the eigenfrequencies and the localization of elastic energy in specific regions of an individual particle is not known. In addition to the characterization on the nanomechanical properties, tailored acoustic confinement will be important for precise phonon management by structural engineering.

In this chapter the mechanical properties of individual particles will be examined by measurement of the particles resonance frequencies by BLS. At first the well known results for plain polystyrene (PS) particles of different sizes will be reviewed, followed by experiments conducted on a binary mixture of PS spheres of different diameters. The mechanical properties of polymethylmethacrylate (PMMA) particles of almost the same size, but with a varying amount of n-butyl acrylate (nBA) (which acts as plasticizer), will then be discussed in the next section. Measurements on silica-core PMMA-shell particles and hollow spheres will conclude this chapter. The peculiar influence of the particle architecture on the mechanical properties of its constituting components will be investigated.

4.6.2. Polystyrene particles and particle mixtures

The first demonstration of the feasibility of the BLS experiment on colloidal particles was shown by Penciu *et al.*[7] in the case of dilute suspensions of giant core–shell micelles. A few years later Kuok *et al.*[8] have extended this application to closely packed monodisperse silica nanospheres in air. Up to six localized particle eigenmodes have been resolved out of the numerous possible modes, probably due to the weak scattering of moderately compressible silica. In a subsequent study of artificial soft colloidal crystals, composed of monodisperse sub-micrometer PS spheres[9] with diameter d between 170 and 856 nm, have been investigated. Up to 21 **q**-independent eigenmodes have been resolved.

Figure 4.6.1 shows three exemplary BLS spectra (all BLS spectra were measured by Tim Still) from colloidal PS opals with diameters of 180, 360, and 550 nm. The resonance frequencies scale with 1/*d* (Figure 4.6.2), which is in perfect agreement with Lamb's theory[12] and the theoretical predictions based on single-phonon scattering cross-section calculations.[14, 15] In the computations, a plane sound wave propagating in air and impinging upon a single PS sphere was considered and, after subtracting the scattering amplitude for a rigid sphere of equal size, the sphere eigenmodes appear as resonance peaks in the plot of scattering cross section versus frequency. Thereby the resonance frequencies f *(i, l)* can be identified as a mode with angular momentum quantum number *l* of i^{th} order.

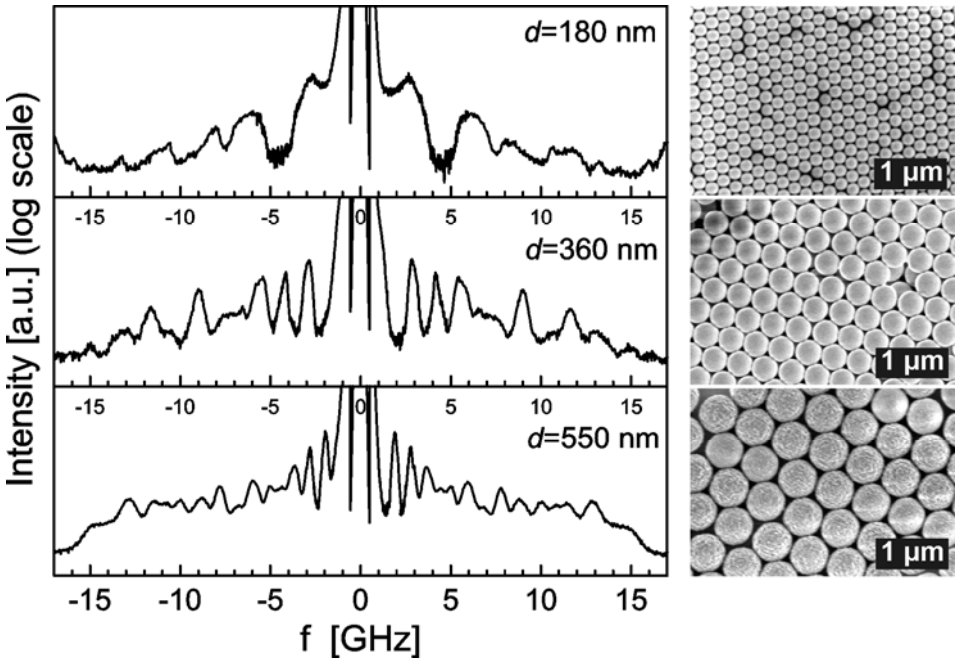

Figure 4.6.1. *Left:* **q***-independent BLS eigenmode spectra of the PS particles. To capture all possible vibrations, two spectra recorded at two different free spectral ranges are superimposed. Spectra are recorded at 20° (q = 0.0041 nm^{-1}). For the thickest particles (d = 550 nm, bottom) there is a clear cutoff bump around 15 GHz, which is the frequency of the acoustic phonon in PS at backscattering geometry. Right: Corresponding SEM images of PS particles of 180 nm, 360 nm, and 550 nm diameter.*

Using the experimental values for the longitudinal sound velocity $c_l = 2350\ ms^{-1}$, the transverse sound velocity $c_t = 1210\ ms^{-1}$ and mass density $\rho = 1050\ kgm^{-3}$ of bulk PS, all resolved frequencies are quantitatively captured within 3 % with no adjustable parameter. The product of frequency and diameter is obtained to be a constant for every mode, as is indicated by the solid lines in Figure 4.6.2, which represent the computed modes (*i, l*). It is shown that the first modes are the same for all samples with the (1, 2) mode being the lowest and most intense one.

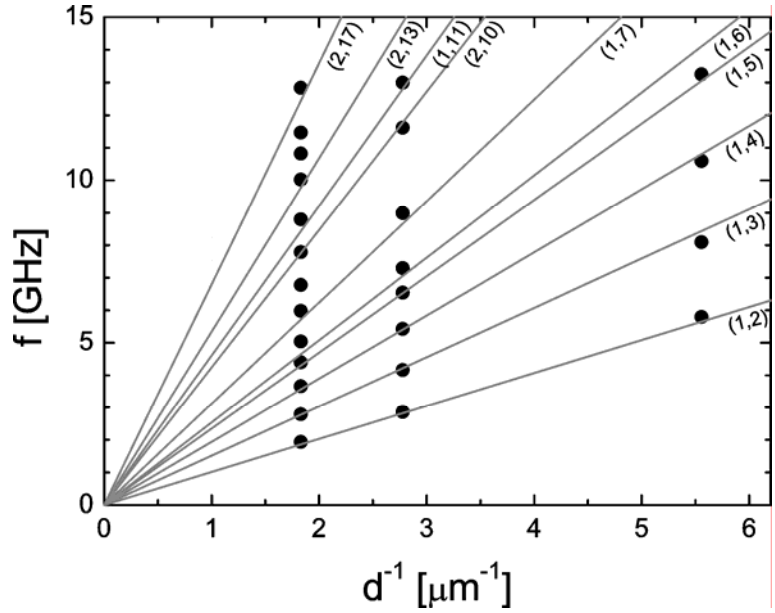

Figure 4.6.2. *Experimental resonance frequencies of the PS opals from Figure 4.6.1 (solid symbols) versus the reciprocal particle diameter. The solid lines denote the computed resonance frequencies.*[9]

From the longitudinal, c_l, and transversal, c_t, sound velocities the elastic constants are directly accessible, as outlined by equations 4.6.2 - 4.6.4 above. Additionally to the elastic constants, even more information can be extracted from these spectra. The peculiar lineshape can be regarded as a sensitive index of the particle size distribution. In particular for the (1, 2) modes (Figure 4 in reference[9]), the experimental lineshape (after deconvolution with the instrument function) can be represented by a convolution of a Lorentzian line and a Gaussian distribution function of the particle size with their variance as the only adjustable parameter besides the amplitude. In conformity with the analysis of the SEM pictures all investigated colloidal samples are found to be quite monodisperse. For the largest particle size in Figure 4.6.1 (or Figure 2 in [9]) there is clearly a kind of cutoff frequency at about 14 – 15 GHz, after which the scattering intensity decreases rapidly towards zero. Because of strong multiple scattering, **q** is not defined. The highest frequency contribution corresponds to the acoustic phonon in bulk PS under backscattering conditions, i.e. $\mathbf{q}_{BS} = 4\pi n/\lambda_0$. Using $n = 1.59$ for the refractive index of PS and for the laser wavelength $\lambda_0 = 532$ nm, $\mathbf{q}_{BS} = 0.0376\ nm^{-1}$ and hence a

cutoff frequency for the longitudinal acoustic phonon (c_l = 2350 ms^{-1}) is indeed expected at 14.05 GHz.

The influence of the particle environment on its eigenmode resonances was studied by preparation of colloidal glasses,[16] i.e. by mixing of two monodisperse particles (d = 300 nm and 360 nm) at a defined ratio. The size polydispersity is then artificially increased and no crystallization takes place, which is affirmed by SEM pictures (Figure 4.6.3 top right panel). The individual particles should experience then a less constraint environment due to the local disorder, which leads to an increased total free volume. The eigenmode acoustic spectra of these dry, mixed films were measured by BLS. The eigenmode spectra of the 1:1 and 3:1 mixture are shown in Figure 4.6.3 left panel along with the eigenmode spectra of the individual one-component opals. Interestingly, the spectrum of the hybrid is a superposition of the individual opals as is indicated by the vertical lines denoting some exemplary resonance frequencies either from the small or the large spheres.

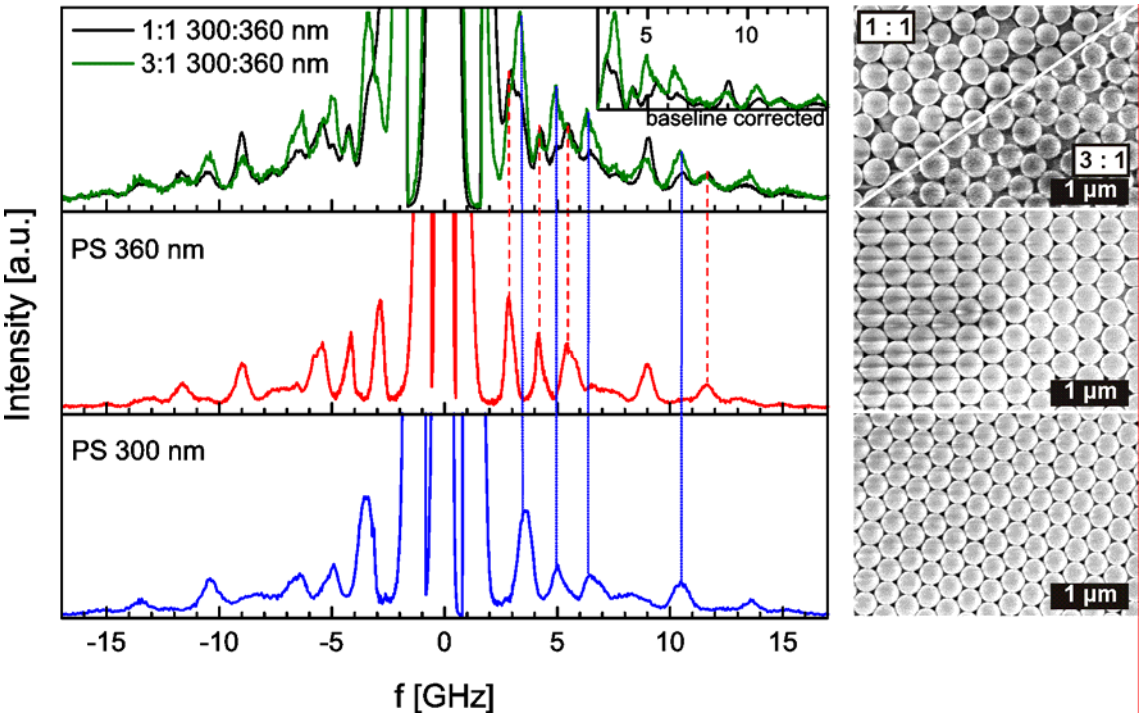

Figure 4.6.3. *Left: eigenmode acoustic spectra of the PS opals with d = 300 nm (blue), d = 360 nm (red) and the PS mixture 1:1/3:1 300 nm:360 nm (black/green) (bottom to top). The vertical lines (solid for d = 300 nm, dashed for d = 360 nm) denote some exemplary eigenmodes appearing in the monomodal opals and in the colloidal glass. In the top right corner the Anti-Stokes side of the mixtures' spectra is compared after baseline correction to better visualize the influence of the composition on the relative intensity of the individual signals. Right: corresponding SEM images of opals and glasses are shown.*

Moreover, changing the relative ratios of the constituent spheres also alters the eigenmode spectra. The intensity of the signals originating from a particular particle size relates to its relative concentration in the mixture. In Figure 4.6.3 this linear composition dependence is shown by superimposing the spectrum of the 1:1 300 nm:360 nm glass

with the spectrum of a 3:1 300 nm:360 nm mixture, normalized to the peak intensity in the 360 nm spheres. For clarity a baseline correction was introduced into the Anti-Stokes side of the colloidal glasses (inset to Figure 4.6.3). Apparently, but somewhat counter-intuitively, the change in contact points between the spheres does not influence their eigenmodes - at least for non-infiltrated, dry films.

To further elucidate this unexpected phenomenon, an asymmetric mixture with a nine to one number ratio of 180 nm and 550 nm PS beads was prepared. While for every dense packing of spheres the number of neighboring spheres, and hence the contact points as indicated by the SEM images, is twelve, this mean number is different for the random packed hybrids depending on their size disparity and their number ratio. For example, in the SEM image for a 9:1 180 nm:550 nm mixture in Figure 4.6.4 (right panel), the number of next neighbors of the large spheres is increased dramatically by small beads that accumulated around the bigger spheres. However, even in this extreme case, the resonances from the 550 nm spheres are mostly unaltered as demonstrated in the BLS spectra (Figure 4.6.4 left).

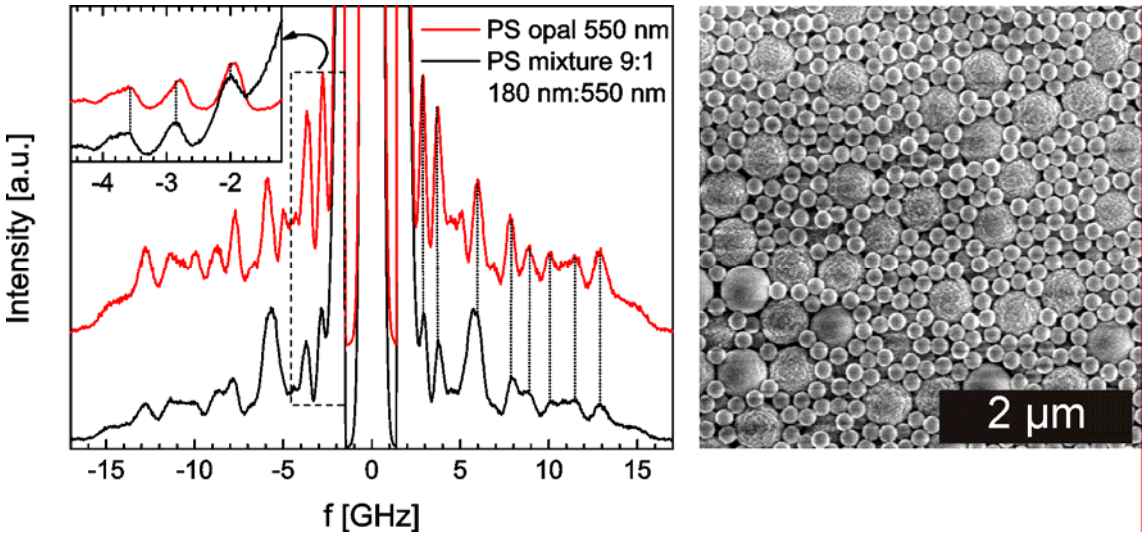

Figure 4.6.4. *Left: Comparison between the eigenmode acoustic spectra of the 550 nm PS single opal and the asymmetric 9:1 180 nm:550 nm PS mixture. Right: Corresponding SEM image of the colloidal glass.*

A careful inspection, however, of the two lowest frequencies reveals a very small shift of the mixture resonance modes towards higher frequencies, as is shown in the inset of Figure 4.6.4 for the Stokes sides of the spectra. The observed effect is subtle (~ 4 % frequency shift) but significant. In this context it is noteworthy to mention that in figure 3 of reference[17], Li *et al.* compare the BLS spectra from a 320 nm silica artificial opal and from a single sphere of the same kind, measured by a micro-Brillouin light scattering setup. In this figure it seems as if there is a shift between single spheres and opal.

Interestingly, the authors describe only the broadening in the opal due to the polydispersity.

4.6.3. PMMA/nBA latex particles

After this general introduction to particle eigenmodes and their insensitivity to the local environment, the focus will be turned on the particles rigidity (as discussed by Lamb, see equation 4.6.1). For this purpose PMMA/nBA copolymer particles of almost identical size (~ 200 nm) were prepared, with an increasing content of nBA (see chapter 3.2). The large difference in Tg of the homopolymers (Tg_{PMMA} = 105 °C, Tg_{PnBA} = -43 °C) allows the adjustment of the particles hardness by varying the monomer composition. For copolymerization of different monomers the relative reactivity ratios, r_1 and r_2, indicate the composition of the final copolymer. In case of MMA and nBA these ratios are $r_{MMA} = 0.91$ and $r_{nBA} = 0.94$, based on their *Q-e* values ($Q_{MMA} = 0.78$, $e_{MMA} = 0.40$, and $Q_{nBA} = 0.38$, $e_{nBA} = 0.85$).[18, 19] This indicates a statistical copolymerization, as these values differ only slightly from $r = 1$. In the resulting statistical copolymer a medium Tg can be found, which can be calculated according to the Gordon-Taylor equation:[20]

$$Tg = \frac{Tg_A \cdot w_A + K \cdot Tg_B \cdot w_B}{w_A + K \cdot w_B} \qquad \text{Equation 4.6.5}$$

$Tg_A < Tg_B$ are the corresponding Tg's of the homopolymers, w_A and w_B are the respective weight fractions. K is a fitting parameter, which was found to be K = 0.82 for MMA/nBA copolymers.[21] The particles under consideration in this study are listed in Table 4.6.1. Their measured and calculated Tg, particle size, and molecular weight of the copolymer are also given.

Table 4.6.1. Properties of PMMA/nBA copolymer particles of various compositions.

x_{nBA}, vol%	d, nm[a]	M_n, gmol^{-1} [b]	PDI[b]	Tg, °C[c]	Tg_{theo}, °C[d]
0	232	92500	4.2	112	105
10	214	89599	4.2	92	89
20	200	84200	3.2	70	73
30	204	110000	3.5	47	58

[a] *determined by SEM images.*
[b] *determined by THF GPC. PMMA standards were used for calibration*
[c] *determined by DSC, the third heating cycle (10 K/min) was used.*
[d] *calculated by the Gordon-Taylor equation with K=0.82, Tg_A=-43 °C, and Tg_B=105 °C.*

The Tg's measured by DSC match by and large with the reported results on similar PMMA/nBA copolymers.[21]

The BLS spectra of the particle eigenmodes are shown in Figure 4.6.5. The frequency axis is normalized to the particle diameter.

The BLS spectra clearly reveal a drop in the particle hardness, since the position of the single eigenmodes shift to smaller frequencies with increasing nBA content (only exceptions are the first and second mode of the 10 vol% nBA sample). Considering equation 4.6.1 two factors can be responsible for this shift: a shift in particle density and/or a shift in particle rigidity. Considering the difference in polymer density between PMMA (ρ_{PMMA} = 1.195 gcm^{-3}) and PnBA (ρ_{PnBA} = 1.035 gcm^{-3}) one can expect that the density of the copolymer particles decreases accordingly. The densities of colloidal particles of 30 vol% and 20 vol% nBA were determined in a gradient density column. Densities of $\rho_{30\ vol\%}$ = 1.145 gcm^{-3} and $\rho_{20\ vol\%}$ = 1.165 gcm^{-3} were found, which agree well with the expected values. However, this density decrease should lead to an increase of the eigenmode frequencies under otherwise constant conditions. Therefore it becomes clear that the particles rigidity decrease even more with increasing nBA content, which leads to a slight, but unambiguous net decrease in eigenmode frequency.

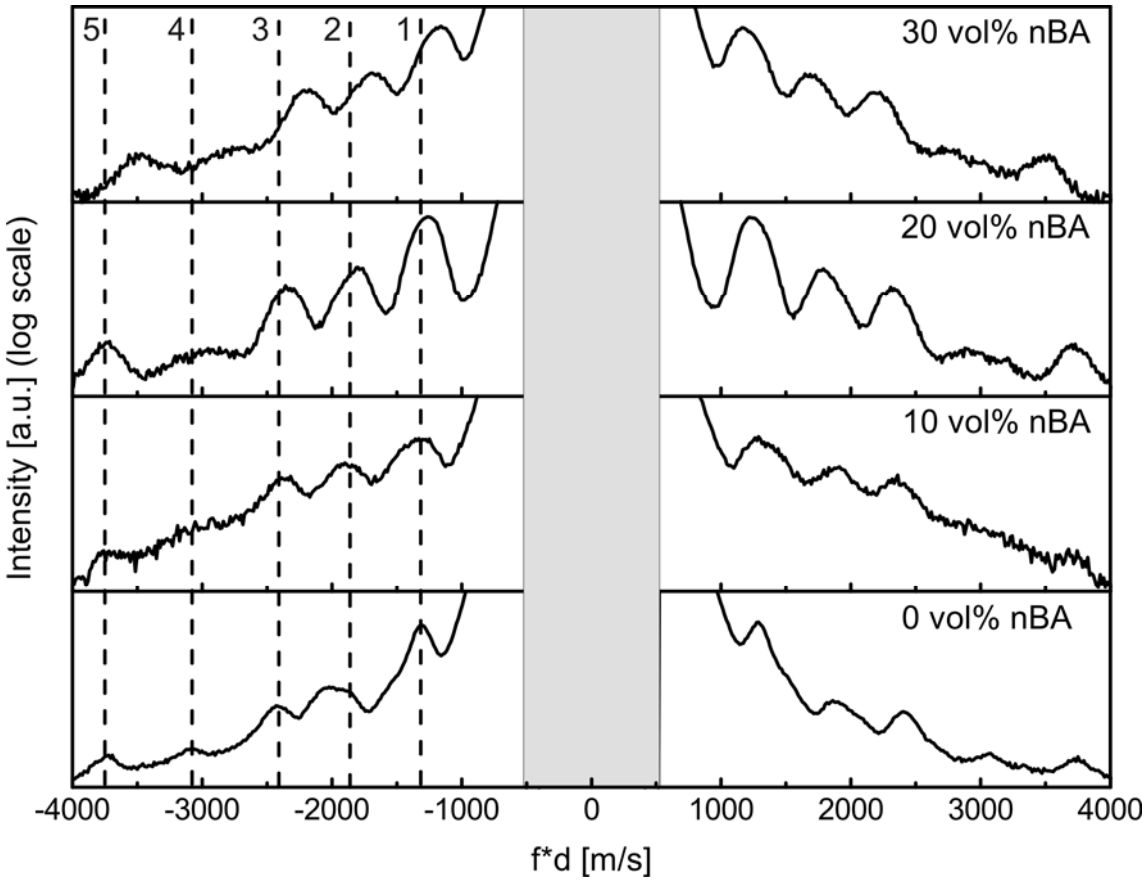

Figure 4.6.5. *BLS spectra of PMMA/nBA particles. The frequency axis is normalized to the product of frequency and particle diameter. Dashed lines in the Stokes side of the spectra indicate the shift of five resonance modes, which could be resolved in a logarithmic intensity scale. The asymmetry of the second 0 vol% nBA mode (bottom spectrum) could be eliminated by measurement at another free spectral range (20 GHz instead of 30 GHz). However, no change in the eigenmode peak position was observed.*

The monotonic decrease of eigenmode frequencies is stressed out in Figure 4.6.6. The normalized peak position for each individual mode is plotted in dependence of the volume fraction of nBA in the monomer mixture.

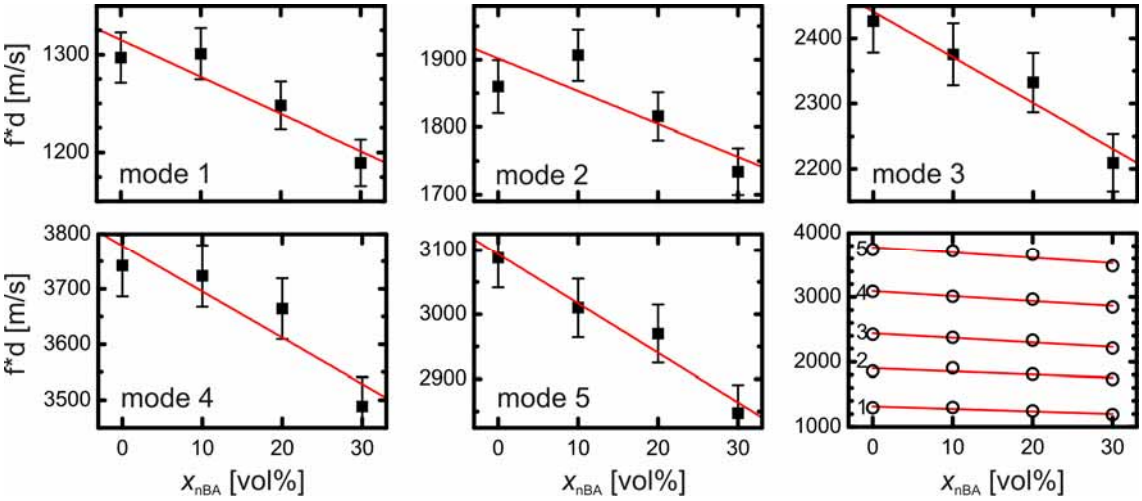

Figure 4.6.6. *Shift of the normalized eigenmodes with nBA content. The mode number corresponds to the number given in Figure 4.6.5. The modes are fitted with a linear function. All fits and measurements are combined in the bottom right window.*

Fitting of the experimental eigenmodes by considering a plane sound wave propagating in air and impinging upon a single colloid in air, will give values of c_t and c_l for fixed parameters of ρ and d. These calculations are currently undertaken and will give deeper insight into the mechanical properties of the particles and more quantitative conclusions can be drawn.

4.6.4. PMMA@SiO_2 core shell particles

Finally the morphology of the colloidal particles was changed. Core-shell particles consisting of a silica core of 181 nm and PMMA shells of varying thickness (25, 57, and 112 nm) were examined alongside with their hollow sphere counterparts. SEM images of the SiO_2-PMMA particles are shown in the right panel of Figure 4.6.7.

Although there is some degeneration of the PMMA by the electron beam at 1 kV or some blurring using lower voltage (200 V), the particles' diameters d can be determined by averaging the software-aided gauged diameters over about 100 spheres for each sample. The size polydispersity is about 5 %, which is confirmed by the formation of crystalline films after vertical lifting deposition from the particle suspensions.[22]

Figure 4.6.7 (left panel) shows the **q**-independent BLS spectra of the bare silica particles and the three core-shell particles. The spectra can be well represented by up to nine Lorentzian line shapes as shown by the solid lines on the Anti-Stokes side of the BLS spectra. The peak position of the spectral lines yields the resonance frequencies of the

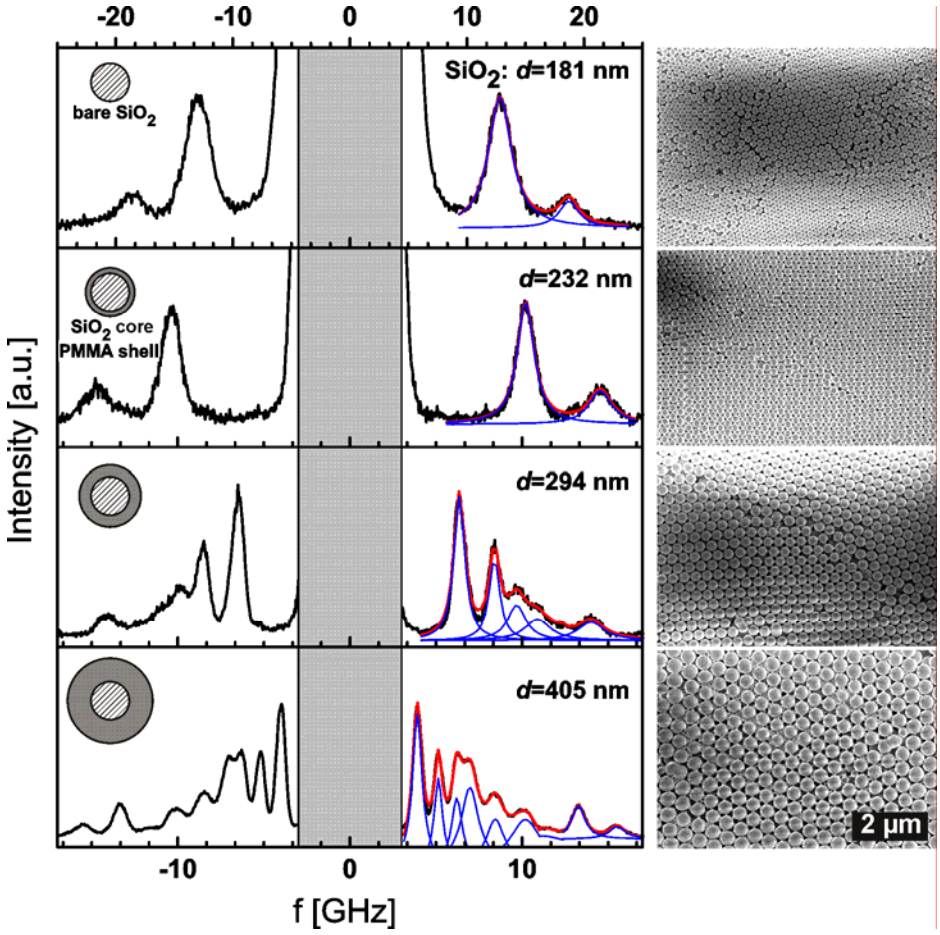

Figure 4.6.7. *Left: BLS eigenmode spectra of bare silica (top) and the three core-shell particle films. The representation of the BLS spectra with up to nine Lorentzians (solid lines) is shown on the Anti-Stokes side (note the different frequency scale for the spectrum in the top). Right: SEM images of the bare silica and the core-shell particles with growing shell (from top to bottom).*

eigenmodes indicated by solid circles, which are compiled in Figure 4.6.8 for all four particles.

An advantage of BLS is that it can, in principle, record all thermally excited modes within one measurement, which is not possible, e.g., in the pump-probe technique. For the bare silica spheres, only two resonance frequencies at about 13 and 19 GHz are resolved. However, with increasing the PMMA shell thickness of the core-shell particles ($d = 232$ nm, $d = 294$ nm, and $d = 405$ nm), the BLS spectra become richer as it was observed for pure polystyrene colloidal particles.[9] For the particle with the thinnest shell, a third weak peak is discernible in the spectrum in the inset of Figure 4.6.8 b, whereas five modes are observed in the medium-thick shell (Figure 4.6.8 c) and even nine modes are resolved in the BLS spectrum of the thickest shell (Figure 4.6.8 d). The increased number of the resolved modes in the BLS with increasing particle size relates to the intensity of the resonance signals which depends on qd. In the present case of strong multiple scattering $q \sim 2k_i$ (the backscattering vector) and the number of resolved modes increases with $2k_id$.[23]

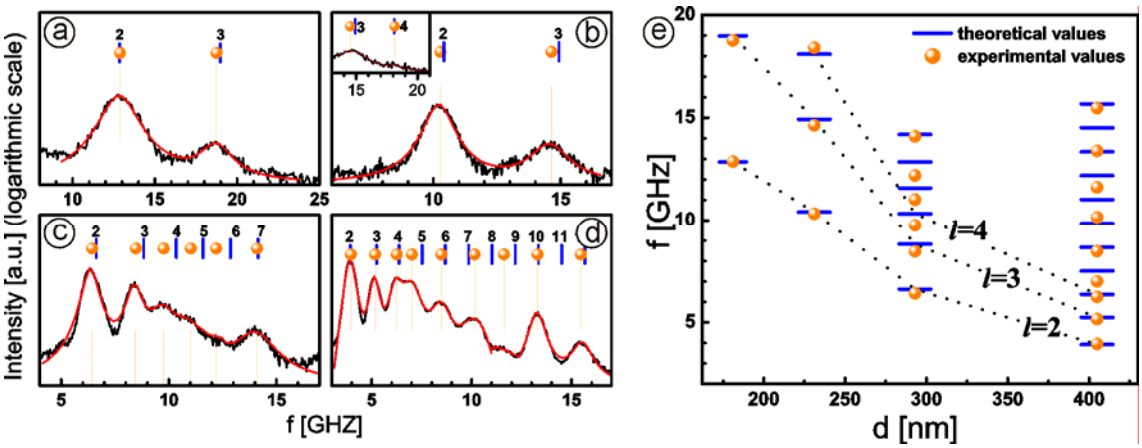

Figure 4.6.8. *Enlarged Anti-Stokes sides of the spectra from Figure 4.6.7 (a, pure silica; b-d, core-shell). The experimental frequencies are accented by orange spheres, the small vertical blue lines denote the corresponding calculated resonance frequencies, each of them characterized by its angular momentum l, shown at the top of the lines. All experimental and theoretical (blue bars) values are summarized in e) with the dotted lines connecting modes of the same angular momentum, l; i = 1 for all observed modes.*

The elastic parameters (longitudinal and transverse velocities, c_l and c_t) of the two constituents (core and shell materials) are not *a priori* known for such nanostructured systems. An access to these material properties at these length scales and high frequencies is important since they can considerably differ from their values in macroscopic systems. The elastic constants are frequency dependent, and BLS specifically yields their limiting high frequency values, which relate to local packing and interactions, as well as the glass transition temperature (as discussed in chapter 4.6.3).[24] The detection of more than two particle elastic excitations in the experimental (BLS) spectra of Figure 4.6.7 allows for an unambiguous determination of the elastic moduli, shear modulus G (equation 4.6.4) and Young modulus E (equation 4.6.3). The experimental values of the resonance frequencies are compared with the resonance frequencies obtained from the calculated density-of-states (DOS) spectra of a single constituent sphere of the experimental systems. The theoretical computations were performed by Rebecca Sainidou using a formalism, appropriately developed for this case and presented elsewhere.[15, 25] Each resonance mode appearing at frequency $f(i,l)$ in these DOS spectra is characterized by the angular momentum l, imposed by the spherical symmetry of the particle, where i denotes the i^{th} order solution for a given l. All the shell-localized modes reported in this section have $i = 1$. The materials elastic parameters (c_l, c_t) and densities are used as adjustable parameters in order to achieve the least deviation between theoretical and experimental eigenfrequencies. Obviously, in the theoretical calculations the constituent spheres are considered as homogeneous and isotropic, and their elastic coefficients are frequency-independent. It is noteworthy that this method provides a full description of the experimentally observed numerous eigenfrequencies for homogeneous polystyrene[9]

and PMMA[26] spheres. However, it is still not settled whether selection rules apply for the BLS from particles with diameters comparable to the wavelength of the incident laser light ($qd \approx 1$). While Li *et al.*,[27] based on group theory considerations, claim that only particle resonances with even l values contribute to BLS eigenmode spectra, according to Montagna[23] resonances with even and odd l values should have comparable activities. In fact, the latter is supported by a BLS study[9] of model PS spheres revealing up to 21 resonance modes theoretically captured with no adjustable parameter.

First, the bare silica particles (Figure 4.6.8 a) are considered. The two sound velocities treated as adjustable parameters are obtained from representation of the two experimental frequencies (orange spheres) by the calculated resonance frequencies (small blue vertical lines in Figure 4.6.8 a). The obtained sound velocities for the bare-silica particles, c_l = 4420 ms^{-1} and c_t = 2780 ms^{-1}, are significantly lower (~25 %) than the values of dense bulk amorphous silica (c_l = 5970 ms^{-1}, c_t = 3760 ms^{-1}, ρ = 2200 kgm^{-3}), indicating the presence of porosity in these particles.[28] It also underlines the necessity of the BLS experiment to determine these values avoiding erroneous assumptions. The mass density does not sensitively affect the DOS spectra, due to the huge impedance difference between silica and air. Nevertheless, these porous silica spheres should be less dense than bulk silica (see below).

Next, we consider the PMMA-coated silica particles consisting of same silica cores. For a first description of the DOS spectra, representing the experimental frequencies seen in the BLS spectra of parts b-d of Figures 4.6.8 (solid circles), the elastic constants measured for the bare silica particles were used and the values for the sound velocity and density of the PMMA shell were fixed on the values for bulk PMMA[26] (c_l = 2800 ms^{-1}, c_t = 1400 ms^{-1}, ρ = 1190 kgm^{-3}). However, this choice for the set of the elastic parameters of both the silica core and the PMMA does not quantitatively represent the experimental resonances in the BLS spectra of Figure 4.6.8, parts b) – d).

A systematic theoretical analysis based on the DOS spectra of the three core-shell spheres has shown that changes in the elastic parameters of *both* materials of the hybrid particles are required. Notably, we found that for the silica core we must assume sound velocities, which are about 3 % higher than those in the bare silica particle, i.e., $c_{l,c}$ = 4540 ms^{-1} and $c_{t,c}$ = 2860 ms^{-1}. This hardening of the silica core is probably due to a partial infiltration of methyl methacrylate in the pores and subsequent polymerization to PMMA during the formation of the shell. Due to the reduced impedance contrast between the silica core and the PMMA shell relative to the bare silica spheres versus air, the core mass density ρ_c has now a substantial influence on the DOS calculations. For

$\rho_c = 1900\ \mathrm{kgm^{-3}}$, the sound velocities in the PMMA shell are $c_{l,s} = 3080\ \mathrm{ms^{-1}}$ and $c_{t,s} = 1540\ \mathrm{ms^{-1}}$, i.e., about 10 % higher than in bulk PMMA; the PMMA mass density was kept at the bulk value. Therewith, nearly all measured signals can be identified as spherical eigenmodes with angular momentum l and can be captured quantitatively by the theory within about 3 %. The calculated resonance frequencies are shown by small vertical lines in Figure 4.6.8 a) – d), and summarized in Figure 4.6.8 f) along with the corresponding experimental values. The Young modulus E and the shear modulus G are directly accessible for both the core and the shell components.

In order to obtain an insight into the nature of the experimentally observed modes (Figure 4.6.7), the elastic field at the resonance frequencies in the region of the sphere was calculated by Rebecca Sainidou, assuming a longitudinal acoustic plane wave of the same frequency, impinging on the sphere. An example of elastic-field intensity plots is given in Figure 4.6.9 for the case of the thickest PMMA shell sample ($d = 405$ nm). Their topology is that of a field intensity having $2l$ maxima on the internal interface of the outer circumference of the core-shell particle: two of them are strong (global) maxima along the direction of the incident field, while the rest $2(l - 1)$ are weaker and distributed equidistantly along the circumference.

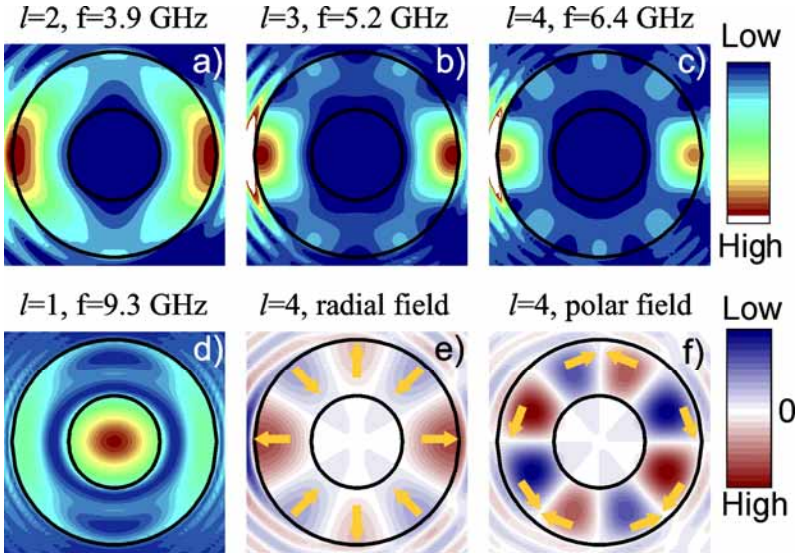

Figure 4.6.9. *a-c) Elastic-field distribution for the first three resonances (i = 1) of the 405 nm core-shell particle (Figure 4.6.8 d) in a cross section through the centre of the sphere. Plane wave incidence is assumed along the horizontal axis from the left. d) An example of core-localized mode with l = 1 (i = 2) at 9.3 GHz, which is not observed experimentally. Plots e) and f) give, respectively, the real part of the radial and polar component of the elastic field for the case shown in c), with the arrows visualizing the vibrational mode of the shell (figure by courtesy of Rebecca Sainidou).*

The vibration of the observed modes is radial at the maxima changing alternatively direction (outward or inward) from maximum to maximum. In the regions of minima the field is directed tangentially. On the basis of Figure 4.6.9, the experimentally observed

modes (Figure 4.6.8 e) are shell-localized with $l = 2 - 4$. Core-localized modes either do not exist within the considered frequency range (films with $d = 232$ nm and 294 nm) or are not observable in the experimental BLS spectra (thickest-shell case, Figure 4.6.8 d), probably due to the very strong localization (virtually delta-functions in the DOS spectra). It is worth mentioning, however, that the elastic parameters affect the frequencies of both core- and shell-like eigenmodes.

Figure 4.6.10 a) shows the BLS spectra of two hollow capsules ($d = 232$ and 294 nm), akin to those of double-shelled hollow carbon microspheres published recently.[29] By comparison of the two spectra, it is apparent that the thicker hollow capsules display significantly sharper peaks than the thinner hollow capsules. For solid spheres, the line width of the spectra is associated with the size polydispersity.[9] For the thin hollow spheres ($d = 232$ nm), however, an additional source for the line broadening is the significant fraction of particles with indentations as seen in Figure 4.6.10 b). These defects are neither uniform in size nor uniform in shape and hence cause a distribution of the elastic properties that further broadens the experimental spectra.

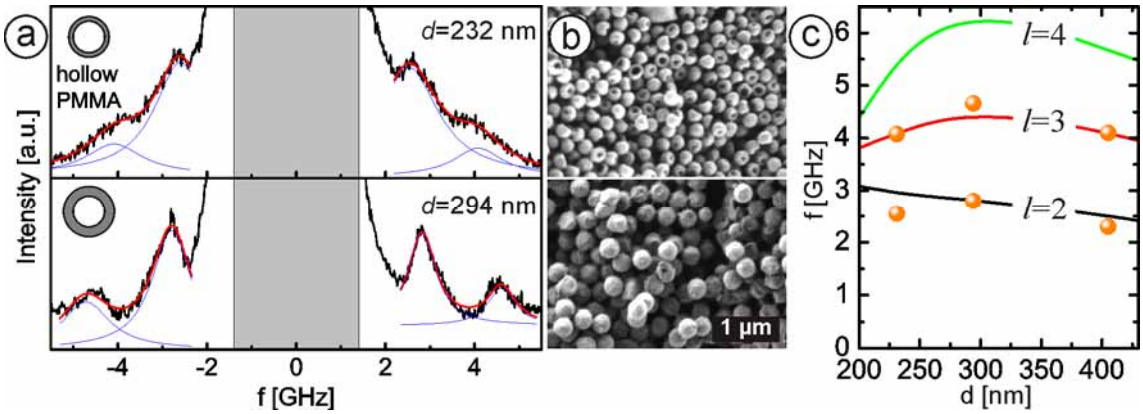

Figure 4.6.10. *a) BLS eigenmode spectra of spherical hollow PMMA capsules with d = 232 nm and d = 294 nm. b) SEM images of the hollow PMMA particles. For the smaller particles (top), indentations in the spheres are observed, whereas there are nearly no defects in the thicker shells (bottom). c) Comparison between calculated (solid lines, different colors for the individual modes) and experimental (spheres) resonance frequencies for the hollow capsules (i = 1).*

In order to identify the nature of the experimental eigenmodes in the two hollow capsules, the resonance frequencies of shell-localized modes were computed, adopting for the PMMA shell the values of the elastic moduli obtained from the representation of the eigenfrequencies of the core-shell particles (Figure 4.6.8 e). Figure 4.6.10 c) shows the calculated (solid lines) eigenfrequencies for several modes characterized by the angular momentum l (= 2 - 4) for hollow PMMA nanoshells with constant inner diameter (181 nm) as a function of the (outer) particle diameter d. The comparison with the experimental frequencies (orange spheres) identifies the observed frequencies in the three hollow PMMA spheres with the two lowest modes with $l = 2$ and $l = 3$. Interestingly,

the frequencies of these two modes vary very little with d due to two competing effects. At a constant particle diameter, the resonance frequencies of hollow particles increase with shell thickness,[30] whereas the resonance frequencies of filled spheres decrease with d since $f(i,l) \sim 1/d$.[7-9] Since in our case both shell thickness and total diameter increase simultaneously, the net effect is essentially the apparent insensitivity of the eigenfrequencies to the d variation of the branches with $l = 2$ and 3 seen in Figure 4.6.10 c). Notably, the elastic parameters of the PMMA were not affected by the core etching.

4.6.5. Conclusions and outlook

A thorough investigation of particle resonant modes was conducted. PS particles show a well known linear dependence on the inverse diameter d of the constituting spheres. The eigenmode spectra are insensitive to the local environment of the individual particles, as it was demonstrated by the fabrication of colloidal glasses. Superimposed eigenmode spectra were obtained for binary particle mixtures, which even reflected the relative particle ratios. Chemically tuning the rigidity of colloidal particles by copolymerization of MMA and nBA led to a systematic decrease in the resonance frequencies, indicating a softening of the particles. Silica core-PMMA shell particles were found to have different mechanical properties compared to their bulk values. Both materials exhibited higher sound velocities, which were revealed by DOS calculations. Removal of the SiO_2 core by HF etching led to hollow PMMA particles. The resonant modes were found to be remarkably insensitive to the particle diameter, whereas the hardening of the PMMA relative to its bulk value remained.

Besides a fundamental interest in understanding the mechanical properties of nanosized particles, the findings presented here might ultimately lead to a detailed nanoparticle structure and vibrational property relationship understanding. This in turn can path the way to rationally design nanoparticles to act as resonators, which might find applications in vibration or heat insulation materials, as well as opto-acoustic or thermoelectric devices.

4.6.6. Experimental part

Particle Synthesis. Colloidal PS and PMMA/nBA copolymer particles were synthesized and purified as outlined in chapter 3. Binary mixtures of PS particles were prepared by mixing calculated amounts of monomodal dispersions. For calculating the particle concentration a mass density of 1.04 gcm^{-3} was assumed for PS. Silica-PMMA core-shell particles were prepared by Peter Spahn[31] and used as received. PMMA hollow capsules were prepared by HF etching of silica-PMMA core-shell particles in a

10 vol% aqueous HF solution for 20 min. In order to avoid etching of the support substrate, the films were prepared on PET transparency foils.

Colloidal Crystal and Film Preparation. Vertical lifting deposition was used for colloidal crystal and film preparation. As outlined in chapter 3.5, lifting speeds ranging from 200 nm/s to 1200 nm/s, at temperatures ranging from 20 °C to 25 °C, and relative humidities ranging from 30 % to 60 % were used. The films were typically deposited on clean glass substrates.

Characterization. SEM measurements were taken as outlined in chapter 2.2. At least 100 spheres were measured manually using ImageJ to determine the mean particle diameter. BLS measurements and data evaluation were conducted by Tim Still in all cases. Calculations were carried out by Rebecca Sainidou.

4.6.7. Bibliography

1. Liff, S. M.; Kumar, N.; McKinley, G. H. *Nat Mater* **2007,** 6, (1), 76-83.
2. Joannopoulos, J. D.; Johnson, S. G.; Winn, J. N.; Meade, R. D., *Photonic Crys tals: Molding the Flow of Light*. 2nd ed ed.; Princeton University Press: 2008.
3. Ozbay, E. *Science* **2006,** 311, (5758), 189-193.
4. Cheng, W.; Wang, J.; Jonas, U.; Fytas, G.; Stefanou, N. *Nat. Mater.* **2006,** 5, 830-836.
5. Duval, E.; Boukenter, A.; Champagnon, B. *Phys. Rev. Lett.* **1986,** 56, (19), 2052.
6. Courty, A.; Mermet, A.; Albouy, P. A.; Duval, E.; Pileni, M. P. *Nat. Mater.* **2005,** 4, (5), 395-398.
7. Penciu, R. S.; Fytas, G.; Economou, E. N.; Steffen, W.; Yannopoulos, S. N. *Phys. Rev. Lett.* **2000,** 85, (21), 4622.
8. Kuok, M. H.; Lim, H. S.; Ng, S. C.; Liu, N. N.; Wang, Z. K. *Phys. Rev. Lett.* **2003,** 90, (25), 255502.
9. Cheng, W.; Wang, J. J.; Jonas, U.; Steffen, W.; Fytas, G.; Penciu, R. S.; Econo mou, E. N. *J. Chem. Phys.* **2005,** 123, 121104.
10. Hodak, J. H.; Henglein, A.; Hartland, G. V. *The Journal of Chemical Physics* **1999,** 111, (18), 8613-8621.
11. Mazurenko, D. A.; Shan, X.; Stiefelhagen, J. C. P.; Graf, C. M.; van Blaaderen, A.; Dijkhuis, J. I. *Physical Review B (Condensed Matter and Materials Physics)* **2007,** 75, (16), 161102-4.
12. Lamb, H. *Proc. London Math. Soc.* **1882,** s1-13, 189.
13. Faatz, M.; Cheng, W.; Wegner, G.; Fytas, G.; Penciu, R. S.; Economou, E. N. *Langmuir* **2005,** 21, (15), 6666-6668.
14. Penciu, R. S.; Kriegs, H.; Petekidis, G.; Fytas, G.; Economou, E. N. *J. Chem. Phys.* **2003,** 118, (11), 5224-5240.
15. Sainidou, R.; Stefanou, N.; Psarobas, I. E.; Modinos, A. *Z. Kristallogr.* **2005,** 220, 848-858.
16. Garcia, P. D.; Sapienza, R.; Blanco, A.; Lopez, C. *Adv. Mater.* **2007,** 19, (18), 2597-2602.
17. Li, Y.; Lim, H. S.; Ng, S. C.; Wang, Z. K.; Kuok, M. H.; Vekris, E.; Kitaev, V.; Peiris, F. C.; Ozin, G. A. *Appl. Phys. Lett.* **2006,** 88, (2), 023112-3.
18. Alfrey, T.; Price, C. C. *J. Polym. Sci.* **1947,** 2, 101.
19. Greenley, R. Z., *Polymer Handbook*. 4th edition ed.; Wiley: Hoboken, 1999.
20. Gordon, M.; Taylor, J. S. *Journal of Applied Chemistry* **1952,** 2, (9), 493-500.
21. Penzel, E.; Rieger, J.; Schneider, H. A. *Polymer* **1997,** 38, (2), 325-337.
22. Dimitrov, A. S.; Nagayama, K. *Langmuir* **1996,** 12, (5), 1303-1311.
23. Montagna, M. *Physical Review B (Condensed Matter and Materials Physics)* **2008,** 77, (4), 045418-9.

24. Cheng, W.; Sainidou, R.; Burgardt, P.; Stefanou, N.; Kiyanova, A.; Efremov, M.; Fytas, G.; Nealey, P. F. *Macromolecules* **2007,** 40, (20), 7283-7290.
25. Sainidou, R.; Stefanou, N.; Modinos, A. *Phys. Rev. B* **2004,** 69, (6), 064301.
26. Still, T.; Cheng, W.; Retsch, M.; Sainidou, R.; Wang, J.; Jonas, U.; Stefanou, N.; Fytas, G. *Phys. Rev. Lett.* **2008,** 100, 194301.
27. Li, Y.; Lim, H. S.; Ng, S. C.; Wang, Z. K.; Kuok, M. H. *Chem. Phys. Lett.* **2008,** 461, (1-3), 111-113.
28. Lim, H. S.; Kuok, M. H.; Ng, S. C.; Wang, Z. K. *Appl. Phys. Lett.* **2004,** 84, (21), 4182-4184.
29. Li, Y.; Lim, H. S.; Ng, S. C.; Kuok, M. H.; Su, F.; Zhao, X. S. *Appl. Phys. Lett.* **2007,** 90, (26), 261916-3.
30. Sainidou, R.; Djafari-Rouhani, B.; Pennec, Y.; Vasseur, J. O. *Physical Review B (Condensed Matter and Materials Physics)* **2006,** 73, (2), 024302-7.
31. Spahn, P. Kolloidale Kristalle aus monodispersen Silika-Polymer Hybridparti keln. PhD thesis, Technische Universität Darmstadt, Darmstadt, 2008.

4.7. Effective Medium and Bandgaps in Liquid Infiltrated Colloidal Crystals and Glasses

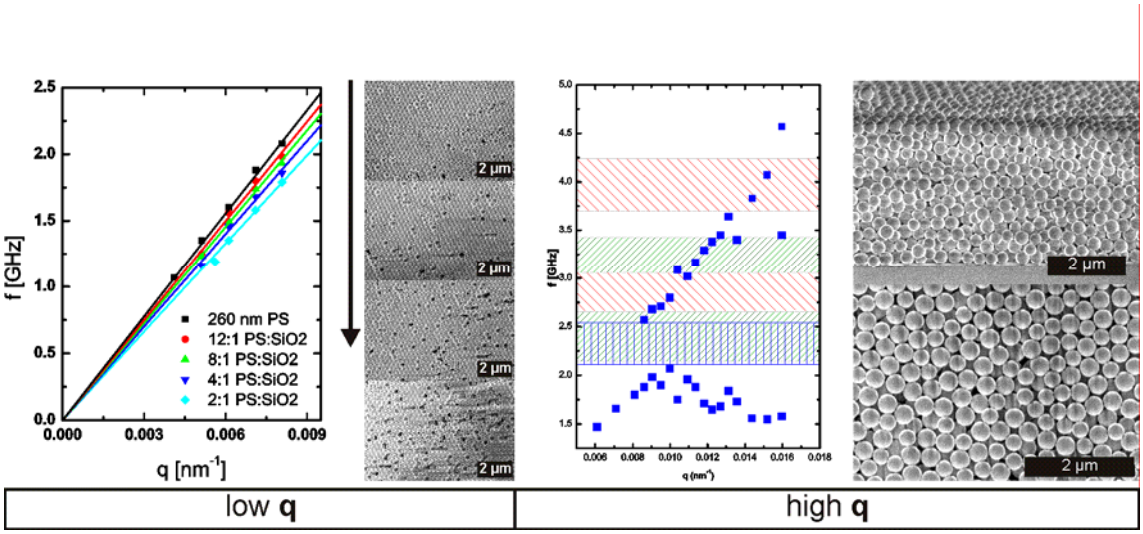

Infiltration of colloidal crystals with a refractive index matching medium allows the measurement of **q**-dependent BLS spectra. Therefore phononic band diagrams can be accessed, from which effective sound velocities in the composite material and phononic band gaps can be determined. Effective sound velocities and band gaps can be assessed in one material by measurement in high and low **q**-ranges. Whereas for low **q** values only the acoustic phonons are probed, the band diagram can become richer for high **q** values. This chapter addresses both regimes separately. The influence of the volume fraction of one component on the effective sound velocity in a defect-doped PS-PDMS crystal will be investigated and the discovery of two distinct phononic band gaps in a colloidal crystal will be shown.

4.7.1. Introduction

Structured materials with a periodic modulation in the density and elastic coefficients, so-called phononic crystals,[1] can exhibit phonon band gaps at Bragg frequencies or wavelengths commensurate to their lattice constant. In addition to Bragg gaps (BG), theory predicts gaps evoked by resonance modes of the constituent components interacting with the extended acoustic branch of the composite structure.[2] These gaps prevent elastic waves with certain frequencies to propagate through the crystal at least in certain crystallographic directions. The width and the position of the BG in general depends on the contrast between the densities (ρ), longitudinal and transverse sound velocities (c_l and c_t) of the component materials, and on the lattice parameter.[3-5] Yet, structures with strong localized resonant elements can shift the gap well below the Bragg frequency associated to the lattice constant.[6, 7] Soon after the first experimental observation of ultrasonic band gaps,[8-12] peculiar phenomena with potential applications dealing with the propagation of elastic waves in periodic composite materials such as tunneling,[13] negative refraction, focusing,[14, 15] and enhanced transmission through one-dimensional gratings[16] have been discovered. Most realized systems deal so far with sonic and ultrasonic phononic crystals with periodicity in the millimeter range.[6, 7, 9-15] To shift the gap to higher frequencies,[17] the creation of periodic patterns at the submicron scale is necessary, which can benefit from techniques currently explored for the fabrication of structures in soft matter.[18] Recently, colloidal self-assembly techniques were employed[19] by vertical lifting deposition to fabricate fcc films of monodisperse polystyrene (PS) spheres on glass substrates with subsequent fluid infiltration. The phononic dispersion relation of such a single crystalline pattern measured by spontaneous Brillouin light scattering (BLS) led to the first observation of a hypersonic BG along high-symmetry crystallographic directions.[20] By varying the particle size and the infiltrated fluid, the hypersonic frequency and the width of the gap could be tuned. More recently, a hypersonic BG was also observed in two-dimensional structures fabricated by optical lithography.[21] In soft opals, the spherical particles represent local resonant elements, and hence the bands, which originate from the multipole modes of these interacting particles, can overlap with the acoustic field of the extended states in the effective medium. As a result of this degeneration or hybridization, a gap opens up in the vicinity of the eigenfrequency of the quadrupole particle modes,[2] which we refer to as hybridization gap (HG). Such gaps originate, in general, from level repulsion when two bands of the same symmetry cross each other, about the crossing point. An optical analogue of this gap is encountered, e.g. in metallodielectric photonic crystals, as a result of hybridiza-

tion between collective particle-plasmon modes and the extended effective-medium band.[22] Albeit there was a hint of HG in colloidal suspensions,[23-26] its demonstration, assignment and the concurrent observation along with the BG has been missing.

In contrast to BLS measurements on dry colloidal films as shown in chapter 4.6 the investigation of phononic band gaps requires the full dispersion relation (scattering vector **q**-dependent measurements). Therefore the strong multiple scattering, inherent in colloidal films due to the high refractive index difference between air and polymer, needs to be suppressed, which is achieved by means of liquid infiltration with a liquid of the same refractive index as the polymer particles. In order to retain a high mechanical contrast polydimethylsiloxane (PDMS), a high boiling point and non-solvent for PS or PMMA, is the liquid of choice. The infiltration has several consequences for the mechanical properties of the composite material. The particle resonance modes shift as they are surrounded by a damping matrix and the speed of sound experiences an effective medium when travelling through the inhomogeneous material.[27] When measuring dispersion relations in liquid infiltrated colloidal films, one can assign two distinct regions of interest. The first measures for low **q** the acoustic branch of the phonon, from which an effective sound velocity can be deduced. For higher **q**'s the scattering and interference of phonons on a local scale is probed, resulting in a deviation from purely acoustic behavior. The phonon spectrum can split up and thus band gaps are revealed.

In the results presented here the focus is first laid on the low **q** range. By designed vacancy-defect doping of colloidal crystals the volume fraction of the constituting PS spheres is systematically changed and the consequences on the photonic properties and the effective sound velocity will be shown. Then the focus will be turned on the high **q** range and the simultaneous occurrence of a phononic Bragg- (BG) and a hybridization gap (HG) will be demonstrated.

4.7.2. Effective medium of liquid infiltrated colloidal crystals

Hybrid colloidal crystals consisting of particles with similar size, but of different materials, were fabricated by mixing of monodisperse particle suspensions, which were used in the vertical lifting deposition. For the system under investigation, a combination of $d = 260$ nm PS particles (PDI = 1.3 %) and $d = 255$ nm SiO_2 particles (PDI = 5.9 %) was used. The dispersions were mixed with particle number ratios of PS:SiO_2 of 0.3:1, 1:1, 2:1, 4:1, 8:1, and 12:1 (assuming a density of the silica nanoparticles of $\rho_{SiO2} = 1.7$ gcm^{-3}),[28] also the respective monomodal crystals were prepared. The corresponding films were fabricated by vertical lifting deposition.

The combination of PS and silica spheres offers two ways to study an effective medium. The first is an effective refractive index stemming from the two distinct constituent spheres PS and SiO_2. This can be characterized by UV/Vis spectroscopy. The second possibility is to remove the SiO_2 particles by HF etching. Within a certain relative particle concentration range, the overall colloidal crystal will remain intact, while including a defined number of point (vacancy) defects. This leads to an increase in the free volume, which can be infiltrated by PDMS, and will consequently change the effective sound velocity.

At first the question had to be addressed, whether the composite colloidal crystals were obtained in the desired number particle ratio and in a homogenous way without regions of phase separation. SEM images are shown in Figure 4.7.1.

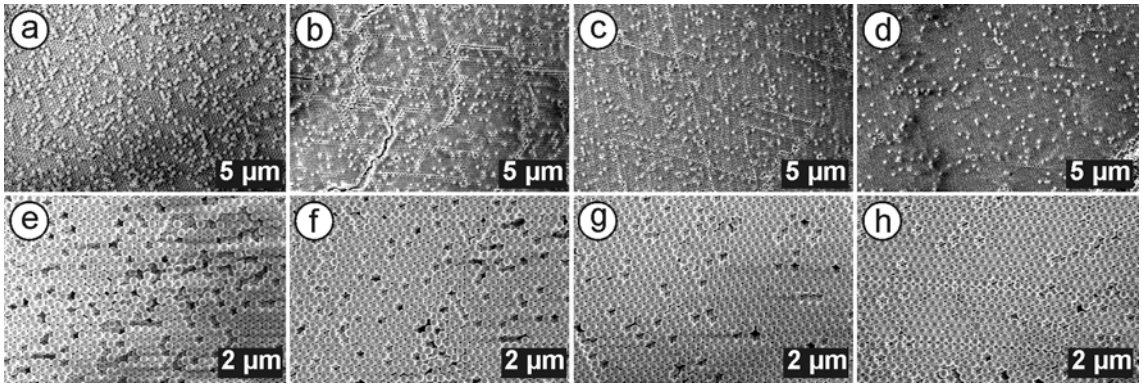

Figure 4.7.1. *Top row: composite PS-SiO_2 colloidal crystals with a suspension particle number ratio of 2:1 (a), 4:1 (b), 8:1 (c), and 12:1 (d). Bottom row (e – h): the corresponding colloidal crystals after removal of the SiO_2 spheres by HF etching.*

PS and SiO_2 particles could be distinguished by their differences in electron scattering at low magnifications. The SiO_2 particles appear as bright spots in the SEM images and are randomly distributed over the entire sample. No regions of particle clusters of one type were found in any case. Due to the higher polydispersity of the silica particles the monocrystalline domain size decreases with increasing silica content. Counting of the SiO_2 particles visible in the SEM measurements reveals that in most cases systematically less SiO_2 particles than expected from the nominal suspension were incorporated into the system (see table 4.7.1). However, the particle ratio could vary between bulk and surface. Furthermore, the evaluation of the SEM images remains difficult, as the contrast difference ceases with higher magnification, whereas the individual particles are barely discernable a lower magnification.

HF treatment of the composite film effectively removes the SiO_2 particles. This happens without affecting the crystalline order of the remaining PS network for composite mixture with PS as the major component.

In order to gain more insight into the bulk composition TGA measurements were performed on all composite mixtures. The measurements are summarized in Figure 4.7.2 a) and Table 4.7.1.

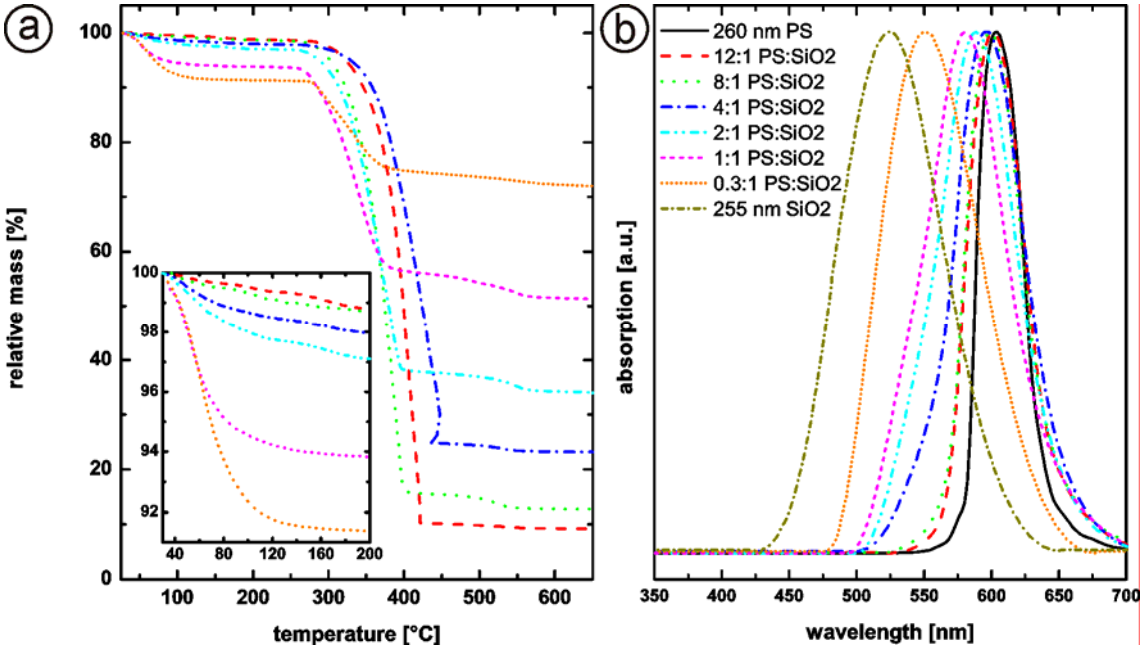

Figure 4.7.2. *a) TGA measurement on composite PS-SiO_2 colloidal crystals. The inset shows the loss of water, before decomposition of the polymer sets in at about 250 -350 °C. b) UV/Vis measurement on composite PS-SiO_2 films of varying mixture. For reasons of clarity the UV/Vis spectra were background corrected and normalized. The legend in b) applies for all graphs.*

A two step weight loss could be found in the TGA measurements. The first step correlates to the loss of intercalated water in the porous SiO_2 particles. Therefore the highest loss was found for the composite film with the highest SiO_2 content (0.3:1, see inset in Figure 4.7.2 a). The next step corresponds to the combustion of PS. Now, the largest loss is found for the 12:1 PS:SiO_2 mixture. In order to compare the experimental results with the expected values the experimental relative mass reduction $x_{\text{mass. loss}}$ was extracted by

$$x_{\text{loss}} = \frac{x_{\text{dry mass, composite}} - x_{\text{mass, silica}}}{x_{\text{dry mass, composite}}} \qquad \text{Equation 4.7.1}$$

$x_{\text{dry mass, composite}}$ is the relative mass after loss of the water and was measured from the plateau in Figure 4.7.2 a), $x_{\text{mass, silica}}$ is the final relative mass after PS combustion (steady line at ~ 600 °C).

The experimental results were compared to the expected value $x_{\text{loss, exp}}$, which was calculated by

$$x_{\text{loss, exp}} = \frac{x_{\text{PS}} \cdot \rho_{\text{PS}} \cdot r_{\text{PS}}^3}{x_{\text{PS}} \cdot \rho_{\text{PS}} \cdot r_{\text{PS}}^3 + x_{\text{SiO}_2} \cdot \rho_{\text{SiO}_2} \cdot r_{\text{SiO}_2}^3} \qquad \text{Equation 4.7.2}$$

x_{PS} and x_{SiO2} are the respective number particle ratios. ρ_{PS} and ρ_{SiO2} are the materials densities, and r_{PS} and r_{SiO2} the particles radius.

The results of both calculations are given in Table 4.7.1. Similar to the findings of the SEM images the experimental mass loss was greater than expected from the nominal suspension composition. Thus less silica particles were incorporated into the composite material. For mass densities of $r_{PS} = 1.05$ gcm^{-3} and $r_{SiO2} = 1.70$ gcm^{-3} a reasonable agreement with the experiment was found, when systematically only 0.8 instead of 1.0 SiO_2 particle from the nominal suspension composition were assumed to be mixed with the respective PS particles. One has to note that it is not possible to unambiguously determine the relative particle ratio with this method, since the expected mass loss only depends on the relative ratios at which the dispersions of set weight fractions were mixed. Nevertheless, TGA confirmed that less SiO_2 particles were found in the composite bulk than expected from the nominal suspension composition and that the difference falls in the same range as proposed by the SEM images. Deviations from the expected values (about 20 % less) can be explained by two problems. The first are inaccuracies in the determination of the particle number concentration in the pristine dispersion. The gravimetric determination of the dispersion weight fraction might be affected by intercalation of water into the porous silica particles and might lead to an overestimation. Furthermore, the density of the silica particles is not exactly known, which is needed for the calculation of the number particle concentration. The second influence could arise from the crystal fabrication process, which is conducted by vertical lifting deposition. Due to the difference in density the PS particles could be slightly preferably incorporated into the colloidal crystal due to their higher hydrodynamic mobility. Indeed, when analyzing a simply dried composite mixture by TGA one finds a higher silica content (~ 2 %) as compared to their colloidal crystal counterparts.

UV/Vis measurements also give insight into bulk properties. As shown in Figure 4.7.2 b) a systematic blue-shift with increasing silica content was found.

Using a modified Bragg equation, with an effective refractive index, one can calculate the expected Bragg peaks, $\lambda_{Bragg,\,exp}$ (compare chapter 2.4):[29]

$$\lambda_{Bragg,\,exp} = 1.63 \cdot d \cdot (0.74 \cdot x_{PS} \cdot n_{PS}^2 + 0.74 \cdot x_{SiO2} \cdot n_{SiO2}^2 + 0.26 \cdot n_{medium}^2)^{0.5} \qquad \text{Equation 4.7.3}$$

d is the diameter of the major component, x_{PS} and x_{SiO2} the particle fractions, n_{PS} and n_{SiO2} are the refractive indices.

In order to match the experimental UV/Vis measurements for the composite materials, the particle parameters were adjusted with the pure monomodal crystals. Refractive indices lower than for the bulk materials ($n_{PS} = 1.55$ and $n_{SiO2} = 1.37$) had to be used to

capture the experimental values. The low value for the silica particles might be rationalized by the intercalation of water into the porous network, as it was already found in the TGA measurements. Using these parameters all peaks could be captured within their experimental error, when taking the same reduction of SiO_2 particles into account as it was found before for the SEM and TGA analysis. The results of all methods are compiled in Table 4.7.1.

Table 4.7.1. Characterization of PS-SiO_2 composite colloidal crystal films by SEM, TGA, and UV/Vis. Experimental results are compared to their expected values.

expected PS/SiO_2 ratio	SEM counting	experimental PS/SiO_2 ratio	$x_{loss,\,exp}$ [a] %	x_{loss} %	$\lambda_{Bragg,\,exp}$ [b] nm	λ_{Bragg} nm
0 / 1	-	0 / 1	-	-	533.7	530.0 ± 7.9
0.33 / 1	0.3 / 2.0	0.3 / 0.8	20.5	21.0	551.9	555.0 ± 6.4
1 / 1	1 / 0.84	1 / 0.8	43.6	45.0	578.8	578.7 ± 3.6
2 / 1	2 / 0.88	2 / 0.8	60.7	64.8	588.3	586.0 ± 1.6
4 / 1	4 / 0.83	4 / 0.8	75.5	76.1	595.3	593.0 ± 3.6
8 / 1	8 / 1.14	8 / 0.8	86.1	87.0	599.7	599.0 ± 0.8
12 / 1	12 / 0.86	12 / 0.8	90.3	90.7	601.4	601.5 ± 0.5
1 / 0	-	1 / 0	-	-	605.0	602.1 ± 3.3

[a] *ρ_{PS}=1.05 gcm^{-3}, ρ_{SiO2}=1.7 gcm^{-3}, r_{PS} = 130 nm, r_{SiO2} = 127.5 nm.*
[b] *n_{PS}=1.55, n_{SiO2}=1.37; d = 260 nm for PS:SiO_2 = 1/1 – 12/1, d = 255 nm for PS:SiO_2 = 0.33/1 and 0/1*

Concluding, composite PS-SiO_2 colloidal crystals of various particle ratios were fabricated. Electromagnetic waves experience an effective refractive index of the composite material, which entails a systematic shift of the Bragg peak. The exact determination of the particle ratio is difficult, since important parameters such as particle density or refractive index are not exactly known for this system. The combination of SEM, TGA, and UV/Vis measurement revealed that systematically less silica particles were incorporated as expected. With the given set of parameters a good match between theory and experimental results could be achieved. However, due to the various interconnected parameters and experimental errors an overall inaccuracy of several percent remains.
Albeit the actual number particle ratios have been shown to be different, the intended numbers (2:1, 4:1, 8:1, and 12:1) will be still used for reason of clarity and simplicity. For calculations the true particle ratios will be used.
As shown in Figure 4.7.1 e) – h) the colloidal crystal matrix remains intact for particle ratios of 2:1, 4:1, 8:1, and 12:1 PS:SiO_2 after silica removal in PDMS. This approach can be regarded as designed defect doping, since a predefined number of holes are introduced into the continuous crystal. As the colloidal crystal itself remains intact the filling fraction of the entire film with PS spheres decreases with increasing number of introduced holes. Therefore the effective sound velocity, which is a function of the vol-

ume fraction of the constituting components,[27] should also change, namely decrease with increasing number of vacancy-defects.

BLS measurements in the low **q** range were conducted by Tim Still on four defect doped samples and the monomodal crystal. The measurements are shown in Figure 4.7.3.

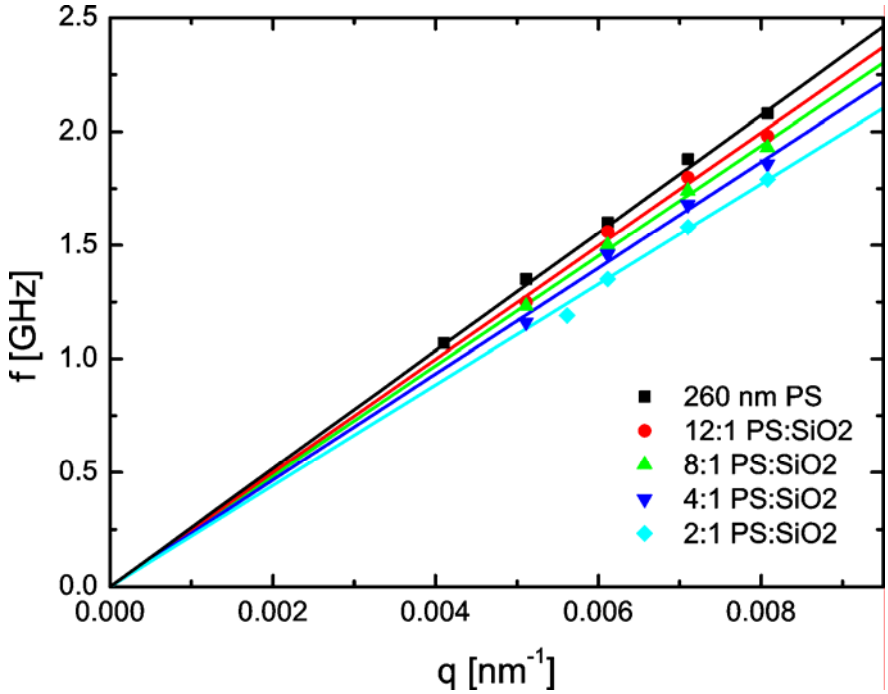

Figure 4.7.3. *BLS measurement on liquid infiltrated defect doped colloidal crystals, constituting of 250 nm PS spheres with an increase of designed vacancy-defects (from top to bottom). Straight lines are linear fits to the data points.*

The BLS measurement confirms the assumption. The monomodal crystal with a volume fraction of 74 % (fcc-crystal) of PS spheres exhibits the highest effective sound velocity, c_{eff}, which can be extracted from the slope of the linear fit by

$$c_{\text{eff}} = \frac{2\pi \cdot f}{q} \qquad \text{Equation 4.7.4}$$

Decreasing the volume fraction of the PS spheres in the overall film from 74 % to 54 % leads to a decrease in c_{eff} from 1565 m/s to 1337 m/s for longitudinal phonons. Transverse phonons are not observed experimentally, probably because PDMS can not support shear waves and the mechanical contact between the particles is weak. The results are listed in Table 4.7.2

Calculations based on the formalism given by Gaunaurd[27] were conducted to calculate the effective sound velocities in dependence of the varying volume fractions. The calculated sound velocities differ from the experimentally determined values in a systematic fashion. The mismatch increases with increasing PS volume fraction and in all cases a lower effective medium velocity was calculated.

Table 4.7.2. Influence of the volume filling fraction of PS spheres in a defect doped fcc crystal on the effective sound velocity, c_{eff}, of the composite material.

intended PS/SiO2 ratio	experimental PS/SiO2 ration	$x_{fcc,\,PS}$, %[a]	c_{eff} calculated, m/s	c_{eff} experimental m/s
2 / 1	2 / 0.8	53.7	1305	1337
4 / 1	4 / 0.8	62.3	1374	1409
8 / 1	8 / 0.8	67.6	1418	1463
12 / 1	12 / 0.8	69.6	1437	1507
1 / 0	1 / 0	74.0	1488	1565

[a] *the slight differences in particle diameter (260 nm to 255 nm) were taken into account.*
[b] $c_{t,\,PS}$ = 1200 m/s, $c_{l,\,PS}$ = 2350 m/s, r_{PS} = 1.05 gcm^{-3}; $c_{t,\,PDMS}$ = 0 m/s, $c_{l,\,PDMS}$ = 1050 m/s, ρ_{PDMS} = 965 gcm^{-3} *were used for calculation according to Gaunaurd and Wertmann.*[27]

The reason for this deviation is not quite clear. Possibly the theory starts to fail in this high frequency regime. Another explanation could be a sort of consolidation of the PS nanoparticles compared to their bulk properties.

4.7.3. Phononic bandgaps in colloidal crystals and glasses

Now, the focus is turned on the high frequency range, where the wave vector **q** reaches the first Brillouin zone (BZ) of the fcc crystal. The system under investigation is shown in Figure 4.7.5.

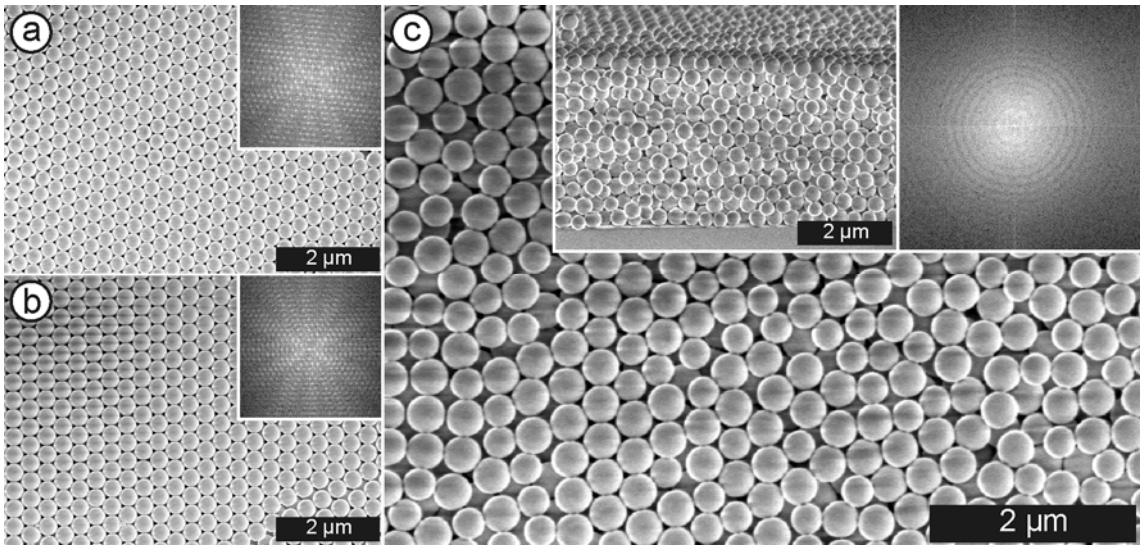

Figure 4.7.5. *a) and b) Monocrystalline regions of fcc crystals constituting of 307 nm and 360 nm PS spheres. c) Colloidal glass formed by mixing of monodisperse latexes of 307 nm and 360 nm in a 1:1 particle ratio. The insets show Fourier transformed images and a side view of the colloidal glass.*

Two monomodal colloidal crystals with 307 nm and 360 nm particle diameter will be investigated (Figure 4.7.5 a and b). As can be seen from the SEM image and its Fourier transform (inset) both sample are highly crystalline with a typical hexagonal arrangement for fcc crystals. Monocrystalline regions typically extend over ~ 100 µm in width

and several 100 µm in length. Mixing of the two monodisperse particle mixtures in a 1:1 particle ratio effectively suppresses the crystallization in an ordered fcc lattice (Figure 4.7.5 c). The Fourier transform and the cross section SEM image evidence the loss of order throughout the entire sample.

Firstly, the phononic band diagrams (all BLS measurements were conducted by Tim Still) of the two monomodal colloidal crystals will be examined. In the present case of fcc lattices the first BZ is a truncated octahedron. The experimental **q** is confined in the hexagon formed by the intersection of the (111) plane with the BZ.[20] The direction of **q** is selected along *Γ–M* (compare Figure 1.4 b) and the evolution of the BLS spectra with **q** near the BZ for the PS wet opal (d = 307 nm) is shown in Figure 4.7.6.

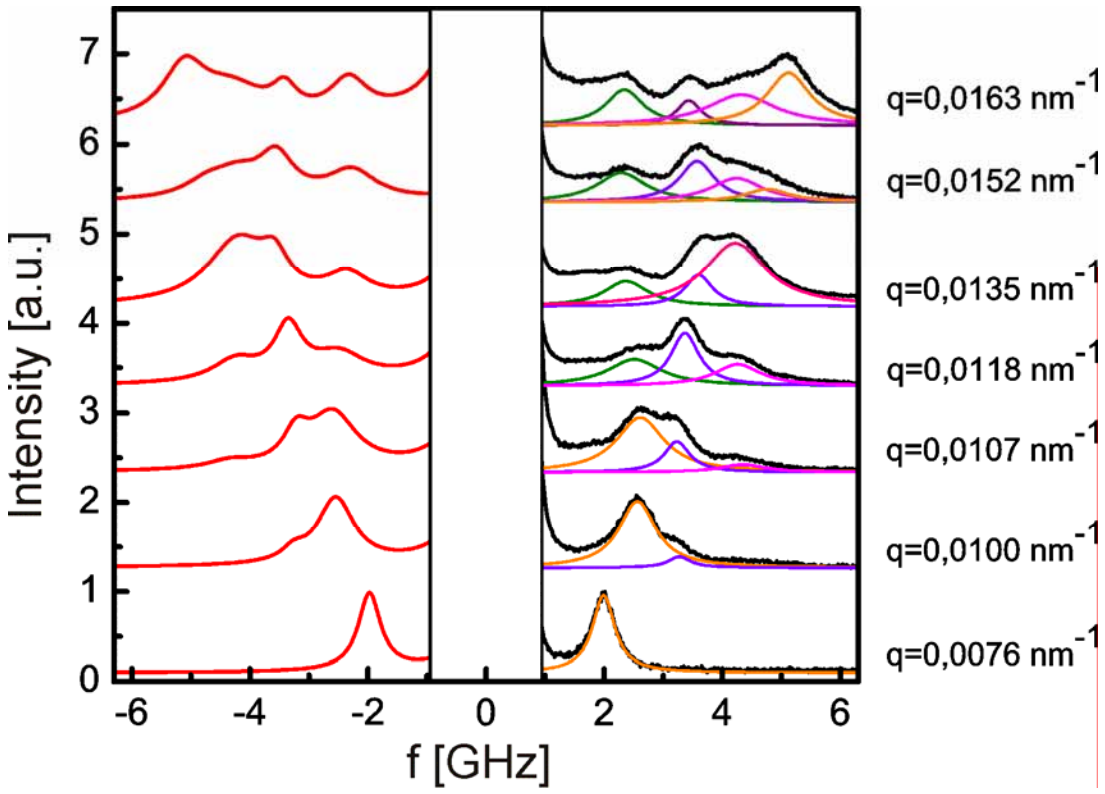

Figure 4.7.6. *BLS spectra of the wet opal of PS spheres with 307 nm diameter in a PDMS matrix at different wave vectors in the Γ-M direction of the fcc crystalline colloidal film. The edge of the BZ along the probed direction corresponds to* $\mathbf{q}_{BZ}$ *= 0.013 nm*$^{-1}$*. The deconvolution in different spectral components is indicated for the Anti-Stokes side of the spectrum, and the representation of the experimental spectra by the superposition of these Lorentzian lines is shown for the Stokes side. Each spectrum is normalized to the total integrated intensity, for comparison of the relative contributions.*

The simple picture of single phonon propagation in the effective medium at low **q** values becomes complex as **q** increases towards the BZ boundary. Up to four Lorentzian curves are required to represent the experimental BLS spectrum. In contrast to the PS–silicon oil opal[20] with a single peak splitting across the BZ boundary, the same opal infiltrated in PDMS providing higher elastic contrast displays richer spectral features and exhibits a second splitting at lower **q** values within the first BZ. The experimental

dispersion relations are depicted in Figure 4.7.7 a). In both hypersonic PS-PDMS crystals (d = 307 nm and d = 360 nm) only one longitudinal phonon branch is observed at low **q** values (**q** < 0.008 nm^{-1}) with c_{eff} = 1670 ms^{-1} and 1570 ms^{-1}, respectively, as outlined above. The most striking feature of the dispersion diagrams is the simultaneous presence of two band gaps at about 3 and 4 GHz in case of the 307 nm opal (Figure 4.7.7 a top) and at about 2.2 and 3.3 GHz for the 360 nm opal (Figure 4.7.7 a bottom). The gaps at higher frequency in each case are clearly BG since they occur at the edge of the BZ, **q** = $\mathbf{q}_{BZ}$ ≈ 0.0133 nm^{-1} and $\mathbf{q}_{BZ}$ ≈ 0.0113 nm^{-1}, that match the distance Γ–M, i.e., $(3/2)^{3/2}\pi/a$, where $a = \sqrt{2}\,d$ is the lattice constant of the given fcc crystal. The position of the Bragg gap shifts to higher frequencies with decreasing particle diameter.

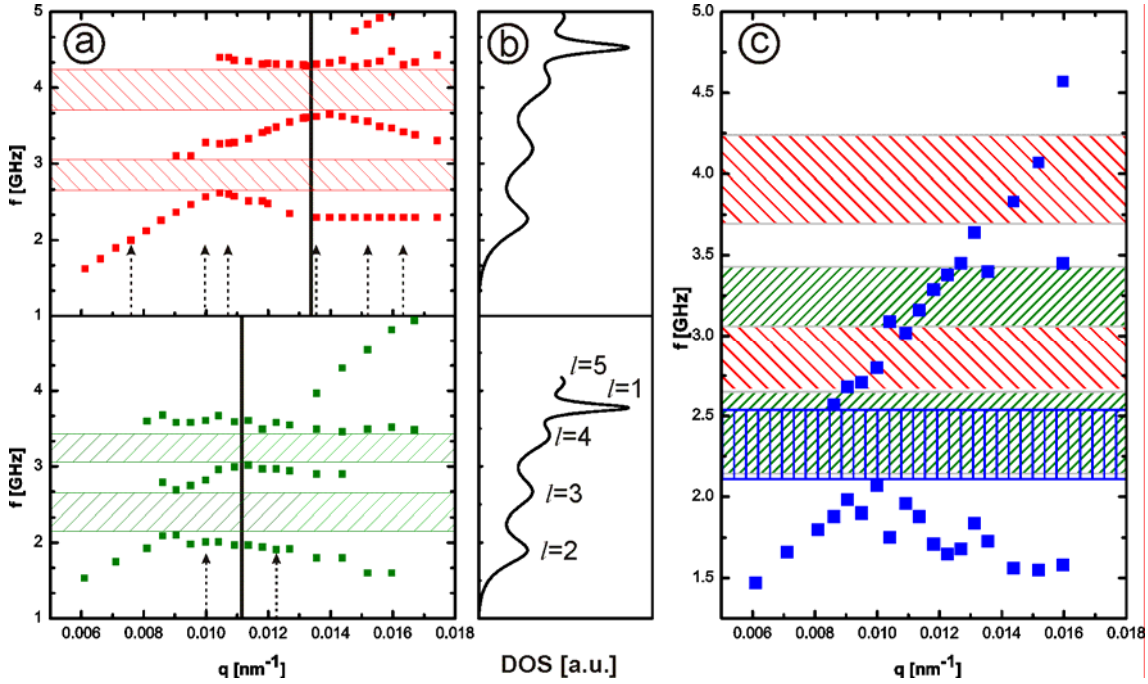

Figure 4.7.7. *a) Phononic band diagrams along the Γ–M direction for PDMS infiltrated PS opals consisting of 307 nm (top, red) and 360 nm (bottom, green) particles. The hatched bands mark the phononic gaps, and the vertical arrows indicate the* **q** *values in the corresponding spectra of Figure 4.7.6 and 4.7.8 below. The vertical lines denote the first BZ limit (for d = 307 nm and d = 360 nm, respectively). b) The change in the DOS induced by the corresponding single PS particle in PDMS is shown for the 307 nm (top) and 360 nm (bottom) particles. c) The phonon band diagram of a 1:1 307:360 nm PS particle mixture. The red and green hatched regions indicate the location of the phononic gaps in the corresponding monomodal crystal. Only a single gap (blue hatching) remains.*

In order to elucidate further the nature of the two gaps, the effect of the crystalline order on the experimental band diagram was examined. The formation of a colloidal glass consisting of a mixture of an equal number of two PS spheres (d = 307 nm and d = 360 nm) artificially broadens the size distribution beyond the polydispersity limit of about 5 % necessary for crystallization and is shown in Figure 4.7.5 c).[30] The effect of loss of crystalline order on the BLS spectra is demonstrated for two wave vectors in Figure 4.7.8.

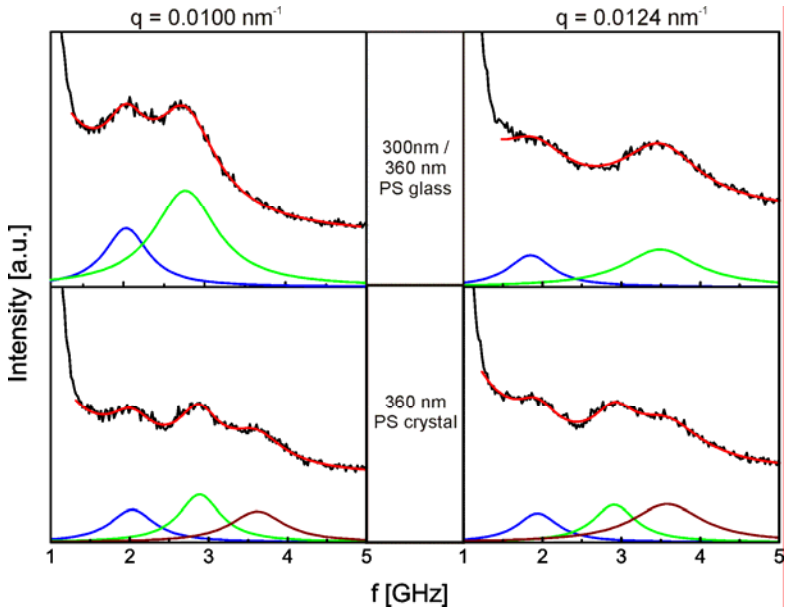

Figure 4.7.8. *Exemplary BLS spectra of the PS (d = 360 nm)/PDMS wet opal (bottom) and the wet PS mixture colloidal film (top) at two* ***q*** *values indicated by the arrows in the corresponding diagram of Figure 4.7.6 a). The deconvolution into different spectral components is shown below each spectrum (note the absence of the BG-induced spectral features in the colloidal glass).*

The deletion of one peak in the spectrum of the colloidal glass (Figure 4.7.8 top) is due to the disappearance of the BG in the disordered mixture, as it is clearly shown in the dispersion plot in Figure 4.7.6 c). Apparently, the crystalline order is a prerequisite for the BG but not for the newly observed lower frequency HG, which is omnidirectional in the colloidal glass. Interestingly, the remaining HG coincides well with the HG of the larger PS spheres. No increase in band width or occurrence of a second HG could be found in case of the colloidal glass. An identification of the latter as a theoretically anticipated HG,[2] through density-of-states (DOS) calculations (carried out by Rebecca Sainidou),[31] is examined in Figure 4.7.6 b). It displays several eigenmodes of the individual PS spheres embedded in the fluid PDMS. The lowest $f(1, 2)$ appears to compare well with the frequency at the crossing with the acoustic branch and the opening of the HG. Moreover, the lowest frequency points at the experimental dispersion at high **q**'s compare very well with the computed $f(1, 2)$. This and the two higher flat bands of localized modes in Fig. 4.7.6 a) cause sufficiently strong inelastic light scattering at high **q**'s[26] and compare well with the particle resonances of higher l. Their presence in the BLS spectra obscures the resolution of the phonons in the second BZ. Interestingly, the bands originating from particle resonant modes appear to be considerably narrower and occur at higher frequency than theoretically predicted.[2] This can be ascribed to viscous losses in the liquid matrix that were not taken into account in the theoretical calculations, and which weaken the interparticle interactions as a result of the reduced overlap between the corresponding wave fields.

4.7.4. Conclusions and outlook

In summary two distinct regions of phononic dispersion relations were separately investigated. The first falls in the range of low **q** values, where only acoustic phonons are measured. In liquid infiltrated colloidal crystals only longitudinal sound waves are found, which travel at an effective sound velocity falling between the sound velocities of their constituting materials. The effective sound velocity depends on the volume fraction of the single components, which was demonstrated by designed defect doping of a colloidal crystal. Comparison of the experimentally obtained effective sound velocities and theory shows a deviation, which increases with increasing PS content. Furthermore, the random incorporation of silica particles into a PS crystal causes a change in the effective refractive index, which results in systematic shift of the Bragg peak position.

The phononic band diagram becomes more complicated for the high **q** range, where significant deviations from the acoustic behavior occur. Two types of band gaps were found in PS colloidal crystals, these being a Bragg- (BG) and a hybridization- (HG) gap. The first occurs at the edge of the first BZ and critically depends on the fcc order in the colloidal film. The latter is insensitive to the order and thus remains even in colloidal glasses. The identification of the newly found HG gap was confirmed by DOS calculations of the resonant modes of PS spheres, which are embedded in PDMS.

Future challenges point to an even better understanding of the parameters governing the existence of phononic BG and HG. Especially the position and width of the HG needs to be elucidated in the light of the individual particle properties and their ensemble in a film. Understanding of these factors can help to effectively mold the flow of sound through designed materials.

4.7.5. Experimental part

Fabrication of PS-SiO_2 hybrid crystals. Monodisperse dispersions of 260 nm PS particles (PDI = 1.3 %) and 255 nm SiO2 particles (PDI = 5.9 %) were mixed in particle ratios of PS:SiO_2 = 1/0, 0.3/1, 1/1, 2/1, 4/1, 8/1, 12/1, 0/1, assuming a density of ρ_{PS}=1.05 gcm^{-3} and ρ_{SiO2}=1.70 gcm^{-3}. The concentration of the binary mixture was adjusted to 1.5 wt%. For BLS measurements on HF etched samples colloidal crystals were fabricated on plasma activated PET transparency foil (3M), else plasma activated glass was used. Vertical lifting deposition was used for colloidal crystal formation. For BLS, SEM and TGA analysis the lifting speed was set to 100 nm/s or 200 nm/s, for the UV/Vis characterization to 800 nm/s or 1000 nm/s at 20 °C to 25 °C and humidity of about 40 %. All binary samples were slightly stirred with a magnetic stirrer to ensure a homogenous dispersion composition during the entire process. Removal of the SiO_2 particles was conducted by HF etching in a 10% aqueous solution for 10 min.
Fabrication of colloidal crystals and glasses. Monodisperse dispersions of 307 nm and 360 nm PS particles were mixed in a 1:1 number particle ratio assuming a density of PS of ρ_{PS} = 1.05 gcm^{-3}. The weight fraction was adjusted to 1.0 wt%. Colloidal crystals and glasses were fabricated on clean glass slide by vertical lifting deposition at RT and ~70 % RH with a speed of 200 nm/s. PDMS of a molecular weight of 970 g/mol (made in-house) was used to infiltrate the colloidal crystal. Excessive PDMS was gently blown away by pressurized air.[20]
Characterization. BLS, SEM, and UV/Vis measurements were conducted as outlined in chapter 2. BLS measurements and data evaluation were carried out by Tim Still. DOS calculations were conducted by Rebecca Sainidou. TGA measurements were conducted on a Mettler TGA/SDTA 85 by Christina Löffler (MC I, University of Bayreuth). A heat rate of 10 K/min was applied for heating from RT to 600 °C, which was held for several hours.

4.7.6. Bibliography

1. Gorishnyy, T.; Maldovan, M.; Ullal, C.; Thomas, E. *Phys. World* **2005,** 18, (12), 24-29.
2. Psarobas, I. E.; Modinos, A.; Sainidou, R.; Stefanou, N. *Phys. Rev. B* **2002,** 65, (6), 064307.
3. Baumgartl, J.; Zvyagolskaya, M.; Bechinger, C. *Phys. Rev. Lett.* **2007,** 99, (20), 205503.
4. Sigalas, M.; Kushwaha, M. S.; Economou, E. N.; Kafesaki, M.; Psarobas, I. E.; Steurer, W. *Z. Kristallogr.* **2005,** 220, 765-809.
5. Kushwaha, M. S.; Halevi, P.; Dobrzynski, L.; Djafari-Rouhani, B. *Phys. Rev. Lett.* **1993,** 71, (13), 2022-2025.
6. Liu, Z. Y.; Zhang, X. X.; Mao, Y. W.; Zhu, Y. Y.; Yang, Z. Y.; Chan, C. T.; Sheng, P. *Science* **2000,** 289, (5485), 1734-1736.
7. Goffaux, C.; Sanchez-Dehesa, J.; Yeyati, A. L.; Lambin, P.; Khelif, A.; Vasseur, J. O.; Djafari-Rouhani, B. *Phys. Rev. Lett.* **2002,** 88, (22), 225502.
8. Martinez-Salazar, R.; Sancho, J.; Sanchez, J. V.; Gomez, V.; Llinares, J.; Meseguer, F. *Nature* **1995,** 378, (6554), 241-241.
9. Montero de Espinosa, F. R.; Jiménez, E.; Torres, M. *Phys. Rev. Lett.* **1998,** 80, (6), 1208-1211.
10. Sanchez-Perez, J. V.; Caballero, D.; Martinez-Sala, R.; Rubio, C.; Sanchez-Dehesa, J.; Meseguer, F.; Llinares, J.; Galvez, F. *Phys. Rev. Lett.* **1998,** 80, (24), 5325-5328.

11. Liu, Z. Y.; Chan, C. T.; Sheng, P.; Goertzen, A. L.; Page, J. H. *Phys. Rev. B* **2000,** 62, (4), 2446-2457.
12. Vasseur, J. O.; Deymier, P. A.; Chenni, B.; Djafari-Rouhani, B.; Dobrzynski, L.; Prevost, D. *Phys. Rev. Lett.* **2001,** 86, (14), 3012-3015.
13. Yang, S. X.; Page, J. H.; Liu, Z. Y.; Cowan, M. L.; Chan, C. T.; Sheng, P. *Phys. Rev. Lett.* **2002,** 88, (10), 104301.
14. Zhang, X. D.; Liu, Z. Y. *Appl. Phys. Lett.* **2004,** 85, (2), 341-343.
15. Yang, S. X.; Page, J. H.; Liu, Z. Y.; Cowan, M. L.; Chan, C. T.; Sheng, P. *Phys. Rev. Lett.* **2004,** 93, (2), 024301.
16. Lu, M.-H.; Liu, X.-K.; Feng, L.; Li, J.; Huang, C.-P.; Chen, Y.-F.; Zhu, Y.-Y.; Zhu, S.-N.; Ming, N.-B. *Phys. Rev. Lett.* **2007,** 99, (17), 174301-4.
17. Gorishnyy, T.; Ullal, C. K.; Maldovan, M.; Fytas, G.; Thomas, E. L. *Phys. Rev. Lett.* **2005,** 94, (11), 115501.
18. Jang, J. H.; Ullal, C. K.; Gorishnyy, T.; Tsukruk, V. V.; Thomas, E. L. *Nano Lett.* **2006,** 6, (4), 740-743.
19. Fustin, C. A.; Glasser, G.; Spiess, H. W.; Jonas, U. *Langmuir* **2004,** 20, (21), 9114-9123.
20. Cheng, W.; Wang, J.; Jonas, U.; Fytas, G.; Stefanou, N. *Nat. Mater.* **2006,** 5, 830-836.
21. Gorishnyy, T.; Jang, J.-H.; Koh, C.; Thomas, E. L. *Appl. Phys. Lett.* **2007,** 91, (12), 121915-3.
22. Yannopapas, V.; Modinos, A.; Stefanou, N. *Phys. Rev. B* **1999,** 60, (8), 5359.
23. Liu, J.; Ye, L.; Weitz, D. A.; Ping, S. *Phys. Rev. Lett.* **1990,** 65, (20), 2602-2605.
24. Ye, L.; Liu, J.; Sheng, P.; Weitz, D. A. *Phys. Rev. E* **1993,** 48, (4), 2805.
25. Jing, X.; Sheng, P.; Zhou, M. *Phys. Rev. Lett.* **1991,** 66, (9), 1240.
26. Penciu, R. S.; Kriegs, H.; Petekidis, G.; Fytas, G.; Economou, E. N. *J. Chem. Phys.* **2003,** 118, (11), 5224-5240.
27. Gaunaurd, G. C.; Wertman, W. *J. Acoust. Soc. Am.* **1989,** 85, (2), 541-554.
28. Bogush, G. H.; Tracy, M. A.; Zukoski, C. F. *J. Non-Cryst. Solids* **1988,** 104, (1), 95-106.
29. Gaillot, D. P.; Graugnard, E.; King, J. S.; Summers, C. J. *Journal of the Optical Society of America B-Optical Physics* **2007,** 24, (4), 990-996.
30. Phan, S. E.; Russel, W. B.; Zhu, J. X.; Chaikin, P. M. *J. Chem. Phys.* **1998,** 108, (23), 9789-9795.
31. Sainidou, R.; Stefanou, N.; Psarobas, I. E.; Modinos, A. *Z. Kristallogr.* **2005,** 220, 848-858.

5. Conclusion and Outlook

The work presented here is based on materials, which require monodisperse particles as essential building blocks. Emulsifier-free emulsion polymerization and the Stöber process were used to fabricate clean, monodisperse polystyrene (PS), polymethylmethacrylate (PMMA), and silica particles with adjusted material properties and surface functionalities. This library of particles with sizes ranging from 100 nm to more than 1 µm was employed to fabricate designed, novel materials for advanced surface patterns by nanosphere lithography (NSL) and for a better understanding of mechanical wave propagation. Self-assembly was the method of choice to autonomously arrange the particles in highly ordered crystalline structures, these being either three-dimensional (3D) face-centered-cubic (fcc) colloidal crystals or two-dimensional (2D) hexagonally packed monolayers.

For 2D monolayers the dry, sparsely distributed particles (*DSDP*) method was introduced and investigated in detail. The key step of this procedure is to float a film of sparsely distributed particles (PS or PMMA), which were dried on a parent substrate, at the air-water interface. Self-assembly takes place instantaneously at the three-phase-contact line (substrate-air-water) by interplay of long-range attractive capillary forces and short range electrostatic repulsion. The method is simple, fast, and versatile yielding monolayers of square-centimeter area with monocrystalline domains of up to hundreds of micrometers. Floating monolayers were fabricated with PS and PMMA particles in a range from 100 nm to 1.1 µm and can be transferred to manifold target substrates due to their mechanical robustness.

A unique property of this monolayer fabrication procedure is the anisotropic shrinkage of the sparsely distributed particle films along the direction of the parent substrate immersion, giving monolayers, which are more compact than their initial sub-monolayers. This method generally provides the possibility to produce patterned hetero-monolayers consisting of particles with different sizes and/or materials in a single step, which has not been possible by other methods so far. Inkjet printing was used to pre-define a pattern of various particle types on the parent substrate, which was preserved during the floating step. Taking into account the extent of shrinkage, which depends on the particle surface coverage, it was possible to fabricate hetero-monolayers of various patterns and feature sizes down to ~ 40 µm, which was even less than the actual printer resolution.

Further improvements in this field can be expected from automation of the entire process leading to larger monocrystalline domains due to less turbulence during the floating

and transfer step. State-of-the-art piezoelectric printers, which dispense only picoliter drops, could decrease the minimum feature sizes. Finally, this method could potentially be implemented into a continuous production process, which is of high importance for future technological applications.

The unique properties of the established monolayers (large monocrystalline domains, high mechanical stability) were used for the fabrication of novel materials by nanosphere lithography.

The high mechanical stability of the floating monolayer from the *DSDP* process was exploited for a transfer to hydrophobic substrates. These hydrophobic substrates were mandatory for the fabrication of ultraflat, laterally nanostructured surfaces in a modified template-stripped-gold process. Gold triangles of only a few 100 nm in side length could be successfully embedded in a silica matrix. Besides the ability to selectively functionalize the nanostructured pattern, it was also possible to employ these materials as reusable sensors due to their embedded localized surface plasmon resonators.

Furthermore, non-close-packed hexagonal monolayers were generated by a homogenous size reduction of the initially contacting PS spheres via plasma etching. These served as templating mask for the fabrication of ordered arrays of golden split-ring resonators. Hexagonally, densely packed arrays of crescents with adjustable size (hundreds of nanometers) and inter-particle spacing (tens of nanometers) were obtained. These dense nanoparticle arrays could be covered with a thin layer of silica allowing the deposition of a second array on top with controlled relative orientation. The optical characterization confirmed the pre-defined mutual orientation of the split-ring resonators between the individual layers. Appropriate design of orientation and spacing of such crescent arrays could lead to potentially chiral metamaterials due to the interaction of the nanoparticle optical near-fields.

Besides the fabrication of nanostructures in two-dimensional planes, a method based on vertical lifting deposition was introduced to fabricate 3D inverse opals with defined structural hierarchy. Into the porous network of a host inverse opal, a second mesostructured network was intercalated, giving rise to the term “inverse opal in inverse opal” (IOIO). The multiple steps of this method allow for a range of material combinations to be used in these hierarchical structures, such as SiO_2, TiO_2, or Al_2O_3; but also mesostructured polymers can be accessed. Such materials might be useful for storage or catalysis applications due to their high internal interface, which is readily accessible through the interconnected macropores.

Three-dimensional colloidal crystals and glasses were also fabricated by vertical lifting deposition to investigate their phononic properties by Brillouin Light Scattering (BLS). At first the vibrational resonant modes of individual particles were measured in dry, opaque colloidal films, which gave access to their mechanical properties. A linear dependence between the particle eigenmodes and their inverse diameter was found. The eigenmode spectra of a mixture of two monodisperse samples showed a superposition of the individual monomodal resonances, indicating independence of these resonances from the local particles environment. PMMA/nBA particles of increasing nBA content were synthesized with a systematic drop in Tg, but of almost identical size (~ 200 nm). The eigenfrequencies of such latex particles exhibited a monotonous shift to lower frequencies with increasing nBA content, which could be attributed to a reduction in particle rigidity. For silica-core/PMMA-shell particles the mechanical properties were determined by fitting their experimental eigenmodes, and both, the core and shell material, were found to be tougher compared to their individual bulk values. Elastic field calculations showed that the resonant modes were localized in the PMMA shell. The eigenmodes of hollow PMMA capsules exhibited an invariance to the particle diameter, which is due to competing effects of particle size and shell thickness.

Infiltration of the opaque colloidal crystals with a refractive index matching liquid (like PDMS) allowed angular dependent measurements. The resulting dispersion relation diagrams can be split into two regions of interest, one spanning the low **q** range, the other spanning the high **q** range. The effective sound velocity of a composite material (like PS particles infiltrated with PDMS) depends on the volume fraction of the constituting components and can be assessed by the low **q** branch. Vacancy-defect doped polystyrene fcc crystals with a volume fraction from 74 % to 54 % exhibited a decrease in effective sound velocity from 1565 m/s to 1337 m/s, which is in qualitative agreement with the effective medium theory.

Measurements in the high **q** range on PS colloidal crystals revealed two distinct phononic band gaps. One gap originated from the order in the fcc crystal, thus termed Bragg gap, whereas the other gap is based on the degenerated eigenmodes of the colloidal particles, and is therefore termed “hybridization gap”. Suppression of crystalline order by a binary mixture of monodisperse PS particles made the Bragg gap vanish, whereas the hybridization gap remained at the position of the larger particles.

More research needs to be conducted to achieve a full understanding of the phononic properties of such nanostructured materials. Knowledge of the mechanical properties of their building blocks – the individual particles – is mandatory to design materials with a

specific phononic behavior. On the long run materials, which effectively mold the flow of hyperfrequent sound, will have a high impact on upcoming technologies, such as opto-acoustic circuits or the control of heat flow in nanostructured materials.

Acknowledgements

This work would not have been possible without the help of many people.

First of all, I want to thank my supervisors from the Materials Research Group (MRG) at the Max Planck Institute for Polymer Research and from the university of Mainz.
I want to express my gratitude to my supervisor, for his myriad of inspiring ideas. Thank you for your support at all times, your motivation, and also for hours of discussion - scientific or not - and the chance to work in Crete.
Amongst many people I worked with, I want to stress out the excellent cooperation with the people on the phononic characterization, which was very productive and fruitful.
Furthermore, I want to thank my other collaboration partners for their input, ideas, help, and patience, which comprise of many people from the MPIP.
I profited a lot from hands-on support from our service groups in a range of practical demands, lab issues, etc., these being the mechanical and electronic workshop as well as the house technicians.
I had the chance to learn and use a range of characterization techniques. Thanks to the instructors and operators for their kind help.
I spent an incredible amount of time in various labs scattered through the institute. I want to thank all the lab technicians for their help with synthetic issues and the good atmosphere in their laboratories.
I had two internship students during my PhD. Thanks for your help and valuable input.
I want to especially thank my friends from the University of Bayreuth, who generously gave me access to their SEM machine, when I needed it most at the end of my lab work.
Finally, I want to express my gratitude to many Diploma and PhD students, Postdocs, and guests from MPIP and the university. I am happy to having met you and worked with you. But even more important thanks to your contribution to make life at the institute and beyond more enjoyable.
For financial and intellectual support I want to thank my Kekulé scholarship provided by the Stiftungsfond Stipendium of the Fonds der Chemischen Industrie, as well as the International Max Planck Research School (IMPRS), the Elite Network Bavaria (ENB), and e-fellows.

List of Publications and Presentations

Accepted publications:

1. Li, Q.; Retsch, M.; Wang, J.; Knoll, W.; Jonas, U., *Porous Networks Through Colloidal Templates*. Topics in Current Chemistry **2008**, http://dx.doi.org/10.1007/128_2008_3.
(chapter **1.2** and **4.5**)

2. Retsch, M.; Zhou, Z.; Rivera, S.; Kappl, M.; Zhao, X. S.; Jonas, U.; Li, Q., *Fabrication of Large Area, Transferable Colloidal Monolayers Utilizing Self-Assembly at the Air-Water Interface.* Macromolecular Chemistry and Physics **2008**, 210, 230-241 (cover page)
(chapter **4.1**)

3. Vogel, N.; Jung, M.; Retsch, M.; Jonas, U.; Knoll, W.; Köper, I., *Laterally Patterned Ultraflat Surfaces.* Small **2008**, http://dx.doi.org/10.1002/smll.200801583.
(chapter **4.4**)

4. Still, T.; Cheng, W.; Retsch, M.; Jonas, U.; Fytas, G., *Colloidal systems: a promising material class for tailoring sound propagation at high frequencies.* Journal of Physics: Condensed Matter **2008**, 20, (40), 404203.
(chapter **4.6**)

5. Still, T.; Sainidou, R.; Retsch, M.; Jonas, U.; Spahn, P.; Hellmann, G. P.; Fytas, G., *The "music" of core-shell spheres and hollow capsules: Influence of the architecture on the mechanical properties at the nanoscale.* Nano Letters **2008**, 8, (10), 3194-3199.
(chapter **4.6**)

6. Still, T.; Cheng, W.; Retsch, M.; Sainidou, R.; Wang, J.; Jonas, U.; Stefanou, N.; Fytas, G., *Simultaneous occurrence of structure-directed and particle-resonance-induced phononic gaps in colloidal films.* Physical Review Letters **2008**, 100, 194301.
(chapter **4.7** and **1.3**)

Publications in Preparation:

7. Retsch, M.; Tamm, M.; Bocchio, N.; Horn, N.; Förch, R.; Jonas, U.; Kreiter, M.; *Parallel Preparation of Densely Packed Arrays of 150 nm Split-Ring Resonators in Three Dimensions.* submitted to Small
(chapter **4.3**)

8. Vogel N.; Jung, M.; Bocchio, N.; Retsch, M.; Kreiter, M.; Köper, I.; *Reusable localized surface plasmon sensors based on ultrastable nanostructures.* in preparation
(chapter **4.4**)

9. Retsch, M.; Dostert, K.-H.; Nett, S.; Gutmann, J.; Jonas, U.; *Template Free Structuring of Colloidal Monolayers using Inkjet Printing.* in preparation
(chapter **4.2**)

10. Retsch, M., Jonas, U.; *Composite Inverse Opals in Inverse Opals.* in preparation
(chapter **4.5**)

Contributed Talks

"Deaf Films and Golden Croissants"

22nd Conference of the European Colloid and Interface Society
Cracow, Poland
31.08. - 05.09.2008

Poster Contributions

"Killing" Bragg – Phononic Band Gaps in Colloidal Films

Bayreuther Polymer Symposium
Bayreuth, Germany
09.09 - 11.09.2007

"Killing" Bragg – Phononic Band Gaps in Colloidal Films

3rd STIPOMAT conference
LesDiablerets, Switzerland
14. - 17.10.2007

Phononic Properties of Colloidal Particles and Nanostructured Films

Makromolekulares Kolloquium 2009
Freiburg, Germany
26. - 28.02.2009
Macromol. Biosci., **2009**, 9, F66

Press

Top down, Bottom up: Working in Harmony

in Nature Nanotechnology, 2008, 3, 641

Wasserbad als Ordnungshilfe

MPG press release, ISSN 0170-4656
Chemie.de, www.chemie.de/news/d/94345/